



HAL
open science

Anharmonicity and Instabilities in Halide Perovskites for Last Generation Solar Cells

Arthur Marronnier

► **To cite this version:**

Arthur Marronnier. Anharmonicity and Instabilities in Halide Perovskites for Last Generation Solar Cells. Materials Science [cond-mat.mtrl-sci]. Université Paris Saclay (COMUE), 2018. English. NNT : 2018SACLX031 . tel-01941725

HAL Id: tel-01941725

<https://pastel.hal.science/tel-01941725>

Submitted on 2 Dec 2018

HAL is a multi-disciplinary open access archive for the deposit and dissemination of scientific research documents, whether they are published or not. The documents may come from teaching and research institutions in France or abroad, or from public or private research centers.

L'archive ouverte pluridisciplinaire **HAL**, est destinée au dépôt et à la diffusion de documents scientifiques de niveau recherche, publiés ou non, émanant des établissements d'enseignement et de recherche français ou étrangers, des laboratoires publics ou privés.

Anharmonicity and Instabilities in Halide Perovskites for Last Generation Solar Cells

Thèse de doctorat de l'Université Paris-Saclay
préparée à l'École Polytechnique

École doctorale n°573 Interfaces : Approches
Interdisciplinaires : Fondements, Application et Innovation

Spécialité de doctorat: **Physique**

Thèse présentée et soutenue à
l'École Polytechnique le 27 juin 2018, par

Arthur Marronnier

Composition du Jury :

Pr. Emmanuelle Deleporte ENS Paris-Saclay, Univ. Paris-Sud (Lab. Aimé Cotton – CNRS)	Présidente
Pr. Matteo Calandra Sorbonne Universités–UPMC (IMPMC – UMR CNRS 7590)	Rapporteur
Pr. Gian-Marco Rignanese Université Catholique de Louvain (IMCN), Belgique	Rapporteur
Dr. Edoardo Mosconi CNR-ISTM Perugia (CLHYO), Italie	Examineur
Dr. Laurent Pedesseau INSA de Rennes (FOTON – CNRS UMR 6082)	Examineur
Pr. Yvan Bonnassieux École Polytechnique (LPICM – CNRS UMR 7647)	Directeur de thèse
Dr. Guido Roma CEA Paris-Saclay (SRMP)	Co-encadrant
Jean-Paul Gaston Product Manager, Horiba Jobin Yvon	Invité

© 2018 - *ARTHUR MARRONNIER*

ALL RIGHTS RESERVED.

Anharmonicity and Instabilities in Halide Perovskites for Last Generation Solar Cells

ABSTRACT

Beyond climate change, the depletion of fossil fuels, waste recycling and other environmental issues compel scientists to find alternative energy sources to the current solutions which are either unsustainable, induce high carbon emissions, or present an important risk for populations. In this context, solar energy appears as one of the strongest contenders considering it is a low-emission, safe, and infinite source of energy. This technology, in particular inorganic solar cells (first generation and thin films), has now become competitive with others in terms of costs and lends itself as much to installation on rooftops as to integration in windows or even in roads (organic solar cells, second generation).

Hybrid halide perovskites (ABX_3) — a third generation — have emerged over the past five years as absorber layers for novel high-efficiency low-cost solar cells combining the advantages of organic (molecule A) and inorganic (metal B and halide X) materials. The main advantages of perovskite solar cells are their easy and low-cost deposition (liquid or thermal evaporation), the use of thin film structures, their strong absorption, slow recombination, high mobility, high defect tolerance and rather optimized band gap for single and tunable for tandem cells. In the race to commercialization, flagship methylammonium-based perovskite $CH_3NH_3PbI_3$ ($MAPbI_3$ or "MAPI"), very sensitive to ambient conditions (temperature, oxygen, humidity, light), will probably be outpaced by more stable cesium-based mixed cation mixed halide structures. Very recently, fully inorganic perovskite quantum dots also showed promising efficiencies, making them a potentially stable and efficient alternative to their hybrid cousins.

The aim of this PhD thesis is to study and better understand both the structural and thermodynamical instabilities of these halide perovskites, with a specific focus on purely inorganic $CsPbI_3$ structures.

We first use various ab-initio techniques, the majority of which are based on Density Functional Theory (DFT) and its linear-response approach (DFPT), to investigate the vibrational properties of the different phases of $CsPbI_3$. While the black γ -phase — crucial for photovoltaic applications — is shown to behave harmonically around equilibrium, for the other three phases our frozen phonon calculations reveal a Brillouin zone-center double-well instability. Using total energy and vibrational entropy calculations, we highlight the strong competition between all the low-temperature phases of $CsPbI_3$ (γ , δ , β) and show that avoiding the order-disorder entropy term arising from double-well instabilities is key in order to prevent the formation of the yellow perovskitoid phase. This metastability is further confirmed in the framework of a collaboration by high resolution in-situ synchrotron X-ray diffraction measurements evidencing the existence of a tetragonal phase and showing that $CsPbI_3$ can be undercooled below its transition temperature and temporarily maintained in its perovskite γ -phase structure down to room temperature. The Rashba effect we found is also inspected through this collaboration using a symmetry-based tight-binding model, validated by self-consistent GW calculations including spin-orbit coupling, for both cubic and tetragonal phases when using the symmetry breaking structures obtained through our frozen phonon calculations. We then analyze in detail Car-Parinello molecular dynamics data in the light of our findings on the anharmonic potential energy surface of the cubic phase of $CsPbI_3$. Lastly, we perform electronic band calculations, including spin-orbit coupling, in order to investigate the space and time dynamics of the Rashba effect found in these materials.

In a second phase, we study the thermodynamical stability of hybrid perovskite $MAPbI_3$. We evidence the light-induced degradation timescales of the electrical (current-voltage studies) and optical (ellipsometry, optical indexes) properties of these materials using various experimental methods. Our study brings better understanding of the chemical decomposition of MAPI into its two precursors, methylammonium and lead iodides, which we predicted using DFT stability diagram calculations and

which we confirm by X-Ray diffraction. Last, we use the results of our optical constant study, completed by ab initio calculations, to prove that hybrid perovskite structure $MAPbI_3$ behaves more like inorganic compounds (high dielectric constant, low exciton binding energy) than like organic materials (low dielectric constant, high exciton binding energy).

Anharmonicit  et instabilit s dans les perovskites halog n es pour les cellules solaires de derni re g n ration

R SUM 

Au-del  de la question du changement climatique, l' puisement des ressources fossiles, le recyclage des d chets et d'autres probl matiques environnementales contraignent les scientifiques   trouver des sources d' nergies alternatives aux sources non durables,   fort rejet de carbone ou pr sentant des risques importants pour les populations. Dans ce contexte, l' nergie solaire appar t comme l'une des meilleures sources d' nergie   faible  mission, sans risques et au potentiel infini   notre  chelle. Cette technologie, en particulier les cellules solaires inorganiques (premi re g n ration et couches minces) est devenue comp titive avec les autres sources d' lectricit  en termes de co ts et peut- tre aussi bien install e sur les toits qu' tre int gr e aux fen tres (cellules solaires organiques, deuxi me g n ration) ou aux routes.

Les p rovskites hybrides halog n es (ABX_3) — la troisi me g n ration — sont utilis es depuis cinq ans comme couches absorbantes pour de nouvelles cellules solaires   bas co t combinant les avantages des mat riaux organiques (mol cule A) et inorganiques (m tal B, halog ne X). Les principaux avantages des cellules photovolta ques p rovskites sont leur m thode de fabrication facile et   bas co t (voie liquide ou  vaporation), l'utilisation de structures en couches minces, leur forte absorption, une recombinaison lente, une mobilit   lev e, une tol rance  lev e aux d fauts et une bande interdite   la fois bien optimis e pour les cellules simples et accordable pour les tandems. Dans la course   la commercialisation, la p rovskite phare   base de m thylamonium $CH_3NH_3PbI_3$ ($MAPbI_3$ ou "MAPI"), tr s sensible aux conditions ambiantes (temp rature, oxyg ne, humidit , lumi re), sera probablement d pass e par des structures plus stables   base de c sium qui m langent diff rents cations et ions halog nes. Tr s r cemment, des cellules solaires   bo tes quantiques   bases de p rovskites purement inorganiques ont

également montré des efficacités prometteuses, ce qui en fait une alternative potentiellement stable et efficace à leurs cousines hybrides.

Le but de cette thèse de doctorat est d'étudier et de mieux comprendre les instabilités structurelles et thermodynamiques de ces pérovskites halogénées, avec un focus sur la pérovskite purement inorganique $CsPbI_3$.

Dans un premier temps les propriétés vibrationnelles des différentes phases de $CsPbI_3$ sont étudiées grâce à différentes techniques ab-initio, dont la plupart sont basées sur la théorie de la fonctionnelle de la densité et sur l'approche de la réponse linéaire (DFPT). Alors que la phase γ noire — cruciale pour les applications photovoltaïques — se comporte de manière harmonique autour de l'équilibre, pour les trois autres phases nos calculs de phonons froids révèlent une instabilité de double puits au centre de la zone de Brillouin. Grâce à des calculs d'énergie totale et d'entropie vibrationnelle, nous mettons en évidence la forte compétition entre toutes les phases à basse température de $CsPbI_3$ (γ, δ, β) et montrons que le terme d'entropie d'ordre-désordre lié aux instabilités de double puits est un facteur clé pour empêcher la formation de la phase perovskitoïde jaune. Cette metastabilité est approfondie et confirmée dans le cadre d'une collaboration grâce à des mesures de diffraction aux rayons X en synchrotron in situ à haute résolution prouvant l'existence d'une phase tétragonale et montrant que $CsPbI_3$ peut être refroidi en dessous de sa température de transition et maintenu temporairement dans sa phase γ pérovskite à température ambiante. L'effet Rashba que nous obtenons est également examiné à travers cette collaboration par un modèle de liaisons fortes basé sur la symétrie, validé par des calculs GW auto-cohérents incluant le couplage spin-orbite, pour les phases cubiques et tétragonales dans le cas de nos structures à symétrie brisée issues des calculs de phonons. Pour la phase cubique de $CsPbI_3$ nous analysons ensuite en détail les données de dynamique moléculaire Car-Parinello à la lumière de nos résultats sur sa surface d'énergie potentielle anharmonique. Enfin, des calculs de structure de bandes

électroniques avec spin-orbite sont menés afin d'étudier la dynamique spatiale et temporelle de l'effet Rashba mis en évidence dans ces matériaux.

Dans un deuxième temps, nous étudions la stabilité thermodynamique de la pérovskite hybride $MAPbI_3$. À l'aide de différentes méthodes expérimentales, nous mettons en évidence les échelles de temps sur lesquelles se produit le vieillissement induit par la lumière ambiante tant au niveau des propriétés électriques (études courant-tension) qu'optiques (ellipsométrie, indices optiques). Notre étude apporte une meilleure compréhension de la décomposition chimique de MAPI en ses deux précurseurs, l'iodure de méthylamonium et l'iodure de plomb, que nous avons prédite grâce à des calculs du diagramme de stabilité DFT et que nous confirmons par diffraction des rayons X. Enfin, nous utilisons les résultats de notre étude sur les constantes optiques de $MAPbI_3$, complétée par des calculs ab initio, pour démontrer que la perovskite hybride $MAPbI_3$ se comporte davantage comme les composés inorganiques (grande constante diélectrique, faible énergie de liaison des excitons) que comme les matériaux organiques (faible constante diélectrique, forte énergie de liaison d'exciton).

À MES REGRETTÉS GRANDS-PARENTS

Preface & Acknowledgments

CHALLENGING AS IT WAS TO PURSUE A PHD in the fast-paced and competitive field of halide perovskites, I have my colleagues to thank for the precious help and contributions without which I could not have gotten to the point of writing this manuscript. This challenge was all the way greater since I enjoyed quite an unusual start - neither did my PhD start as the following up of an internship nor did I apply to a ready and preconceived thesis topic. I chose to start a project combining ab-initio calculations at a lab specialized in nuclear materials (SRMP at CEA Saclay) with experiments at the LPICM team at Polytechnique, where, when I started my PhD in 2015, hybrid perovskites were a brand new topic, in particular in terms of modeling.

When a few months before starting my PhD I organized a meeting between Yvan (Polytechnique) and Guido (CEA) to try to build together a project, there was no guarantee that we could mold my motivation into a fruitful project. I am deeply grateful to Guido for accepting to take up this challenge with me, for introducing me to the subtleties of DFT and for always coming up with new ideas of future developments after each interesting result. I cannot thank Guido enough for his flexibility, understanding and patience; after 2 years away from quantum mechanics it took me quite some time to get back in the game. Guido has provided me with clear and precious guidance throughout the various projects of my PhD, and it is due to his deep knowledge of DFT for materials that we managed to give, little by little, a meaningful direction to my PhD, always taking into account our resources and the latest trends in the - insanely prolific - literature on perovskites. Finally, I would like to thank him for his ever attentive help rigorously proofreading my articles as well as this manuscript.

During this multi-faceted project (ellipsometry and synchrotron experiments, ab-initio calculations,

teaching) I could always count on Yvan to give me the bigger perspective on my work, on where we were going, and on how to find synergies with the other PhD candidates of the team. On this matter, the bi-monthly perovskite team meetings (with Bernard, Denis, Jean-Éric, Warda, Heejae, Éric, Chloé) were very precious, and were an ideal complement to the more isolated work I did at CEA with Guido. I would like to thank Yvan in particular for giving me many great opportunities to share and present my work with the perovskite community at various international conferences (PSCO Lausanne, PSCO Genoa, EUPVSEC Amsterdam, HOPV Japan, IEEE-PVSC Hawaii). I realize how lucky I am to have been financially supported each time I was accepted to be an oral speaker at an international conference, and to spend time working in other labs (Rennes and Perugia, Italy). On the financial aspects, I am grateful towards the French Department of Energy and the Graduate School of École des Ponts ParisTech for funding my doctorate project. I also acknowledge Polytechnique for choosing me as their candidate for the Siebel Award in Energy Science as well as Leo Liberti, Guido, Yvan, Luc de Marliave and Jean-Paul Gaston; without their help in building my application I would not have won the Siebel. I also thank Holger and Fatima for their help with GENCI applications.

I would like to thank Heejae Lee for our great scientific collaboration and friendship that has grown during our PhD projects. In Heejae I found an amazing lab partner, with a complementary background (device and experiments for him, theory and calculations for me), and it was a pleasure to represent jointly the Polytechnique Perovskite Team at various conferences. I take this opportunity to sincerely thank all the support teams of the lab (BEER team, Laurence, Carine, Fabienne, Gaby, Patricia, Fred for donatello!).

I thank Bernard for helping me construct my PhD scholarship application and for his continuous advice during our team meetings, Denis for his precious experimental knowledge and Jean-Éric for his theoretical insights.

It is important to me to thank many people when it comes to the ellipsometry-based degradation study we performed in collaboration with Horiba. I would like to acknowledge the contributions of Céline and Jean-Paul, as well as the help of Heejae and Heeryung (sample preparation) and Minjin (XRD measurements).

The fruitful collaboration I started with Jacky Even (FOTON, Rennes) was the result of an inspiring discussion with Pere Roca, head of the PICM lab, who told me to always be looking for new advisors to enlarge my horizons and resources. I would like to acknowledge Pere also for his constant availability and for his precious help when I started teaching and was in charge of the lab class on photovoltaics for the 2nd year Polytechnique advanced engineering program. On this matter, it is crucial to mention that I

would not have been able to build such a class - almost from scratch - without the help of Dimitri, Chiara, Federico, Heejae and Heeryung on the different experimental setups I introduced to the students.

As for the collaboration with Rennes, I would like to thank all the team and in particular Jacky, Laurent, Claudine and Soline. The idea to focus on anharmonicity as a follow up of the work I started on phonons was given to me by Jacky. This advice, given at a crucial point of my PhD, allowed me to refine and mature my PhD topic at the end of my first year and to find an area that was not exhausted yet. We also all worked together with Prof. Kanatzidis and Dr. Stoumpos from Northwestern University (USA) and I am thankful to all the members of this fruitful three-party collaboration.

I got the chance to work for 2 months in the CLHYO Lab in Perugia, Italy. I would like to thank Filippo De Angelis for welcoming me in his group and for the great collaboration with him and Edoardo on the molecular dynamics trajectories, as well as Eros (God of gnuplot), Lucia, Daniele, and Gonzalo for this great time working and traveling together (Forza Grifo !). I will luckily visit their lab again at the end of May in order to make the most of our results.

But a working environment is nothing without all the nice moments shared with colleagues, and I would like to thank my officemate Pierre at CEA as well as all the "SMRPépère" team. We share a lot with Pierre - both state engineers, eco-friendly, Tesla fans - and had a lot of fun trying to start a new habit of working standing in our "innovation office". I also had a great time with the lunch group at Polytechnique, in particular during our picnics by the lake (Anna, Sanghyuk/Thomas, Chiara, Elmar, Alba, Federico, Tanguy), and had the chance to meet very nice people when playing for LPICM's soccer team. I also want to thank all my friends (Rony, the Condorcet team, Marc, and Yoann with whom I discovered perovskite PV during our master's at Stanford University).

Back to many years ago, I would also like to thank my high-school physics professor M. Fleckinger who deviated from the program to expose us to the many branches of physics, from basic quantum mechanics to Planck's model for black bodies. He whetted my appetite with this first glance at the breadth of physics! I am equally grateful to my inspiring mathematics professor Mme Traisnel as well as my undergraduate physics professor M. Barnier, from whom I learned scientific rigor.

I think being a doctoral researcher is the best time in a career to do research: no money hunting, flexibility and time to get your hands dirty at doing the research yourself, recognition of your work with articles and conferences, time for teaching and science popularization. However, these 3 years of research have been both an intellectual and personal challenge that I could not have undertaken without the support and presence of my parents Denis and Marie and my brother Léo. It has been an amazing

experience that not only consisted of moments of happiness and recognition when I obtained results but also encompassed periods of doubts: what direction to choose, how to get through the various obstacles... My fiancée Arminé was always there for me during these various moments, supporting me during the tough periods and celebrating with me the good moments. As an editor and American citizen, her English proofreading and editing contributions were highly precious for my articles and this very manuscript. I took a risk when choosing to do a PhD instead of starting directly a career at the French ministry of Energy, and I can say it has been an exciting adventure with her on my side.

Préface & Remerciements

COMMENCER UN DOCTORAT dans le domaine, très compétitif, des pérovskites hybrides fut grand défi, et je tiens à remercier mes collègues pour leur aide précieuse et leurs contributions sans lesquelles je n'aurais pas pu en arriver à l'écriture de ce manuscrit. Ce défi fut d'autant plus important que j'ai pris un départ plutôt inhabituel – mon projet de thèse ne s'est pas construit à la suite d'un stage, et ne correspondait pas à un sujet préconçu. J'ai choisi de démarrer un projet combinant une partie calculs ab-initio dans un laboratoire spécialisé dans les matériaux pour le nucléaire (SRMP au CEA Saclay) avec une partie expérimentale au sein du laboratoire LPICM de Polytechnique où, quand j'ai commencé mon doctorat en 2015, les pérovskites hybrides étaient un sujet tout nouveau, en particulier en termes de modélisation.

Quand quelques mois avant de commencer mon doctorat, j'ai organisé une réunion entre Yvan (Polytechnique) et Guido (CEA), il n'y avait aucune garantie que nous puissions construire tous ensemble un projet fructueux. Je suis profondément reconnaissant envers Guido d'avoir accepté de relever ce défi avec moi, de m'avoir initié aux subtilités de la DFT et d'avoir toujours proposé de nouvelles idées de développements à chaque nouveau résultat obtenu. Je ne peux que remercier Guido pour sa flexibilité, sa compréhension et sa patience ; après deux ans passés loin de mécanique quantique, il m'a fallu du temps pour me remettre dans le bain. Guido m'a fourni des conseils clairs et pertinents tout au long des différents projets de mon doctorat, et c'est grâce à sa connaissance approfondie de la DFT pour les matériaux que nous avons réussi à donner, petit à petit, une direction significative à ma thèse, en prenant toujours en compte les ressources de calcul disponibles et les dernières tendances de la littérature - incroyablement prolifique - sur les pérovskites. Enfin, je tiens à le remercier pour son aide dans la relecture précise et rigoureuse de mes articles ainsi que de ce manuscrit.

Au cours de ce projet aux multiples facettes (expériences d'ellipsométrie et de synchrotron, calculs ab-initio, enseignement), j'ai toujours pu compter sur Yvan pour donner un éclairage différent sur mon travail, sur la direction à prendre et sur la façon de trouver des synergies avec les autres doctorant.e.s de l'équipe. À ce propos, les réunions bimensuelles de l'équipe pérovskite (avec Bernard, Denis, Jean-Éric, Warda, Heejae, Éric, Chloé) furent très utiles et complémentaires du travail plus isolé que je faisais au CEA avec Guido. Je tiens à remercier Yvan en particulier pour m'avoir donné l'opportunité de présenter mon travail et de partager mes résultats avec la communauté pérovskite lors de nombreuses conférences internationales (PSCO Lausanne, PSCO Gênes, EUPVSEC Amsterdam, HOPV Japon, IEEE-PVSC Hawaii). Je me rends compte à quel point j'ai eu de la chance d'avoir été soutenu financièrement à chaque fois que j'ai été sélectionné pour donner un oral à une conférence internationale, ainsi que pour aller travailler dans d'autres laboratoires (Rennes et Pérouse, Italie) dans le cadre de collaborations. Sur le plan financier, je suis reconnaissant envers le Ministère de l'Énergie (METS) et l'École des Ponts ParisTech pour le financement de mon projet de doctorat. Je remercie également Polytechnique pour m'avoir choisi comme candidat au Prix Siebel en Sciences de l'Énergie, ainsi que Leo Liberti, Guido, Yvan, Luc de Marliave et Jean-Paul Gaston; sans leur aide dans la construction de ma candidature, je n'aurais pas pu remporter le Siebel. Je remercie également Holger et Fatima pour leur aide pour les candidatures GENCI.

Je tiens à remercier Heejae Lee à la fois pour notre collaboration scientifique et pour notre amitié qui s'est développée au cours de nos projets de thèse. J'ai trouvé en Heejae un super partenaire de laboratoire, avec un bagage complémentaire (dispositifs et expériences pour lui, théorie et calculs pour moi), et ce fut un plaisir de représenter ensemble l'équipe «Polytechnique Perovskite» lors de diverses conférences. J'en profite pour remercier sincèrement toutes les équipes support du labo (équipe BEER, Laurence, Carine, Fabienne, Gaby, Patricia, Fred pour donatello !).

Je remercie Bernard pour son aide lors de l'élaboration de ma candidature pour le financement de mon doctorat, et pour ses nombreux conseils lors des réunions d'équipe, Denis pour ses précieuses connaissances expérimentales et Jean-Éric pour ses apports sur la théorie.

Il y a nombreuses personnes que je souhaite remercier pour leur aide dans l'étude de la dégradation par ellipsométrie que nous avons réalisée en collaboration avec Horiba. Je tiens à reconnaître en particulier les contributions précieuses de Céline et Jean-Paul, ainsi que l'aide de Heejae et Heeryung (préparation d'échantillons) et Minjin (mesures de DRX).

La collaboration que j'ai entamée avec Jacky Even (FOTON, Rennes) a été le fruit d'une discussion inspirante avec Pere Roca, directeur du laboratoire PICM, qui m'a expliqué qu'il était toujours bénéfique

d'interagir avec un maximum de chercheurs afin d'avoir une grande diversité de points de vue et de conseils sur mon projet de thèse. Je voudrais aussi remercier Pere pour sa disponibilité et pour son aide précieuse quand j'ai commencé à enseigner et que j'étais en charge du cours expérimental sur le photovoltaïque pour les polytechniciens de deuxième année. À ce sujet, il me semble très important de mentionner que je n'aurais pas été capable de construire ce cours - presque à partir de zéro - sans l'aide de Dimitri, Chiara, Federico, Heejae et Heeryung sur les différents dispositifs expérimentaux que j'ai présentés aux étudiant.e.s. Quant à la collaboration avec Rennes, je tiens à remercier toute l'équipe et en particulier Jacky, Laurent, Claudine et Soline. L'idée de se concentrer sur l'anharmonicité comme une suite à donner au travail commencé sur les phonons m'a été donnée par Jacky. Ce conseil, donné à un moment crucial de mon doctorat, m'a permis d'affiner et d'approfondir mon sujet de thèse à la fin de ma première année et de trouver une voie qui n'était pas encore épuisée. Nous avons également travaillé ensemble avec le Professeur Kanatzidis et le Dr. Stoumpos de Northwestern University (USA) et je suis reconnaissant envers tous les membres de cette collaboration à trois pôles qui s'est avérée très fructueuse.

J'ai eu l'opportunité de travailler pendant 2 mois au laboratoire CLHYO à Pérouse en Italie. Je voudrais remercier Filippo De Angelis pour m'avoir accueilli dans son groupe et pour ce beau projet élaboré avec lui et Edoardo sur les trajectoires de dynamique moléculaire, ainsi que Eros (Dieu de gnuplot), Lucia, Daniele et Gonzalo pour tous les bons moments au laboratoire comme en dehors (Forza Grifo!). J'aurai la chance de retourner travailler Pérouse à la fin du mois de mai afin d'exploiter nos résultats.

Un environnement de travail n'est rien sans tous les bons moments partagés avec mes collègues, aussi je remercie mon collègue et ami Pierre au CEA de même que toute l'équipe "SMRPépère". Nous partageons beaucoup avec Pierre - tous deux ingénieurs d'état, sensibles aux questions environnementales, fans de Tesla - et avons passé de bons moments dans notre «bureau innovation», notamment à s'essayer au travail debout ! J'ai aussi beaucoup apprécié les déjeuners avec le groupe des jeunes chercheurs à Polytechnique, notamment lors de nos pique-niques au bord du lac (Anna, Sanghyuk/Thomas, Chiara, Elmar, Alba, Federico; Tanguy), ainsi qu'à l'occasion des matches de l'équipe de foot du labo. Je tiens également à remercier tous mes amis (notamment Rony, l'équipe Condorcet, Marc, et Yoann avec qui j'ai découvert les cellules pérovskites pendant notre master à l'université de Stanford). Je voudrais également remercier mon professeur de physique de lycée M. Fleckinger qui n'hésitait pas à s'éloigner grandement du programme pour nous initier aux nombreux domaines de la physique, des bases de la mécanique quantique de base au modèle de Planck pour les corps noirs. Ce premier aperçu de l'étendue des théories physiques a éveillé ma curiosité et mon goût pour cette science. Je suis également reconnaissant envers

ma professeure de collègue Mme Traisnel, qui m'a initié aux joies des mathématiques, ainsi qu'à mon professeur de physique de prépa, M. Barnier, avec qui j'ai appris la rigueur scientifique.

Je pense qu'être chercheur doctorant est sans doute la meilleure position et le meilleur moment pour faire de la recherche: flexibilité, temps pour vraiment «mettre les mains dans le cambouis», reconnaissance du travail avec l'écriture d'articles et les présentations en conférences, disponibilité pour l'enseignement et la vulgarisation scientifique; je crois avoir vraiment pu profiter pleinement de cette riche expérience. Cependant, ces trois années de recherche ont été également un défi intellectuel et personnel et je n'aurais pas pu le relever sans le soutien et la présence de mes parents Denis et Marie et de mon frère Léo. Ce fut une expérience unique qui a consisté non seulement de moments de bonheur et de reconnaissance quand j'ai obtenu des résultats mais aussi de périodes de doutes : choix de la direction à prendre, nombreux obstacles à franchir ... Ma fiancée Arminé était toujours là pour moi pendant ces différents moments, pour me soutenir pendant les périodes difficiles et célébrer avec moi les bons moments. Éditrice et citoyenne américaine, ses contributions à la relecture en anglais de mes articles et de ce manuscrit ont été très précieuses. J'ai pris un risque en choisissant de me lancer dans un doctorat au lieu de commencer directement une carrière au ministère de l'énergie, et je peux dire que ce fut une aventure passionnante avec elle à mes côtés.

Contents

1	THE ERA OF SOLAR ENERGY	1
1.1	Climate change and energy transition	2
1.2	Solar energy: a mature, clean and infinite source of energy	5
1.3	The Holy Grail of solar energy research	11
	References	15
2	THE HYBRID PEROVSKITES REVOLUTION	19
2.1	Hybrid organic-inorganic perovskites	20
2.2	The efficiency race	23
2.3	What makes metal halide perovskites so special?	29
2.4	The issue of stability	33
2.5	Hysteretic phenomena in perovskites: origins and consequences	35
2.6	Cesium perovskites: a game changer?	38
2.7	Thesis motivations and approach	40
	References	41
3	DENSITY FUNCTIONAL THEORY	53
3.1	From quantum physics to materials modeling	54
3.2	Density Functional Theory (DFT)	57
3.3	Band structure: Rashba effect	65
3.4	Vibrational and dielectric properties: linear-response approach (DFPT)	66
3.5	Molecular dynamics methods	69

References	69
4 CESIUM PEROVSKITES: ANHARMONICITY AND INSTABILITIES	73
4.1 Vibrational properties of halide perovskites	74
4.2 [Publication 1] Structural instabilities related to highly anharmonic phonons	77
4.3 [Publication 2] Anharmonicity and disorder in the black phases of cesium lead iodide	96
4.4 Rashba effect and molecular dynamics study	115
References	133
5 ENVIRONMENTAL INSTABILITIES IN HALIDE PEROVSKITES	139
5.1 Stability issues: from ab-initio calculations to experiments	140
5.2 Ab initio perspective: stability diagrams	142
5.3 [Publication 3] Light-induced degradation of perovskite thin films	146
5.4 Hybrid Perovskites: organic or inorganic semiconductors?	161
5.5 Oxygen defects in MAPI	163
5.6 [Publication 4] Hysteresis and ionic migration	173
References	174
6 CONCLUSION & PERSPECTIVES	179
7 PUBLICATIONS, COLLABORATIONS & AWARDS	183
A APPENDIX	189
A.1 Brillouin zone conventions	189
References	192
LISTING OF FIGURES	193

As the saying goes, the Stone Age did not end because we ran out of stones; we transitioned to better solutions. The same opportunity lies before us with energy efficiency and clean energy.

Steven Chu, Physics Nobel Prize winner and 12th United States Secretary of Energy

1

The Era of Solar Energy

IN THE CONTEXT OF climate change and in light of the energy transitions initiated by developed countries in the 1990s after the world finally became aware of the consequences of human activity on the climate imbalance, the countries' choices in terms of energy production mix have become a major public policy issue. In this introductory chapter, we set the scene for what has finally brought, after living in the shadow for decades, solar energy research to the forefront and revealed photovoltaics not only as the most cost-efficient mass renewable energy but also as one of the key solutions to the transition to cleaner sources of energy production.

Contents

1.1	Climate change and energy transition	2
1.2	Solar energy: a mature, clean and infinite source of energy	5
1.2.1	The cost-learning curve of solar PV	6
1.2.2	Integration to the electricity market	7
1.3	The Holy Grail of solar energy research	11
1.3.1	Inorganic photovoltaics: efficiency and stability	12
1.3.2	Organic photovoltaics (OPV): flexibility and low-cost	14
	References	15

1.1 CLIMATE CHANGE AND ENERGY TRANSITION

Before addressing the state of the art of solar energy research in section 1.3, and getting to the heart of the matter, perovskite solar cells, in chapter 2, here we aim to give the reader a comprehensive - yet brief - societal and economical context to the rise of renewable energies.

Genuine awareness of climate change caused by human activity arose in the early 1990s, in particular with the first IPCC (Intergovernmental Panel on Climate Change) report [1] which showed that the increase of the greenhouse gases' concentration in the Earth's atmosphere results for a substantial part from emissions related to human activities. In this report, the IPCC also made a prospective study to show the potential impact of public policies to control greenhouse gas emissions. Without drastic measures, they showed that the Earth's average temperature would be 3 celsius degrees higher in 2100 than it was the pre-industrial era.

In 1997, at the 3rd Conference of the Parties (COP 3) in Kyoto an international protocol was signed urging parties to reduce, by 2012, the emissions of the main greenhouse gases by at least 5 % with respect to 1990. While this agreement marked the first effort of a worldwide dialogue, it has never been ratified by the United States, and it was not until eight years later in 2005 that it came into effect once 55% of the parties had ratified the protocol.

In addition, after the third IPCC report of 2001, alerting the world to the acceleration of global warming in the 1990s (the warmest decade of the 1860-2000 period), a global controversy arose about the validity of the theory attributing global warming mostly to human causes as previously demonstrated by the IPCC. As a movement opposing this so-called alarmist vision emerged in the 2000s, the climate issue became pivotal in the political sphere.

We will not further draw the reader into the details of the debate, but point to figures 1.1.1 and 1.1.2 which show respectively the increase of the Earth's average temperature and the global carbon emissions from fossil fuels over the last century.

GLOBAL LAND-OCEAN TEMPERATURE INDEX

Data source: NASA's Goddard Institute for Space Studies (GISS). Credit: NASA/GISS

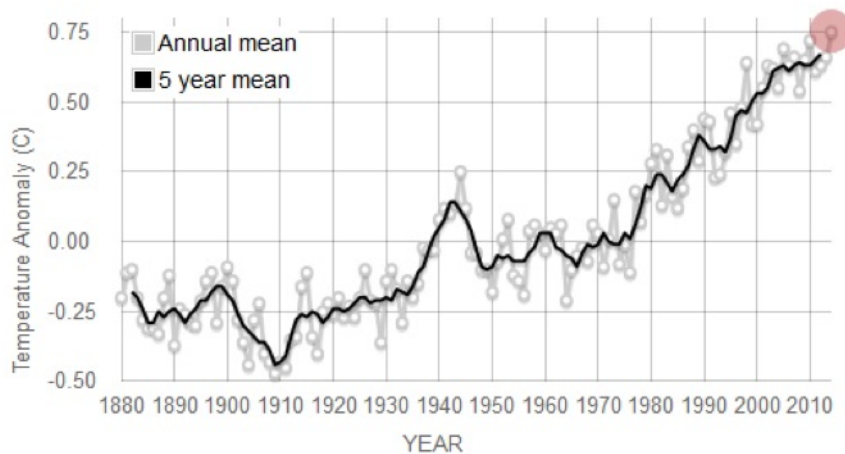
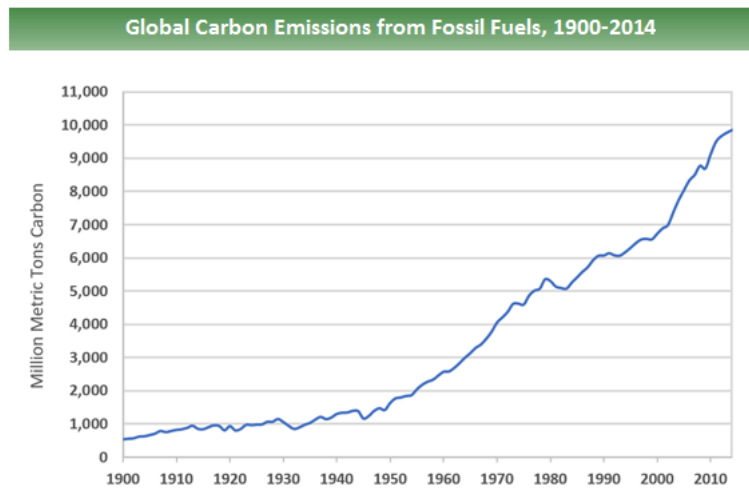


Figure 1.1.1: Evolution of the Earth's average temperature.



Source: Boden, T.A., Marland, G., and Andres, R.J. (2017). [Global, Regional, and National Fossil-Fuel CO2Emissions](#). Carbon Dioxide Information Analysis Center, Oak Ridge National Laboratory, U.S. Department of Energy, Oak Ridge, Tenn., U.S.A. doi 10.3334/CDIAC/00001_V2017.

Figure 1.1.2: Evolution of the global carbon emissions due to fossil fuels over the last century.

1.2 SOLAR ENERGY: A MATURE, CLEAN AND INFINITE SOURCE OF ENERGY

Beyond climate change, the depletion of fossil fuels, waste recycling and other environmental issues compel scientists to find alternative energy sources to the current solutions which are either unsustainable, induce high carbon emissions, or present an important risk for populations. Thus, the conversion of solar energy into electrical energy (photovoltaic energy), chemical (solar hydrogen battery) or thermal (thermal power plants, solar water heaters) is one of the greatest challenges our modern society faces. Solar energy, an inexhaustible source on our scale (see figure 1.2.1), is also a decentralized source of energy as it can be easily integrated everywhere: from rooftops to windows and even on the roads of the future (Solar Roadways project [2]).

Thanks to a complete technological revolution, very similar to the microcomputer industry's in the 70's, photovoltaic (PV) energy has become the most decentralized, clean and competitive source of electricity.

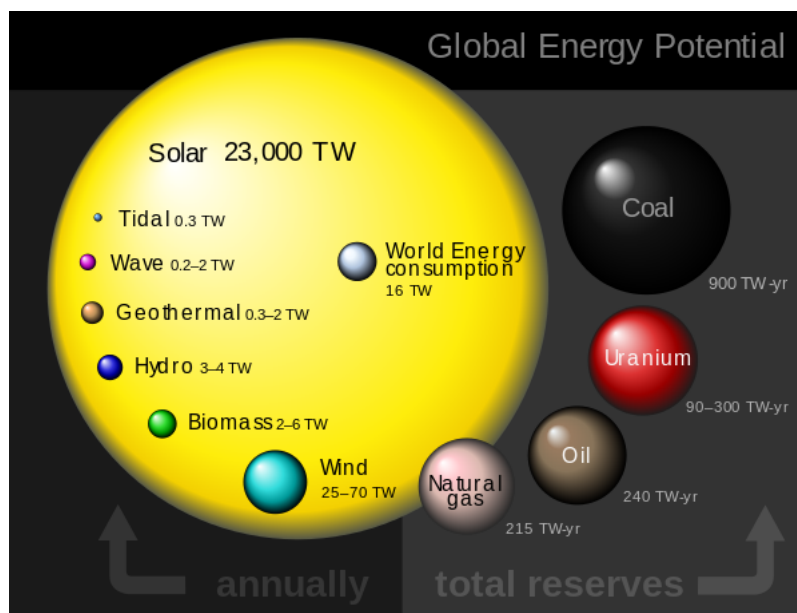


Figure 1.2.1: Comparison between the amount of solar energy absorbed by the Earth in one year and the fossil fuel recoverable reserves. Ref. [3]

1.2.1 THE COST-LEARNING CURVE OF SOLAR PV

In general, photovoltaic cells rely on semiconductor materials, due to which the price of photovoltaic energy has been decreasing at an extraordinary speed worthy of Moore's law in microcomputing: figure 1.2.2 shows that the cost per cell has been divided by 50 since 1980 and by 20 since 2000. This drop is to be attributed as much to solar cell efficiency gains as to the semiconductor industry's economies of scale and more generally to cost engineering. As shown by the result of the study presented in figure 1.2.3 about module cost engineering, future cost gains have to be drained as much by industrial process optimization as by technological innovations.

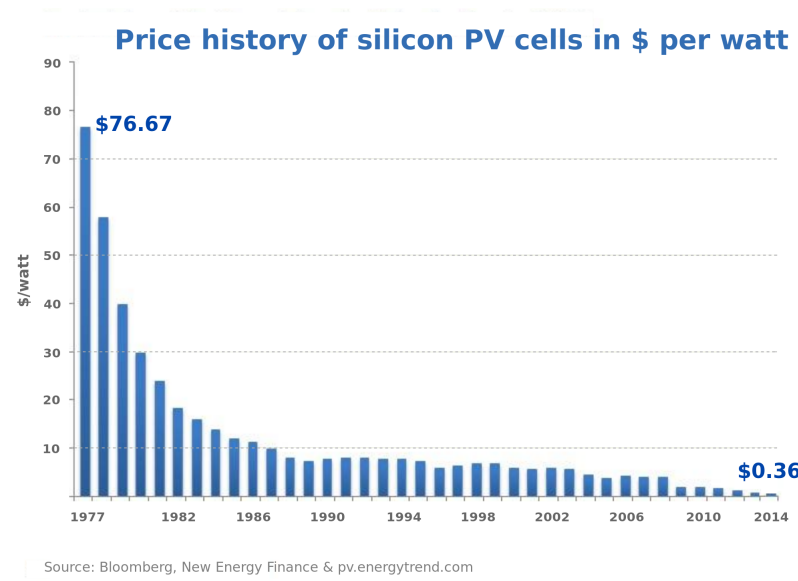


Figure 1.2.2: Evolution of the energy cost (in dollars per watt peaks) for silicon-based solar cells since 1977. Source: Bloomberg, 2014.

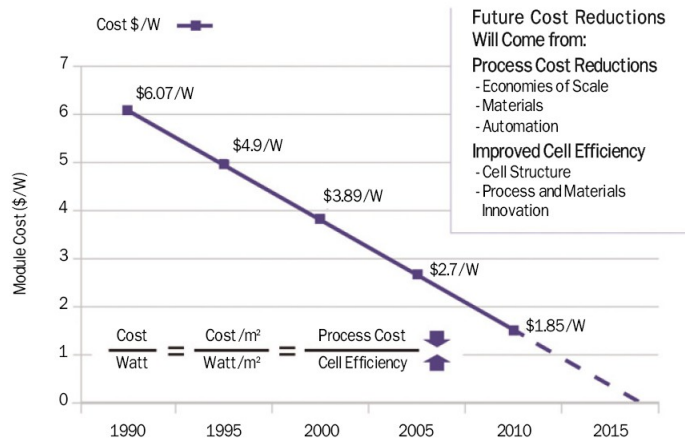


Figure 1.2.3: Evolution and forecast of the watt cost for a PV **module** and possible future cost reduction triggers. To give a point of reference, a price of \$1 per Watt is the target cost to achieve to be competitive on the market. Source : SEMI PV Group, 2010.

1.2.2 INTEGRATION TO THE ELECTRICITY MARKET

In order to compare the cost of PV to the cost of electricity from other sources, one takes in addition into account the annual solar yield in the country of study and the solar panel lifetime (20 to 25 years in general). The corresponding data, shown on figure 1.2.4 for residential PV, evidences that by 2020 it will be cheaper to produce PV energy than to buy electricity from the grid in many countries, as it is already the case in Spain, Germany and Italy for instance.

The competitiveness of PV naturally raises the question of its integration in the electricity network, as PV, unlike other source of energies, is a variable energy source with a zero-marginal cost ("solar fuel" is free).

The issues raised by the emergence of PV on a market that was built for centralized and constant sources of energy is far beyond these introductory words, we invite the curious reader to refer to [4]. We provide in figures 1.2.5 and 1.2.7 an illustration of the challenges that the electricity network faces today, now that the great - 30 year long - scientific effort to reduce the cost of PV has started to bear fruit. There are three main challenges. The first one is to adapt networks that were built to spread electricity from production centers to consumption spots to an increasingly decentralized production of electricity. The

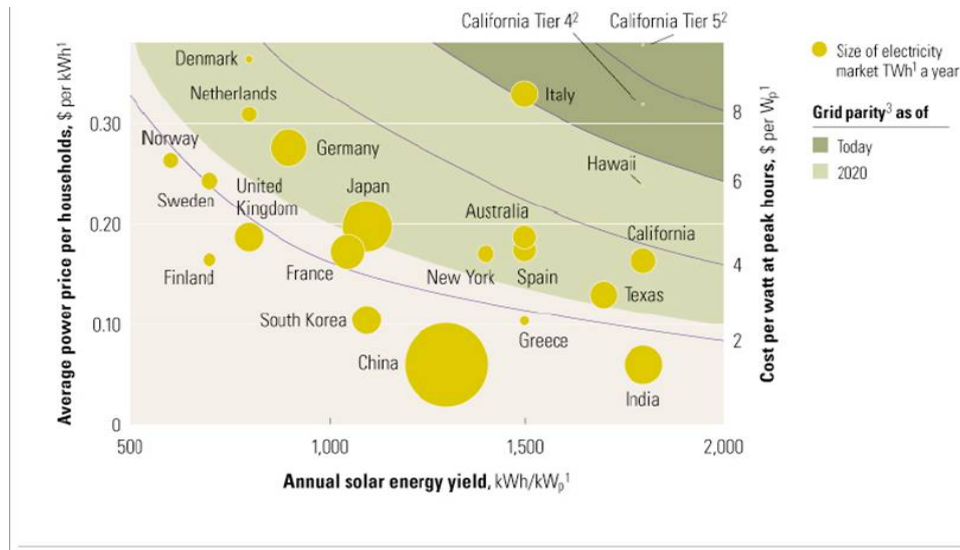


Figure 1.2.4: Comparison between residential PV energy cost and the electricity cost in several countries. Source : McKinsey, 2014.

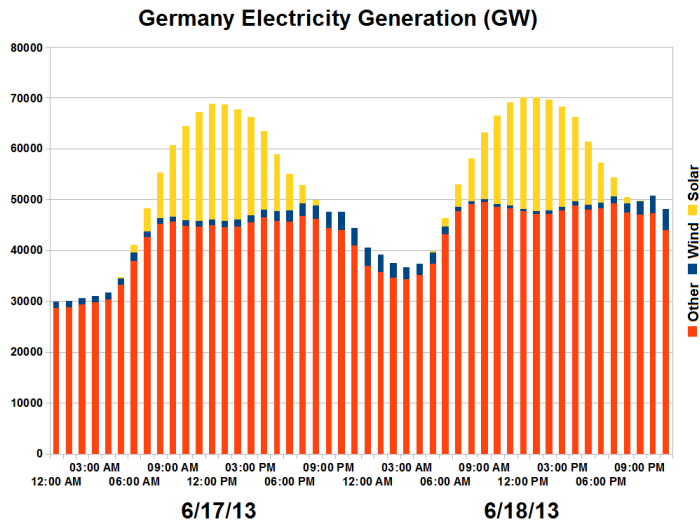


Figure 1.2.5: In Germany, the emergence of PV already has a noticeable impact on the overall country's electricity production profile. Source: German Ministry of Energy, 2013.

second challenge arises from the variable characteristic of PV: smart and agile systems, with batteries, are required to balance consumption at every second. This issue is in general considered to have a substantial impact only for a penetration of variable energies higher than 20-25 % for European networks [5]. In France, a recent report evidenced concrete solutions to achieve a 100% renewable electricity mix by 2050 [6]. The third challenge resides in the fact that PV has a zero marginal cost: PV producers never have any incentive to stop production, contrary to conventional fuel-based electricity sources. Since the market was mostly designed to send economical signals to fuel-based sources, and since for example in France lots of measures pushed consumers to report their consumption to night hours when the nuclear plants produce excess electricity, the introduction of PV on the market can cause episodes of negative prices around noon when PV production is at its maximum and the consumption is low. This means that at noon the conventional sources do not have any incentive to run, but that they need to be turned on very quickly at the end of the afternoon, which is complicated for these non-flexible sources. The phenomenon is illustrated on the so-called "duck curve" shown figure 1.2.6.

A new electricity market design [4] that is able to generate a profitability model for all types of necessary energy sources (flexible but variable and constant but not flexible) is yet to be invented.

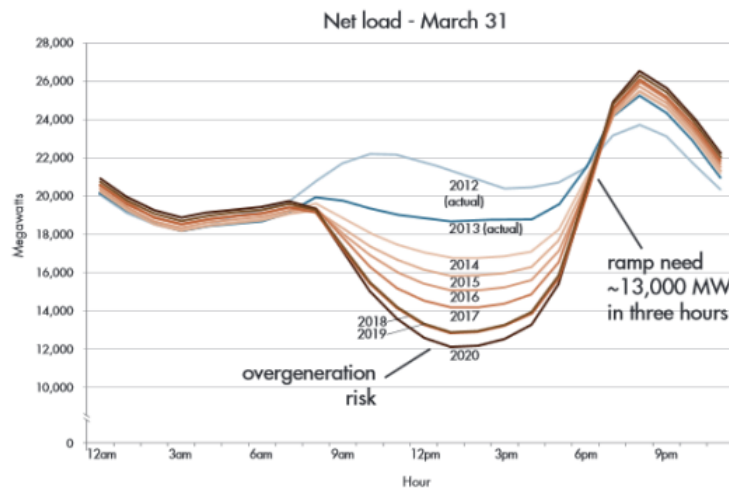


Figure 1.2.6: Electricity load needed in addition to the production of variable energies ("net" load). Source: CAISO/Jordan Wirfs-Brock

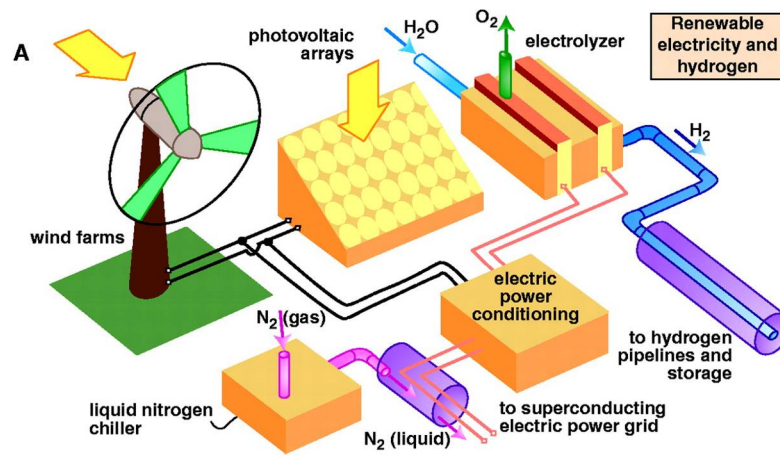


Figure 1.2.7: Electricity production, in particular through solar PV, is only one element of the complex energy transition landscape. Ref. [7]

1.3 THE HOLY GRAIL OF SOLAR ENERGY RESEARCH

Now that we introduced the main societal and economic issues at stake in the emergence of PV, we conclude this first chapter by giving the reader a quick overview of the landscape of PV technologies that emerged throughout the last 30 years of solar research.

The first goal of solar energy research is to obtain as low a price as possible in **\$ per Watts**. This price is given by two components :

- The material cost, in **\$ per m²**
- The efficiency η , dimensionless parameter, which directly gives the surface power density (**Watts per m²**) once multiplied by the solar spectrum density.

One should keep in mind that the lifetime, that is to say the stability of the technology of study is then to be taken into account in order to calculate the final **energy price in \$ per Watt-hour**.

As this thesis work does not focus on the working principles of solar cells but rather on the physics of perovskite materials themselves, we only recall in this introduction the natural definition and the limits for the efficiency η :

$$\eta = \frac{P_{out}}{P_{in}}$$

where P_{out} is the output power produced by the solar cell and P_{in} the input light power.

For a single junction solar cell, the efficiency strongly depends on the absorption properties of the chosen semiconductor and in particular on its band gap. There is a trade-off on the band gap value:

- if the band gap is too large, not enough photons are absorbed
- but if the band gap is small, the carriers will be extracted at low energy and produce a low voltage (thermal losses)

which means that there should be an optimal band gap value maximizing the efficiency. Since sunlight is not monochromatic but rather corresponds to a broad spectrum, the efficiency versus band gap curve is not a unit step function, but rather a smooth bell curve shown figure 1.3.1.

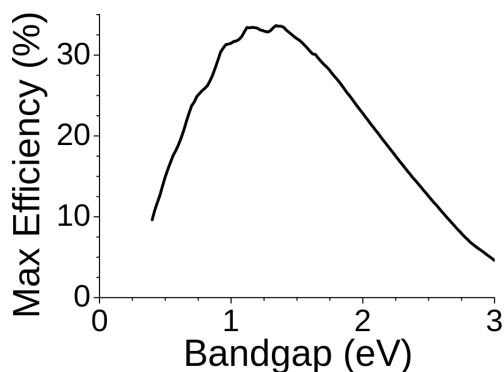


Figure 1.3.1: Shockley–Queisser limit. Ref [8]

Assuming a direct band gap semiconductor, and further taking into account thermal losses, radiative recombination and impedance matching losses, the efficiency value is constrained by the so-called Shockley–Queisser limit [8]: as seen on figure 1.3.1, **the theoretical maximum efficiency value for a single junction cell is 33.7% and is obtained for an ideal band gap of 1.34 eV**. For silicon (1.14 eV band gap), the maximum efficiency is about 32%.

Given this technological limit, in 2001 [9], much before the rise of hybrid perovskites, Martin Green defined three main generations of solar cells (figure 1.3.2). At that time the Holy Grail of solar research (generation III on the graph) was to be able to find very highly efficient materials at a cost comparable to the previously developed technologies. We will see in the next chapter that the emergence of halide perovskites has profoundly changed this paradigm. Let us now move on to the brief description of these three generations.

1.3.1 INORGANIC PHOTOVOLTAICS: EFFICIENCY AND STABILITY

The first generation is made of single crystal solar cells and reaches more than 20% efficiency. It is mostly based on Si (band gap 1.14 eV at 300 K) - and GaAs (1.43 eV) [10]. Because of the high level of purity required and since they usually contain thick layers of material (several microns), single crystal cells can be rather expensive.

The second generation shown on figure 1.3.2 corresponds to thin film solar cells, based on materials such as amorphous silicon (band gap of 1.7 eV) or CdTe (1.5 eV). Only a few hundred of nanometers

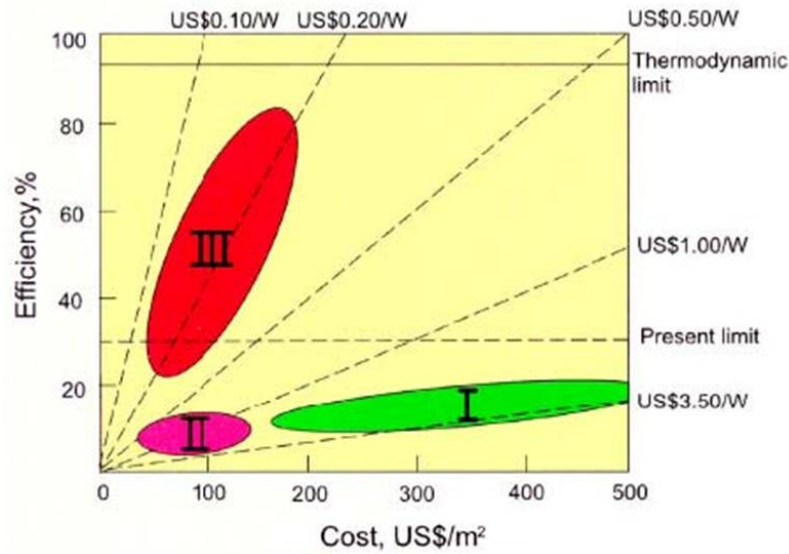


Figure 1.3.2: Main generations of solar cells as defined by Martin Green in 2001 [9], much before the rise of perovskite materials as light absorbers.

thick, these cells have a much lower cost and can be flexible but present a lower efficiency (13 to 20 %). Thin film solar cells also include organic materials, which we choose here to introduce separately in the next section.

In general and as explained in section 1.2.1, the cost of the main class of inorganic solar cells (silicon cells) has decreased extraordinary fast thanks to process engineering and the economies of scale. In addition, they are very stable [11].

The third generation usually designs solar cells that are potentially able to overcome the Shockley–Queisser limit, thus aiming at finding a way to engineer very high efficiency cells at costs which are comparable to the one of thin films. They include multi-layer cells (“tandems” for two layers) made of amorphous silicon or gallium arsenide, but also using novel concepts such as hot-carrier effects, multiple-carrier ejection, quantum dots and photon conversion.

Another way to describe the multifarious variety of PV technologies, which I think is better adapted to our work on hybrid perovskites, is to divide them into inorganic and organic solar cells. We will use this dual classification when it comes to comparing the physical properties of hybrid perovskites to other materials throughout this manuscript.

To summarize, inorganic solar cells are generally:

- highly efficient ($> 20\%$)
- rather expensive (complex processes)
- very stable

1.3.2 ORGANIC PHOTOVOLTAICS (OPV): FLEXIBILITY AND LOW-COST

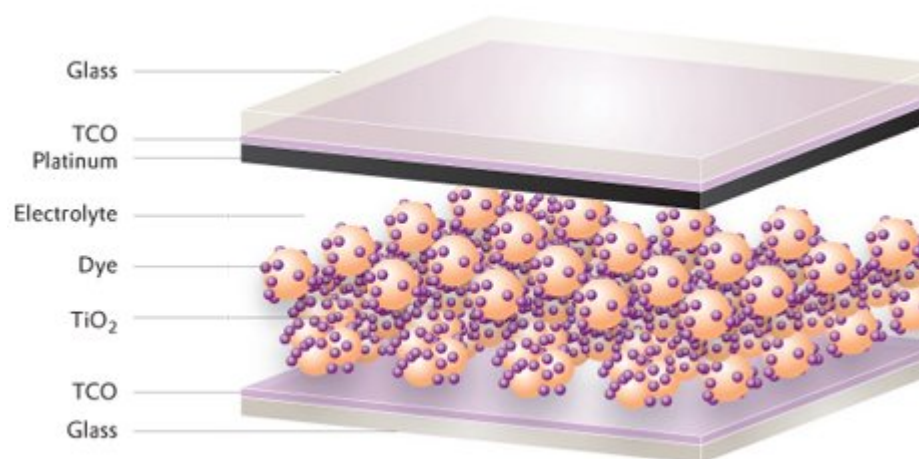


Figure 1.3.3: General architecture of a Dye Sensitized Solar Cell (DSSC). The charges are photo-generated by the photosensitive dye and separated at the surface between the dye, the TiO_2 semiconductor and electrolyte. They are then transported through the electrolyte layer to the transparent conductive oxides (TCO). Source: wikipedia

On the other hand, organic solar cells, born in 1991 when the first dye-sensitized solar cell (DSSC, figure 1.3.3) able to overcome 10% efficiency was reported [12], are much easier to fabricate (solution or evaporation processes), use very little material (a few hundreds of nm) and are thus much cheaper than inorganic solar cells in general. Even though they belong to the second generation (thin film materials), they have never been able to reach efficiencies much higher than 10%, and are substantially less stable

[13] than other thin films like CdTe or CIGS ($CuInGaSe_2$). We will come back to the crucial issue of stability in the next chapter (section 2.4) and in chapter 5.

To summarize, organic solar cells possess the following characteristics:

- low-cost
- flexibility
- low efficiency (around 10 %)

REFERENCES

- [1] GIEC. Scientific aspects of climate change. URL www.ipcc.ch.
- [2] Hossein Roshani, Samer Dessouky, Arturo Montoya, and AT Papagiannakis. Energy harvesting from asphalt pavement roadways vehicle-induced stresses: a feasibility study. *Applied Energy*, 182: 210–218, 2016.
- [3] R. Perez and M. Perez. A fundamental look at energy reserves for the planet. *The IEA SHC Solar Update*, 50(2), April 2009. URL <https://www.ieashc.org/data/sites/1/publications/2015-11-A-Fundamental-Look-at-Supply-Side-Energy-Reserves-for-the-Planet.pdf>.
- [4] Arthur Marronnier. *Inventing a new electricity market design to boost the integration of photovoltaics energy within the European legal framework*. Thesis, Ecole des Ponts - ParisTech, July 2015. URL https://www.researchgate.net/publication/322937370_Inventing_a_new_electricity_market_design_to_boost_the_integration_of_photovoltaics_energy_within_the_European_legal_framework.
- [5] Ye Wang, Vera Silva, and Miguel Lopez-Botet Zulueta. Impact of high penetration of variable renewable generation on frequency dynamics in the continental europe interconnected system. 11 2015.
- [6] ADEME, Artelys, ARMINES-PERSEE, and ENERGIES DEMAIN. A 100% renewable electricity mix, analyses and optimisations. January 2016. URL <http://www.ademe.fr/node/122931>.
- [7] Martin I Hoffert, Ken Caldeira, Gregory Benford, David R Criswell, Christopher Green, Howard Herzog, Atul K Jain, Haroon S Kheshgi, Klaus S Lackner, John S Lewis, et al. Advanced technology paths to global climate stability: energy for a greenhouse planet. *Science*, 298(5595):981–987, 2002.
- [8] William Shockley and Hans J Queisser. Detailed balance limit of efficiency of p-n junction solar cells. *Journal of applied physics*, 32(3):510–519, 1961.
- [9] Martin Green. Third generation photovoltaics: Solar cells for 2020 and beyond. 14:65–70, 2002.

- [10] Ben G Streetman, Sanjay Banerjee, et al. *Solid state electronic devices*, volume 2. Prentice-Hall Englewood Cliffs, NJ, 1995.
- [11] Martin A Green. Crystalline and thin-film silicon solar cells: state of the art and future potential. *Solar energy*, 74(3):181–192, 2003.
- [12] Brian O’regan and Michael Grätzel. A low-cost, high-efficiency solar cell based on dye-sensitized colloidal tio₂ films. *Nature*, 353(6346):737, 1991.
- [13] Pei Cheng and Xiaowei Zhan. Stability of organic solar cells: challenges and strategies. *Chem. Soc. Rev.*, 45:2544–2582, 2016.

The only constant in the technology industry is change.

Marc Benioff, entrepreneur, author and philanthropist

2

The Hybrid Perovskites Revolution

THE RECENT EMERGENCE OF HYBRID PEROVSKITE MATERIALS has profoundly changed the PV technologies landscape as we drew it in the previous chapter. As we will show in this rather bibliographic chapter, the new generation of hybrid organic-inorganic perovskites, born in 2009, appears to be at the crossing between the world of inorganic solar cells and the generation of organic photovoltaics, combining what seems to be the best of both worlds. In this chapter, we aim at summarizing the main properties and challenges of perovskite solar cells (PSCs) by providing a brief state of the art for each topic that will be directly or indirectly addressed in this thesis.

Contents

2.1	Hybrid organic-inorganic perovskites	20
2.2	The efficiency race	23
2.3	What makes metal halide perovskites so special?	29
2.4	The issue of stability	33
2.5	Hysteretic phenomena in perovskites: origins and consequences	35
2.6	Cesium perovskites: a game changer?	38
2.7	Thesis motivations and approach	40
	References	41

2.1 HYBRID ORGANIC-INORGANIC PEROVSKITES

The perovskite structure, after the name of the Russian mineralogist L.A. Perovski, is a crystalline structure commonly found in oxides ($CaTiO_3$ e.g.). Oxide perovskite structures have always been of high interest to material scientists because of the great variety of physical properties they exhibit, among which: ferroelasticity ($SrTiO_3$), ferroelectricity ($BaTiO_3$), antiferroelectricity ($PbZrO_3$), ferromagnetism ($YTiO_3$) and antiferromagnetism ($LaTiO_3$). Some perovskites can even exhibit simultaneously several of these properties, and are then called multiferroic materials [1].

The general perovskite chemical formula is ABX_3 , where A and B are cations and X is an anion. In order for this structure to be stable, the A atoms need to be larger than the B atoms. The ideal cubic structure (figure 2.1.1) is composed of octahedrons of anions bound to one B cation (6-fold coordination) with the A cation in the middle of 8 octahedrons (12-fold cuboctahedral coordination).

The first observation of the photoconductive properties of halide ($X=Cl, Br$ or I) perovskites was done in 1959 by Møller [3] who showed that the lead cesium-based $CsPbX_3$ compounds should behave as semiconductors. We will come back in more detail to these inorganic cesium perovskites in chapter 4 since they constitute the main material of our ab-initio study.

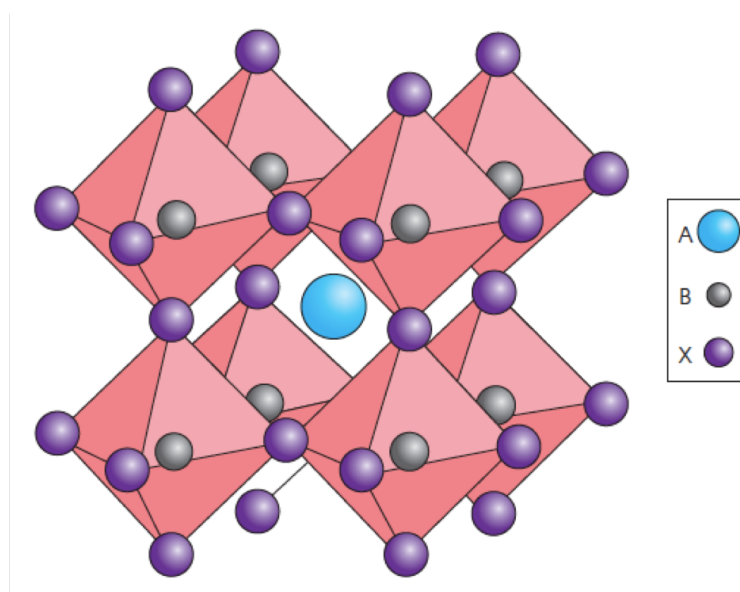


Figure 2.1.1: Ideal perovskite cubic structure (ABX₃). Ref. [2]

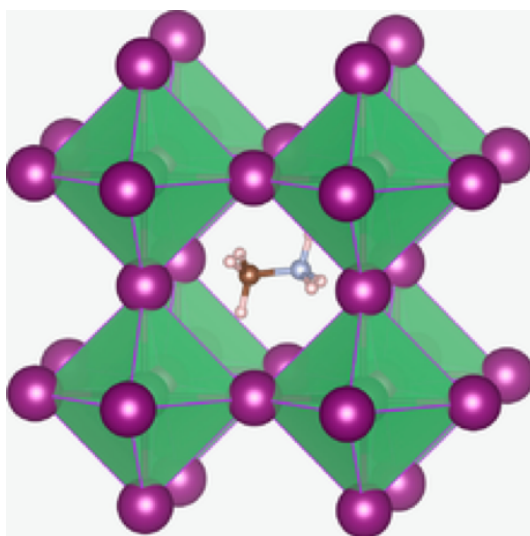


Figure 2.1.2: Crystal structure of the flagship hybrid organic-inorganic material for PV CH₃NH₃PbI₃, also referred to as MAPbI₃ or "MAPI".

Hybrid organic-inorganic perovskites were born in 1978 when Weber [4, 5] was able to replace in the A element by an organic ion, namely methylammonium ($CH_3NH_3^+$, also called MA^+), thus synthesizing for the first time $CH_3NH_3BX_3$ (B=Pb, Sn and X=Cl, Br or I) perovskites (figure 2.1.2). Even though Weber reported the absorption properties of such compounds, noting the change of color upon changing the halide anion, the use of hybrid methylammonium halide perovskites as photovoltaic materials did not appear before 2009, when Miyasaka *et al.* [6] were the first group to replace the absorbing layer in a dye-sensitized solar cell (DSSC, see section 1.3.2) by methylammonium lead iodide ($CH_3NH_3PbI_3$) showing a surprising efficiency of about 3.8% and thus realizing the first working hybrid perovskite solar cell.

2.2 THE EFFICIENCY RACE

Since then, within the context of a very fast efficiency race, the architecture of perovskite solar cells has evolved drastically, in particular in 2012 when Park *et al.* [7] solved the stability problem arising from the liquid electrolyte in perovskite DSSCs by replacing it with a solid hole-transporting material (or "hole interface layer", see figures 2.2.1 and 2.2.2). Generally, the selection of the electron and hole transporting layers is of crucial importance for both the cost and the efficiency of the solar cell. Finding cheap and efficient selective contacts for electrons and more crucially for holes in perovskite solar cells has thus become an intense area of research [8, 9].

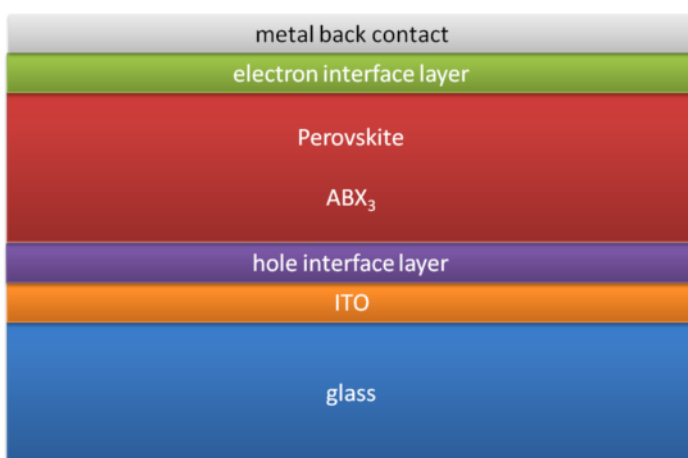


Figure 2.2.1: General architecture of a solid-state perovskite solar cell. The electron (resp. hole) interface layer is also called the electron (resp. hole) transporting layer (ETL) (resp. HTL). Ref. [10]

We will not go into too much detail about the complex evolutionary path of the different perovskite solar cell architectures, though figure 2.2.3 shows a summarized timeline of the main developments.

As shown on figure 2.2.3 and more precisely on figure 2.2.4, the efficiency of perovskite solar cells has jumped from about 4% in 2009 to 22.1% in 2016. As of January 2018, the highest certified efficiency is 22.7% [13]. Comparing perovskite solar cells to other emerging thin film technologies (figure 2.2.4) or

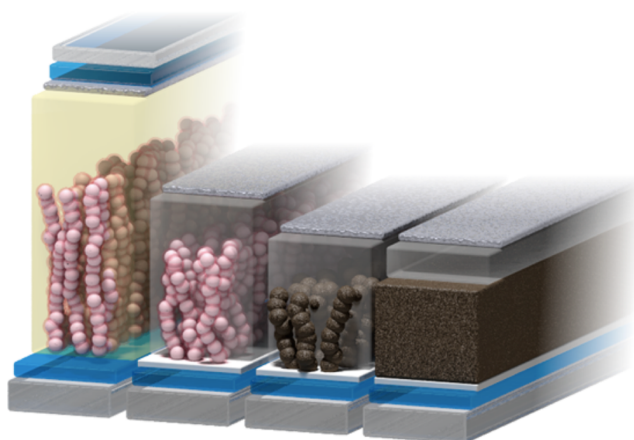


Figure 2.2.2: Evolution of perovskite solar cells structures from DSSCs to solid-state cells. Ref. [11]

Perovskite Solar Cell Development Timeline

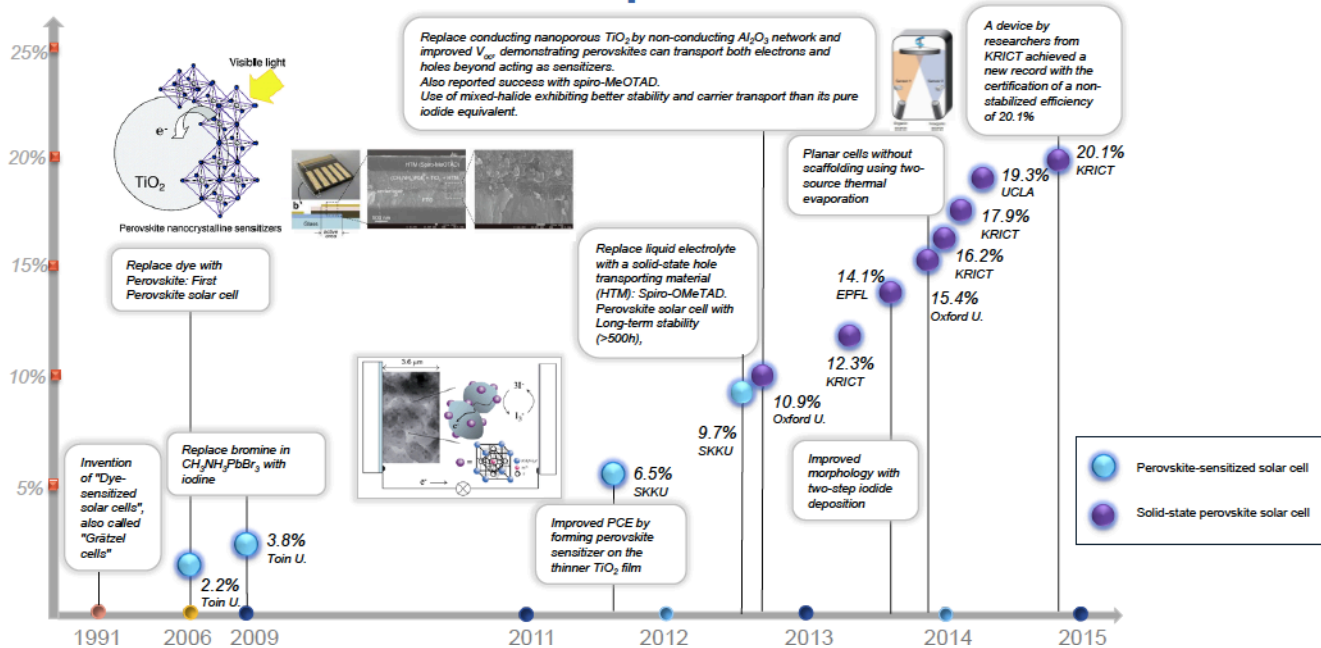


Figure 2.2.3: Overview of the perovskite solar cells structure's evolutionary paths. Ref. [12]

even to the complete set of PV technologies (figure 2.2.5) shows that such a fast efficiency rise is unprecedented in the history of PV.

In terms of cost, according to first forecasts based on the closest commercial technology (CdTe) [12], perovskite solar modules should be able to produce power for less than 0.3 \$ per Watts (see figure 2.2.6), taking advantage of the low-cost processes and material similarities with DSSCs (low-temperature, solution or evaporation processes [2, 14]).

To summarize, hybrid organic-inorganic solar cells seem to profit from the advantages of both types of materials:

- low in cost
- flexible
- highly efficient

They constitute thus the first truly low-cost, highly-efficient generation of solar cells, having caught up in only 5 years with the some of the best inorganic solar cells in terms of efficiency. We will come back in section 2.4 to the stability issue in perovskite solar cells which is the major issue limiting the readiness level of this technology.

The fact that perovskite solar cells are made of flexible materials [14, 15] and are highly efficient means that their applications range from semi-transparent photovoltaic windows to car roofs and portable electronics, in addition to possibly competing with silicon solar cells for residential roofs and large-scale solar plants.

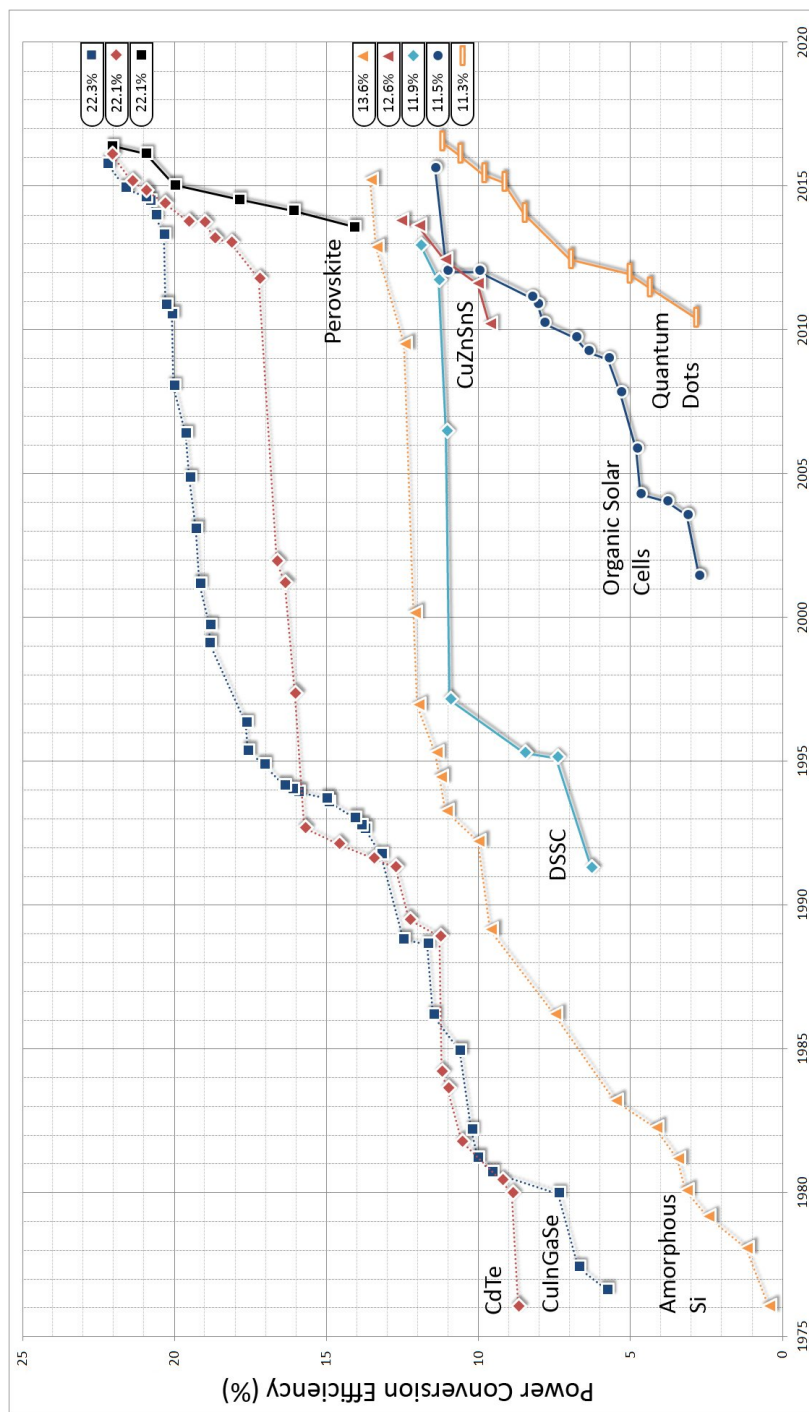


Figure 2.2.4: Emerging thin film technologies. Ref. [13]

2.2. THE EFFICIENCY RACE

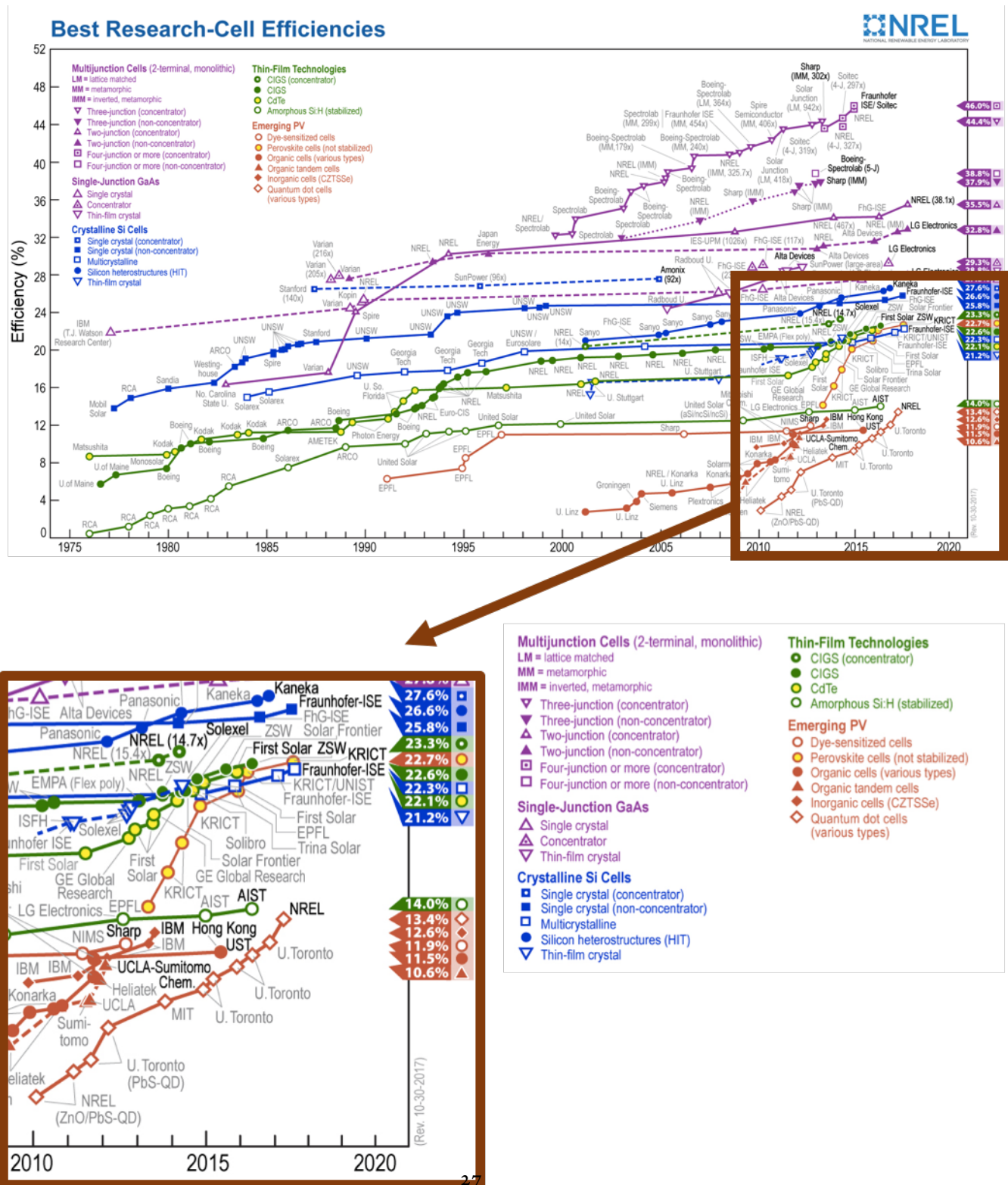


Figure 2.2.5: NREL efficiency chart. Multijunction cells, for which the Shockley–Queisser limit of 33.7% does not apply, are shown for comparison. Ref [13]

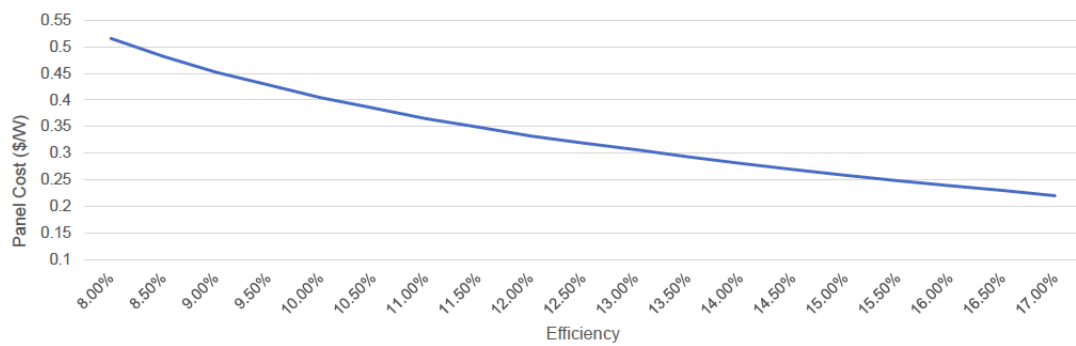


Figure 2.2.6: Estimation of the cost of a perovskite module depending on its power conversion efficiency. Ref. [2, 12]

2.3 WHAT MAKES METAL HALIDE PEROVSKITES SO SPECIAL?

In this section, we aim at giving the reader a comprehensive review on the main optical and electronic properties of hybrid perovskite thin films. We focus here on the flagship hybrid material MAPbI_3 (MAPI), more details are given about mixed cation - mixed halide compounds in section 2.6.

Although HOMO/LUMO models, inherited from OPV [16], are still used to understand the physics of perovskite solar cells, it is now considered a proven fact that methylammonium lead iodide behaves mostly as an intrinsic semiconductor and that its electronic properties can be explained using the general band theory of solids [17]. Transistor measurements confirmed that MAPI is able to transport both electrons and holes [18, 19].

Even *et al.* [20] and Mosconi *et al.* [21] reported for the first time in 2012 and 2013 the ab initio calculated electronic band structure of MAPbI_3 , using density functional theory (DFT, see next chapter). They revealed a calculated value of the **direct band gap of 1.55 eV**, very close to the experimental band gap values (1.56 eV) [6, 22–24]. Even *et al.* [25] showed that this is due to an error cancellation between the general underestimation of the band gap in DFT ground state calculations (see next chapter) and the giant spin-orbit coupling (SOC) that was found for the conduction band. Umari *et al.* [26] then developed an effective GW method incorporating spin-orbit coupling which allows to accurately model the electronic, optical and transport properties of $\text{CH}_3\text{NH}_3\text{SnI}_3$ and $\text{CH}_3\text{NH}_3\text{PbI}_3$. Note-worthily, a similar giant SOC effect was found for CsPbI_3 where it induces a large band gap correction of about 1.1 eV [25].

Figure 2.3.1 summarizes the electronic band structure for the cubic phase of MAPI [27]. The valence band is mostly composed of iodide 5p orbitals with small contributions of lead 6s states. The conduction band mostly consists of lead 6p orbitals. This means that the organic molecule does not participate in the formation of the valence and conduction bands.

It was shown more recently [28] in 2016, that in fact methylammonium lead iodide presents a weakly indirect bandgap 60 meV below the direct bandgap transition. This is a consequence of spin-orbit coupling resulting in Rashba-splitting of the conduction band, as we will show in the case of CsPbI_3 in section 4.3. This is coherent with time-resolved photo-conductance measurements showing that the generation of free mobile charges is maximized for excitation energies just above the indirect band gap [29].

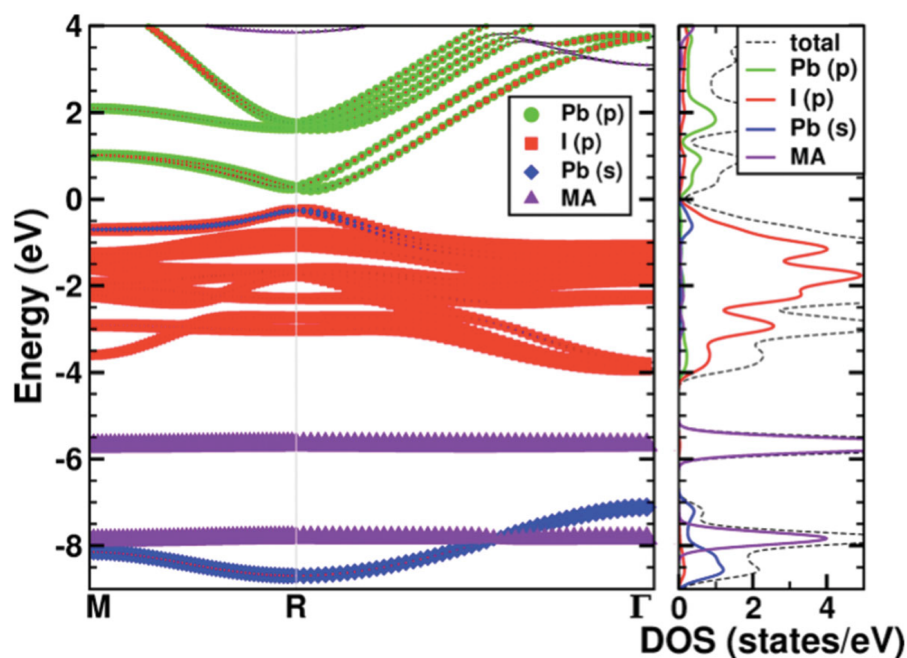


Figure 2.3.1: Band structure (left) and density of states (right) of $MAPbI_3$ in its cubic phase calculated with density functional theory (PBE), including spin-orbit coupling. Ref. [27]

It is crucial to note here that the band gap value of 1.5 - 1.6 eV for $MAPbI_3$ corresponds to a Shockley–Queisser limit of about 31%, which is very close to the 34% value corresponding to an ideal band gap material (see figure 2.3.2).

This value is also very close to the optimal band gap required for a material to form a tandem solar cell on top of a silicon sub-cell, making silicon/perovskite tandems very likely to be the first industrial application of PSCs. In addition, it was shown that this band gap value can be tuned from 1.48 to 2.3 eV by using mixed-halide structures (I/Br/Cl) [22] and/or replacing methylammonium by formamidinium [31] (see section 2.6). This has opened a whole new field of research aiming at tuning the band gap for optimized (>25% efficient) silicon-perovskite [32, 33] or even (>20%) perovskite-perovskite tandem solar cells [34]. In the beginning of 2018, 23.9% CIGS/Perovskite tandems were reported [35].

As for its optical properties, MAPI exhibits a very high absorption coefficient over the whole visible solar emission spectrum (10^5 cm^{-1} for $\lambda < 1000 \text{ nm}$ [6]). The generated exciton has a weak energy of about 15 to 50 meV [36]; we will come back to this point in detail in section 5.4. Once separated by the electric

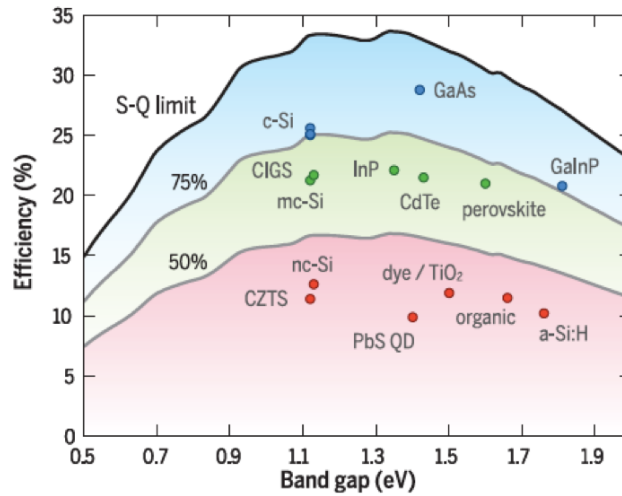


Figure 2.3.2: Summary of the main PV materials' band gaps and record efficiencies. Ref [30]

field induced between the ETL and the HTL, the carriers (electrons and holes) have been measured to both have small effective masses [37] and thus high carrier mobilities ($7.5 \text{ cm}^2 \text{V}^{-1} \text{s}^{-1}$ for electrons and 12.5 to $66 \text{ cm}^2 \text{V}^{-1} \text{s}^{-1}$ for holes [38]).

A very remarkable fact [39] about MAPI is the exceptional carrier-diffusion lengths for both holes and electrons (from 100 nm to even 1 micron when it is doped with chlorine [40–42]). This means a timescale of hundreds of nanoseconds for the carrier recombination. It is of particular interest to note that the direct-indirect nature of the band gap could explain the apparent contradiction of strong absorption and long charge carrier lifetime [28].

Another key point to bear in mind in order to understand the exceptional properties of hybrid perovskites is the unusual defect physics that govern these materials. Indeed, Yin *et al.* [43] showed with DFT calculations that the intrinsic defects that create deep levels in the band gap and could in theory largely reduce the open circuit voltage, such as I_{Pb} , I_{MA} , Pb_i and Pb_I , all have high formation energies and are thus very unlikely to be present in the material at room temperature. As for extrinsic defects, very recently Meggiolaro *et al.* [44] provided a model to explain the high defect tolerance of MAPI and the deactivation of electron traps using the specificities of iodine redox chemistry in these materials. They also showed that an O_2 -rich environment can lock down the remaining hole traps. These results provide further understanding in the role played by oxygen in the interaction between hybrid perovskites and

their environment. In section 5.5 we give an insight on the thermodynamical stability of oxygen defects in the pseudocubic phase of MAPbI_3 , as well as their consequence on the electronic band structure.

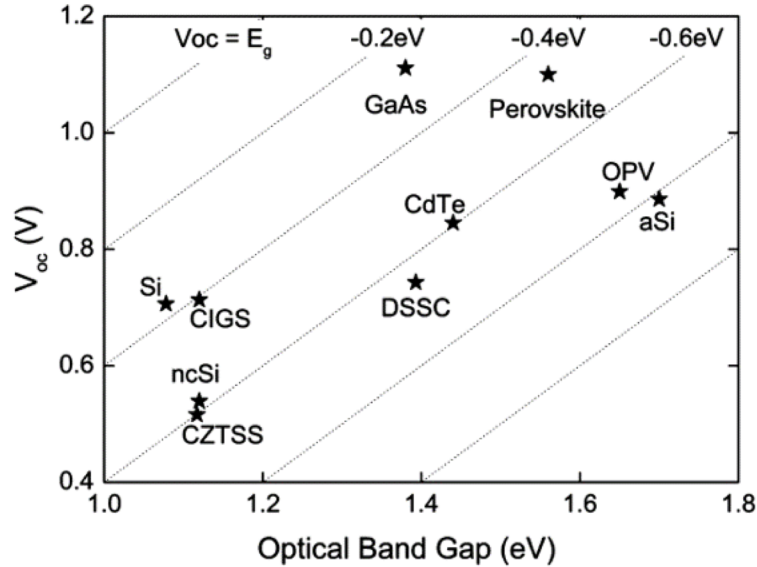


Figure 2.3.3: Comparison of the V_{OC} drop (difference between the optical band gap and the actual V_{OC} value) for different materials. Ref. [11]

This very high defect tolerance is one of the main reasons behind the long carrier diffusion lengths and explains why perovskite solar cells perform much better than other thin films like CdTe or amorphous silicon in terms of open-circuit voltage (drop of about 0.4 eV from the optical band gap, figure 2.3.3).

This defect tolerance could be explained by several reasons [27], including their energy band structure, their hybrid organic-inorganic character, the relative ease of motion and redistribution of the ions, the possibility of phase separation into low defect phases, or the polarizability of the ions.

Even though it is far beyond the scope of this thesis, it is worth mentioning that hybrid perovskite materials have also shown a potential for light emission [45–47], and could be used in other energy-related fields such as thermoelectrics [48].

2.4 THE ISSUE OF STABILITY

In spite of all their exceptional optical and electronic properties (strong absorption, slow recombination, high mobility, rather optimized band gap for single and tunable for tandem cells), perovskite solar cells still have to overcome one major issue on their path to commercialization: their instability. Together with efficiency and cost, stability is one of the three major characteristics used to classify the different generations of solar cells. For the sake of comparison with what we will detail in this section, the reader should keep in mind that silicon solar cells are usually guaranteed to be stable over 20 to 25 years, meaning that the power output should not be less than 80% of rated power after 25 years.

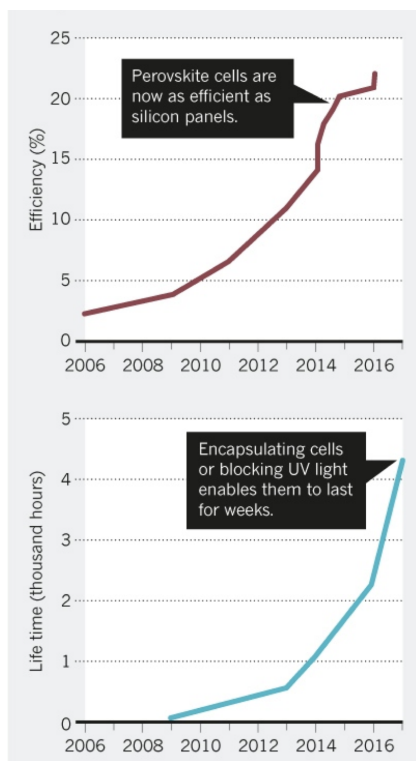


Figure 2.4.1: Perovskite solar cells: parallel between the efficiency race and the quest for stability. Ref [49]

As shown in figure 2.4.1, in 2009 when perovskite solar cells were born their life time was reportedly only a few days, and it was not before 2013 that they could last at least 1 month without severe

degradation. Much more work is needed for PSCs to reach the level of stability required by the market.

Niu *et al.* [50] gave a first general understanding of the possible pathways of the chemical decomposition of the perovskite layer in 2015. This fast degradation has been attributed to different factors, among them: humidity, temperature, oxygen, and light [51]. We will come back to the influence of oxygen and light in chapter 5. In particular, a more detailed bibliography review on the specific issue of light-induced degradation will be given as an introduction to my ellipsometry-based degradation study (section 5.3).

Last, another major issue limiting the readiness level of PSCs is the fact that lead has been a major constituent of nearly all highly efficient perovskite cells to date, raising toxicity issues during device fabrication, installation and recycling [52]. Without going much into detail, several approaches have been used in order to synthesize efficient lead-free perovskite solar cells:

- The tin cousins of MAPI, namely $MA\text{SnI}_3$ [53, 54] and CsSnI_3 [55] have shown a rather high potential for PV applications, but they present an extreme sensitivity to oxygen [39].
- Double perovskites, of general formula $A_2BB'X_6$, allow the replacement of lead by two metallic components and to maintain the photovoltaic and optoelectronic properties of the perovskite structure. In 2016 nontoxic Bi_3^+ was incorporated into the perovskite lattice $\text{Cs}_2\text{AgBiBr}_6$ which shows long carrier recombination lifetimes and a band gap of 1.95 eV [56], which is a reasonable value for solar energy harvesting. A few months later, a comprehensive ab-initio study [57] was able to derive with high accuracy the electronic structure of both $\text{Cs}_2\text{BiAgCl}_6$ and $\text{Cs}_2\text{BiAgBr}_6$ and confirmed the experimental values. This novel class of double perovskite semiconductors has become an active research topic in the PSC community.

2.5 HYSTERETIC PHENOMENA IN PEROVSKITES: ORIGINS AND CONSEQUENCES

The very fast efficiency increase of perovskite solar cells has raised many questions about measurement processes, given the observation that current-voltage scans show ambiguous efficiency values [58, 59]. Indeed, it was shown [60] that the power conversion efficiency strongly depends on the scanning conditions (scan direction, scan speed, light soaking, biasing) and on the cell architecture (figure 2.5.1). Even though hysteresis is a common phenomenon in other types of solar cells (mostly DSSCs, OPV and Si-based solar cells), it is only in perovskites that such impact on the efficiency is observed and that the term "anomalous hysteresis" was used. The risk is that the efficiency value can be overestimated if the scanning rate is too high for the cell to reach its electronic steady-state equilibrium. This means that the published efficiency values for PSC should always be treated cautiously.

It is interesting to note that in general, TiO_2 -based meso-structured ("direct" architectures) show more hysteresis than "inverted" structures using PCBM (common abbreviation for the fullerene derivative [6,6]-phenyl-C61-butyric acid methyl ester) as an electron transporting layer [61]. This fact suggests that the interfaces might play a crucial role since the major difference between the inverted and the direct architectures is that an organic n-type contact is used instead of a metal oxide.

Several hypotheses have been proposed in order to explain this hysteretic behavior :

- Similarly to oxide perovskite materials such as $BaTiO_3$, **ferroelectric domains** within the perovskite layer could induce a memory effect and a modification of the energy band levels at the interfaces due to the polarization of these domains [38, 62, 63]. Indeed, it was shown that hybrid perovskites exhibit spontaneous electric polarization [64]. This strong polarization has two potential interests for energy conversion: [65, 66] enhanced charge separation and improved carrier lifetimes on one hand, and an open circuit voltages possibly above the band gap of the material on the other hand.
- This ferroelectric behavior should be linked to a **high value of the dielectric constant**. Some groups even reported a so-called giant photo-induced low-frequency dielectric constant for halide perovskites [67]. Part of my thesis work aims at determining the dielectric function for cubic $MAPbI_3$ and the different phases of $CsPbI_3$, we will come back to this point in sections 5.3 and 5.4.
- The direct observation of **ion migration** within the halide perovskite layer by different

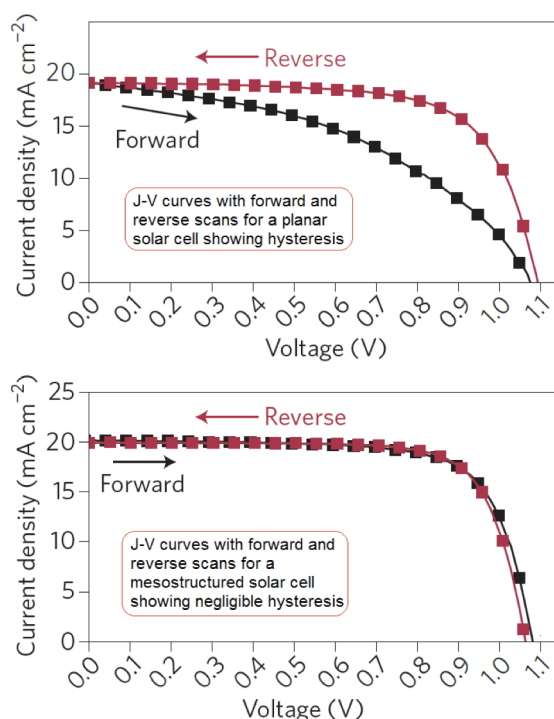


Figure 2.5.1: The hysteretic behavior strongly depends on the solar cell architecture. Ref. [60]

experimental methods (MA^+ [68] or I^- migration, including our group's work [69, 70]) has confirmed previous suggestions [71] that this phenomenon could be at the root of the current–voltage hysteresis. It could also explain many other phenomena [72] such as the switchable photovoltaic effect [73], giant dielectric constant [74], photo-induced phase separation, self-poling effect, and the electrical-field driven reversible conversion [75] between PbI_2 and $MAPbI_3$ (see section 5.2). The activation energies for ionic migration in MAPI were derived from first principles calculations [76] which allowed to identify vacancy-assisted migration of iodide as the most likely channel of ionic conduction (activation energy of 0.6 eV). This suggests that hybrid halide perovskites behave as ionic–electronic conductors.

- The perovskite materials may have a very large defect concentration at the surface, creating interface states [77]. These states could behave as **traps** for electrons and holes. This mechanism could nicely explain why the hysteretic behavior strongly depends on the architecture, since the

latter directly influences the trapping and detrapping times of surface defects. Very recently, it was shown that reducing the interfacial trap density through the use of mechanochemically synthesized perovskites [78] can significantly decrease the hysteretic behavior of PSCs.

Since these four phenomena will be recurrent topics throughout this manuscript, the reader will find in Table 2.5.1 a summary of the different occurrences and references for each physical property.

Phenomenon	References	Section of the manuscript
Ferroelectric domains	[38, 62–64]	4.2 and 4.3
Giant dielectric constant	[67, 79]	5.3 and 5.4
Ionic migration	[68–70, 75]	5.6
Trap states	[77]	5.5

Table 2.5.1: Main phenomena that could be at the origin of the hysteretic behavior of perovskite solar cells, and corresponding sections where they are further investigated in this manuscript.

2.6 CESIUM PEROVSKITES: A GAME CHANGER?

In the race to commercialization, the flagship methylammonium-based perovskite $CH_3NH_3PbI_3$ (MAPbI₃ or "MAPI") will probably be outpaced by more stable perovskite structures because of its poor stability.

One of the first ways that was investigated in order to improve hybrid perovskites' stability was to replace methylammonium by the only other organic cation that could fit in between the PbI_6 octahedra: formamidinium (FA). Replacing MA by FA was also an attempt to overcome the halide segregation induced by light-soaking that was reported by Hoke *et al.* [80] in $MAPb(I_{1-x}Br_x)_3$ compounds used to tune the band gap for tandem applications.

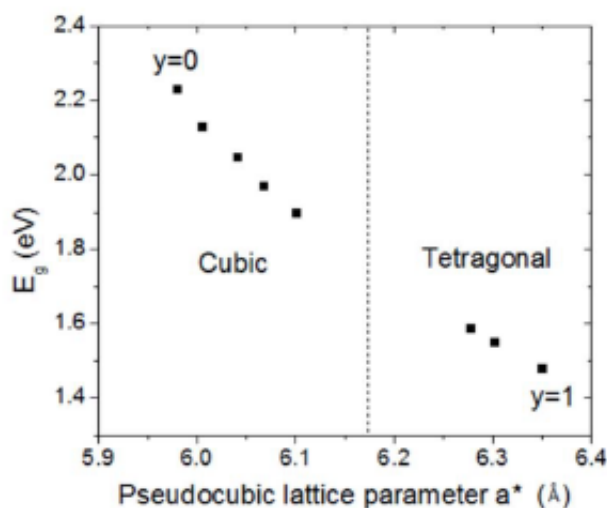


Figure 2.6.1: The band gap tunability of $FAPbI_yBr_{3-y}$ is limited for tandem applications: no structure is found in the 1.6 - 1.8 eV window. Ref [31]

$FAPbX_3$ perovskites are in general much more thermally stable [31] than $MAPbX_3$ structures, and the band gap of formamidinium lead iodide (1.47 eV) allows broader absorption of the solar spectrum relative to conventional methylammonium lead iodide. Even though Yang *et al.* [81] managed to fabricate $FAPbI_3$ -based PSCs with power conversion efficiencies greater than 20%, for tandem applications when iodide is substituted with bromide a crystal phase transition occurs from a trigonal to a cubic structure and the material is unable to crystallize, resulting in an apparently "amorphous" phase (figure 2.6.1) with

high levels of energetic disorder and unexpectedly low absorption [31, 82].

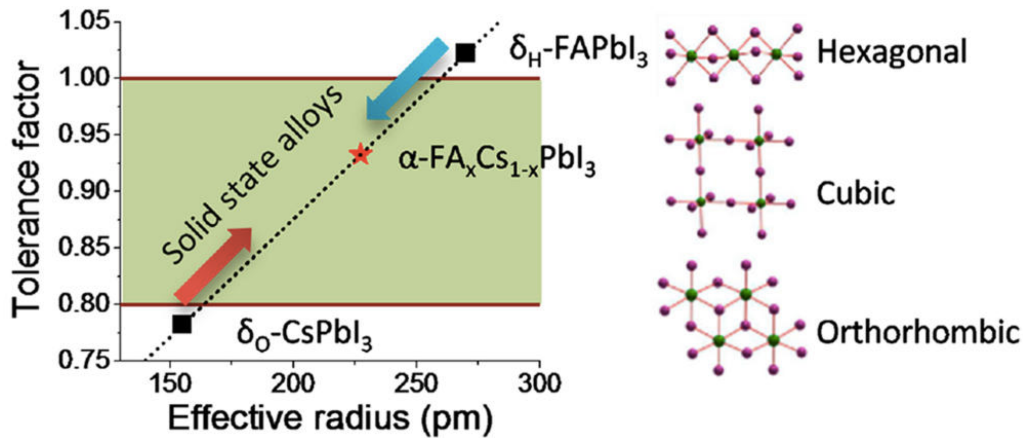


Figure 2.6.2: Mixing FA and Cs allows the formation of solid-state alloys and prevents the formation of their δ -phases. Ref [83]

At the end of 2015, Li *et al.* [83] partially replaced FA by Cs to form $FA_{0.85}Cs_{0.15}PbI_3$ which demonstrated much improved stability in a high-humidity environment, and allowed the formation of solid-state alloys, thus avoiding the yellow δ -phases of $FAPbI_3$ and $CsPbI_3$ (figure 2.6.2).

This discovery brought cesium lead halide perovskites in the spotlight: a few months later, an optimized (band gap of 1.74 eV) and stable mixed-cation lead mixed-halide perovskite absorber for tandem solar cells was synthesized ($[HC(NH_2)_2]_{0.83}Cs_{0.17}Pb(I_{0.6}Br_{0.4})_3$), and used to demonstrate [82] the feasibility of achieving > 25% silicon-perovskite four-terminal tandem cells.

Since then, purely inorganic metal halide perovskites, in particular $CsPbI_3$, have attracted more and more attention from the PSC community. A detailed bibliography review on cesium perovskites will be given in chapter 4.

2.7 THESIS MOTIVATIONS AND APPROACH

In the first two introductory chapters, we saw that perovskite solar cells exhibit exceptional optical and electrical properties which make them the potentially first low-cost high-efficient generation of solar cells. According to all the chemical and physical features reported in the literature, PSCs seem to combine the advantages of inorganic materials (high efficiency, long diffusion length, high mobility) with those of organic materials (low-cost evaporation or solution processes, flexibility). However, as we explained, they face several challenges on their way to commercialization, among them:

- **instability** caused by air, temperature, humidity and light
- **hysteretic behavior** which could be explained by ferroelectric domains, ion migration, high dielectric constant and trap states

Throughout this manuscript, we will consistently try to make a link between our results, obtained using different ab-initio and experimental techniques, and these crucial issues.

As ab-initio calculations, also called first-principle methods, — in particular density functional theory (DFT) — constitute the heart of my thesis work, **chapter 3** is dedicated to giving the reader a comprehensive yet brief overview of DFT and its application to solid-state physics.

In **chapter 4** — which includes 2 of my publications [84, 85] — we focus mostly on fully inorganic cesium perovskites and study the vibrational properties of all the phases of $CsPbI_3$ using the linear response approach of DFT and frozen-phonon methods. Our findings allow us to investigate the **structural instabilities** linked to the anharmonic behavior of $CsPbI_3$ around equilibrium, as well as to rationalize the Rashba effect at the origin of the direct-indirect band gap of halide perovskites. The effects of temperature on the aforementioned instabilities are further investigated using molecular dynamics. We also briefly analyze in that chapter the potential consequences of such anharmonic behavior in terms of ferroelasticity.

The **environmental stability** of hybrid perovskites is addressed in **chapter 5** where we use both experiments (real-time ellipsometry, X-ray diffraction, IV measurements) and ab-initio techniques to investigate the thermodynamics of the dissociation of $MAPbI_3$ into its precursors under light exposure (third publication [79]). This detailed study allows us to derive the dielectric properties of MAPI and determine whether it behaves as an organic or an inorganic semiconductor. As for air-induced

degradation, thanks to additional calculations we give an insight at the possible at the most energetically favorable ways for oxygen defects to form in the structure.

Last, we **conclude** and bring perspectives on the future work needed to a better understanding of the structural and environmental instabilities of halide perovskites.

REFERENCES

- [1] Nicola A. Hill. Why are there so few magnetic ferroelectrics? *The Journal of Physical Chemistry B*, 104(29):6694–6709, 2000. doi: 10.1021/jp000114x. URL <https://doi.org/10.1021/jp000114x>.
- [2] Martin A Green, Anita Ho-Baillie, and Henry J Snaith. The emergence of perovskite solar cells. *Nature Photonics*, 8(7):506–514, 2014.
- [3] Christian KN. Møller. The structure of perovskite-like caesium plumbo trihalides. *Mat. Fys. Medd. Dan. Vid. Sels.*, 32, No 2(2), 1959.
- [4] Dieter Weber. $CH_3NH_3PbX_3$, ein Pb (ii)-system mit kubischer perowskitstruktur/ $CH_3NH_3PbX_3$, a Pb (ii)-system with cubic perovskite structure. *Zeitschrift für Naturforschung B*, 33(12):1443–1445, 1978.
- [5] Dieter Weber. $CH_3NH_3SnBr_xI_{3-x}$ ($x=0-3$), ein sn (ii)-system mit kubischer perowskitstruktur/ $CH_3NH_3SnBr_xI_{3-x}$ ($x=0-3$), a sn (ii)-system with cubic perovskite structure. *Zeitschrift für Naturforschung B*, 33(8):862–865, 1978.
- [6] Akihiro Kojima, Kenjiro Teshima, Yasuo Shirai, and Tsutomu Miyasaka. Organometal halide perovskites as visible-light sensitizers for photovoltaic cells. *J. Am. Chem. Soc.*, 131(17):6050–6051, 2009. doi: 10.1021/ja809598r. URL <http://dx.doi.org/10.1021/ja809598r>.
- [7] Hui-Seon Kim, Chang-Ryul Lee, Jeong-Hyeok Im, Ki-Beom Lee, Thomas Moehl, Arianna Marchioro, Soo-Jin Moon, Robin Humphry-Baker, Jun-Ho Yum, Jacques E Moser, et al. Lead iodide perovskite sensitized all-solid-state submicron thin film mesoscopic solar cell with efficiency exceeding 9%. *Scientific reports*, 2, 2012.
- [8] Jian Liu, Yongzhen Wu, Chuanjiang Qin, Xudong Yang, Takeshi Yasuda, Ashraful Islam, Kun Zhang, Wenqin Peng, Wei Chen, and Liyuan Han. A dopant-free hole-transporting material for efficient and stable perovskite solar cells. *Energy & Environmental Science*, 7(9):2963–2967, 2014.
- [9] Michael Saliba, Simonetta Orlandi, Taisuke Matsui, Sadig Aghazada, Marco Cavazzini, Juan-Pablo Correa-Baena, Peng Gao, Rosario Scopelliti, Edoardo Mosconi, Klaus-Hermann Dahmen, et al. A

REFERENCES

- molecularly engineered hole-transporting material for efficient perovskite solar cells. *Nature Energy*, 1:15017, 2016.
- [10] Perovskites and perovskite solar cells: An introduction. <https://www.ossila.com/pages/perovskites-and-perovskite-solar-cells-an-introduction>. Accessed: 2018-1-7.
- [11] Henry J Snaith. Perovskites: the emergence of a new era for low-cost, high-efficiency solar cells. *The Journal of Physical Chemistry Letters*, 4(21):3623–3630, 2013.
- [12] Xiaoxi He and Harry Zervos. Perovskite photovoltaics 2015-2025. *IDTechEx Reports*, 2015.
- [13] Best research-cell efficiencies (nrel). <https://www.nrel.gov/pv/assets/images/efficiency-chart.png>. Accessed: 2018-1-7.
- [14] Jingbi You, Ziruo Hong, Yang Michael Yang, Qi Chen, Min Cai, Tze-Bin Song, Chun-Chao Chen, Shirong Lu, Yongsheng Liu, Huanping Zhou, et al. Low-temperature solution-processed perovskite solar cells with high efficiency and flexibility. 2014.
- [15] Cristina Roldán-Carmona, Olga Malinkiewicz, Alejandra Soriano, Guillermo Mínguez Espallargas, Ana Garcia, Patrick Reinecke, Thomas Kroyer, M Ibrahim Dar, Mohammad Khaja Nazeeruddin, and Henk J Bolink. Flexible high efficiency perovskite solar cells. *Energy & Environmental Science*, 7(3):994–997, 2014.
- [16] Harald Hoppe and Niyazi Serdar Sariciftci. Organic solar cells: An overview. *Journal of materials research*, 19(7):1924–1945, 2004.
- [17] Victoria Gonzalez-Pedro, Emilio J Juarez-Perez, Waode-Sukmawati Arsyad, Eva M Barea, Francisco Fabregat-Santiago, Ivan Mora-Sero, and Juan Bisquert. General working principles of $CH_3NH_3PbX_3$ perovskite solar cells. *Nano letters*, 14(2):888–893, 2014.
- [18] Michael M Lee, Joël Teuscher, Tsutomu Miyasaka, Takurou N Murakami, and Henry J Snaith. Efficient hybrid solar cells based on meso-superstructured organometal halide perovskites. *Science*, 338(6107):643–647, 2012.

- [19] Lioz Etgar, Peng Gao, Zhaosheng Xue, Qin Peng, Aravind Kumar Chandiran, Bin Liu, Md K Nazeeruddin, and Michael Grätzel. Mesoscopic $\text{CH}_3\text{NH}_3\text{PbI}_3/\text{TiO}_2$ heterojunction solar cells. *Journal of the American Chemical Society*, 134(42):17396–17399, 2012.
- [20] J. Even, L. Pedesseau, M.-A. Dupertuis, J.-M. Jancu, and C. Katan. Electronic model for self-assembled hybrid organic/perovskite semiconductors: Reverse band edge electronic states ordering and spin-orbit coupling. *Phys. Rev. B*, 86:205301, Nov 2012. doi: 10.1103/PhysRevB.86.205301. URL <https://link.aps.org/doi/10.1103/PhysRevB.86.205301>.
- [21] Edoardo Mosconi, Anna Amat, Md K Nazeeruddin, Michael Grätzel, and Filippo De Angelis. First-principles modeling of mixed halide organometal perovskites for photovoltaic applications. *The Journal of Physical Chemistry C*, 117(27):13902–13913, 2013.
- [22] Jun Hong Noh, Sang Hyuk Im, Jin Hyuck Heo, Tarak N. Mandal, and Sang Il Seok. Chemical management for colorful, efficient, and stable inorganic–organic hybrid nanostructured solar cells. *Nano Letters*, 13(4):1764–1769, 2013. doi: 10.1021/nl400349b. URL <http://dx.doi.org/10.1021/nl400349b>. PMID: 23517331.
- [23] Kenichiro Tanaka, Takayuki Takahashi, Takuma Ban, Takashi Kondo, Kazuhito Uchida, and Noboru Miura. Comparative study on the excitons in lead-halide-based perovskite-type crystals $\text{CH}_3\text{NH}_3\text{PbBr}_3$. *Solid state communications*, 127(9):619–623, 2003.
- [24] Masakatsu Hirasawa, Teruya Ishihara, and Takenari Goto. Exciton features in 0-, 2-, and 3-dimensional networks of $[\text{PbI}_6]$ 4-octahedra. *Journal of the Physical Society of Japan*, 63(10): 3870–3879, 1994.
- [25] Jacky Even, Laurent Pedesseau, Jean-Marc Jancu, and Claudine Katan. Importance of spin–orbit coupling in hybrid organic/inorganic perovskites for photovoltaic applications. *The Journal of Physical Chemistry Letters*, 4(17):2999–3005, 2013.
- [26] Paolo Umari, Edoardo Mosconi, and Filippo De Angelis. Relativistic gw calculations on $\text{CH}_3\text{NH}_3\text{PbI}_3$ and $\text{CH}_3\text{NH}_3\text{SnI}_3$ perovskites for solar cell applications. *Scientific reports*, 4:4467, 2014.

REFERENCES

- [27] Joseph Berry, Tonio Buonassisi, David A Egger, Gary Hodes, Leeor Kronik, Yueh-Lin Loo, Igor Lubomirsky, Seth R Marder, Yitzhak Mastai, Joel S Miller, et al. Hybrid organic–inorganic perovskites (hoips): Opportunities and challenges. *Advanced Materials*, 27(35):5102–5112, 2015.
- [28] Tianyi Wang, Benjamin Daiber, Jarvist M Frost, Sander A Mann, Erik C Garnett, Aron Walsh, and Bruno Ehrler. Indirect to direct bandgap transition in methylammonium lead halide perovskite. *Energy & Environmental Science*, 10(2):509–515, 2017.
- [29] Eline M Hutter, María C Gélvez-Rueda, Anna Osherov, Vladimir Bulović, Ferdinand C Grozema, Samuel D Stranks, and Tom J Savenije. Direct-indirect character of the bandgap in methylammonium lead iodide perovskite. *Nature materials*, 16(1):115–120, 2017.
- [30] Albert Polman, Mark Knight, Erik C Garnett, Bruno Ehrler, and Wim C Sinke. Photovoltaic materials: Present efficiencies and future challenges. *Science*, 352(6283), 2016.
- [31] Giles E Eperon, Samuel D Stranks, Christopher Menelaou, Michael B Johnston, Laura M Herz, and Henry J Snaith. Formamidinium lead trihalide: a broadly tunable perovskite for efficient planar heterojunction solar cells. *Energy & Environmental Science*, 7(3):982–988, 2014.
- [32] Colin D Bailie and Michael D McGehee. High-efficiency tandem perovskite solar cells. *Mrs Bulletin*, 40(8):681–686, 2015.
- [33] Michael D. McGehee. Perovskite tandem solar cells with greater than 25 enhanced stability (conference presentation), 2017. URL <https://doi.org/10.1117/12.2273043>.
- [34] Giles E Eperon, Tomas Leijtens, Kevin A Bush, Rohit Prasanna, Thomas Green, Jacob Tse-Wei Wang, David P McMeekin, George Volonakis, Rebecca L Milot, Richard May, et al. Perovskite-perovskite tandem photovoltaics with optimized band gaps. *Science*, 354(6314):861–865, 2016.
- [35] Heping Shen, The Duong, Jun Peng, Daniel Jacobs, Nandi Wu, Junbo Gong, Yiliang Wu, Siva Krishna Karuturi, Xiao Fu, Klaus Weber, Xudong Xiao, Thomas P. White, and Kylie Catchpole. Mechanically-stacked perovskite/cigs tandem solar cells with efficiency of 23.9 *Energy Environ. Sci.*, 11:394–406, 2018.

- [36] Atsuhiko Miyata, Anatolie Mitioğlu, Paulina Plochocka, Oliver Portugall, Jacob Tse-Wei Wang, Samuel D Stranks, Henry J Snaith, and Robin J Nicholas. Direct measurement of the exciton binding energy and effective masses for charge carriers in organic-inorganic tri-halide perovskites. *Nature Physics*, 11(7):582–587, 2015.
- [37] David B Mitzi. Templating and structural engineering in organic–inorganic perovskites. *Journal of the Chemical Society, Dalton Transactions*, (1):1–12, 2001.
- [38] Constantinos C Stoumpos, Christos D Malliakas, and Mercouri G Kanatzidis. Semiconducting tin and lead iodide perovskites with organic cations: phase transitions, high mobilities, and near-infrared photoluminescent properties. *Inorganic chemistry*, 52(15):9019–9038, 2013.
- [39] Michael Grätzel. The light and shade of perovskite solar cells. *Nature materials*, 13(9):838–842, 2014.
- [40] Guichuan Xing, Nripan Mathews, Shuangyong Sun, Swee Sien Lim, Yeng Ming Lam, Michael Grätzel, Subodh Mhaisalkar, and Tze Chien Sum. Long-range balanced electron-and hole-transport lengths in organic-inorganic $\text{CH}_3\text{NH}_3\text{PbI}_3$. *Science*, 342(6156):344–347, 2013.
- [41] Samuel D Stranks, Giles E Eperon, Giulia Grancini, Christopher Menelaou, Marcelo JP Alcocer, Tomas Leijtens, Laura M Herz, Annamaria Petrozza, and Henry J Snaith. Electron-hole diffusion lengths exceeding 1 micrometer in an organometal trihalide perovskite absorber. *Science*, 342(6156):341–344, 2013.
- [42] Carlito S Ponceca Jr, Tom J Savenije, Mohamed Abdellah, Kaibo Zheng, Arkady Yartsev, Tobjörn Pascher, Tobias Harlang, Pavel Chabera, Tonu Pullerits, Andrey Stepanov, et al. Organometal halide perovskite solar cell materials rationalized: ultrafast charge generation, high and microsecond-long balanced mobilities, and slow recombination. *Journal of the American Chemical Society*, 136(14):5189–5192, 2014.
- [43] Wan-Jian Yin, Tingting Shi, and Yanfa Yan. Unusual defect physics in $\text{CH}_3\text{NH}_3\text{PbI}_3$ perovskite solar cell absorber. *Applied Physics Letters*, 104(6):063903, 2014.
- [44] Daniele Meggiolaro, Silvia G. Motti, Edoardo Mosconi, Alex J. Barker, James Ball, Carlo Andrea Riccardo Perini, Felix Deschler, Annamaria Petrozza, and Filippo De Angelis. Iodine chemistry

REFERENCES

- determines the defect tolerance of lead-halide perovskites. *Energy Environ. Sci.*, 11:702–713, 2018. doi: 10.1039/C8EE00124C. URL <http://dx.doi.org/10.1039/C8EE00124C>.
- [45] Konstantinos Chondroudis and David B Mitzi. Electroluminescence from an organic- inorganic perovskite incorporating a quaterthiophene dye within lead halide perovskite layers. *Chemistry of materials*, 11(11):3028–3030, 1999.
- [46] I Koutselas, P Bampoulis, E Maratou, T Evagelinou, G Pagona, and GC Papavassiliou. Some unconventional organic- inorganic hybrid low-dimensional semiconductors and related light-emitting devices. *The Journal of Physical Chemistry C*, 115(17):8475–8483, 2011.
- [47] Zhi-Kuang Tan, Reza Saberi Moghaddam, May Ling Lai, Pablo Docampo, Ruben Higler, Felix Deschler, Michael Price, Aditya Sadhanala, Luis M Pazos, Dan Credgington, et al. Bright light-emitting diodes based on organometal halide perovskite. *Nature nanotechnology*, 9(9):687–692, 2014.
- [48] Yuping He and Giulia Galli. Perovskites for solar thermoelectric applications: A first principle study of $\text{CH}_3\text{NH}_3\text{Al}_3$ (A= Pb and Sn). *Chemistry of Materials*, 26(18):5394–5400, 2014.
- [49] Yang Yang and Jingbi You. Make perovskite solar cells stable. *Nature*, 544(7649):155–156, 2017.
- [50] Guangda Niu, Xudong Guo, and Liduo Wang. Review of recent progress in chemical stability of perovskite solar cells. *J. Mater. Chem. A*, 3:8970–8980, 2015.
- [51] Dian Wang, Matthew Wright, Naveen Kumar Elumalai, and A Uddin. Stability of perovskite solar cells. *Sol. Energy Mater. Sol. Cells*, 147:255–275, 04 2016.
- [52] Aslihan Babayigit, Anitha Ethirajan, Marc Muller, and Bert Conings. Toxicity of organometal halide perovskite solar cells. *Nature materials*, 15(3):247–251, 2016.
- [53] Feng Hao, Constantinos C Stoumpos, Duyen Hanh Cao, Robert PH Chang, and Mercuri G Kanatzidis. Lead-free solid-state organic-inorganic halide perovskite solar cells. *Nature Photonics*, 8(6):489–494, 2014.
- [54] Nakita K Noel, Samuel D Stranks, Antonio Abate, Christian Wehrenfennig, Simone Guarnera, Amir-Abbas Haghighirad, Aditya Sadhanala, Giles E Eperon, Sandeep K Pathak, Michael B

- Johnston, et al. Lead-free organic–inorganic tin halide perovskites for photovoltaic applications. *Energy & Environmental Science*, 7(9):3061–3068, 2014.
- [55] Mulmudi Hemant Kumar, Sabba Dharani, Wei Lin Leong, Pablo P Boix, Rajiv Ramanujam Prabhakar, Tom Baikie, Chen Shi, Hong Ding, Ramamoorthy Ramesh, Mark Asta, et al. Lead-free halide perovskite solar cells with high photocurrents realized through vacancy modulation. *Advanced Materials*, 26(41):7122–7127, 2014.
- [56] Adam H Slavney, Te Hu, Aaron M Lindenberg, and Hemamala I Karunadasa. A bismuth-halide double perovskite with long carrier recombination lifetime for photovoltaic applications. *Journal of the American Chemical Society*, 138(7):2138–2141, 2016.
- [57] Marina R Filip, Samuel Hillman, Amir Abbas Haghighirad, Henry J Snaith, and Feliciano Giustino. Band gaps of the lead-free halide double perovskites $Cs_2BiAgCl_6$ and $Cs_2BiAgBr_6$ from theory and experiment. *The journal of physical chemistry letters*, 7(13):2579–2585, 2016.
- [58] Henry J Snaith, Antonio Abate, James M Ball, Giles E Eperon, Tomas Leijtens, Nakita K Noel, Samuel D Stranks, Jacob Tse-Wei Wang, Konrad Wojciechowski, and Wei Zhang. Anomalous hysteresis in perovskite solar cells. *The Journal of Physical Chemistry Letters*, 5(9):1511–1515, 2014.
- [59] EL Unger, ET Hoke, CD Bailie, WH Nguyen, AR Bowring, T Heumüller, MG Christoforo, and MD McGehee. Hysteresis and transient behavior in current–voltage measurements of hybrid-perovskite absorber solar cells. *Energy & Environmental Science*, 7(11):3690–3698, 2014.
- [60] Nam Joong Jeon, Jun Hong Noh, Young Chan Kim, Woon Seok Yang, Seungchan Ryu, and Sang Il Seok. Solvent engineering for high-performance inorganic–organic hybrid perovskite solar cells. *Nature materials*, 13(9):897–903, 2014.
- [61] Zhengguo Xiao, Cheng Bi, Yuchuan Shao, Qingfeng Dong, Qi Wang, Yongbo Yuan, Chenggong Wang, Yongli Gao, and Jinsong Huang. Efficient, high yield perovskite photovoltaic devices grown by interdiffusion of solution-processed precursor stacking layers. *Energy & Environmental Science*, 7(8):2619–2623, 2014.

REFERENCES

- [62] Hsin-Wei Chen, Nobuya Sakai, Masashi Ikegami, and Tsutomu Miyasaka. Emergence of hysteresis and transient ferroelectric response in organo-lead halide perovskite solar cells. *The Journal of Physical Chemistry Letters*, 6(1):164–169, 2014.
- [63] Hui-Seon Kim, Sung Kyun Kim, Byeong Jo Kim, Kyung-Sik Shin, Manoj Kumar Gupta, Hyun Suk Jung, Sang-Woo Kim, and Nam-Gyu Park. Ferroelectric polarization in $\text{CH}_3\text{NH}_3\text{PbI}_3$ perovskite. *The Journal of Physical Chemistry Letters*, 6(9):1729–1735, 2015.
- [64] Jarvist M Frost, Keith T Butler, Federico Brivio, Christopher H Hendon, Mark Van Schilfgaarde, and Aron Walsh. Atomistic origins of high-performance in hybrid halide perovskite solar cells. *Nano letters*, 14(5):2584–2590, 2014.
- [65] SY Yang, J Seidel, SJ Byrnes, P Shafer, C-H Yang, MD Rossell, P Yu, Y-H Chu, JF Scott, JW Ager, et al. Above-bandgap voltages from ferroelectric photovoltaic devices. *Nature nanotechnology*, 5(2):143–147, 2010.
- [66] Ilya Grinberg, D Vincent West, Maria Torres, Gaoyang Gou, David M Stein, Liyan Wu, Guannan Chen, Eric M Gallo, Andrew R Akbashev, Peter K Davies, et al. Perovskite oxides for visible-light-absorbing ferroelectric and photovoltaic materials. *Nature*, 503(7477):509–512, 2013.
- [67] Emilio J Juarez-Perez, Rafael S Sanchez, Laura Badia, Germá Garcia-Belmonte, Yong Soo Kang, Ivan Mora-Sero, and Juan Bisquert. Photoinduced giant dielectric constant in lead halide perovskite solar cells. *The Journal of Physical Chemistry Letters*, 5(13):2390–2394, 2014.
- [68] Yongbo Yuan, Jungseok Chae, Yuchuan Shao, Qi Wang, Zhengguo Xiao, Andrea Centrone, and Jinsong Huang. Photovoltaic switching mechanism in lateral structure hybrid perovskite solar cells. *Advanced Energy Materials*, 5(15), 2015.
- [69] Tae-Youl Yang, Giuliano Gregori, Norman Pellet, Michael Grätzel, and Joachim Maier. The significance of ion conduction in a hybrid organic–inorganic lead-iodide-based perovskite photosensitizer. *Angewandte Chemie*, 127(27):8016–8021, 2015.
- [70] Heejae Lee, Sofia Gaiaschi, Patrick Chapon, Arthur Marronnier, Heeryung Lee, Jean-Charles Vanel, Denis Tondelier, Jean-Eric Boureé, Yvan Bonnassieux, and Bernard Geffroy. Direct experimental

- evidence of halide ionic migration under bias in $CH_3NH_3PbI_{3-x}Cl_x$ -based perovskite solar cells using g-d-oes analysis. *ACS Energy Letters*, 2(4):943–949, 2017.
- [71] Wolfgang Tress, Nevena Marinova, Thomas Moehl, Shaik Mohammad Zakeeruddin, Mohammad Khaja Nazeeruddin, and Michael Grätzel. Understanding the rate-dependent j–v hysteresis, slow time component, and aging in $CH_3NH_3PbI_3$ perovskite solar cells: the role of a compensated electric field. *Energy & Environmental Science*, 8(3):995–1004, 2015.
- [72] Yongbo Yuan and Jinsong Huang. Ion migration in organometal trihalide perovskite and its impact on photovoltaic efficiency and stability. *Accounts of chemical research*, 49(2):286–293, 2016.
- [73] Zhengguo Xiao, Yongbo Yuan, Yuchuan Shao, Qi Wang, Qingfeng Dong, Cheng Bi, Pankaj Sharma, Alexei Gruverman, and Jinsong Huang. Giant switchable photovoltaic effect in organometal trihalide perovskite devices. *Nature materials*, 14, 12 2014.
- [74] Qianqian Lin, Ardalan Armin, Ravi Chandra Raju Nagiri, Paul L Burn, and Paul Meredith. Electro-optics of perovskite solar cells. *Nature Photonics*, 9(2):106–112, 2015.
- [75] Yongbo Yuan, Qi Wang, Yuchuan Shao, Haidong Lu, Tao Li, Alexei Gruverman, and Jinsong Huang. Electric-field-driven reversible conversion between methylammonium lead triiodide perovskites and lead iodide at elevated temperatures. *Advanced Energy Materials*, 6(2), 2016.
- [76] Christopher Eames, Jarvist M Frost, Piers RF Barnes, Brian C O’regan, Aron Walsh, and M Saiful Islam. Ionic transport in hybrid lead iodide perovskite solar cells. *Nature communications*, 6:7497, 2015.
- [77] Hui-Seon Kim, Ivan Mora-Sero, Victoria Gonzalez-Pedro, Francisco Fabregat-Santiago, Emilio J Juarez-Perez, Nam-Gyu Park, and Juan Bisquert. Mechanism of carrier accumulation in perovskite thin-absorber solar cells. *Nature communications*, 4:2242, 2013.
- [78] Daniel Prochowicz, Pankaj Yadav, Michael Saliba, Marcin Sasaki, Shaik M Zakeeruddin, Janusz Lewinski, and Michael Grätzel. Reduction in the interfacial trap density of mechanochemically synthesized $MAPbI_3$. *ACS Applied Materials & Interfaces*, 9(34):28418–28425, 2017.

REFERENCES

- [79] Arthur Marronnier, Heeryung Lee, Heejae Lee, Minjin Kim, Céline Eypert, Jean-Paul Gaston, Guido Roma, Denis Tondelier, Bernard Geffroy, and Yvan Bonnassieux. Electrical and optical degradation study of methylammonium-based perovskite materials under ambient conditions. *Solar Energy Materials and Solar Cells*, 178:179–185, 2018.
- [80] Eric T Hoke, Daniel J Slotcavage, Emma R Dohner, Andrea R Bowring, Hemamala I Karunadasa, and Michael D McGehee. Reversible photo-induced trap formation in mixed-halide hybrid perovskites for photovoltaics. *Chemical Science*, 6(1):613–617, 2015.
- [81] Woon Seok Yang, Jun Hong Noh, Nam Joong Jeon, Young Chan Kim, Seungchan Ryu, Jangwon Seo, and Sang Il Seok. High-performance photovoltaic perovskite layers fabricated through intramolecular exchange. *Science*, 348(6240):1234–1237, 2015.
- [82] David P McMeekin, Golnaz Sadoughi, Waqaas Rehman, Giles E Eperon, Michael Saliba, Maximilian T Hörlantner, Amir Haghighirad, Nobuya Sakai, Lars Korte, Bernd Rech, et al. A mixed-cation lead mixed-halide perovskite absorber for tandem solar cells. *Science*, 351(6269):151–155, 2016.
- [83] Zhen Li, Mengjin Yang, Ji-Sang Park, Su-Huai Wei, Joseph J Berry, and Kai Zhu. Stabilizing perovskite structures by tuning tolerance factor: formation of formamidinium and cesium lead iodide solid-state alloys. *Chemistry of Materials*, 28(1):284–292, 2015.
- [84] Arthur Marronnier, Heejae Lee, Bernard Geffroy, Jacky Even, Yvan Bonnassieux, and Guido Roma. Structural instabilities related to highly anharmonic phonons in halide perovskites. *The Journal of Physical Chemistry Letters*, 8(12):2659–2665, 2017.
- [85] Arthur Marronnier, Guido Roma, Soline Boyer-Richard, Laurent Pedesseau, Jean-Marc Jancu, Yvan Bonnassieux, Claudine Katan, Constantinos C. Stoumpos, Mercouri G. Kanatzidis, and Jacky Even. Anharmonicity and disorder in the black phases of cesium lead iodide used for stable inorganic perovskite solar cells. *ACS Nano*, 2018. doi: 10.1021/acsnano.8b00267. URL <https://doi.org/10.1021/acsnano.8b00267>. PMID: 29565559.

God does not play dice with the universe.

Albert Einstein

3

Density Functional Theory

THE ABILITY TO DERIVE, from an ab initio perspective, the fundamental physical properties of solids has been the Holy Grail of an intense research field that opened after the completeness of the quantum theory was achieved in the 1930's. In this chapter the goal is to give the fundamental equations and approximations that constitute the backbone of the Density Functional Theory (DFT) method that I used for my calculations, and explain briefly how they constitute a powerful tool to derive the vibrational, electronic and optical properties of materials. We do not aim to give a comprehensive account of DFT, but would rather like to provide readers who are not familiar with DFT with the notions needed to understand the technical specificities of the ab initio calculations of chapters 4 and 5.

Contents

3.1	From quantum physics to materials modeling	54
3.1.1	Hartree potential: classical electronics	55
3.1.2	Hartree-Fock equations: exclusion principle	56
3.1.3	Kohn-Sham equations: including correlation	56
3.2	Density Functional Theory (DFT)	57
3.2.1	Hohenberg-Kohn theorem	57
3.2.2	Self-consistent total energy calculations	58
3.2.3	Relaxation and structure optimization	58
3.2.4	The Local Density Approximation (LDA)	60
3.2.5	DFT for solids: plane waves, pseudopotentials and k-points	62
3.3	Band structure: Rashba effect	65
3.4	Vibrational and dielectric properties: linear-response approach (DFPT)	66
3.5	Molecular dynamics methods	69
	References	69

3.1 FROM QUANTUM PHYSICS TO MATERIALS MODELING

Quantum mechanics, born in the beginning of the twentieth century, is one of the major breakthroughs in physics in the sense that it produces a unified theory allowing the understanding of a vast number of properties of materials at an atomic scale, under a unique mathematical formulation, the Schrödinger equation.

It is only in 1964, thanks to the discovery of the Hohenberg-Kohn theorem and the formulation of Kohn-Sham equations, that approximations to the many-body Schrödinger equations which were both not too extreme to give faithful results and powerful enough to drastically reduce the computing time were found. These two discoveries lead to the Density Functional Theory (DFT) method for materials.

The general Schrödinger equation of a solid with N electrons of position vectors r_1, \dots, r_N reads:

$$\left[-\sum_i \frac{\nabla_i^2}{2} + \sum_i V_n(r_i) + \frac{1}{2} \sum_{i \neq j} \frac{1}{|r_i - r_j|} \right] \Psi = E\Psi \quad (3.1)$$

where V_n is the attraction Coulomb potential between one electron and all the nuclei (considered clamped), and where the notations were simplified by measuring energies in units of Hartrees E_{Ha} , distances in units of the Bohr radius a_0 and masses in units of the electron mass m_e defined as:

$$1 \text{ Ha} = 27.2114 \text{ eV}$$

$$1 \text{ bohr} = 0.529177 \text{ \AA}$$

$$1 \text{ a.u. of mass} = 9.10938291 \times 10^{-31} \text{ kg}$$

Note that in this manuscript we will sometimes use Rydberg units for energies, defined as follows:

$$1 \text{ Ry} = 0.5 \text{ Ha}$$

As the complexity and thus the computational time required to solve these N coupled equations grows exponentially with the size of the system, several approximations have been implemented to allow the study of solids on the atomic level.

3.1.1 HARTREE POTENTIAL: CLASSICAL ELECTRONICS

While purely neglecting the third energy term in 3.1 corresponding to the electron-electron interaction is not reasonable, the mean-field approximation, developed by Hartree in 1928 [1], manages to both transform the 3N-dimensional many-body Schrödinger equation into N three-dimensional equations and take into account the electron-electron repulsion using the classical electrostatic potential:

$$\left[-\frac{\nabla^2}{2} + V_n(r) + V_H(r) \right] \varphi_i = \varepsilon_i \varphi_i \quad (3.2)$$

where V_H is the so-called Hartree potential which corresponds to the energy of the electrons immersed

in the electrostatic potential created by the distribution of electronic charge $n(\mathbf{r})$ itself:

$$\nabla^2 V_H(\mathbf{r}) = -4\pi n(\mathbf{r}) \quad (3.3)$$

$$n(\mathbf{r}) = \sum_i |\varphi_i(\mathbf{r})|^2 \quad (3.4)$$

3.1.2 HARTREE-FOCK EQUATIONS: EXCLUSION PRINCIPLE

This simplified picture given by Hartree, using classical electrostatics and considering the electrons as totally independent, neglects two main phenomena: the quantum nature of electrons and the fact that they are fermions. In order to take into account the latter, Fock applied the Pauli exclusion principle and used a variational approach, giving rise to the so called Hartree-Fock equations (Eqs. 3.3, 3.4 and 3.5) [2]:

$$\left[-\frac{\nabla^2}{2} + V_n(\mathbf{r}) + V_H(\mathbf{r})\right]\varphi_i + \int d\mathbf{r}' V_X(\mathbf{r}, \mathbf{r}')\varphi_i(\mathbf{r}') = \varepsilon_i \varphi_i \quad (3.5)$$

where the **non-local** potential V_X , called the Fock-exchange potential, prevents two electrons from occupying the same quantum state:

$$V_X(\mathbf{r}, \mathbf{r}') = - \sum_j \frac{\varphi_j^*(\mathbf{r}')\varphi_j(\mathbf{r})}{|\mathbf{r} - \mathbf{r}'|}$$

3.1.3 KOHN-SHAM EQUATIONS: INCLUDING CORRELATION

The only missing part of the picture is now the quantum correlations between electrons, and can be included in a correlation potential term V_c to obtain the general Kohn-Sham equations:

$$\left[-\frac{\nabla^2}{2} + V_n(\mathbf{r}) + V_H(\mathbf{r}) + V_x(\mathbf{r}) + V_c(\mathbf{r})\right]\varphi_i = \varepsilon_i \varphi_i \quad (3.6)$$

where V_x is a simplified local version of the exchange potential V_X . We do not give further details in this manuscript about these equations, the curious reader can find more details in Ref. [3, 4]. In the following sections, we will use the condensed notation V_{xc} for the term $V_x + V_c$.

3.2 DENSITY FUNCTIONAL THEORY (DFT)

So far, we have seen that it is possible to simplify the $3N$ -dimensional many-body Schrödinger equation to N three-dimensional equations with the electron-electron Coulomb repulsion being replaced by a mean-field term (Hartree) plus exchange-correlation potentials. Although this substantially simplifies the calculation of the energy eigenvalues of the system, the major breakthrough which lead to the formulation of Density Functional Theory and made it possible to effectively and efficiently compute many fundamental properties of materials starting from the first principles of quantum mechanics was the Hohenberg-Kohn theorem.

3.2.1 HOHENBERG-KOHN THEOREM

In 1964, Hohenberg and Kohn [5] observed and proved that for a given density of particles in the ground state $n_o(r)$ there exists only one corresponding wave function of the ground state $\Psi_o(r_1, \dots, r_N)$. This means that the ground state energy E_o is a functional of the electron density only:

$$E_o = F[n_o]$$

Thus, all the terms in the Kohn-Sham equations 3.6 can be rewritten in terms of functionals of the electron density n . The variational problem of minimizing the total energy functional $E[n]$ was then solved by Kohn and Sham in 1965 [3], who showed that **there must be** a functional $E_{xc}[n]$ which gives the exact ground-state energy and density using equations 3.6, and which is associated to a potential:

$$V_{xc}(r) = \left. \frac{\delta E_{xc}[n]}{\delta n} \right|_{n(r)}$$

To summarize, the density functional theory, developed starting from 1964, together with Hartree and Fock's previous work from the late 1920's on the simplification of the electron-electron interaction, constitutes a very powerful, practical, and time-efficient tool in order to calculate the properties of the **ground state** of any material, using only first-principles physics and taking as the only input the atomic number of the constituents of the material to be studied. Its back stone equations are:

$$\left[-\frac{\nabla^2}{2} + V_n(r) + V_H(r) + V_{xc}(r) \right] \varphi_i = \varepsilon_i \varphi_i \quad (3.7)$$

$$\nabla^2 V_H(r) = -4\pi n(r) \quad (3.8)$$

$$n(r) = \sum_i |\varphi_i(r)|^2 \quad (3.9)$$

$$V_{xc}(r) = \left. \frac{\delta E_{xc}[n]}{\delta n} \right|_{n(r)} \quad (3.10)$$

There are two main types of DFT calculations one can run from this model: calculating the total energy of a system, or trying to minimize this energy by changing the nuclei's position (structure optimization).

3.2.2 SELF-CONSISTENT TOTAL ENERGY CALCULATIONS

In order to calculate the total energy of the system, one should notice that the equation sets 3.7 to 3.10 are self-consistent in the sense that the potential energy V depends itself on the unknown functions φ_i . This means that an initial guess for the potential, or similarly for the density, is necessary in order to start the convergence algorithm which will stop when self-consistency is obtained (up to a chosen convergence threshold). This algorithm is summarized on figure 3.2.1.

3.2.3 RELAXATION AND STRUCTURE OPTIMIZATION

The second type of DFT calculations consists of structure optimizations, also called relaxation calculations. Here, the goal is to minimize the total energy of the system with respect to the positions of the nuclei which had been assumed clamped so far. The equilibrium structure corresponds to the one where the total forces acting on the nuclei go to zero.

Without going into too much detail, all DFT codes use the following three properties or approximations in order to efficiently optimize the structure of a given system:

- The **Born-Oppenheimer approximation** [6], also called adiabatic approximation, which decouples the dynamics of the electrons from that of the nuclei, thus assuming that the nuclei move so slowly that electrons always have enough time to reach a new equilibrium state. Practically, this means that for each new nuclei positions the code will use the self-consistency algorithm

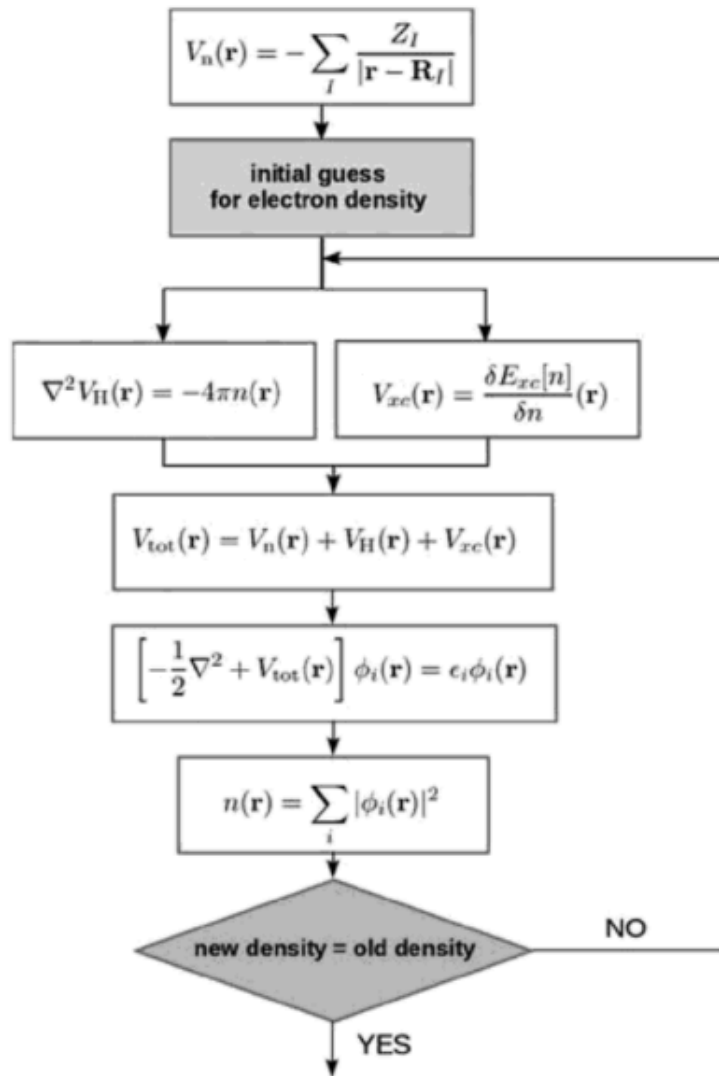


Figure 3.2.1: DFT self-consistency algorithm [4].

schematized in figure 3.2.1 before changing the positions again (except for Car-Parinello molecular dynamics, see section 3.5).

- Quantum mechanics is not necessary to describe the dynamics of the nuclei.
- The calculation of the forces for all the M atoms requires the knowledge of the electron density only, instead of requiring $3M+1$ total energy calculations corresponding to each degree of freedom of the all the nuclei. This result, called the Hellmann-Feynman theorem [7, 8], is part of the more general " **$2n+1$ theorem**" [9] which states that calculating the derivative of order $2n+1$ of the eigen energy E (here the first order derivative, the force) only requires the knowledge of the derivative of order n of the eigenfunction Ψ (here the eigenfunction itself).

To summarize, the relaxation algorithm proceeds as schematized in figure 3.2.2.

Even though DFT only gives access to the physical properties of the ground state of the system, several approximations and methods have been developed since [10] in order to explore the physics of the excited states. As for the other properties we studied for our perovskite materials (vibrations, Rashba splitting in the electronic band structure, dielectric function), we will briefly come back to the methods we used in sections 3.3 and 3.4.

Before doing so, we discuss in the next two subsections the practical methods that can be used to describe the exchange-correlation functional.

3.2.4 THE LOCAL DENSITY APPROXIMATION (LDA)

In this thesis work, we used two of the most common approximations for the exchange-correlation functional : the Local Density Approximation (LDA) on one hand, and the PBE [11] (for Perdew, Burke, Ernzerhof) xc-functional, which belongs to the class of Generalized Gradient Approximations (GGA), on the other hand.

We explain only the LDA approximation, for which our physical intuition and some quantum theory textbook notions will be enough to understand the method.

The LDA was developed in the 1980s [12, 13] using the homogeneous electron gas model as a local approximation to evaluate the exchange-correlation of a real material. Indeed, the calculation of the exchange energy of a homogeneous free electron gas contained in a volume V with a density n is a classic textbook exercise (using stationary waves [14]):

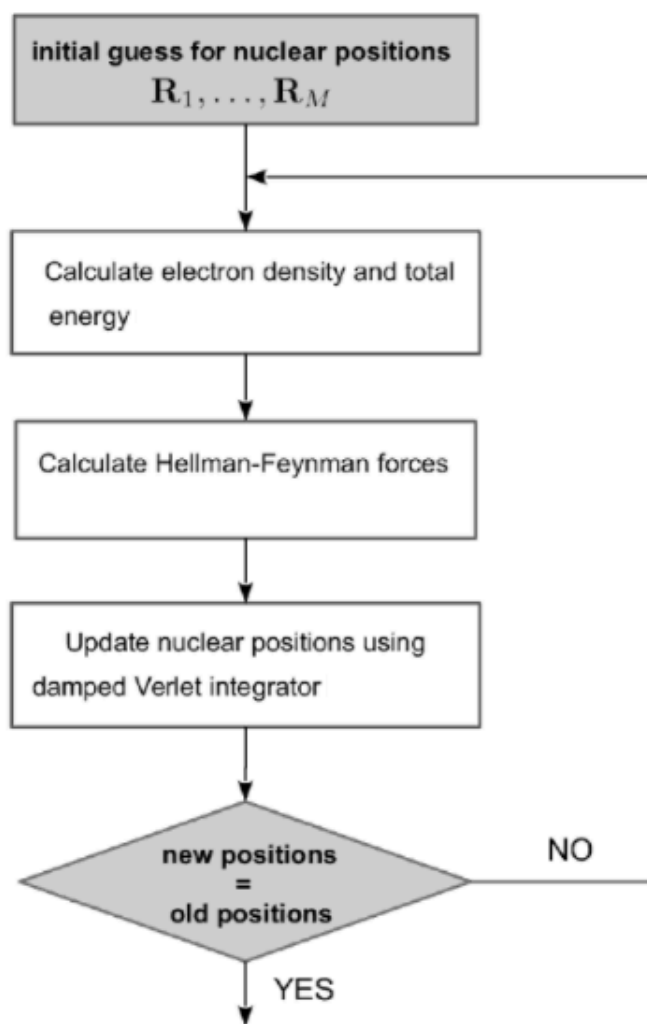


Figure 3.2.2: DFT geometry optimization algorithm [4]. A damping term is introduced to update the nuclear position and navigate in the potential-energy surface towards the global energy minimum.

$$E_X = -\frac{3}{4} \left(\frac{3}{\pi}\right)^{\frac{1}{3}} n^{\frac{1}{3}} V$$

However, deriving the correlation energy of such a system is not possible analytically. Ceperley and Alder [12] used stochastic numerical methods to directly solve the many-body Schrödinger equation and produced reference data which were later parametrized by Perdew and Zunger [13].

Now that we have both the exchange and the correlation energy for this toy model, the idea of the LDA is to approximate the non local exchange-correlation energy density of a real material by the one corresponding to an homogeneous electron gas (HEG) of density given by the local density n at the point of interest:

$$E_{xc}^{LDA}[n] = \int \mathcal{E}_{xc}^{HEG}[n(r)]n(r)dr$$

where $\mathcal{E}_{xc}^{HEG}[n]$ is the exchange-correlation energy density of a homogeneous electron gas of density n .

The LDA, in spite of its simplicity, is a rather accurate and fast method to obtain the ground state energy and structure of a solid. LDA usually underestimates the optimized lattice constants. [4].

Even more used nowadays than the LDA is the **Generalized Gradient Approximations (GGA)**, for which the exchange-correlation energy density is a function not only of the local density $n(r)$ but also of its gradient $\nabla n(r)$. Contrary to LDA, GGA usually overestimates the optimized lattice constants [4].

In general, both LDA and GGA are not able to reproduce well the electronic properties of semiconductors, in particular the band gap value which they both underestimate.

Last, we also used in this work hybrid functionals, but only at some very specific steps, in order to check that our results were not affected by the choice of the exchange-correlation functional. Hybrid functionals mix in general a portion of exact exchange from Hartree–Fock theory with local or semi-local exchange-correlation terms, and give more accurate values for the band gap [15]. For our additional calculations we used the so-called HSE (Heyd-Scuseria-Ernzerhof [16]) functional, which is a hybrid functional based on PBE. A comprehensive review can be found in Ref. [10].

3.2.5 DFT FOR SOLIDS: PLANE WAVES, PSEUDOPOTENTIALS AND K-POINTS

From now on, we restrict the scope of our discussion to solids. The periodic nature of atom arrangements in solids makes it much more convenient (Bloch's theorem) to:

- define plane waves as basis functions for the Kohn-Sham wavefunctions (operators become matrices, wavefunctions become vectors),
- define a primitive cell for the crystal lattice,
- use Fourier transforms in order to simplify calculations,
- define a reciprocal lattice and a **Brillouin zone sampling** in the reciprocal space in order to replace integrals by discrete sums. The definition of Brillouin zones and the high-symmetry points for different crystal structures (cubic, tetragonal, orthorhombic) is given in Appendix A.1.

While in theory the basis of plane waves should be of infinite size, in practice one sets a maximum value for the basis' wave vectors K_{max} , or similarly for their energy :

$$E_{cutoff} = \frac{K_{max}^2}{2}$$

Given the variational principle, increasing the cutoff energy always decreases the converged ground state energy.

One additional step to reduce the computing time of DFT is to divide electrons in two groups: valence electrons and inner core electrons. Given that the core electrons do not participate in chemical bonds, are strongly bound to the nucleus (inducing a screening effect), and converge very slowly with respect to the plane wave basis, we can exclude the core electrons from the potential ("frozen-core approximation") and correct the resulting potential applied to the valence electrons. This corrected potential is called a **pseudopotential**.

This is all the more judicious in our case where we study metals and semiconductors, since for this class of materials the binding and electronic properties mainly come from the interaction of the valence electrons. In some cases treating explicitly only the last shell of electrons (valence) is not sufficiently accurate. In this case one or two further shells are included, labeled as semicore electrons.

A detailed review of the different kinds of pseudopotentials used in DFT calculations can be found in Ref. [10, 17]. In this work we mostly used norm-conserving or ultrasoft pseudopotentials, and found the use of scalar relativistic potentials necessary for lead. We took into account full relativistic effects only to check that our conclusions were not affected by spin-orbit coupling or when required by the calculation (for electronic band structures and the Rashba effect e.g.).

Last, among the various DFT codes available, I chose to use Quantum-Espresso (PWSCF [18]) for all the calculations on defect-less crystals - which constitutes the vast majority of my work - and the VASP code (Vienna Abinitio Simulation Package [19]) for the defects calculations in supercells (section 5.5).

In general, we provide all the technical details for each DFT calculation (number of valence electrons and pseudopotentials, exchange-correlation functional, k-point grid, energy cutoffs, convergence thresholds and relativistic effects) in the corresponding sections of the manuscript.

In the remaining sections of this chapter, we briefly describe the numerical methods we used in conjunction with DFT in order to go further than the basic properties of the ground state (energy and equilibrium structure) and get a physical understanding of the vibrational, electronic and dielectric properties of our perovskite materials.

3.3 BAND STRUCTURE: RASHBA EFFECT

Before doing so, we introduce and describe here the Rashba/Dresselhaus effect that affects the electronic band structures of materials under specific conditions.

The Rashba effect is a spin degeneracy lift originating from spin-orbit coupling (SOC) under inversion symmetry breaking. Dresselhaus and Rashba were the first to explain how SOC affects non-centrosymmetric zincblende [20] and wurtzite [21] structures using group theory. It was shown a few decades later that this also holds true for 2D systems [22]. A comprehensive and local explanation of Rashba and Dresselhaus effects was published recently by Zunger *et al.* [23].

Spin splitting has various potential consequences on the structure of solid-state systems. In particular, such effects are of high interest for spintronics [24, 25]. As for photovoltaics, spin splitting can have strong impact on the absorption and transport properties of materials. For instance, the presence of spin and momentum forbidden transitions can mitigate or even remove electron-hole recombination [26]. Last, for semiconductors such an effect can transform a direct band gap semiconductor into an indirect band one.

We will come back to these effects in chapter 4.

3.4 VIBRATIONAL AND DIELECTRIC PROPERTIES: LINEAR-RESPONSE APPROACH (DFPT)

The vibrational properties of solids can be obtained using the linear response approach of DFT, also known as **DFPT (Density-Functional Perturbation Theory)** [27]. This approach, based on DFT, gives access in general to the second-order derivatives of the energy. In particular, the phonon dispersion spectrum of a material along high-symmetry lines of the Brillouin zone and the corresponding phonon density of states can be computed using DFPT.

As for the dielectric function, its ab initio calculation depends on the frequency range of study. As schematized in figure 3.4.1, whereas the high-frequency regime is mostly dominated by the electronic contributions, the dipolar contributions need to be taken into account in the static regime (low frequency).

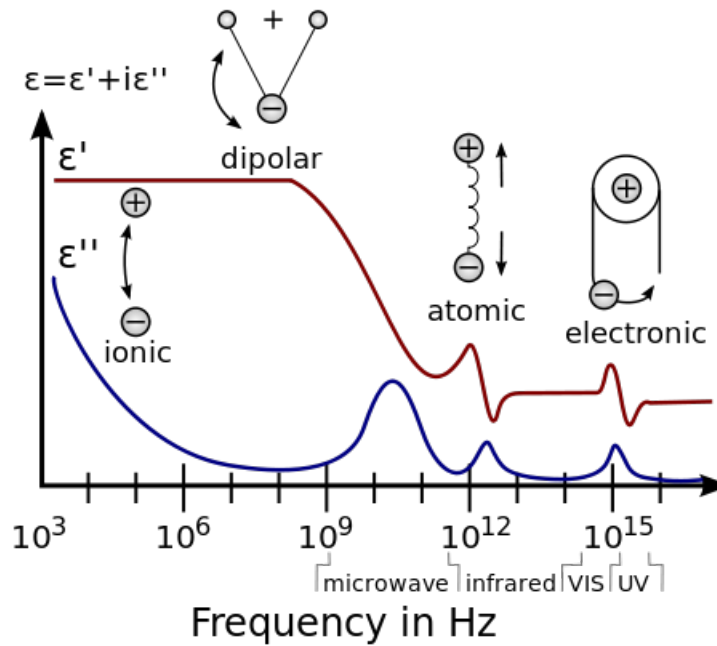


Figure 3.4.1: Schematic view of the dielectric function in its different frequency regimes. Source: wikipedia.

When taking into account the coupling of phonons with a macroscopic electric field \mathcal{E} , the potential

energy surface is described as [28]:

$$E(u, \mathcal{E}) = \frac{1}{2}M\omega_0^2u^2 - \frac{\Omega}{8\pi}\epsilon_\infty\mathcal{E}^2 - eZ^*u \cdot \mathcal{E} \quad (3.11)$$

where u is the displacement along the potential energy surface, M the mass, ω_0 the eigen frequency, Ω the volume, Z^* the Born effective charge.

The polarization P (contributing to the induction $D = \mathcal{E} + 4\pi P$) is then composed of two terms: the electronic polarization

$$P_{el} = \chi_\infty \mathcal{E}$$

where $\epsilon_\infty = 4\pi\chi_\infty + 1$; and the ionic polarization

$$P_{ion} = eZ^*u$$

In the high frequency regime (visible range, electronic contributions only), the dielectric function can be obtained within the Random Phase Approximation (RPA) from Kohn-Sham eigenvalues and eigenvectors by calculating the proper coefficients of each allowed transition between states v in the valence band and states c in the conduction band [4]:

$$\epsilon'(\omega) = 1 + \sum_{c,v} f_{c,v} \frac{\omega_p^2}{\omega_{c,v}^2 - \omega^2} \quad (3.12a)$$

$$\epsilon''(\omega) = \frac{\pi}{2} \sum_{c,v} f_{c,v} \frac{\omega_p^2}{\omega} \delta(\omega - \omega_{c,v}) \quad (3.12b)$$

$\omega_{c,v}$ being the transition's oscillator frequency, and ω_p the plasma frequency of the solid.

In particular, the high-frequency limit ϵ_∞ can be directly obtained using the second derivative of the total energy with respect to the electric field, thus using the DFPT method.

In order to obtain the dielectric constant in the static regime, ϵ_0 , one needs to take into account the relaxation with dipolar contributions, as the term arising from the Born effective charges in the susceptibility must be included [29]:

$$\epsilon_{a\beta}^0 = \epsilon_{a\beta}^\infty + \sum_m \Delta\epsilon_{m,a\beta}$$

with [30]:

$$\Delta\epsilon_{m,a\beta} = \frac{4\pi e^2}{M_0 V} \frac{\tilde{Z}_{ma}^* \tilde{Z}_{m\beta}^*}{\omega_m^2}$$

where ω_m is the frequency of mode m .

The mode effective charges \tilde{Z}_{ma}^* are defined as the following sum over atoms i and directions γ [31]:

$$\tilde{Z}_{ma}^* = \sum_{i,\gamma} Z_{a\gamma}^*(i) \left(\frac{M_0}{M_i}\right)^{\frac{1}{2}} \xi_m(i\gamma)$$

where ξ_m is the dynamical matrix eigenvector and Z^* the Born effective charge tensor :

$$Z_{ia\beta}^* = -\frac{\partial^2 E}{\partial d_{ia} \partial \mathcal{E}_\beta}$$

and d_{ia} is the uniform displacement of the atomic sublattice i in Cartesian direction a from its position in the equilibrium unit cell, with derivatives taken in zero macroscopic field. This relationship means that low values of mode frequencies imply large lattice contributions to the static dielectric permittivity tensor.

As a conclusion, one can use the linear response approach of DFT to calculate the dielectric constant in the static regime from the Born effective charges and the high-frequency dielectric tensor.

3.5 MOLECULAR DYNAMICS METHODS

The last calculation type we want to explain here is ab initio molecular dynamics. Indeed, in all DFT calculations, and in particular when optimizing the geometry, the temperature effects are always neglected: DFT is said to be a zero Kelvin method.

In molecular dynamics, temperature effects are taken into account via a random distribution of velocities (such as a Maxwell–Boltzmann distribution) whose scale parameter is a function of temperature. The forces are then computed (by using an empirical potential, or as it is the case with MD based on DFT, using the DFT wave function) in order to calculate the new positions induced by thermal agitation. The temperature is recalculated at each step and reset (for example to its initial value) after a certain number x of steps. This general method is summarized in figure 3.5.1.

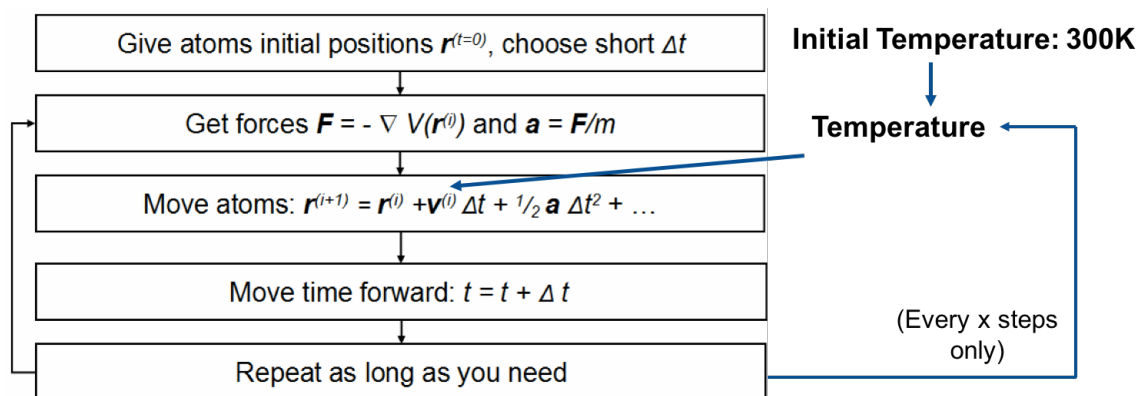


Figure 3.5.1: Schematic view of a molecular dynamics algorithm. The initial temperature and the number x are inputs to the code.

There are two main methods of ab initio molecular dynamics :

- In the Born-Oppenheimer method [6], the electronic structure is solved directly within the time-independent Schrödinger equation at each step,
- In the Car-Parinello method [32], the wave function parameters are propagated as classical degrees of freedom.

In this thesis work we use exclusively Car-Parinello molecular dynamics (CPMD).

REFERENCES

- [1] Douglas R Hartree. The wave mechanics of an atom with a non-coulomb central field. part i. theory and methods. In *Mathematical Proceedings of the Cambridge Philosophical Society*, volume 24, pages 89–110. Cambridge University Press, 1928.
- [2] Vladimir Fock. Näherungsmethode zur lösung des quantenmechanischen mehrkörperproblems. *Zeitschrift für Physik A Hadrons and Nuclei*, 61(1):126–148, 1930.
- [3] W. Kohn and L. J. Sham. Self-consistent equations including exchange and correlation effects. *Phys. Rev.*, 140:A1133–A1138, Nov 1965. doi: 10.1103/PhysRev.140.A1133. URL <https://link.aps.org/doi/10.1103/PhysRev.140.A1133>.
- [4] Feliciano Giustino. *Materials Modelling using Density Functional Theory*. Oxford University Press, 2014.
- [5] Pierre Hohenberg and Walter Kohn. Inhomogeneous electron gas. *Physical review*, 136(3B):B864, 1964.
- [6] Max Born and Robert Oppenheimer. Zur quantentheorie der molekeln. *Annalen der Physik*, 389(20):457–484, 1927.
- [7] H Hellmann. Zur rolle der kinetischen elektronenenergie für die zwischenatomaren kräfte. *Zeitschrift für Physik A Hadrons and Nuclei*, 85(3):180–190, 1933.
- [8] Richard Phillips Feynman. Forces in molecules. *Physical Review*, 56(4):340, 1939.
- [9] Xavier Gonze. Perturbation expansion of variational principles at arbitrary order. *Physical Review A*, 52(2):1086, 1995.
- [10] Richard M Martin. *Electronic structure: basic theory and practical methods*. Cambridge university press, 2004.
- [11] John P Perdew, Kieron Burke, and Matthias Ernzerhof. Generalized gradient approximation made simple. *Physical review letters*, 77(18):3865, 1996.

REFERENCES

- [12] David M Ceperley and BJ Alder. Ground state of the electron gas by a stochastic method. *Physical Review Letters*, 45(7):566, 1980.
- [13] John P Perdew and Alex Zunger. Self-interaction correction to density-functional approximations for many-electron systems. *Physical Review B*, 23(10):5048, 1981.
- [14] Charles Kittel. *Introduction to Solid State Physics*. Wiley, New York, 1976.
- [15] Fabien Tran and Peter Blaha. Accurate band gaps of semiconductors and insulators with a semilocal exchange-correlation potential. *Physical review letters*, 102(22):226401, 2009.
- [16] Jochen Heyd, Gustavo E. Scuseria, and Matthias Ernzerhof. Hybrid functionals based on a screened coulomb potential. *The Journal of Chemical Physics*, 118(18):8207–8215, 2003. doi: 10.1063/1.1564060. URL <https://doi.org/10.1063/1.1564060>.
- [17] Marvin L Cohen. Application of the pseudopotential model to solids. *Annual Review of Materials Science*, 14(1):119–144, 1984.
- [18] Paolo Giannozzi, Stefano Baroni, Nicola Bonini, Matteo Calandra, Roberto Car, Carlo Cavazzoni, Davide Ceresoli, Guido L Chiarotti, Matteo Cococcioni, Ismaila Dabo, et al. Quantum espresso: a modular and open-source software project for quantum simulations of materials. *Journal of physics: Condensed matter*, 21(39):395502, 2009.
- [19] Georg Kresse and Jürgen Furthmüller. Efficiency of ab-initio total energy calculations for metals and semiconductors using a plane-wave basis set. *Computational materials science*, 6(1):15–50, 1996.
- [20] G. Dresselhaus. Spin-orbit coupling effects in zinc blende structures. *Phys. Rev.*, 100:580–586, Oct 1955. doi: 10.1103/PhysRev.100.580. URL <https://link.aps.org/doi/10.1103/PhysRev.100.580>.
- [21] EI Rashba. Symmetry of energy bands in crystals of wurtzite type. 1. symmetry of bands disregarding spin-orbit interaction. *Soviet Physics-Solid State*, 1(3):368–380, 1959.
- [22] Yu A Bychkov. Ya bychkov and ei rashba, jetp lett. 39, 78 (1984). *JETP Lett.*, 39:78, 1984.

- [23] Xiuwen Zhang, Qihang Liu, Jun-Wei Luo, Arthur J Freeman, and Alex Zunger. Hidden spin polarization in inversion-symmetric bulk crystals. *Nature Physics*, 10(5):387, 2014.
- [24] Igor Žutić, Jaroslav Fabian, and S Das Sarma. Spintronics: Fundamentals and applications. *Reviews of modern physics*, 76(2):323, 2004.
- [25] Jaroslav Fabian, Alex Matos-Abiague, Christian Ertler, Peter Stano, and Igor Zutic. Semiconductor spintronics. *arXiv preprint arXiv:0711.1461*, 2007.
- [26] C Motta. C. motta, f. el-mellouhi, s. kais, n. tabet, f. alharbi, and s. sanvito, nat. commun. 6, 7026 (2015). *Nat. Commun.*, 6:7026, 2015.
- [27] Stefano Baroni, Stefano de Gironcoli, Andrea Dal Corso, and Paolo Giannozzi. Phonons and related crystal properties from density-functional perturbation theory. *Rev. Mod. Phys.*, 73:515–562, Jul 2001. doi: 10.1103/RevModPhys.73.515. URL <http://link.aps.org/doi/10.1103/RevModPhys.73.515>.
- [28] P Umari, Alfredo Pasquarello, and Andrea Dal Corso. Raman scattering intensities in α -quartz: A first-principles investigation. *Physical Review B*, 63(9):094305, 2001.
- [29] Craig J. Fennie and Karin M. Rabe. Structural and dielectric properties of sr_2tio_4 from first principles. *Phys. Rev. B*, 68:184111, Nov 2003. doi: 10.1103/PhysRevB.68.184111. URL <https://link.aps.org/doi/10.1103/PhysRevB.68.184111>.
- [30] Max Born and Kun Huang. *Dynamical theory of crystal lattices*. Clarendon press, 1954.
- [31] Xinyuan Zhao and David Vanderbilt. Phonons and lattice dielectric properties of zirconia. *Physical Review B*, 65(7):075105, 2002.
- [32] Roberto Car and Michele Parrinello. Unified approach for molecular dynamics and density-functional theory. *Physical review letters*, 55(22):2471, 1985.

Everything in life is vibration.

Albert Einstein

4

Cesium Perovskites: Anharmonicity and Instabilities

IN THIS CHAPTER, we use various ab-initio techniques, the majority of which are based on DFT, to investigate the vibrational properties of halide perovskites. Here, even though we sometimes compare the results to the case of the hybrid $MAPbI_3$ perovskite material, we focus our study mainly on the case of $CsPbI_3$. This study is of crucial importance as we have seen in the previous chapter that according to recent findings, the purely inorganic $CsPbI_3$ perovskite could compete with its hybrid cousins to be the absorber material for stable and highly efficient perovskite solar cells.

Contents

4.1	Vibrational properties of halide perovskites	74
4.2	[Publication 1] Structural instabilities related to highly anharmonic phonons	77
4.2.1	Article and supplemental information	77
4.2.2	Short ferroelasticity study	93
4.3	[Publication 2] Anharmonicity and disorder in the black phases of cesium lead iodide	96
4.4	Rashba effect and molecular dynamics study	115
4.4.1	Methods	116
4.4.2	Spatial domains	119
4.4.3	Time dynamics: CPMD	121
4.4.4	Dynamical Rashba effect	131
	References	133

4.1 VIBRATIONAL PROPERTIES OF HALIDE PEROVSKITES

Before getting to the heart of the matter, I intend to give the reader a general idea of the phase landscape of $CsPbI_3$. More details and bibliography can be found in the body of publications 1 and 2 in sections 4.2 and 4.3.

Since it has not been fully elucidated yet, the best way to approach the phase landscape in this material is to look at it through the study of its tin cousin, $CsSnI_3$.

In general, for $CsMI_3$ ($M=Pb, Sn$), four phases are expected [1, 2]: cubic (α), tetragonal (β), and two orthorhombic phases (a black γ - and a non-perovskite yellow δ -phase), thus including transitions between perovskite phases and non-perovskite polytypes (perovskitoids) [3] at low-temperature (see figure 4.1.1). All the phases of $CsSnI_3$ have been thoroughly characterized [2, 4] as well as the room temperature δ -phase of $CsPbI_3$ [1, 4, 5].

This means that the stable phase of $CsPbI_3$ at room temperature is a non-perovskite yellow phase (the δ -phase) which should be avoided for photovoltaics applications. The closest (in temperature) black

phase that should be aimed at for PV is thus the orthorhombic γ -phase. At this point, it is also worth noting that before our recent article published in ACS Nano [6], the existence of a tetragonal phase for $CsPbI_3$ had only been suggested but never experimentally evidenced.

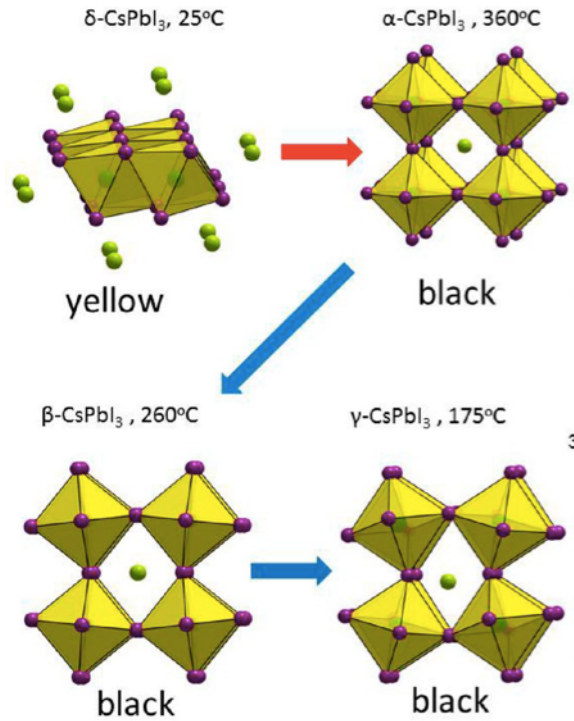


Figure 4.1.1: Given the similarities with its tin cousin $CsSnI_3$, four phases are expected for $CsPbI_3$. The red arrow represent the phase transformation upon heating from the room temperature δ -phase while the blue ones represent the phases encountered while cooling. Figure taken from Ref [7]

This chapter will be structured as follows.

In **section 4.2**, which corresponds to the first publication during my PhD [8], we use the linear response approach of DFT, density functional perturbation theory (DFPT) to investigate the energy landscape of both the cubic α -phase and the orthorhombic δ -phase of $CsPbI_3$. We use the frozen phonon methods to further study the structural instabilities found in the phonon spectrum. In this section I also include additional more recent calculations hypothesizing the possible ferroelastic behaviour of some of the phases of $CsPbI_3$.

In **section 4.3**, corresponding to the second publication of my PhD [6], we use high resolution in-situ synchrotron X-ray diffraction (XRD) measurements to reveal for the first time the existence of a tetragonal phase for CsPbI_3 and study in detail the structural phase transitions between its 4 phases. In this article, we then apply similar ab-initio methods to the ones used in section 4.2 to the tetragonal β -phase and the black orthorhombic γ -phase which is crucial for photovoltaics applications. Using total energy and vibrational entropy calculations, we highlight the strong competition between all the low-temperature phases of CsPbI_3 (γ, δ, β). We also study in detail the electronic properties of the 4 phases using a symmetry-based tight-binding model, further validated by self-consistent GW calculations including spin-orbit coupling.

In **section 4.4**, we post-process and analyze in detail Car-Parinello molecular dynamics (CPMD) data in the light of our finding on the anharmonic potential energy surface of the cubic phase of CsPbI_3 . We also perform electronic band calculations, including spin-orbit coupling, in order to investigate the space and time dynamics of the Rashba effect found in these materials. Here, we show only preliminary results of this ongoing study.

4.2 [PUBLICATION 1] STRUCTURAL INSTABILITIES RELATED TO HIGHLY ANHARMONIC PHONONS

4.2.1 ARTICLE AND SUPPLEMENTAL INFORMATION

This paper, based on ab-initio calculations only, focuses primarily on the two phases of $CsPbI_3$ that were first historically evidenced and characterized: the α -cubic phase and the non-perovskite yellow δ -phase. I performed myself all the calculations present in this work and wrote the entire article. Some supplemental calculations (see Supporting Information) were computed by G. Roma.

It is worth noting that we were originally interested in the vibrational properties of $MAPbI_3$ and $CsPbI_3$ in order to derive, from ab-initio calculations, the static and high dielectric constants in these materials. As a matter of fact, as of 2015 the PSC community had for some time had trouble agreeing on hybrid $MAPbI_3$'s exciton binding energy, and on whether it behaves more like organic compounds (high exciton binding energy, low dielectric constant) or vice-versa like inorganic compounds. Looking in detail at the dielectric constant ϵ is thus one way to answer this question. As explained in the DFT methods chapter (section 3.4), while the high-frequency value of ϵ can be calculated using the second derivative of the energy provided by DFPT, the calculation of the low-frequency (static) limit of ϵ requires to take into account the dipolar contributions which can be computed by phonon calculations.

The phonon calculations presented in this chapter will be used and compared to ellipsometry measurements in section 5.3 in order to answer this controversy.

Structural Instabilities Related to Highly Anharmonic Phonons in Halide Perovskites

Arthur Marronnier,^{*,†,‡} Heejae Lee,[†] Bernard Geffroy,^{†,§,‡} Jacky Even,^{‡,‡} Yvan Bonnassieux,[†] and Guido Roma^{*,¶}

[†]LPICM, CNRS, Ecole Polytechnique, Université Paris-Saclay, 91128 Palaiseau, France

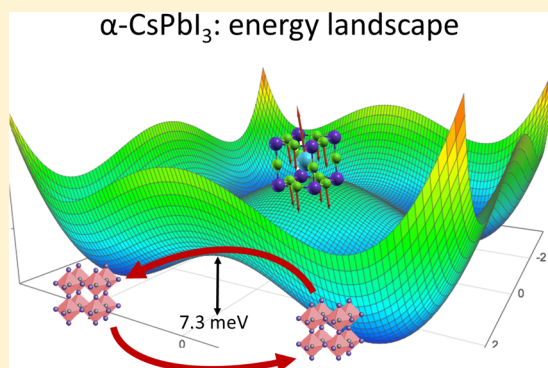
[‡]Université Européenne de Bretagne, INSA, FOTON, UMR 6082, 35708 Rennes, France

[¶]DEN - Service de Recherches de Métallurgie Physique, CEA, Université Paris-Saclay, 91191 Gif sur Yvette, France

[§]LICSEN, NIMBE, CEA, CNRS, Université Paris-Saclay, 91191 Gif sur Yvette, France

Supporting Information

ABSTRACT: Hybrid perovskites have emerged over the past five years as absorber layers for novel high-efficiency low-cost solar cells combining the advantages of organic and inorganic semiconductors. Unfortunately, electrical transport in these materials is still poorly understood. Employing the linear response approach of density functional theory, we reveal strong anharmonic effects and a double-well phonon instability at the center of the Brillouin zone for both cubic and orthorhombic phases of inorganic CsPbI₃. Previously reported soft phonon modes are stabilized at the actual lower-symmetry equilibrium structure, which occurs in a very flat energy landscape, highlighting the strong competition between the different phases of CsPbI₃. Factoring these low-energy phonons into electron–phonon interactions and band gap calculations could help better understand the electrical transport properties in these materials. Furthermore, the perovskite oscillations through the corresponding energy barrier could explain the underlying ferroelectricity and the dynamical Rashba effect predicted in halide perovskites for photovoltaics.



Hybrid perovskite solar cells (PSCs), a new generation of solar cells that combine the advantages of organic and inorganic semiconductors, were born only a few years ago after perovskites were used as absorbing materials in dye-sensitized solar cells (DSCs).¹ After a mere 6 years of research, the efficiency of PSCs has jumped from 4% in 2009 to certified efficiencies over 20%² in 2015 and a record efficiency of 22.1%³ in 2016, becoming the first truly low-cost and highly efficient generation of solar cells.

Researchers started phonon calculations of hybrid MAPbI₃ perovskites as early as 2013, when Quarti et al.⁴ measured its Raman spectrum, assisted by density functional theory (DFT) calculations, which showed the importance of the torsional mode of the methylammonium cations as a marker of the orientational disorder of the material. As shown by various groups since then,^{5–7} this picture is further complicated by the reorientational dynamics of the organic component similar to what is usually observed in plastic crystals, since quasielastic neutron scattering measurements showed that dipolar CH₃NH₃⁺ ions reorientate between the faces quite rapidly. Very recently, Whalley et al.⁸ and Beecher et al.⁹ found double-well instabilities present at the Brillouin Zone (BZ) boundary of MAPbI₃, much like what we report here in the CsPbI₃ case, as well as short phonon quasiparticle lifetimes and mean free

paths. However, contrary to our findings for CsPbI₃, they did not find any instabilities at the center of the BZ for MAPbI₃. These structural effects in organohalide perovskites were studied in detail by Amat et al.¹⁰ who showed that the interplay of spin–orbit coupling (SOC) and octahedra tilting can have a strong impact on their electronic and optical properties, including the band gap.

It is only in the past two years that inorganic (mostly cesium-based) perovskites for photovoltaics have attracted more and more attention from the PSC community after being incorporated into complex but more stable mixed-halide mixed-cation perovskite structures (such as [HC(NH₂)₂]_{0.83}Cs_{0.17}Pb(I_{0.6}Br_{0.4})₃) demonstrating the feasibility of achieving above 25% efficiency four-terminal tandem cells¹¹ at the beginning of 2016.

In particular, the vibrational properties of inorganic and lead-free perovskite CsSnI₃ have been studied in detail using ab initio calculations. Lora da Silva et al. employed¹² the quasiharmonic approximation to study the temperature-dependent lattice dynamics of the four different phases of

Received: April 4, 2017

Accepted: May 29, 2017

cesium tin iodide. Patrick et al. reported¹³ strong anharmonic effects in CsSnI₃ (including soft phonon modes) using self-consistent phonon theory and frozen phonons, and showed that these soft modes were stabilized at experimental conditions through anharmonic phonon–phonon interactions between the Cs ions and their iodine cages. They further calculated the renormalization of the band gap due to vibrations. These two works demonstrate the important role of temperature in accurately analyzing anharmonic perovskite materials like CsSnI₃.

The role of phonons in the phase transitions of perovskites containing lead and cesium was recognized long ago (e.g., CsPbCl₃¹⁴). This suggests that vibrational properties could control the structural transitions also for CsPbI₃, which is crucially important for most recent PSCs.

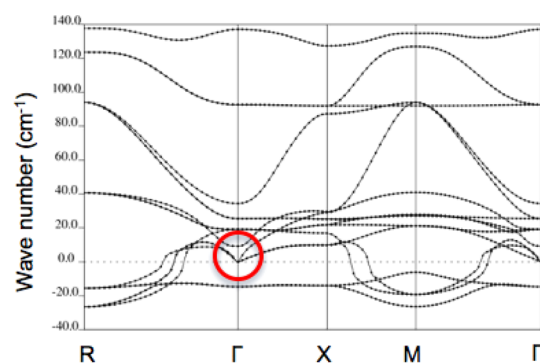
The vibrational properties of inorganic CsPbI₃ perovskites have not been extensively studied so far. Stoumpos et al. studied the dependence of CsPbI₃'s band gap on temperature and the reversibility of its phase changes from nonperovskite structures to perovskite structures at high temperature. They showed¹⁵ that the room temperature stable δ -phase (yellow) converts to the black perovskite α -phase upon heating above 360 °C. On cooling, the perovskite structure converts to the black perovskite β - and γ -phases at 260 and 175 °C, respectively. After a few days, a full recovery of the initial δ -phase is observed. A prediction of possible structural instabilities in CsPbI₃ and RbPbI₃ perovskite was made, on the basis of relatively high values of the Born effective charges, by Brgoch and co-workers;¹⁶ but to the best of our knowledge it has remained a speculation until we present our results here.

In this paper, we study the vibrational properties of both the high-temperature cubic α -phase and the orthorhombic δ -phase of CsPbI₃, and compare them to the phonons of MAPbI₃'s cubic phase. For both phases, phonon spectra, derived using the linear response approach of density functional theory (density functional perturbation theory or DFPT), showed the existence of instabilities which we investigated in detail using total energy calculations along the corresponding phonon eigenvectors (frozen phonons framework). More information about the DFT and DFPT calculations can be found in the [Computational Methods](#) section at the end of the paper. Additional calculations on the influence of spin–orbit coupling on these results are also detailed in the [Supporting Information](#) file.

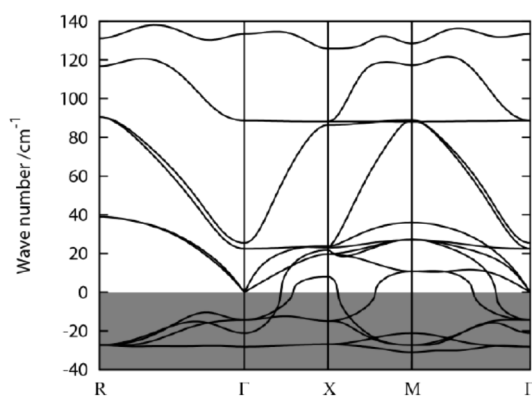
The phonon dispersion relations of inorganic perovskite CsPbI₃ in the cubic high temperature α -phase, with commonly accepted space group $Pm\bar{3}m$,¹⁷ are reported in [Figure 1a](#). The presence of soft modes at different high-symmetry points in the Brillouin zone can be explained by the fact that the α -phase is stable only at high temperature, where both energetic and entropic contributions determine the free energy F , and not at the (zero) temperature of DFT calculations. In principle, these modes are stabilized by taking into account temperature, i.e., the vibrational entropy and its contribution to the free energy.

What is more surprising is the presence of imaginary modes at the Γ -point (one triply degenerated mode at -15 cm^{-1}), where one expects to find acoustic modes, linearly going to zero at Γ , as the lowest frequency modes. These instabilities and in particular this anomaly at Γ for the cubic phase of CsPbI₃ have already been reported by Kawai et al.¹⁸ (see [Figure 1b](#)), but they were offered no explanation or further analysis.

As circled in red on [Figure 1a](#), the acoustic sum rule (ASR) was imposed in our calculations through postprocessing of the dynamical matrix to ensure translational invariance. The ASR



(a) This work (very tight convergence threshold)



(b) Results from Kawai *et al.*, reprinted with permission from¹⁸ (copyright 2015 American Chemical Society)

Figure 1. Phonon modes of cubic CsPbI₃.

did bring back to zero the 3-fold degenerated acoustic branches at the Γ -point but did not affect the soft mode, confirming its nature as an optical mode. We analyzed the dynamical matrix's eigenvector corresponding to this soft mode, and its antisymmetrical characteristics (see [Figure 2](#)) are consistent with the irreducible representations of the $Pm\bar{3}m$ symmetry group as reported by Even et al.⁷

The soft modes obtained here are coherent with previous neutron scattering measurements, clearly indicating that the energy of the whole acoustic phonon density of states is remarkably low at 80 °C.⁷ In particular, it was shown for CsPbCl₃ that the transverse acoustic (TA) branches always stay

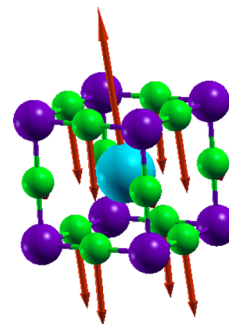


Figure 2. Displacement eigenvector corresponding to the soft phonon mode found at Γ for cubic CsPbI₃. Its irreducible representation is the infrared-active Γ_4^- representation. The blue, purple, and green atoms respectively denote Cs, Pb, and I.

under 2 meV (16 cm^{-1})¹⁴ and that the optical phonons close to the R and M points also lie in the same energy range ($<2 \text{ meV}$). Here, our calculations show instabilities of the same order of magnitude (around 20 cm^{-1}) coming from optical modes close to the M point (see Figure 1a). Similar conclusions were drawn more recently for $\text{CH}_3\text{NH}_3\text{PbI}_3$ ⁹ and $\text{CH}_3\text{NH}_3\text{PbBr}_3$.¹⁹

We think that these instabilities indicate strong anharmonic effects (also confirmed by the unusually large Debye–Waller factors measured previously for MAPbX_3 compounds^{7,20}) and a very flat energy profile around equilibrium in CsPbI_3 . This very flat profile could affect the reported low-to-negative frequency values in two ways: (i) by affecting the evaluation of the frequency values itself (due to numerical noise), and (ii) by preventing the structural relaxation algorithm to find the ground state structure. In order to assess these two hypotheses, we first (i) used smaller and smaller convergence thresholds and second (ii) performed frozen phonon calculations to investigate anharmonicity up to the fourth order.

The use of very tight thresholds for total energy convergence, forces during relaxations, and self-consistency of the linear response calculations (see Computational Methods section) reduced the number of imaginary phonons at Γ , but one triply degenerated soft mode remained (see Figure 1a), compared to five as published by Kawai et al.¹⁸ (Figure 1b).

Unfortunately the most widely used approach to go further than the harmonic approximation and to calculate the free energy F by adding a volume (thus temperature) dependent vibrational free energy, the quasi-harmonic approximation,²¹ cannot be straightforwardly applied¹² due to the presence of these unstable phonon modes. Another technique is to guess the unstable directions using phonon eigenvectors obtained with the linear response approach of DFT. Here, we computed frozen phonon-perturbed total energies for the soft optical mode at Γ . A displacement of the form

$$\mathbf{u}_\kappa(\eta) = \eta \cdot \mathbf{x}_{\kappa\Gamma}(\mathbf{q}_\Gamma) \quad (1)$$

was imposed on each ion κ , starting from the relaxed positions, and for various values of the unitless displacement parameter η , where \mathbf{x} is the chosen soft mode eigenvector obtained from harmonic DFPT phonon calculations.

Using Laudau theory²² and the adiabatic approximation, which assumes the electronic system instantaneously changes after new ionic positions are reached, the anharmonic energy^{14,23} as a function of displacement is given by

$$U(\eta) = U_0 + \frac{\eta^2}{4} \hbar \omega_{\nu\Gamma}(\mathbf{q}_\Gamma) + \frac{\eta^4}{24} \Phi_{4,\nu\Gamma} + O(\eta^6) \quad (2)$$

The results, shown in Figure 3, fit well with this fourth-order model, confirming anharmonic effects in cubic CsPbI_3 and the hypothesis (ii) that we were not at the equilibrium structure. Given the very small height of the barrier (7.3 meV), we can assume that the perovskite structure actually oscillates between both equilibrium positions. To get an idea of the order of magnitude of these oscillations, one can write

$$\tau = \tau_0 e^{E/k_B T} \quad (3)$$

where k_B is the Boltzmann constant and E the energy barrier. Even if we consider, for τ_0 , the period of the lowest frequency optical phonon ($\omega \approx 17 \text{ cm}^{-1}$), this gives an oscillation time scale at room temperature of around $0.7 \times 10^{-12} \text{ s}$. These frozen phonon calculations are performed following the soft phonon mode and thus the new minimum here is not relaxed in

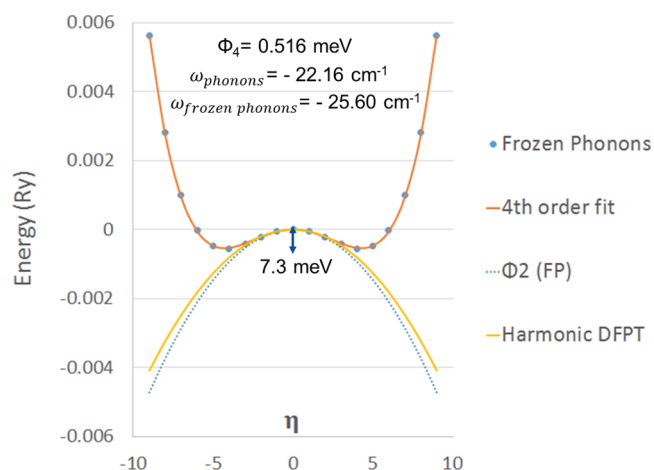


Figure 3. Potential energy surface from frozen phonon calculations of cubic CsPbI_3 along the eigenvector of the unstable optical phonon at Γ as a function of displacement parameter η . The 3N-dimensional displacement needed to reach the new minimum corresponds to around 0.43 Å. $\omega_{\text{frozen phonons}}$ and Φ_4 are obtained by fitting eq 2. As expected, the results show good agreement between frozen phonon and DFPT estimations of the second order coefficient (ω).

volume. After volume relaxation, the energy barrier reads 8.4 meV.

The soft mode (infrared-active Γ_4^- representation, Figure 2) that corresponds to the high-symmetry high-energy structure is a polar soft mode induced by the displacement of positively charged cesium ions in one direction, and the displacement of negatively charged iodine ions in the opposite direction. The oscillations of the perovskite along this polar soft mode and between the two low-symmetry equilibrium structures could explain why ferroelectricity has not been observed at a macroscopic scale in these perovskites, considering that a ferroelectric behavior is more likely induced at the scale of these fast fluctuations. Similarly, it was shown recently that for hybrid methylammonium-based perovskites, the coupled inorganic–organic degrees of freedom give rise to a spatially local and dynamical Rashba effect which fluctuates on the subpicosecond time scale typical of the methylammonium cation dynamics.²⁴ We think that the oscillations predicted here in the cubic and orthorhombic phases of CsPbI_3 could also be at the origin of a similar dynamical Rashba effect. Additional calculations on the dynamical Rashba effect induced by this symmetry breaking can be found in the Supporting Information file.

Performing new phonon calculations at the new (volume relaxed) equilibrium positions definitively removed the remaining soft mode (see Figure 4). In conclusion, both (i) using smaller convergence thresholds and (ii) finding the actual minimum using frozen phonon calculations allowed us to investigate and abolish the soft modes at Γ for the cubic phase of CsPbI_3 . Similar phonon dispersions are obtained when taking into account SOC, as shown in the Supporting Information file, although caution must be observed due to the reduced band gap.

This means that this strongly anharmonic mode at Γ will not condensate at lower temperatures; it does not correspond to the transition to the yellow phase. On the contrary, the remaining phonon instabilities at the M and R points at the edge of the Brillouin zone are related to soft modes which condensate at lower temperatures to yield the β tetragonal and γ orthorhombic black phases of CsPbI_3 .^{7,15}

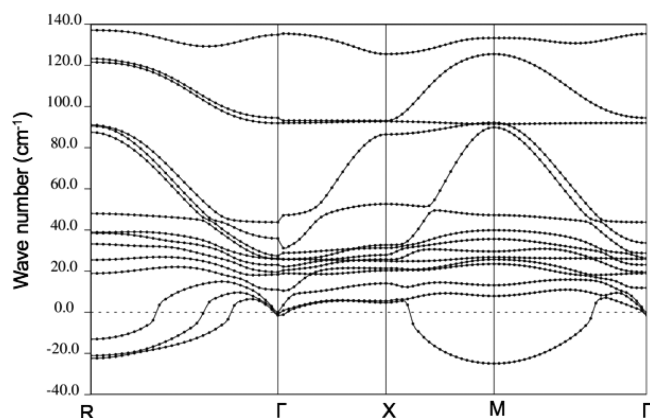


Figure 4. Phonon modes of cubic CsPbI₃ at the new equilibrium position determined in Figure 3 after volume relaxation. Using both tight convergence thresholds and the results of our frozen phonon calculations allowed us to remove the soft modes at Γ .

The orthorhombic, yellow, low-temperature, δ -phase of CsPbI₃ was studied experimentally quite a long time ago by Moeller²⁵ in 1959, who proposed a structure with the *Pnma* space group. A similar *Pnma* orthorhombic structure was obtained recently by Trots et al.¹⁷ in 2008 by powder diffraction studies. This structure is referred to as the yellow δ -phase and does not correspond to a simple distortion of the reference cubic perovskite lattice.²⁶ We relaxed the two structures and found a slightly lower energy for the second structure. As the difference in energy was very small, we interpolated a few configurations between them to check for a barrier, and, to our surprise, we found an even lower minimum (see Figure 5), with a relatively flat energy landscape. The conclusions are the same when taking into account spin-orbit coupling and lead semicore electrons.

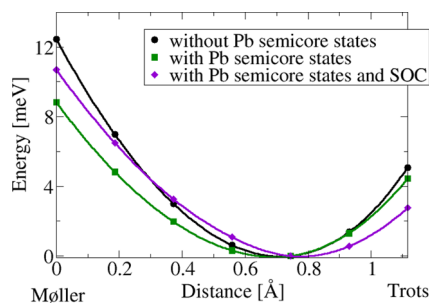


Figure 5. Equilibrium energy of CsPbI₃'s orthorhombic δ -phase ($T < 530$ K). The five intermediate position sets are linearly interpolated between sets 1 ("Moeller")²⁵ and 7 ("Trots"),¹⁷ which are equilibrium positions relaxed from experimental initial structures. The distance is given in $3N$ dimensions.

This is another signature of a possible anharmonic behavior in CsPbI₃. A further confirmation of this fact is that, even for the lowest energy structure of Figure 5, we again found a few soft modes at the Γ -point, as shown in Figure 6.

This phase being the stable phase at low temperature, we did not find any soft modes at other high symmetry points. Similar to our work with the cubic phase, we followed the eigenvectors of the soft modes in order to explore the energy landscape. As with the cubic phase, frozen phonon calculations around the lowest energy structure of Figure 5 were fitted up to the fourth order and showed (see Figure 7) a similar double-well

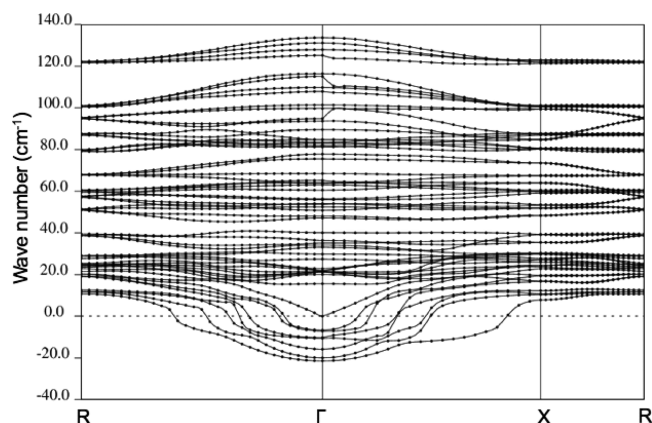


Figure 6. Phonon modes of orthorhombic δ -CsPbI₃ in the lowest energy structure of Figure 5.

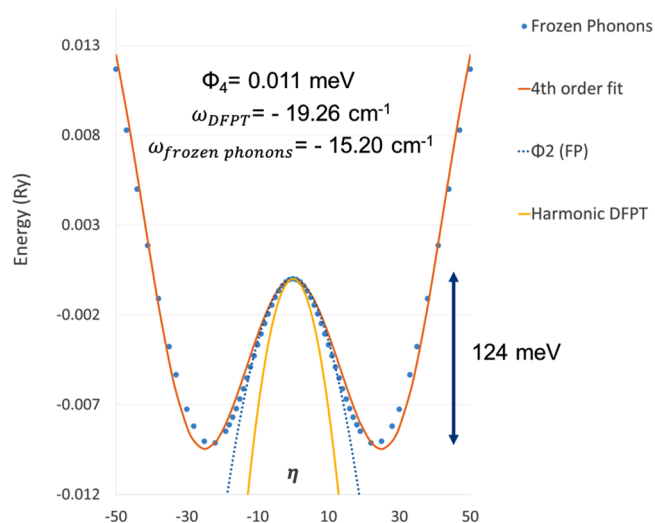


Figure 7. Potential energy surface from frozen phonon energy calculations of orthorhombic δ -CsPbI₃ along the eigenvector of the lowest soft phonon at Γ as a function of displacement parameter η . The $3N$ -dimensional displacement needed to reach the new minimum corresponds to around 2.2 Å. $\omega_{\text{frozen phonons}}$ and Φ_4 are obtained by fitting eq 2. The results show good agreement between frozen calculations and DFPT on the second order coefficient (ω).

instability with a higher potential barrier (124 meV, meaning an oscillation time of around 0.6×10^{-10} s at room temperature), and once more a good agreement between frozen calculations and DFPT on the second order coefficient. We recall that these frozen phonon calculations are performed following a soft phonon mode and thus that the new minimum here is not relaxed in volume. After volume relaxation, the energy barrier reads the much higher value of 2.39 eV. We think that this very significant difference could be the sign of a strong ferroelasticity in the δ -phase of CsPbI₃.

As in the cubic case, phonons were recalculated at the (volume-relaxed) new equilibrium positions, and all the soft modes at Γ were eliminated (see Figure 8). This stable structure has a lower symmetry than the *Pnma* space group and, as such, does not match with the black γ -phase described by Stoumpos,¹⁵ nor with the structure of the γ -phase of CsSnI₃.²⁷

We then compared the vibrational properties of the inorganic CsPbI₃ to those of MAPbI₃. The phonon spectrum of the pseudocubic phase of the hybrid perovskite MAPbI₃, obtained

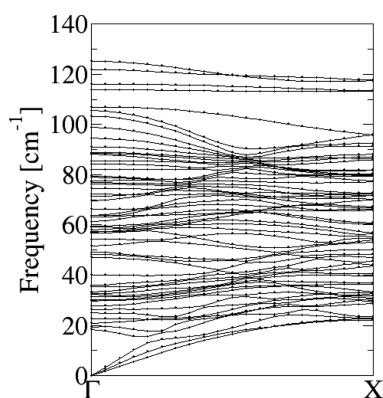


Figure 8. Phonon modes of orthorhombic δ -CsPbI₃ at the new equilibrium position determined in Figure 7 after volume relaxation. Using both tight convergence thresholds and the results of our frozen phonon calculations allowed us to remove the soft modes at Γ .

similarly using DFPT calculations, did not show any soft modes at Γ (Figure 9). This spectrum also differs significantly as it contains high-frequency optical modes around 3000 cm⁻¹, which are the signature of the MA⁺ organic molecule vibrations.

This could suggest that MAPbI₃ behaves noticeably more harmonically than CsPbI₃. However, as shown very recently,^{8,9} this is due to the fact that symmetry breaking is facilitated by the presence of the organic molecule, but a similar behavior, with a double well potential around the most symmetric structure, is also present in MAPbI₃. This double-well instability was found at the edge of the BZ (M and R points) and not at the Γ point. The barrier was reported to be somewhat higher, between 0.02 and 0.04 eV. Furthermore, we think that our simulation here is not able to capture the dynamical translation-rotation coupling (recently experimentally observed¹⁹), which may yield further contribution to the anharmonicity of the phonon modes in MAPbI₃.

To summarize, through energy landscape and phonon calculations for the inorganic perovskite CsPbI₃ we reveal that the assumed equilibrium structure of the high-temperature α -phase, of space group $Pm\bar{3}m$, results from a dynamical average between lower symmetry configurations in a very flat energy landscape.

For the orthorhombic low-temperature phase, similarly, we find a rather flat energy landscape between the two experimentally proposed variants of the yellow δ -phase, a

lower symmetry equilibrium configuration and double-well potentials with energy barriers on the order of a tenth of an electronvolt around it.

As for the hybrid MAPbI₃ perovskite, translation–rotation coupling of the organic molecule needs to be considered in order to fully investigate its anharmonicity.

These findings highlight the strong competition between the yellow δ -phase and the black $\alpha/\beta/\gamma$ -phases, and suggest that the cation network suffers from dynamical disorder even at relatively low temperature. The unrealized ferroelectricity in these perovskites could be replaced by the polar structural fluctuations we report here, also leading to a dynamical Rashba effect as previously proposed for similar perovskite structures.^{24,28,29} Since SOC almost closes the electronic band gap for the α -phase, the calculation of phonon frequencies close to the metallic transition might well be affected by numerical instabilities (see Supporting Information). The effect of spin orbit coupling on the vibrational properties of halide perovskites, both organic and inorganic, will certainly be of high interest in future studies.

Further work is needed to take into account these low-energy highly occupied phonon states in order to give new theoretical estimates of electronic and optical properties (e.g., the band gap or the exciton binding energy³⁰). It could also help improve electron–phonon coupling calculations, as it was shown that this coupling can deeply impact the charge-carrier mobilities^{31,32} in these perovskites. Mixing Cs with other cations, like the organic ones used in most recent versions of hybrid PSCs, affects the coupling in the double-well network, which could help explain the mechanisms through which mixed-cation PSCs have shown interesting improvements in efficiency and stability with respect to MAPbI₃-based perovskite solar cells.

Further work is needed to take into account these low-energy highly occupied phonon states in order to give new theoretical estimates of electronic and optical properties (e.g., the band gap or the exciton binding energy³⁰). It could also help improve electron–phonon coupling calculations, as it was shown that this coupling can deeply impact the charge-carrier mobilities^{31,32} in these perovskites. Mixing Cs with other cations, like the organic ones used in most recent versions of hybrid PSCs, affects the coupling in the double-well network, which could help explain the mechanisms through which mixed-cation PSCs have shown interesting improvements in efficiency and stability with respect to MAPbI₃-based perovskite solar cells.

COMPUTATIONAL METHODS

Electronic-structure calculations were performed within the DFT^{33,34} framework, as implemented in the Quantum Espresso code.³⁵

All total energy and force calculations in this work were performed with the local density approximation (LDA), expanding the wave functions in a plane-wave basis set. Unless otherwise specified, nonrelativistic (scalar-relativistic for Pb) and norm-conserving pseudopotentials were used, with the Cs [*5s²5p⁶6s¹*], I [*5s²5p⁵*], and Pb [*5d¹⁰6s²6p²*] electrons treated as valence states. We also performed additional calculations with

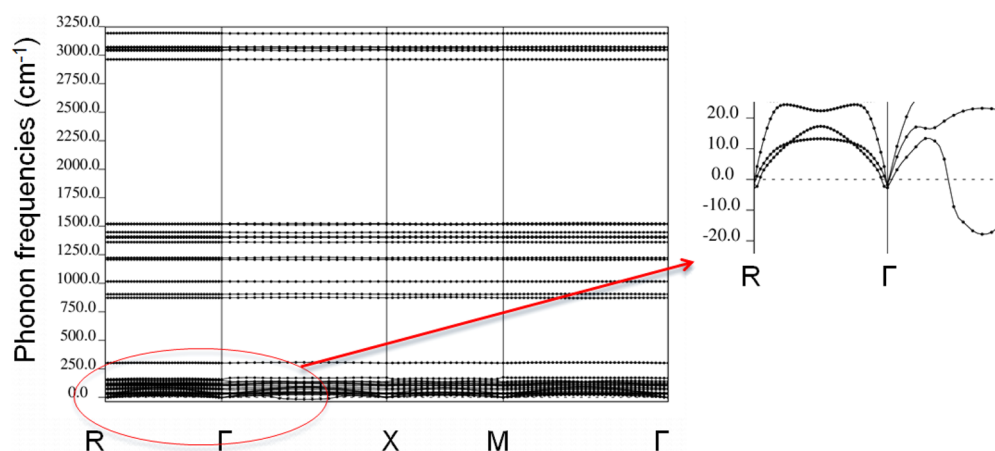


Figure 9. Phonon frequencies of pseudocubic MAPbI₃.

fully relativistic US pseudopotentials (for Pb) and PAW (Cs and I) data sets (with the same number of valence electrons as in the scalar or nonrelativistic case) in order to check the influence of spin-orbit coupling (see results in the [Supporting Information](#) file). These relativistic pseudopotentials were generated using the PS Library 0.2.2.³⁶

Plane-wave cutoffs of 70 Ry (CsPbI₃) and 80 Ry (MAPbI₃) were used. The Brillouin zone (BZ) was sampled with Γ -centered Monkhorst-Pack meshes³⁷ with subdivisions of α -CsPbI₃: $8 \times 8 \times 8$; δ -CsPbI₃: $10 \times 5 \times 3$, and MAPbI₃: $8 \times 8 \times 8$.

Phonon calculations were performed using the linear response approach of DFT, as known as DFPT,²¹ as implemented in the Quantum Espresso code.³⁵ High-frequency dielectric tensors and Born effective charges were calculated with the linear response and used to calculate long-range contributions to the dynamical matrices at Γ . All phonon dispersions were performed using at least 5 q-points/Å⁻¹ in each Cartesian direction.

In order to eliminate some of the soft phonon modes, very tight convergence thresholds of 10^{-4} Ry/bohr for the force calculations and 10^{-14} for the phonon self-consistent algorithm were used.

■ ASSOCIATED CONTENT

Supporting Information

The Supporting Information is available free of charge on the ACS Publications website at DOI: [10.1021/acs.jpcllett.7b00807](https://doi.org/10.1021/acs.jpcllett.7b00807).

Checks made in order to show that some of the approximations used in this paper do not affect its conclusions; in particular, most of the results presented in the paper have been obtained by neglecting spin-orbit coupling (PDF)

■ AUTHOR INFORMATION

Corresponding Author

*E-mail: arthur.marronnier@polytechnique.edu.

ORCID

Arthur Marronnier: 0000-0003-0984-1140

Bernard Geffroy: 0000-0001-8654-6140

Jacky Even: 0000-0002-4607-3390

Notes

The authors declare no competing financial interest.

■ ACKNOWLEDGMENTS

A.M.'s Ph.D. project is funded by the French Department of Energy (MEEM) and by the Graduate School of École des Ponts ParisTech. This work was granted access to the HPC resources of TGCC and CINES under the allocation 2016090642 made by GENCI. J.E.'s work has been performed within the GOTSOLAR FETOPEN project, which has received funding from the European Union's Horizon 2020 research and innovation program under grant agreement No 687008. The information and views set out in this work are those of the authors and do not necessarily reflect the official opinion of the European Union. Neither the European Union institutions and bodies nor any person acting on their behalf may be held responsible for the use which may be made of the information contained herein. The authors would also like to thank A. Garcia Barker for her editing and proofreading contributions.

■ REFERENCES

- (1) Kojima, A.; Teshima, K.; Shirai, Y.; Miyasaka, T. Organometal Halide Perovskites as Visible-Light Sensitizers for Photovoltaic Cells. *J. Am. Chem. Soc.* **2009**, *131*, 6050–6051.
- (2) Yang, W. S.; Noh, J. H.; Jeon, N. J.; Kim, Y. C.; Ryu, S.; Seo, J.; Seok, S. I. High-performance Photovoltaic Perovskite Layers Fabricated through Intramolecular Exchange. *Science* **2015**, *348*, 1234–1237.
- (3) Best research-cell efficiencies. <https://www.nrel.gov/pv/assets/images/efficiency-chart.png> (Accessed March 17, 2017).
- (4) Quarti, C.; Grancini, G.; Mosconi, E.; Bruno, P.; Ball, J. M.; Lee, M. M.; Snaith, H. J.; Petrozza, A.; Angelis, F. D. The Raman Spectrum of the CH₃NH₃PbI₃ Hybrid Perovskite: Interplay of Theory and Experiment. *J. Phys. Chem. Lett.* **2014**, *5*, 279–284.
- (5) Leguy, A. M. A.; Frost, J. M.; McMahon, A. P.; Sakai, V. G.; Kockelmann, W.; Law, C.; Li, X.; Foglia, F.; Walsh, A.; O'Regan, B. C. The Dynamics of Methylammonium Ions in Hybrid Organic-Inorganic Perovskite Solar Cells. *Nat. Commun.* **2015**, *6*, 7124.
- (6) Chen, T.; Foley, B. J.; Ipek, B.; Tyagi, M.; Copley, J. R. D.; Brown, C. M.; Choi, J. J.; Lee, S.-H. Rotational Dynamics of Organic Cations in the CH₃NH₃PbI₃ Perovskite. *Phys. Chem. Chem. Phys.* **2015**, *17*, 31278–31286.
- (7) Even, J.; Carignano, M.; Katan, C. Molecular Disorder and Translation/Rotation Coupling in the Plastic Crystal Phase of Hybrid Perovskites. *Nanoscale* **2016**, *8*, 6222–6236.
- (8) Whalley, L. D.; Skelton, J. M.; Frost, J. M.; Walsh, A. Phonon Anharmonicity, Lifetimes, and Thermal Transport in CH₃NH₃PbI₃ from Many-body Perturbation Theory. *Phys. Rev. B: Condens. Matter Mater. Phys.* **2016**, *94*, 220301.
- (9) Beecher, A. N.; Semonin, O. E.; Skelton, J. M.; Frost, J. M.; Terban, M. W.; Zhai, H.; Alatas, A.; Owen, J. S.; Walsh, A.; Billinge, S. J. L. Direct Observation of Dynamic Symmetry Breaking above Room Temperature in Methylammonium Lead Iodide Perovskite. *ACS Energy Lett.* **2016**, *1*, 880–887.
- (10) Amat, A.; Mosconi, E.; Ronca, E.; Quarti, C.; Umari, P.; Nazeeruddin, M. K.; Grätzel, M.; De Angelis, F. Cation-Induced Band-Gap Tuning in Organohalide Perovskites: Interplay of Spin-Orbit Coupling and Octahedra Tilting. *Nano Lett.* **2014**, *14*, 3608–3616.
- (11) McMeekin, D. P.; Sadoughi, G.; Rehman, W.; Eperon, G. E.; Saliba, M.; Hörantner, M. T.; Haghighirad, A.; Sakai, N.; Korte, L.; Rech, B.; et al. A Mixed-cation Lead Mixed-halide Perovskite Absorber for Tandem Solar Cells. *Science* **2016**, *351*, 151–155.
- (12) da Silva, E. L.; Skelton, J. M.; Parker, S. C.; Walsh, A. Phase Stability and Transformations in the Halide Perovskite CsSnI₃. *Phys. Rev. B: Condens. Matter Mater. Phys.* **2015**, *91*, 144107.
- (13) Patrick, C. E.; Jacobsen, K. W.; Thygesen, K. S. Anharmonic Stabilization and Band Gap Renormalization in the Perovskite CsSnI₃. *Phys. Rev. B: Condens. Matter Mater. Phys.* **2015**, *92*, 201205.
- (14) Fujii, Y.; Hoshino, S.; Yamada, Y.; Shirane, G. Neutron-scattering Study on Phase Transitions of CsPbCl₃. *Phys. Rev. B* **1974**, *9*, 4549–4559.
- (15) Stoumpos, C. C.; Kanatzidis, M. G. The Renaissance of Halide Perovskites and Their Evolution as Emerging Semiconductors. *Acc. Chem. Res.* **2015**, *48*, 2791–2802.
- (16) Brgoch, J.; Lehner, A. J.; Chabiny, M.; Seshadri, R. Ab Initio Calculations of Band Gaps and Absolute Band Positions of Polymorphs of RbPbI₃ and CsPbI₃: Implications for Main-Group Halide Perovskite Photovoltaics. *J. Phys. Chem. C* **2014**, *118*, 27721–27727.
- (17) Trots, D.; Myagkota, S. High-temperature Structural Evolution of Caesium and Rubidium Triiodoplumbates. *J. Phys. Chem. Solids* **2008**, *69*, 2520–2526.
- (18) Kawai, H.; Giorgi, G.; Marini, A.; Yamashita, K. The Mechanism of Slow Hot-Hole Cooling in Lead-Iodide Perovskite: First-Principles Calculation on Carrier Lifetime from Electron-Phonon Interaction. *Nano Lett.* **2015**, *15*, 3103–3108.
- (19) Létoublon, A.; Paofai, S.; Rufflé, B.; Bourges, P.; Hehlen, B.; Michel, T.; Ecolivet, C.; Durand, O.; Cordier, S.; Katan, C.; et al. Elastic Constants, Optical Phonons, and Molecular Relaxations in the

High Temperature Plastic Phase of the $\text{CH}_3\text{NH}_3\text{PbBr}_3$ Hybrid Perovskite. *J. Phys. Chem. Lett.* **2016**, *7*, 3776–3784.

(20) Baikie, T.; Barrow, N. S.; Fang, Y.; Keenan, P. J.; Slater, P. R.; Piltz, R. O.; Gutmann, M.; Mhaisalkar, S. G.; White, T. J. A combined Single Crystal Neutron/X-ray Diffraction and Solid-State Nuclear Magnetic Resonance Study of the Hybrid Perovskites $\text{CH}_3\text{NH}_3\text{PbX}_3$ ($X = \text{I, Br and Cl}$). *J. Mater. Chem. A* **2015**, *3*, 9298–9307.

(21) Baroni, S.; de Gironcoli, S.; Dal Corso, A.; Giannozzi, P. Phonons and Related Crystal Properties from Density-Functional Perturbation Theory. *Rev. Mod. Phys.* **2001**, *73*, 515–562.

(22) Cowley, R. Structural Phase Transitions I. Landau Theory. *Adv. Phys.* **1980**, *29*, 1–110.

(23) Rousseau, B.; Bergara, A. Giant Anharmonicity Suppresses Superconductivity in AlH_3 under Pressure. *Phys. Rev. B: Condens. Matter Mater. Phys.* **2010**, *82*, 104504.

(24) Etienne, T.; Mosconi, E.; De Angelis, F. Dynamical Origin of the Rashba Effect in Organohalide Lead Perovskites: A Key to Suppressed Carrier Recombination in Perovskite Solar Cells? *J. Phys. Chem. Lett.* **2016**, *7*, 1638–1645.

(25) Moeller, C. K. *The Structure of Caesium Plumbo Iodide CsPbI_3* ; Matematisk-fysiske meddelelser; Munksgaard: København, Denmark, 1959; Volume 32.

(26) Stoumpos, C. C.; Malliakas, C. D.; Kanatzidis, M. G. Semiconducting Tin and Lead Iodide Perovskites with Organic Cations: Phase Transitions, High Mobilities, and Near-Infrared Photoluminescent Properties. *Inorg. Chem.* **2013**, *52*, 9019–9038.

(27) Yamada, K.; Funabiki, S.; Horimoto, H.; Matsui, T.; Okuda, T.; Ichiba, S. Structural Phase Transitions of the Polymorphs of CsSnI_3 by means of Rietveld Analysis of the X-Ray Diffraction. *Chem. Lett.* **1991**, *20*, 801–804.

(28) Even, J.; Pedesseau, L.; Jancu, J.-M.; Katan, C. DFT and k.p Modelling of the Phase Transitions of Lead and Tin Halide Perovskites for Photovoltaic Cells. *Phys. Status Solidi RRL* **2014**, *8*, 31–35.

(29) Azarhoosh, P.; McKechnie, S.; Frost, J. M.; Walsh, A.; van Schilfhaarde, M. Research Update: Relativistic Origin of Slow Electron-Hole Recombination in Hybrid Halide Perovskite Solar Cells. *APL Mater.* **2016**, *4*, 091501.

(30) Bokdam, M.; Sander, T.; Stroppa, A.; Picozzi, S.; Sarma, D. D.; Franchini, C.; Kresse, G. Role of Polar Phonons in the Photo Excited State of Metal Halide Perovskites. *Sci. Rep.* **2016**, *6*, 28618.

(31) Wright, A. D.; Verdi, C.; Milot, R. L.; Eperon, G. E.; Pérez-Osorio, M. A.; Snaith, H. J.; Giustino, F.; Johnston, M. B.; Herz, L. M. Electron Phonon Coupling in Hybrid Lead Halide Perovskites. *Nat. Commun.* **2016**, *7*, 11755.

(32) Sendner, M.; Nayak, P. K.; Egger, D. A.; Beck, S.; Müller, C.; Epding, B.; Kowalsky, W.; Kronik, L.; Snaith, H. J.; Pucci, A.; et al. Optical Phonons in Methylammonium Lead Halide Perovskites and Implications for Charge Transport. *Mater. Horiz.* **2016**, *3*, 613–620.

(33) Hohenberg, P.; Kohn, W. Inhomogeneous Electron Gas. *Phys. Rev.* **1964**, *136*, B864–B871.

(34) Kohn, W.; Sham, L. J. Self-Consistent Equations Including Exchange and Correlation Effects. *Phys. Rev.* **1965**, *140*, A1133–A1138.

(35) Giannozzi, P.; Baroni, S.; Bonini, N.; Calandra, M.; Car, R.; Cavazzoni, C.; Ceresoli, D.; Chiarotti, G. L.; Cococcioni, M.; Dabo, I.; et al. Quantum Espresso: a Modular and Open-source Software Project for Quantum Simulations of Materials. *J. Phys.: Condens. Matter* **2009**, *21*, 395502.

(36) Dal Corso, A. Pseudopotentials Periodic Table: From H to Pu. *Comput. Mater. Sci.* **2014**, *95*, 337–350.

(37) Monkhorst, H. J.; Pack, J. D. Special Points for Brillouin-zone Integrations. *Phys. Rev. B* **1976**, *13*, 5188–5192.

Supporting Information:

Structural Instabilities related to Highly
Anharmonic Phonons in Halide Perovskite

Arthur Marronnier,[†] Heejae Lee,[†] Bernard Geffroy,^{†,§} Jacky Even,[‡] Yvan
Bonnassieux,[†] and Guido Roma^{*,¶}

[†]*LPICM, CNRS, Ecole Polytechnique, Université Paris-Saclay, 91128 Palaiseau, France*

[‡]*Université Européenne de Bretagne, INSA, FOTON, UMR 6082, 35708 Rennes, France*

[¶]*DEN - Service de Recherches de Métallurgie Physique, CEA, Université Paris-Saclay,
91191 Gif sur Yvette, France*

[§]*LICSEN, NIMBE, CEA, CNRS, Université Paris-Saclay, 91191 Gif sur Yvette, France*

E-mail: arthur.marronnier@polytechnique.edu

This supporting information file is devoted to presenting some checks we made in order to show that the approximations used in this paper do not affect its conclusions. In particular, most of the results presented in the paper have been obtained by neglecting spin-orbit coupling.

Spin Orbit Coupling

Energy landscape

Spin-Orbit Coupling (SOC) is known to significantly affect the electronic band structure of lead halide perovskites. However our calculations suggest that its influence on the complex energy landscape of CsPbI₃, which is the subject of this paper, is not crucial. We have performed calculations with SOC using the PWSCF code of the QE package, with fully relativistic pseudopotentials obtained with the earlier 0.2.2 version of the pseudopotential library.¹ The relativistic pseudopotentials used have the same number of valence electrons as the scalar relativistic ones used for calculations without SOC (i.e., 9 for Cs, 7 for I, and 14 valence electrons for Pb).

First, as we have shown in the main paper, the energy landscape between the two proposed structures of the orthorhombic δ -phase, as shown in figure 5 of the article, is hardly affected by SOC. Furthermore, we present here below the comparison of the energy profiles of figures 3 and 7 with and without SOC.

The profiles shown in figures 3 and 7 of the main text, as well as in figure 1 here, are obtained from the equilibrium lattice parameter of the symmetric structure, for which the soft phonon eigenmode was calculated. As such, the non-symmetric structures have non-zero pressure. In order to check the pressure when taking into account SOC, we show in figure 2 the comparison of calculated pressures along the phonon profile for the orthorhombic structure. We noticed that the pressure is much lower in the cubic phase than in the orthorhombic one, which could be ferroelastic.

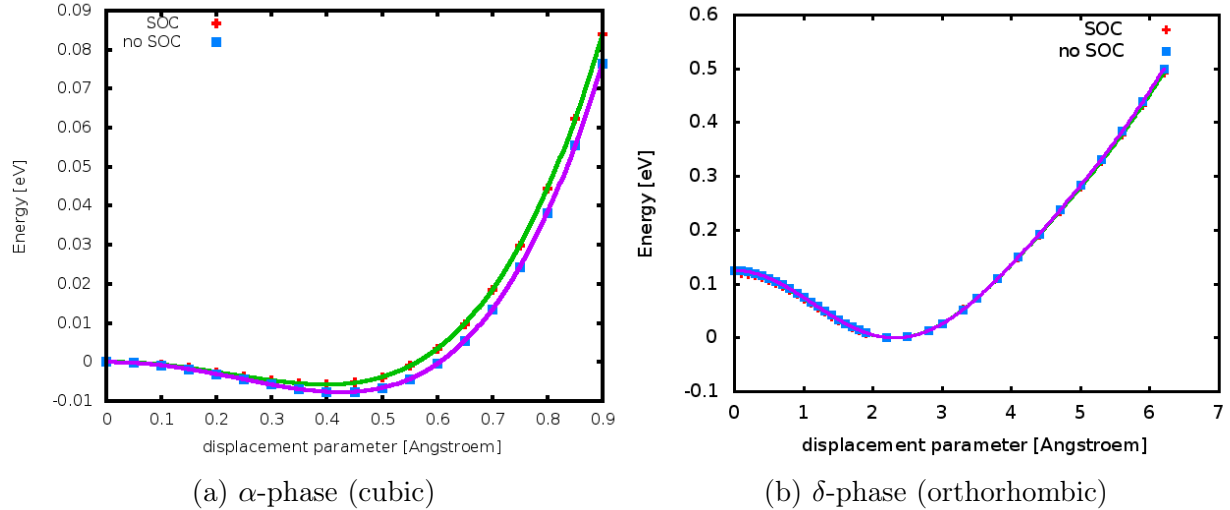


Figure 1: Energy profiles along soft phonon modes described in the main text as obtained with and without SOC. The abscissa is the distance in $3N$ dimensions (N =number of atoms). Lines are splines interpolations.

Rashba splitting

As predicted for $MAPbI_3$, SOC induces Rashba splitting, making the band gap indirect.²⁻⁵ This is a consequence of the pseudocubic symmetry, associated to the presence of the organic molecule, as well as the strong spin-orbit coupling due to the Pb $6p$ states. The α -phase of $CsPbI_3$ is supposed to be cubic, with space group $Pm\bar{3}m$, and as such no Rashba splitting is expected. However, as a consequence of the instability that we have unveiled by following a soft mode eigenvector, the actual minimum indeed breaks the symmetry and allows for a dynamical Rashba splitting. We show in figure 3 that a significant Rashba splitting occurs at the true minimum of the now pseudocubic structure (corresponding to the minima of figure 3 from the main article), not only in the conduction band (as predicted for $MAPbI_3$) but also in the valence band.

Phonon frequencies

In this section we present some results for phonon modes calculated with spin orbit coupling. In figure 4 the dispersion relations for the cubic α -phase in the fully relaxed structure ob-

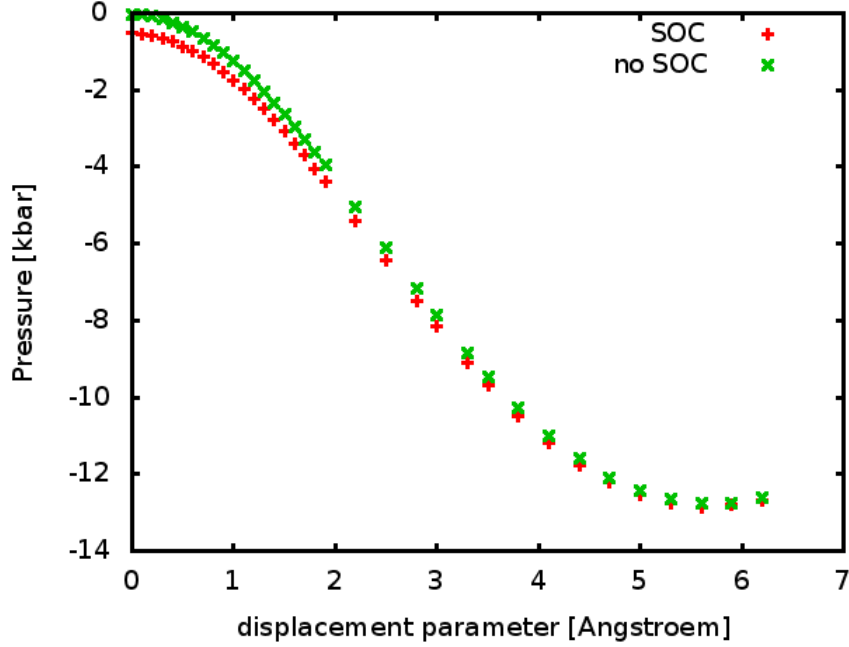


Figure 2: Pressure of calculated structures along the soft phonon eigenmode of the orthorhombic δ -phase with and without SOC.

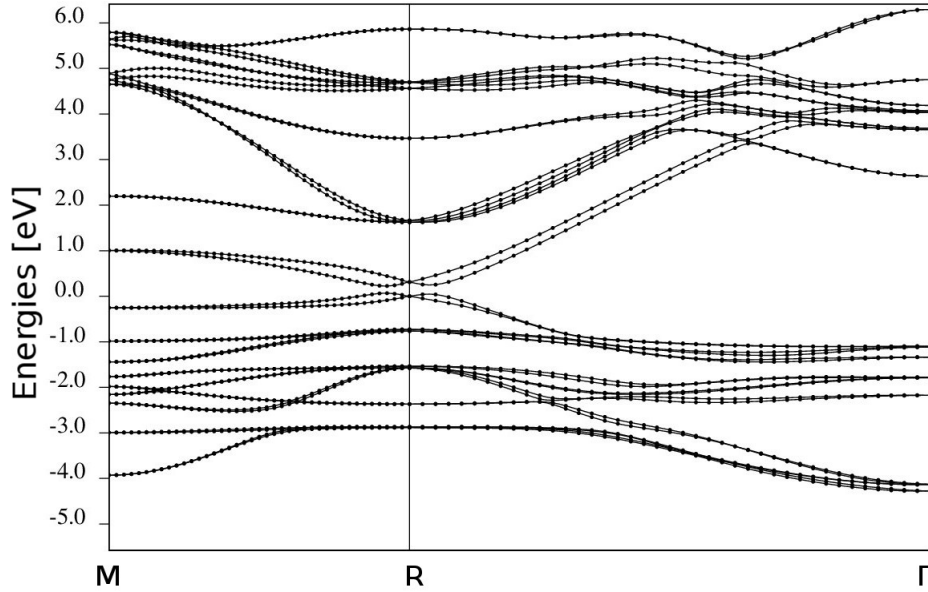


Figure 3: Band structure of distorted α -CsPbI₃ (the minimum of the energy profile in figure 3 of the main paper) along the M-R- Γ path in the Brillouin zone with SOC. Rashba splitting at the R-point occurs both in the valence and conduction bands.

tained from the minimum of figure 1a are presented. The branches are quite close to those obtained without SOC, with the exception that we still have a slightly negative eigenvalue at the Γ -point. We think that this might be an artifact coming from the electronic structure.

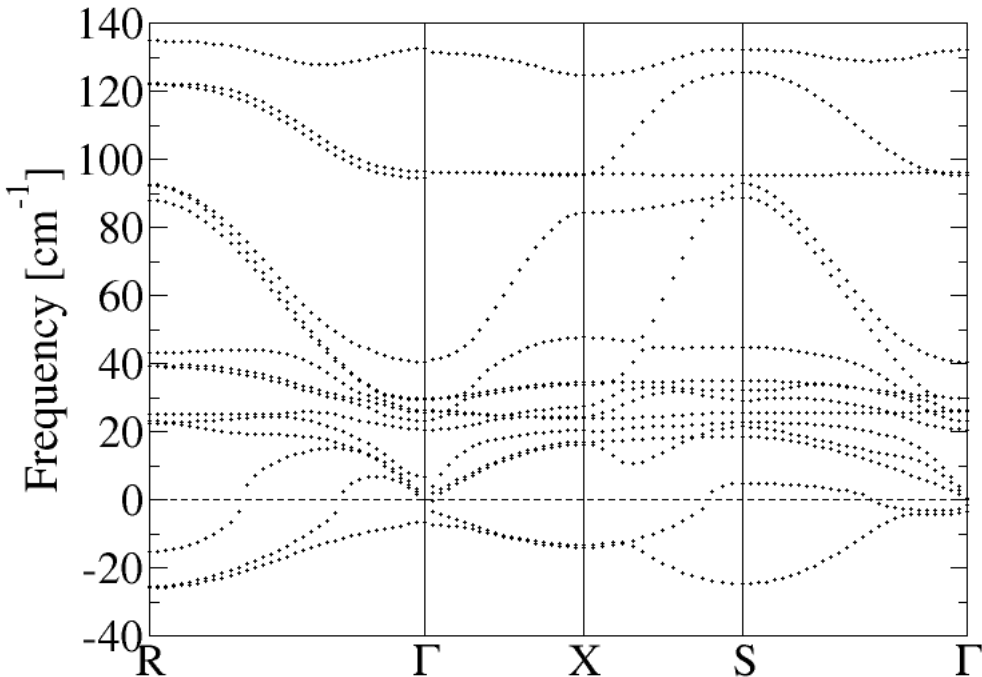


Figure 4: Phonon dispersions of the cubic α -phase of CsPbI_3 obtained with calculations including SOC.

The reader might have remarked, in the previous section, that taking into account SOC almost closes the electronic band gap for the α -phase. This known fact^{2,6} is probably affecting the phonons at Γ , where the enforcement of the acoustic sum rule is crucially dependent on the dielectric tensor and the Born effective charges. Close to the metallic transition, the calculation of these second derivatives of the energy might well be affected by numerical instabilities.

The effect of spin orbit coupling on the vibrational properties of halide perovskites, both organic and inorganic, will certainly be of high interest in future studies.

References

- (1) Dal Corso, A. Pseudopotentials Periodic Table: From H to Pu. *Comput. Mater. Sci.* **2014**, *95*, 337 – 350.
- (2) Even, J.; Pedesseau, L.; Jancu, J.-M.; Katan, C. DFT and $k \cdot p$ Modelling of the Phase Transitions of Lead and Tin Halide Perovskites for Photovoltaic Cells. *Phys. Status Solidi RRL* **2014**, *8*, 31–35.
- (3) Amat, A.; Mosconi, E.; Ronca, E.; Quarti, C.; Umari, P.; Nazeeruddin, M. K.; Grätzel, M.; De Angelis, F. Cation-Induced Band-Gap Tuning in Organohalide Perovskites: Interplay of Spin–Orbit Coupling and Octahedra Tilting. *Nano Lett.* **2014**, *14*, 3608–3616.
- (4) Motta, C.; El-Mellouhi, F.; Kais, S.; Tabet, N.; Alharbi, F.; Sanvito, S. Revealing the Role of Organic Cations in Hybrid Halide Perovskite $\text{CH}_3\text{NH}_3\text{PbI}_3$. *Nat. Commun.* **2015**, *6*, 7026.
- (5) Azarhoosh, P.; McKechnie, S.; Frost, J. M.; Walsh, A.; van Schilfhaarde, M. Research Update: Relativistic Origin of Slow Electron-Hole Recombination in Hybrid Halide Perovskite Solar Cells. *APL Mater.* **2016**, *4*, 091501.
- (6) Brgoch, J.; Lehner, A. J.; Chabynyc, M.; Seshadri, R. Ab Initio Calculations of Band Gaps and Absolute Band Positions of Polymorphs of RbPbI_3 and CsPbI_3 : Implications for Main-Group Halide Perovskite Photovoltaics. *J. Phys. Chem. C* **2014**, *118*, 27721–27727.

4.2.2 SHORT FERROELASTICITY STUDY

In the study of the previous section (Publication 1), the frozen phonon method was first computed with a constant volume (only displacing the individual atoms along the soft phonon eigenvector), and we noticed that in the orthorhombic δ -phase the energy barrier of the double well drastically increases from 1.24 meV to 2.39 eV after volume relaxation from the minimum of the double well. We would like now to give insight into how the potential energy landscape is changed when the volume can vary as well. Figures 4.2.1 and 4.2.2 both show (with different energy scales) the comparison between the fixed-volume frozen phonon energy profile and the energy of various points obtained by an interpolation of both atomic positions and volume between the maximum and the volume-relaxed minimum structures.

The data show that the volume relaxed points form a double well similar to the frozen phonon trajectory. However, when zooming around the maximum one can see that the local maximum is in fact a local minimum in this energy landscape. This could be another explanation for why the DFT relaxation algorithm had trouble finding the true global minimum and was doomed to fall onto this local maximum structure instead.

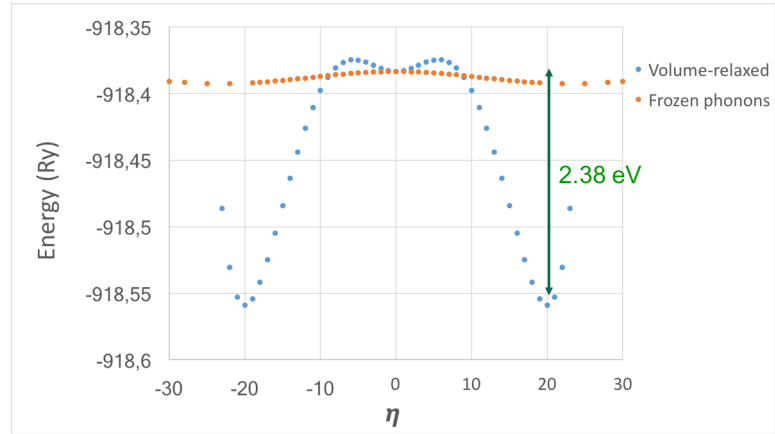


Figure 4.2.1: Potential energy surface of the orthorhombic δ -phase of $CsPbI_3$.

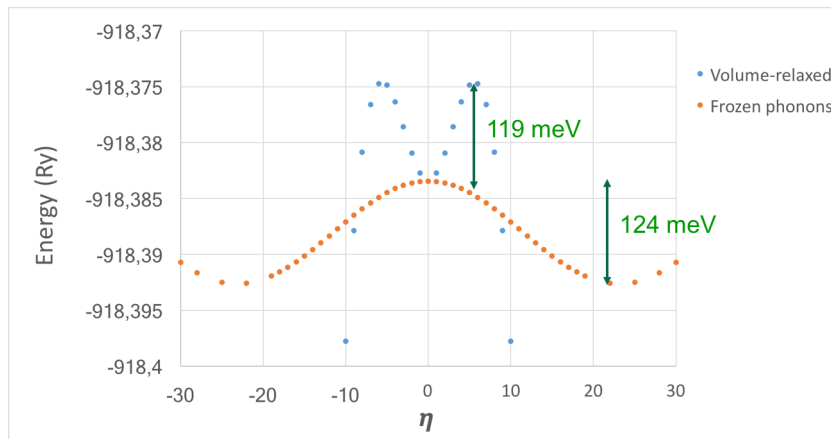


Figure 4.2.2: Zoom from figure 4.2.1.

Even though to the best of our knowledge nanoscale periodic domains have never been predicted nor experimentally observed for $CsPbI_3$, distinct domains were reported [9] in the piezoresponse of $MAPbI_3(Cl)$ grains, indicating the presence of ferroelasticity in these materials. Later, in 2017, Strelcov *et al.* [10] evidenced ferroelastic domains in both $CH_3NH_3PbI_3$ polycrystalline films and single crystals both with and without applied stress.

These ferroelasticity features should be considered in relation to the underlying ferroelectricity in these

4.2. [PUBLICATION 1] STRUCTURAL INSTABILITIES RELATED TO HIGHLY ANHARMONIC PHONONS

materials. As we saw in the previous section, since the soft modes used for the frozen phonons method are polar, the double-well profiles could explain the ferroelectricity previously observed in halide perovskites [11–14]. We performed few complementary calculations along the frozen phonon path on the polarization versus the reaction coordinate η as well as versus the electric field. We have not yet made enough progress in this direction for us to include the first results in this manuscript.

4.3 [PUBLICATION 2] ANHARMONICITY AND DISORDER IN THE BLACK PHASES OF CESIUM LEAD IODIDE

The work published in this second article [6] is both experimental and theoretical. We analyze in detail the structural phase transitions between the 4 phases of $CsPbI_3$, and apply the ab-initio methods we used in the previous paper on the new experimentally characterized phases. We discuss the consequences of the revealed structural instabilities and symmetry breaking on the electronic properties.

This work made possible through a three-party collaboration between our group at Saclay, INSA Rennes (FOTON team, France), and Prof. Kanatzidis's group in Northwestern University, which has extensive experience in the experimental study of perovskite structures' phase transitions. My personal work encompasses the components on the vibrational properties and the phase competition, while the experimental part, as well as the tight-binding and many-body DFT calculations were performed by the other contributors of this article.

To be precise, my contribution includes :

- writing and revising the article
- performing the major part of the phonon calculations and the eigenmode analysis,
- the entirety total energy calculations, including spin-orbit coupling calculations,
- the vibrational entropy calculations.

Anharmonicity and Disorder in the Black Phases of Cesium Lead Iodide Used for Stable Inorganic Perovskite Solar Cells

Arthur Marronnier,^{*,†} Guido Roma,[‡] Soline Boyer-Richard,[§] Laurent Pedesseau,[§] Jean-Marc Jancu,[§] Yvan Bonnassieux,[†] Claudine Katan,[⊥] Constantin C. Stoumpos,^{*,||} Mercuri G. Kanatzidis,^{||} and Jacky Even^{*,§}

[†]LPICM, CNRS, Ecole Polytechnique, Université Paris-Saclay, 91128 Palaiseau, France

[‡]DEN - Service de Recherches de Métallurgie Physique, CEA, Université Paris-Saclay, 91191 Gif sur Yvette, France

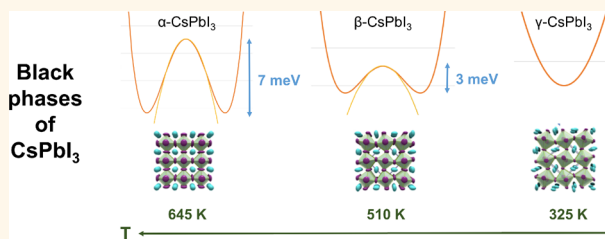
[§]Univ Rennes, INSA Rennes, CNRS, Institut FOTON - UMR 6082, F-35000 Rennes, France

[⊥]Univ Rennes, ENSCR, INSA Rennes, CNRS, ISCR (Institut des Sciences Chimiques de Rennes), UMR 6226, F-35000 Rennes, France

^{||}Department of Chemistry and Argonne–Northwestern Solar Energy Research (ANSER) Center, Northwestern University, Evanston, Illinois 60208, United States

Supporting Information

ABSTRACT: Hybrid organic–inorganic perovskites emerged as a new generation of absorber materials for high-efficiency low-cost solar cells in 2009. Very recently, fully inorganic perovskite quantum dots also led to promising efficiencies, making them a potentially stable and efficient alternative to their hybrid cousins. Currently, the record efficiency is obtained with CsPbI₃, whose crystallographical characterization is still limited. Here, we show through high-resolution *in situ* synchrotron XRD measurements that CsPbI₃ can be undercooled below its transition temperature and temporarily maintained in its perovskite structure down to room temperature, stabilizing a metastable perovskite polytype (black γ -phase) crucial for photovoltaic applications. Our analysis of the structural phase transitions reveals a highly anisotropic evolution of the individual lattice parameters *versus* temperature. Structural, vibrational, and electronic properties of all the experimentally observed black phases are further inspected based on several theoretical approaches. Whereas the black γ -phase is shown to behave harmonically around equilibrium, for the tetragonal phase, density functional theory reveals the same anharmonic behavior, with a Brillouin zone-centered double-well instability, as for the cubic phase. Using total energy and vibrational entropy calculations, we highlight the competition between all the low-temperature phases of CsPbI₃ (γ , δ , β) and show that avoiding the order–disorder entropy term arising from double-well instabilities is key to preventing the formation of the yellow perovskitoid phase. A symmetry-based tight-binding model, validated by self-consistent GW calculations including spin–orbit coupling, affords further insight into their electronic properties, with evidence of Rashba effect for both cubic and tetragonal phases when using the symmetry-breaking structures obtained through frozen phonon calculations.



KEYWORDS: inorganic perovskite solar cells, anharmonicity, cesium, phonons, DFT, SXRD, Rashba

The interest of the photovoltaics community for hybrid perovskite solar cells (PSCs) has been growing rapidly since the first demonstration in 2009,¹ mainly because PSCs combine ease and low-cost fabrication of organic electronics with efficiencies which compete with those of traditional sectors, considering the highest certified efficiency of 22.7%.² In the race to commercialization, the methylammonium-based perovskite CH₃NH₃PbI₃ (MAPbI₃ or “MAPI”) will probably be outpaced by more stable perovskite structures because of its poor stability.³ Several strategies are currently

being explored, such as mixed cation recipes,⁴ layered perovskites,⁵ and nanostructures such as quantum dots.⁶ In fact, after Eperon *et al.* found in 2015 a new experimental method to maintain CsPbI₃ stability in its black phase at room temperature and realized the first working cesium lead iodide solar cell,⁷ a cell exceeding 10% efficiency was reported in

Received: January 11, 2018

Accepted: March 22, 2018

Published: March 22, 2018

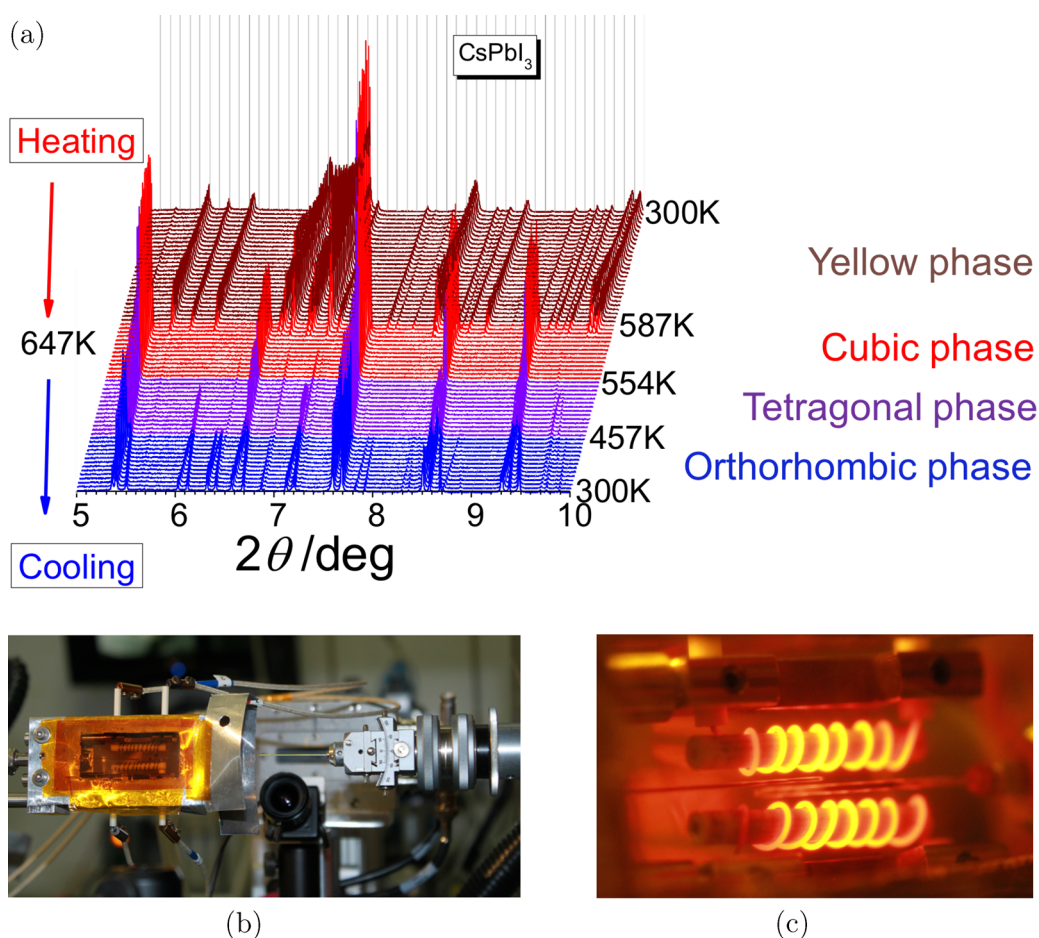


Figure 1. Temperature-dependent synchrotron X-ray diffraction (SXRD). (a) SXRD spectra for CsPbI₃. The original yellow phase converts to the black phase upon heating but does not return to the original structure upon cooling. (b,c) Experimental setup used for the *in situ* SXRD measurement of CsPbI₃ before and during the experiments. Photos (b) and (c) are courtesy of 11BM of Advanced Photon Source at Argonne National Laboratory.

2016.⁸ It was also shown⁹ that adding a small quantity of EDAPbI₄ (EDA = ethylenediamine) prevents the formation of the non-perovskite yellow phase of CsPbI₃ and leads to a reproducible efficiency of 11.8%. The recent report of a 13.4% efficient cesium lead iodide perovskite quantum dot solar cell⁶ demonstrated that purely inorganic perovskite solar cells have definitively become a stable and efficient alternative to their hybrid cousins. A four-terminal tandem cell using the formamidinium organic cation along with a small fraction of cesium as well as halogen alloying, in order to be able to tune the band gap, has reached more than 25% efficiency.¹⁰

It is currently well-known that the crystal structure has a direct impact on device performance, and it is thus of crucial importance to have high-quality crystallographic data to obtain valuable references for structural characterization of thin films or quantum dots used in those devices. So far, the structure of CsPbI₃ has mainly been studied through its similarities with the lead-free perovskite CsSnI₃. In fact, the structure of the black orthorhombic γ -phase of CsSnI₃ was experimentally measured in 1991,¹¹ and 20 years later, all its crystallographic phases have reached a comprehensive understanding (experimental and theoretical).^{1,12–16} For CsMI₃ (M = Pb, Sn), four phases are expected:^{12,17} cubic (α), tetragonal (β), and two orthorhombic phases (a black γ and a non-perovskite yellow δ -phase), thus including transitions between perovskite phases and non-perovskite polytypes (perovskitoids)¹⁸ at low temperature. All

the phases of CsSnI₃ have been thoroughly characterized,^{12,19} as well as the room temperature δ -phase of CsPbI₃.^{17,19,20} More recently, some of us investigated the temperature dependence of CsPbI₃'s band gap and how reversible the non-perovskite to perovskite structural transformations at high temperature²¹ can be. It was shown that, after heating the samples above 360 °C, the room temperature δ -phase (yellow) converts to the black perovskite α -phase. At variance, during the cooling step, the perovskite structure converts at 260 °C to the β -phase and at 175 °C to the γ -phase; both of these phases are black. Only after a few days the yellow δ -phase is obtained again. This work was the first report on the black orthorhombic γ -phase that is crucial in the context of photovoltaics applications.

In addition, vibrational properties of cesium halide perovskites have proven to be a key factor in determining the stability of phases with temperature. In CsPbCl₃, the role of phonons in phase transitions was pointed out already in the 1970s.²² Recently, first-principles calculations on CsSnI₃ revealed soft phonon modes and strong anharmonicity.^{23,24} Conversely, in the case of CsPbI₃ (and RbPbI₃), the role of vibrational properties in determining the phase stability is still understudied, although large values of Born effective charges hinted toward possible structural instabilities.²⁵ Very recently, some of us evidenced unexpected anharmonic features in the form of Brillouin zone (BZ)-centered double-well instability for both the cubic α -phase and the yellow orthorhombic δ -phase of

CsPbI₃,²⁶ but due to a lack of experimental data on the other phases, our understanding remained incomplete. For hybrid perovskites, several groups^{27,28} revealed small lifetimes for the phonons, a consequence of double-well potential energy profiles at M and R points in the BZ of cubic CH₃NH₃PbI₃. These structural effects in hybrid organic–inorganic perovskites, complicated by the rotational motion of the cation, have an influence on the optoelectronic properties. For instance, octahedral tilting has been shown to have a direct impact on the continuum band gap.^{29,30} This was further investigated by Yang *et al.*,³¹ who considered the influence of temperature on the electronic band structure as well as on the optical absorption threshold of cubic MAPbI₃. However, from this and other works,^{27,32} it seems that the influence of soft phonon modes on the absorption threshold in MAPbI₃ can be neglected.

In this paper, we report the detailed experimental structures of the crucial black γ -phase of CsPbI₃ at 325 K, along with the structures of the α -phase (645 K) and β -phase (510 K), using synchrotron X-ray powder diffraction (SXRD). The temperature distortion of these three phases is studied. Using DFPT (density functional perturbation theory) methods similar to our previous work,²⁶ we investigate the vibrational properties and the energy landscape of both the low-temperature orthorhombic γ -phase and the tetragonal β -phase of CsPbI₃. For the tetragonal phase, the instabilities at the Γ point are further studied by performing total energy calculations on a path following the soft phonon eigenvectors (frozen phonons method). The energy competition between the low-temperature phases of CsPbI₃ is studied using total energy and vibrational entropy calculations. Finally, we used symmetry-based tight-binding modeling and the self-consistent many-body (scGW) approximation to derive the electronic band structure, using our experimental data on the different phases of CsPbI₃ and a previously developed tight-binding model for hybrid perovskite MAPbI₃.³³ We explore the Rashba effect for both cubic and tetragonal phases using the new symmetry-breaking structures revealed by our frozen phonon calculations.

RESULTS AND DISCUSSION

Structural Distortion of the Black Phases of CsPbI₃

CsPbI₃ is one of the earliest known ternary plumbohalides, originally discovered by Møller,²⁰ having the distinctive characteristic that it adopts a different “perovskitoid”¹⁸ structure compared to its well-known congeners CsPbBr₃ and CsPbCl₃ that adopt a regular perovskite structure.³⁴ Later studies have, in fact, shown that CsPbI₃ can become a perovskite at elevated temperatures (around 310 °C),¹⁷ but its structural reconfiguration as it cools back to room temperature is unknown. We show here that CsPbI₃ can be undercooled below its transition temperature and temporarily retain its perovskite structure down to room temperature, as shown by high-resolution synchrotron X-ray diffraction (Figure 1a), using an *in situ* experimental setup (Figure 1b,c). The structural analysis confirms the change of the yellow phase (δ -phase) to its black polytype (α -phase) on heating, but upon cooling, the perovskite does not return to its original yellow phase immediately. Instead, CsPbI₃ adopts the metastable perovskite polytype on cooling back to room temperature, revealing a phase transition pathway reminiscent of CsPbBr₃,^{35,36} CsSnBr₃,^{37,38} and CsSnI₃,^{12,39} where the high-symmetry cubic phase (α -phase) distorts initially to a tetragonal phase (β -phase) followed by a further change to the orthorhombic (γ -phase), which persists down to room temperature (Figure 2).

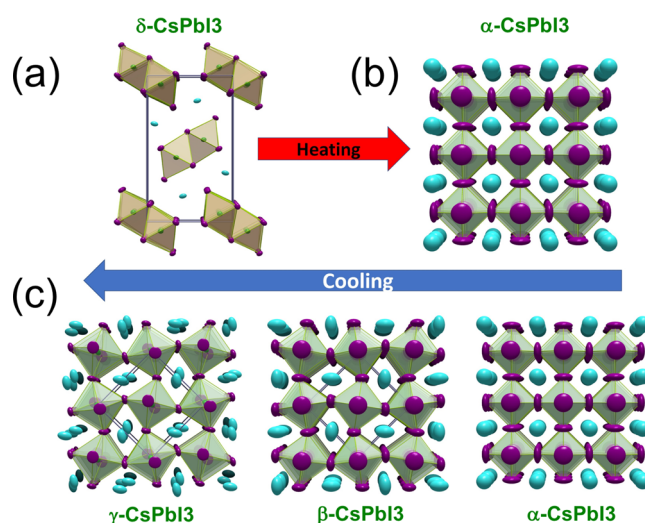


Figure 2. Structural phase transitions in CsPbI₃ versus temperature. (a) Initial yellow perovskitoid phase (δ -CsPbI₃, NH₄CdCl₃-type) converts to (b) black perovskite phase (α -CsPbI₃, CaTiO₃-type) as the temperature exceeds the transition temperature. (c) Upon cooling, the black perovskite phase is retained and can be undercooled below the transition temperature, where the typical perovskite distortions (tetragonal β -CsPbI₃, orthorhombic γ -CsPbI₃) can be observed all the way to room temperature. These phases are metastable and transform to the thermodynamic δ -CsPbI₃ upon standing.

The conversion of the δ -CsPbI₃ to the α -CsPbI₃ involves a dramatic change in the unit cell volume (Figure 3a,b), which is compensated by a large increase in the thermal parameters of the iodide ions, signaling a very large increase in the dynamic motion of the corner-connected [PbI_{6/2}]⁻ octahedra. The dynamic motion, which is corroborated by the emergence of stereochemical activity at higher temperature, known as “emphansis”,^{40,41} progressively relaxes to less dynamic states (β -CsPbI₃, γ -CsPbI₃) as the perovskite cools. Quite remarkably, whereas the overall thermal expansion coefficient is positive, the evolution of the individual lattice parameters is highly anisotropic involving a combination of negative and positive thermal expansion coefficients (Figure 3c). Initially, the crystallographic *c*-axis expands on cooling in the tetragonal phase regime, followed by a large expansion of the crystallographic *b*-axis in the orthorhombic phase, which is largely compensated by the enormous decrease in the crystallographic *a*-axis. The competing thermal expansion leads to a crossing of the increasing *b*-axis and the decreasing *c*-axis, which become equivalent slightly above room temperature. The complex phase transitions in CsPbI₃ have also been confirmed by differential thermal analysis (DTA), which supports all the phase changes observed experimentally by XRD.

Vibrational Properties and Phase Competition. In order to get further insight into these black perovskite phases, we used DFT for structural optimization, which is mandatory to allow inspection of vibrational properties (phonons). We start from the above experimental crystal structures (Figure S4) for the α -phase (645 K), β -phase (510 K), and γ -phase (325 K) having, respectively, *Pm*3*m*, *P4*/*mbm*, and *Pbnm* space groups. Relaxing the structure from these experimental data sets, we obtain a good agreement on the lattice constants between our XRD experiments (Table 1) and our DFT calculations (Table 2), with the latter corresponding to a temperature of 0 K. For

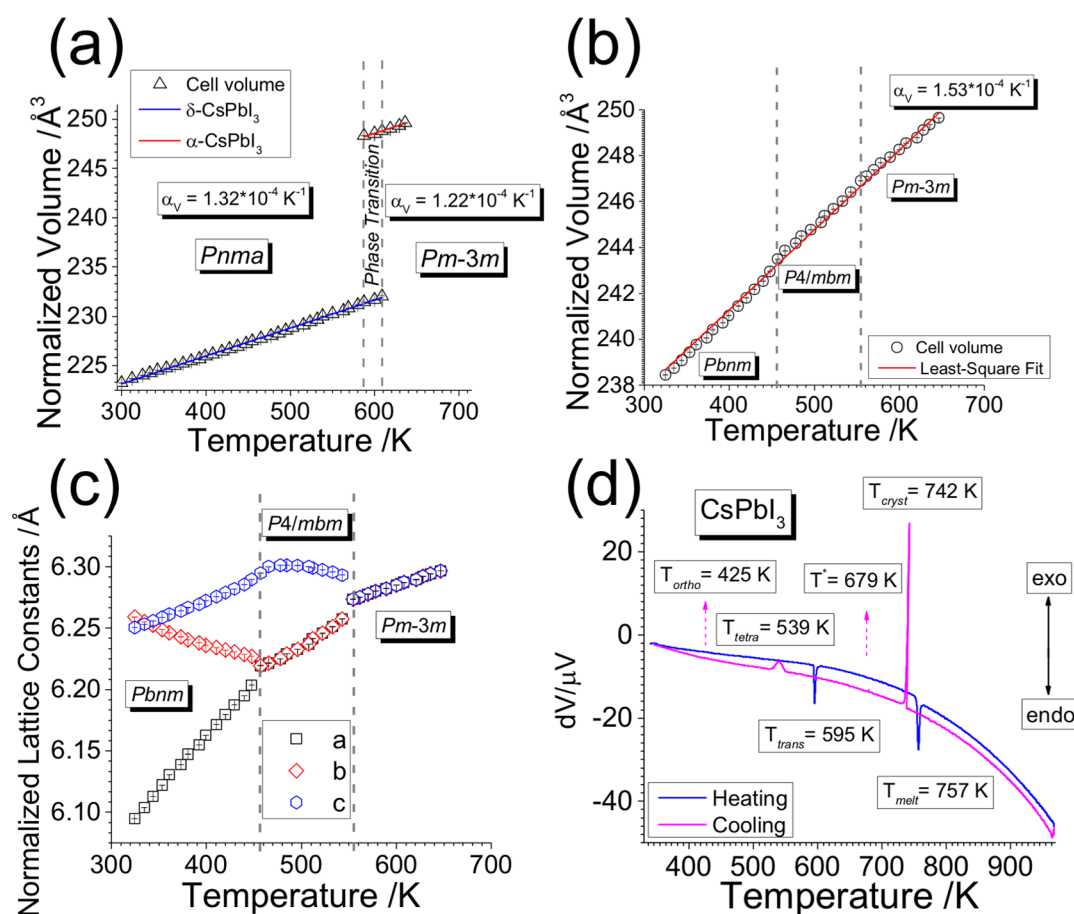


Figure 3. Temperature evolution of CsPbI₃. (a) δ -CsPbI₃ (*Pnma*) expands linearly on heating to the transition temperature at around 600 K, where the phase transition to α -CsPbI₃ (*Pm-3m*) produces a large increase in the cell volume. (b) On cooling, α -CsPbI₃ undergoes successive phase transitions to β -CsPbI₃ (*P4/mbm*) and γ -CsPbI₃ (*Pbnm*) without converting back to the original δ -CsPbI₃ phase. (c) Anisotropic temperature evolution of the CsPbI₃ perovskite revealing competitive negative and positive thermal expansion trends among the individual lattice parameters of the low-temperature phases. (d) Differential thermal analysis (DTA) is in good agreement with XRD experiments. T_{melt} = melting point, T_{cryst} = crystallization point, T_{trans} = δ - to α -CsPbI₃ transition, T_{tetra} = α - to β -CsPbI₃ transition, T_{ortho} = β - to γ -CsPbI₃ transition, T^* = Cs₄PbI₆ formation.

Table 1. Normalized Lattice Constants (Å) and Octahedral Tilting Angles⁴² of the Three Black Phases of CsPbI₃ from SXRD

	<i>Pbnm</i> exp. (324.6 K)	<i>P4/mbm</i> exp. (511.7 K)	<i>Pm-3m</i> exp. (646.5 K)
<i>a</i>	6.095	6.241	6.297
<i>b</i>	6.259	6.241	6.297
<i>c</i>	6.250	6.299	6.297
angle β	11°5	8°6	0
angle δ	9°9	0	0

instance, the normalized volume at 0 K can be extrapolated from Figure 3b, and we found 227 Å³, which is in good agreement with the DFT value obtained for the δ -phase (215 Å³). We also report in Tables 1 and 2 the octahedral tilting with angles β (in-plane) and δ (out-of-plane) calculated as in ref 42, as increased octahedral tilting can be directly traced back to an increase of the continuum band gap in addition to the direct impact of the expansion/contraction of the unit cell parameters. Note that for the orthorhombic phase in the DFT calculations (and later in the phonon calculations), we use the *Pnam* convention, which is equivalent to *Pbnm* by a permutation of axes.

Table 2. Normalized Lattice Constants (Å) and Octahedral Tilting Angles⁴² of the Three Black Phases of CsPbI₃ As Derived from DFT Calculations (at 0 K)^a

	<i>Pnam</i>	<i>P4/mbm</i> ($\eta = 0$)	<i>P4/mbm</i> ($\eta \neq 0$)	<i>Pm-3m</i> ($\eta = 0$)	<i>Pm-3m</i> ($\eta \neq 0$)
<i>a</i>	6.335	5.973	5.717	6.149 ²⁶	6.183 ²⁶
<i>b</i>	5.606	5.973	6.222	6.149 ²⁶	6.183 ²⁶
<i>c</i>	6.112	6.273	6.248	6.149 ²⁶	6.183 ²⁶
angle β	0	16°5	10°3–22°8	0	2°9–3°3
angle δ	0	0	3°7	0	3°6

^aWe give both the symmetric structures ($\eta = 0$ in Figure 4b) and the new equilibrium structures ($\eta \neq 0$ in Figure 4b) of the double well found for the *P4/mbm* and *Pm-3m* phases.

The orthorhombic, low-temperature, γ -phase of CsPbI₃ matches the corresponding phase studied experimentally for similar perovskite CsSnI₃ in 1991 by Yamada *et al.*,¹¹ who identified it with the *Pbnm* space group symmetry. This is a totally different phase compared to the *Pnma* orthorhombic structure (yellow δ -phase) obtained by Trots¹⁷ and whose phonon spectrum was already investigated using first-principles calculations.²⁶ The γ -phase's structure corresponds to an antiferro distortion of the *Pm-3m* perovskite structure, as shown previously.¹⁹ Contrary to our previous findings for the

α - and δ -phases,²⁶ the phonon dispersion of the orthorhombic γ -phase of CsPbI₃, calculated with DFPT, does not present any imaginary modes at the Γ point (see Figure 4d). Furthermore, there are no unstable phonons at the other high-symmetry points. This was expected because, at low temperature, this phase is the most stable perovskite phase.

The phonon dispersions of CsPbI₃ in the tetragonal phase (space group $P4/mbm$), with the structure (denoted as “ $\eta = 0$ ” in Table 2) optimized starting from our experimental data, are shown in Figure 4a. The imaginary modes that can be found at different high-symmetry points in the Brillouin zone arise from

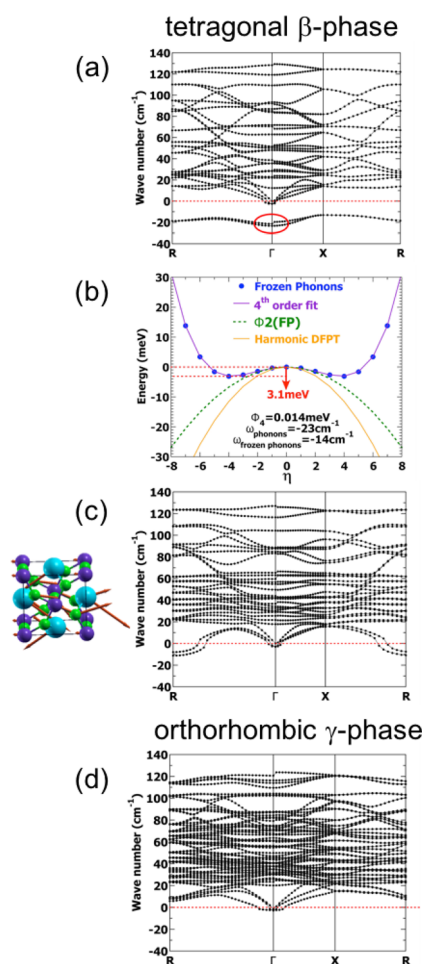


Figure 4. Phonon modes in CsPbI₃. (a) Phonon modes of the tetragonal β -phase of CsPbI₃ in the structure optimized from our experimental data (denoted as “ $\eta = 0$ ” in Table 2). Given that the tetragonal structure relaxes to a slightly orthorhombic one when breaking the symmetry (c), we use for this figure the same orthorhombic convention for the high-symmetry points of the Brillouin zone as the one used in (c,d). (b) Potential energy surface for tetragonal CsPbI₃ on a path following the most unstable optical phonon’s eigenvector at Γ versus displacement parameter η . A 0.38 Å 3 N dimensional displacement is required to attain the new minimum. $\omega_{\text{frozen phonons}}$ and Φ_4 are obtained by fitting eq 1. (c) Phonon modes of tetragonal CsPbI₃ at the true equilibrium structure (slightly orthorhombic) obtained through geometry optimization of the symmetry-broken structure (denoted as “ $\eta \neq 0$ ” in Table 2). The imaginary modes at Γ were eliminated due to tight convergence thresholds and the frozen phonon method. (d) Phonon modes of the orthorhombic γ -phase of CsPbI₃ in the structure optimized from our experimental data (see Table 2).

the instabilities of the tetragonal phase in this 0 K DFT calculation. These modes should be stabilized when including temperature effects *via* vibrational entropy.

The presence of soft modes is less expected at the Γ point (one doubly degenerated phonon at -23 cm^{-1} , circled in red), where only acoustic modes should be found. Consistent with earlier findings on the α - and δ -phases,²⁶ these instabilities correspond to previous neutron scattering experiments showing very low acoustic phonon density of states at 80 °C.⁴³ Similar results were obtained more recently for CH₃NH₃PbI₃²⁸ and CH₃NH₃PbBr₃.⁴⁴ These instabilities, especially the one at Γ , were previously reported and analyzed by some of us²⁶ for both the δ -phase and the α -phase in inorganic CsPbI₃. In order to solve this anomaly and to further explore the energy landscape around equilibrium, we use here a similar method of frozen phonons, which we do not detail further in this paper.

Using Landau theory⁴⁵ and the adiabatic approximation, the anharmonic energy^{22,46} as a function of displacement is given by

$$U(\eta) = U_0 + \frac{\eta^2}{4} \hbar \omega_{\nu\Gamma}(\mathbf{q}_\Gamma) + \frac{\eta^4}{24} \Phi_{4,\nu\Gamma} + O(\eta^6) \quad (1)$$

This model fits well with the results shown in Figure 4. This means that the previous structure was not the proper equilibrium state and that the tetragonal phase of CsPbI₃ behaves anharmonically around equilibrium. The structure will thus oscillate between the two minima and through this very weak energy barrier (3.1 meV). In order to estimate the frequency of these oscillations, one can write

$$\tau = \tau_0 e^{E/k_B T} \quad (2)$$

for an energy barrier E (and the Boltzmann constant k_B). Assuming for τ_0 the lowest optical phonon frequency ($\omega \approx 23 \text{ cm}^{-1}$), one finds a typical oscillation time of $0.4 \times 10^{-12} \text{ s}$ at room temperature. After relaxation from the minimum structure obtained by fitting the fourth-order model, the energy barrier increases to 8.1 meV. This leads to the new equilibrium structure denoted as “ $\eta \neq 0$ ”.

After the atomic positions were relaxed in the new symmetry-breaking structure ($\eta \neq 0$), we could totally eliminate the soft modes at Γ (see Figure 4c). To conclude, for the tetragonal phase of CsPbI₃, the imaginary modes at Γ were eliminated due to both tight convergence thresholds and the frozen phonon method. As a result, this anharmonic phonon at Γ will not condense at low temperatures and will not yield one of the orthorhombic phases, whereas the remaining instabilities at the R point correspond to phonon modes that condense at lower temperatures to transition to the orthorhombic black γ -phase.^{21,43}

To summarize our comprehensive vibrational study, we have shown here and in ref 26 that CsPbI₃ presents this anharmonic feature in three out of four phases, at variance with MAPbI₃ for which instabilities at the center of the BZ were not found.

Next, we briefly investigate the phase competition and vibrational entropy of the low-temperature phases. Table 3 summarizes the total energies of the two different orthorhombic phases of CsPbI₃ along with that computed for the tetragonal β -phase. For each phase, we report here the lowest energy obtained by DFT optimization, which means using the symmetry-breaking structures for the δ - and β -phases ($\eta \neq 0$). We find that the γ -phase has a total energy lower than that of the δ -phase, contrary to what one would expect given their

Table 3. Total Energies (U) and Free Energies (F) of CsPbI₃ Phases, Given Per Formula Unit of 5 Atoms

phase	experimental temperature (K)	U (meV)	F at 400 K (meV)
δ	325	34 ²⁶	88.5
γ	450	0	0
β	510	54	

respective temperature of stability. We carefully checked that this conclusion is not changed when using PBE or even HSE exchange-correlation instead of local density approximation (LDA) or when spin-orbit coupling is taken into account (see Supporting Information). Given the structural instabilities of these structures, especially for the δ -phase,²⁶ one can anticipate relatively high values for the vibrational entropies, potentially reversing this order for the free energy $F = U - TS$. We calculated the free energy F by including the $-TS_{\text{vib}}$ term (quasiharmonic approximation⁴⁷). This method, using the phonon density of states, cannot be straightforwardly applied²³ when unstable phonon modes are present and can thus be used only for low-temperature orthorhombic phases once their unstable modes at Γ have been removed (see the Methods section for technical details).

The results show that taking into account the vibrational entropy does not change the conclusion: the γ -phase is calculated to have a lower energy than the δ -phase (Table 3). This might be due to the fact the δ -phase could actually be further stabilized through an additional order-disorder ΔS stochastic entropy term⁴⁸ associated with the structural instabilities (and related to the fourth-order term in eq 1 that we reported for this phase). This term naturally does not apply to the more stable γ -phase.

We think that avoiding the disorder of the non-perovskite phase is key to keeping CsPbI₃ in its stable black phases. In a very recent paper,⁹ Zhang *et al.* noticed that the stabilization of α -CsPbI₃ is accompanied by a significant reduction in grain size. In light of our findings on the ferroelectric disorder of the δ -phase,²⁶ the reduced grain size could prevent the perovskite from forming very small ferroelectric domains and allow it to remain in its ordered black phases.

Electronic Properties of the Black Perovskite Phases.

We further use the aforementioned XRD and DFT-optimized structures for the different perovskite phases of CsPbI₃ to investigate their electronic properties. To this end, we employ both semiempirical and state-of-the-art many-body DFT techniques (see the Methods section for details). To model noncubic phases of CsPbI₃, we customized the sp^3 tight-binding (TB) model recently developed for the cubic phase of MAPbI₃,³³ considering a simple d^{-2} Harrison law⁴⁹ to handle bond length variations, along with the matrix elements as given by Slater and Koster.⁵⁰ Given the very limited experimental data available for the black phases of CsPbI₃, we used the TB parameters reported previously and optimized for MAPbI₃.³³

The electronic band structures computed with the TB model using the experimental crystallographic data recorded for the α -phase (645 K), β -phase (510 K), and γ -phase (325 K) of CsPbI₃ are shown in Figure 5a–c, respectively. All electronic band gaps are direct, and corresponding values are summarized in Table 4. For the cubic α -phase, the computed band gap (1.6 eV) agrees nicely with the experimental one (1.7 eV).^{7,51} As expected, because of band folding,⁵² the band gap of CsPbI₃ shifts from the R point of the Brillouin zone in the cubic α -phase to Z and Γ for the β - and γ -phases, respectively. The

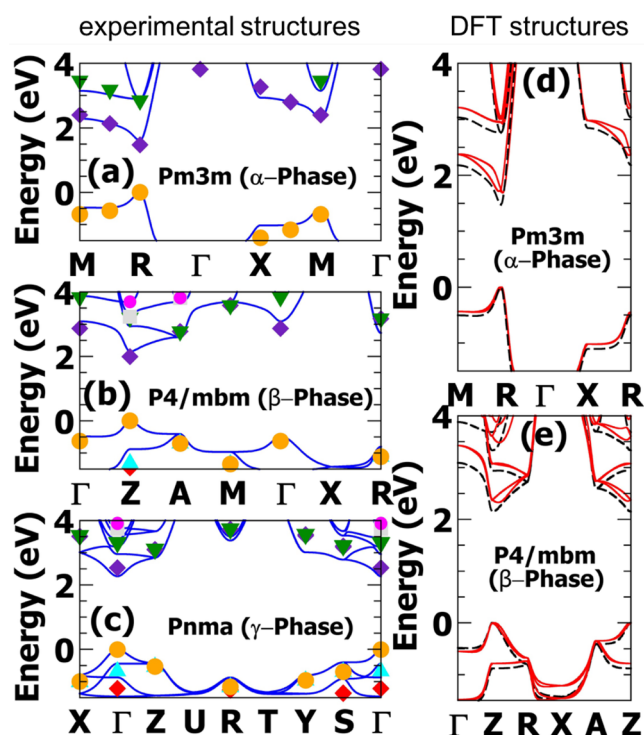


Figure 5. Electronic band structures. (a–c) Computed electronic band structures using the TB model (solid lines) and at the scGW+SOC level of theory (symbols) for the experimentally determined crystal structures (Figure 2c). (d,e) Electronic band structures calculated from the TB method for the DFT-optimized structures: (d) cubic α -phase and (e) tetragonal β -phase. Dashed lines correspond to the symmetric structures ($\eta = 0$), whereas straight lines correspond to the new equilibrium structures ($\eta \neq 0$).

Table 4. Comparison of Electronic Band Gaps Obtained within the TB Model and from scGW Calculations Including SOC for the Experimentally Determined Crystal Structures (Figure 2c)

phase	E_G (eV)		
	TB	scGW+SOC	exp.
γ	2.25	2.53	
β	1.83	1.89	
α	1.61	1.48	1.73 ^{7,51}

electronic band gap undergoes a progressive increase when going from the cubic phase to the more distorted β - and γ -phases. This increase is a direct consequence of the lead iodide octahedra rotations that stabilize the top of the valence band maximum and destabilizes the bottom of the conduction band minimum due to, respectively, antibonding and bonding character of the orbital overlaps.⁵²

Given the limited experimental data, we also performed calculations at a relevant level of theory required to assess band gaps, namely, using the quasiparticle self-consistent GW theory (scGW) along with spin-orbit coupling (SOC).^{53,54} The agreement with the TB model is fairly good (Table 4 and Figure 5a–c), particularly because the parameters of our TB model have not been refined to match any experimental data nor those computed at the scGW+SOC level. The latter confirm the progressive decrease of the band gap from the γ -phase to the α -phase. These predictions clearly prompt further

detailed experimental investigation of all three perovskite black phases.

Next, we further use our TB model to investigate the electronic properties of the DFT-optimized crystal structures of CsPbI₃ (Table 2). Corresponding electronic band structures are shown in Figure 5d,e, and band gaps are summarized in Table 5. Overall, for the high-symmetry structures ($\eta = 0$), the

Table 5. Data Relevant to the Rashba Effect: Band Gap Energies for the DFT-Optimized Structures of the Cubic α - and Tetragonal β -Phases^a

phase	E_G (eV)		k_{minCB} ($\pi/a, \pi/b, \pi/c$)	ΔE_C (eV)
	$\eta = 0$	$\eta \neq 0$		
β	2.15	2.38	(0.166, 0, 1)	0.05
α	1.47	1.75	0.963 (1, 1, 1)	0.06

^a $\eta = 0$ and $\eta \neq 0$ (Figure 4b) correspond to the symmetric and new equilibrium structures, respectively. k_{minCB} indicates the position in reciprocal space of the conduction band minimum. ΔE_C is the energy shift between R point for the α -phase (Z point for the β -phase) and the new conduction band minimum.

computed band structures reveal the very same features as those obtained for the experimental crystal structures (Figure 5). The band gap of the cubic $Pm\bar{3}m$ structure is significantly reduced as a result of the smaller unit cell parameter (Table 5). For the low-symmetry structures ($\eta \neq 0$), band gaps of both the cubic and tetragonal structures undergo a significant increase consistent with octahedral distortions (*vide supra*). In addition, the energy minima are shifted away from the high-symmetry points of the Brillouin zone (R and Z for the α - and β -phases, respectively) due to the Rashba effect that lifts the spin degeneracy.⁵³

Thus, these results strongly support the hypothesis of dynamical Rashba effect in CsPbI₃. They also demonstrate that it is an intrinsic property of the inorganic lattice, even though its strength might be influenced by the nature of the organic cations such as MA or FA.

CONCLUDING REMARKS

Using high-resolution synchrotron XRD measurements, we showed that CsPbI₃ can be undercooled below its transition temperature and temporarily retain its perovskite structure down to room temperature, stabilizing a metastable perovskite polytype (black γ -phase). Our detailed study of the temperature distortion revealed complex phase transitions with a highly anisotropic evolution of the individual lattice parameters and even a crossing of the b -axis and c -axis in the $Pbnm$ phase. Our *ab initio* vibrational calculations have shown that out of the three black phases of CsPbI₃, the only phase that presents a harmonic energy landscape around equilibrium is the orthorhombic γ -phase. Avoiding the anharmonic order-disorder entropy term of the non-perovskite δ -phase is key to keeping CsPbI₃ in its black phase at room temperature. For the new tetragonal β -phase, we evidenced unexpected anharmonic effects in the form of a Brillouin zone-centered double well. This instability could affect, in particular, the static dielectric constant through the coupling between phonons and the electric field in these materials.⁵⁵ In addition, the perovskite oscillations through the double well could be at the origin of the dynamical Rashba effect and the ferroelectricity foreseen in halide perovskites.⁵³ In fact, we evidenced this Rashba effect for the cubic and tetragonal phase and studied the electronic

structure of all three black phases of CsPbI₃ combining tight-binding modeling and self-consistent GW calculations in the framework of many-body perturbation theory.

METHODS

Synthesis. PbO (100 mmol, 22.32 g) was dissolved in 100 mL of 57% aqueous HI. Cs₂CO₃ (50 mmol, 16.29 g) was dissolved in 100 mL of 57% aqueous HI. A yellow solid was obtained from the mixture of CsI and PbO solutions, leaving an essentially colorless supernatant liquid (usually pale yellow because of the presence of dissolved I₂; colorless starting HI should give a practically colorless supernatant). The addition was done slowly, under constant stirring at the initial steps to avoid local concentration of CsI. The mixture was left to cool to ambient temperature and immediately filtered through a fritted dish funnel under vacuum. The solid was washed with 5% aqueous HI (five parts water/one part concentrated HI) followed by methanol and left for overnight drying. The solid was further dried in an oven at about 70 °C in air. The yield was 72 g (around 100%).

An amount of 36 mg (0.05 mmol) of CsPbI₃ was mixed with 57 mg (0.95 mmol) of fused SiO₂ and transferred into a mortar, which were thoroughly ground into a homogeneous pale yellow powder. The resulting powder was transferred in a 0.5 mm o.d. fused SiO₂ capillary, filling it to around 2/3 of its length. Neat fused SiO₂ was added on top to facilitate sealing. The capillary was transferred into a vacuum line and flame-sealed through the neat SiO₂ at 10⁻⁴ mbar. For measuring, the capillary was placed into a brass pin sample holder base, held in place by fast drying epoxy, mounted on the goniometer, and measured under the following conditions.

High-Resolution Temperature-Dependent X-ray Diffraction. High-resolution synchrotron powder diffraction experiments were performed at the beamline 11BM of the Advanced Photon Source (APS), Argonne National Laboratory. An average wavelength of $\lambda = 0.413906$ Å was used.⁵⁶

A homemade resistive heater device was used to control the temperature of the samples over the range of 300–650 K (see Figure 1b). The temperature was ramped at a rate of 2.5 K/min, and diffraction patterns were recorded every 4 min, covering a temperature window of around 10 K/pattern. A thermocouple, protected by a fused SiO₂ sheath, was used to measure the temperature close to the bottom of the sample capillary, from where the data were collected (see Figure 1c). The diffractometer was controlled using the EPICS code.⁵⁷

Powder Pattern Refinements. The powdered patterns were refined using the cyclic refinement function of Jana2006.⁵⁸ The initial room temperature pattern was refined using a pseudo-Voigt peak shape model with 20 Legendre polynomial terms used to model the background. The atomic coordinates of the known structure of δ -CsPbI₃ were used to initiate the Rietveld refinement with all atoms being refined anisotropically. The higher temperature patterns were refined in an automated manner, with the initial guesses for each pattern being provided by the preceding one. Upon each phase transition, where the fitting quality decreased significantly, a new initial structural refinement was made manually, and the cyclic refinement was repeated until the next phase transition. The initial guesses for the space groups and the atomic positions of α -CsPbI₃, β -CsPbI₃, and γ -CsPbI₃ were found based on screening through the most common perovskite tilting modes.⁵⁹ The detailed refinement data are given in the Supporting Information.

Density Functional Theory for Vibrational Properties Study. Electronic structure calculations were performed within the DFT^{60,61} framework, as implemented in the Quantum Espresso code.⁶² The vibrational properties were studied using the LDA and plane waves with a cutoff of 70 Ry. The details of the pseudopotentials that we used here, both the scalar relativistic ones and the fully relativistic used to check the influence of spin-orbit coupling, are described in ref 26. Additional calculations to test the effect of the exchange correlation functionals, using PBE and HSE, are described in the Supporting Information. The following Monkhorst–Pack meshes⁶³ (centered on Γ) were used to describe the various phases: δ -CsPbI₃, 10 × 5 × 3; α -CsPbI₃, 8 × 8 × 8; β -CsPbI₃, 7 × 5 × 5; and γ -CsPbI₃, 6 × 6 × 4.

We used DFPT⁴⁷ to compute the phonon spectra, as implemented in the Quantum Espresso code.⁶² Born effective charges and high-frequency dielectric tensors were computed with linear response theory and gave us access to the long-range contributions to the dynamical matrices. A resolution of 5 q-points/Å⁻¹ was chosen for the phonon spectra. To remove spurious phonon modes, we used strict convergence thresholds of 10⁻⁴ Ry/bohr (forces) and 10⁻¹⁴ (phonon self-consistency).

The vibrational entropy was estimated for the δ - and γ -phases by adding a temperature-dependent term to the free energy (quasiharmonic approximation⁴⁷). The phonon density of states was calculated from the dynamical matrices obtained by DFPT. We neglect thermal expansion; that is, the phonon frequencies used for the calculation of the vibrational entropy are computed once for all at the zero temperature ground state. The densities of states are shown in Figure S6, and the corresponding vibrational entropies used for the free energies for the two phases are shown in Figure S7. The free energy of the γ -phase is always lower than that of the δ -phase.

Many-Body Perturbation Theory for Electronic Properties (scGW). DFT calculations, as a starting point for perturbation theory, were performed using the plane-wave projector-augmented wave (PAW) implementation available in the VASP software.^{64–66} The generalized gradient approximation (GGA-PBE) was used for the exchange-correlation functional.^{67,68} The spin-orbit coupling, mandatory for achieving relevant electronic structure calculations on lead-based perovskites,^{52–54} was used as implemented in the VASP code and detailed in ref 69. To avoid the underestimation of the electronic band gaps of semilocal DFT with SOC,^{52–54} we used quasiparticle self-consistent GW theory^{70,71} (scGW) as implemented in the VASP code.^{72–74} We used the GGA-PBE relativistic pseudopotentials available in VASP with Cs [5s²5p⁶6s¹], Pb [6s²6p²5d¹⁰], and I [5s²5p⁵]. A plane-wave basis set with an energy cutoff of 500 eV was used to expand the electronic wave functions. The reciprocal space integration is performed over a 2 × 2 × 2, 2 × 2 × 2, and 4 × 4 × 4 Monkhorst–Pack grid⁷⁵ for the γ -, β -, and α -phases, respectively. To reach energy convergence, we imposed a tolerance factor of 5 × 10⁻⁷ eV on the residual potential.

Tight-Binding Model. The sp³ TB model presented here has been adapted from the one recently developed for the hybrid organic perovskites MAPbI₃ in its cubic phase.³³ It is based on a set of 16 basis functions when SOC is disregarded and 32 basis functions when SOC is included. For a cubic AMX₃ halide perovskite, it consists of one s and three p orbitals for the M atom, and the same holds for X atoms. No basis function is needed for the A cation, and the model includes nearest neighbor interactions between M and X atoms. The nine parameters to consider (without SOC) are (i) four matrix elements related to M and X atoms, E_{sM} , E_{pM} , E_{sX} , and E_{pX} , and (ii) five matrix elements referring to the atomic overlap integrals, V_{ss} , V_{sMpX} , V_{pMsX} , V_{pp} , and V_{ppx} . With SOC, the degenerate p states split into $J = 1/2$ and $3/2$ bands, and this splitting is taken into account for both the metal (Δ_{s0M}) and halogens (Δ_{s0X}). To model the perovskite black phases of CsPbI₃, we used the parameters determined for MAPbI₃³³ without further refinement. To address the noncubic structures having different metal–halogen bond lengths, we adapted this TB model considering the expression for the matrix elements reported in the seminal work by Slater and Koster⁵⁰ and an additional d^{-2} Harrison law,⁴⁹ without the need for any additional parameter (for instance, no adjustable prefactor).

ASSOCIATED CONTENT

Supporting Information

The Supporting Information is available free of charge on the ACS Publications website at DOI: 10.1021/acsnano.8b00267.

Additional information about the temperature-dependent XRD measurements (refined patterns of mixed phases); detailed structures; study of the influence of SOC on the energy landscape; results on the phase competition when considering alternative exchange-correlation functionals

(PBE, HSE) and SOC; and details on the vibrational entropies (PDF)

Crystallographic information files (ZIP)

AUTHOR INFORMATION

Corresponding Authors

*E-mail: arthur.marronnier@polytechnique.edu.

*E-mail: konstantinos.stoumpos@northwestern.edu.

*E-mail: jacky.even@insa-rennes.fr.

ORCID

Arthur Marronnier: 0000-0003-0984-1140

Guido Roma: 0000-0002-9779-4868

Soline Boyer-Richard: 0000-0002-0880-0999

Laurent Pedesseau: 0000-0001-9414-8644

Claudine Katan: 0000-0002-2017-5823

Constantinos C. Stoumpos: 0000-0001-8396-9578

Mercouri G. Kanatzidis: 0000-0003-2037-4168

Jacky Even: 0000-0002-4607-3390

Notes

The authors declare no competing financial interest.

ACKNOWLEDGMENTS

The PhD project of A.M. is funded by the Graduate School of École des Ponts ParisTech and the French Department of Energy (MTES). HPC resources of TGCC and CINES were used through allocation 2017090642 and x20170906724 GENCI projects. The work at FOTON and ISCR was funded by the European Union's Horizon 2020 program, through a FET Open research and innovation action under the Grant Agreement No. 687008. This work was supported by the U.S. Department of Energy, Office of Science, Basic Energy Sciences under Award No. DE-SC-0012541 (sample synthesis, X-ray synchrotron, radiation, and structural analysis). Use of the Advanced Photon Source at Argonne National Laboratory was supported by the U.S. Department of Energy, Office of Science, Office of Basic Energy Sciences, under Contract No. DE-AC02-06CH11357. The authors would also like to thank A. Garcia Barker for her editing and proofreading contributions.

REFERENCES

- (1) Kojima, A.; Teshima, K.; Shirai, Y.; Miyasaka, T. Organometal Halide Perovskites as Visible-Light Sensitizers for Photovoltaic Cells. *J. Am. Chem. Soc.* **2009**, *131*, 6050–6051.
- (2) Best research-cell efficiencies; <https://www.nrel.gov/pv/assets/images/efficiency-chart.png> (accessed Nov 7, 2017).
- (3) Wang, D.; Wright, M.; Elumalai, N. K.; Uddin, A. Stability of Perovskite Solar Cells. *Sol. Energy Mater. Sol. Cells* **2016**, *147*, 255–275.
- (4) Saliba, M.; Matsui, T.; Seo, J.-Y.; Domanski, K.; Correa-Baena, J.-P.; Nazeeruddin, M. K.; Zakeeruddin, S. M.; Tress, W.; Abate, A.; Hagfeldt, A.; Grätzel, M. Cesium-containing Triple Cation Perovskite Solar Cells: Improved Stability, Reproducibility and High Efficiency. *Energy Environ. Sci.* **2016**, *9*, 1989–1997.
- (5) Tsai, H.; Nie, W.; Blancon, J.-C.; Stoumpos, C. C.; Asadpour, R.; Harutyunyan, B.; Neukirch, A. J.; Verduzco, R.; Crochet, J. J.; Tretiak, S.; Pedesseau, L.; Even, J.; Alam, M. A.; Gupta, G.; Lou, J.; Ajayan, P. M.; Bedzyk, M. J.; Kanatzidis, M. G.; Mohite, A. D. High-efficiency Two-dimensional Ruddlesden-Popper Perovskite Solar Cells. *Nature* **2016**, *536*, 312–316.
- (6) Sanehira, E. M.; Marshall, A. R.; Christians, J. A.; Harvey, S. P.; Ciesielski, P. N.; Wheeler, L. M.; Schulz, P.; Lin, L. Y.; Beard, M. C.; Luther, J. M. Enhanced Mobility CsPbI₃ Quantum Dot Arrays for

Record-efficiency, High-voltage Photovoltaic Cells. *Sci. Adv.* **2017**, *3*, ea04204.

(7) Eperon, G. E.; Paterno, G. M.; Sutton, R. J.; Zampetti, A.; Haghighirad, A. A.; Cacialli, F.; Snaith, H. J. Inorganic Caesium Lead Iodide Perovskite Solar Cells. *J. Mater. Chem. A* **2015**, *3*, 19688–19695.

(8) Swarnkar, A.; Marshall, A. R.; Sanhira, E. M.; Chernomordik, B. D.; Moore, D. T.; Christians, J. A.; Chakrabarti, T.; Luther, J. M. Quantum Dot-induced Phase Stabilization of α -CsPbI₃ Perovskite for High-efficiency Photovoltaics. *Science* **2016**, *354*, 92–95.

(9) Zhang, T.; Dar, M. I.; Li, G.; Xu, F.; Guo, N.; Grätzel, M.; Zhao, Y. Bication Lead Iodide 2D Perovskite Component to Stabilize Inorganic α -CsPbI₃ Perovskite Phase for High-efficiency Solar Cells. *Sci. Adv.* **2017**, *3*, e1700841.

(10) McMeekin, D. P.; Sadoughi, G.; Rehman, W.; Eperon, G. E.; Saliba, M.; Hörlantner, M. T.; Haghighirad, A.; Sakai, N.; Korte, L.; Rech, B.; Johnston, M. B.; Herz, L. M.; Snaith, H. J. A Mixed-cation Lead Mixed-halide Perovskite Absorber for Tandem Solar Cells. *Science* **2016**, *351*, 151–155.

(11) Yamada, K.; Funabiki, S.; Horimoto, H.; Matsui, T.; Okuda, T.; Ichiba, S. Structural Phase Transitions of the Polymorphs of CsSnI₃ by means of Rietveld Analysis of the X-Ray Diffraction. *Chem. Lett.* **1991**, *20*, 801–804.

(12) Chung, I.; Song, J.-H.; Im, J.; Androulakis, J.; Malliakas, C. D.; Li, H.; Freeman, A. J.; Kenney, J. T.; Kanatzidis, M. G. CsSnI₃: Semiconductor or Metal? High Electrical Conductivity and Strong Near-infrared Photoluminescence from a Single Material. High Hole Mobility and Phase-transitions. *J. Am. Chem. Soc.* **2012**, *134*, 8579–8587.

(13) Im, J.-H.; Lee, C.-R.; Lee, J.-W.; Park, S.-W.; Park, N.-G. 6.5% Efficient Perovskite Quantum-dot-Sensitized Solar Cell. *Nanoscale* **2011**, *3*, 4088–4093.

(14) Chung, I.; Lee, B.; He, J.; Chang, R. P.; Kanatzidis, M. G. All-solid-state Dye-sensitized Solar Cells with High Efficiency. *Nature* **2012**, *485*, 486.

(15) Etgar, L.; Gao, P.; Xue, Z.; Peng, Q.; Chandiran, A. K.; Liu, B.; Nazeeruddin, M. K.; Grätzel, M. Mesoscopic CH₃NH₃PbI₃/TiO₂ Heterojunction Solar Cells. *J. Am. Chem. Soc.* **2012**, *134*, 17396–17399.

(16) Lee, M. M.; Teuscher, J.; Miyasaka, T.; Murakami, T. N.; Snaith, H. J. Efficient Hybrid Solar Cells based on Meso-superstructured Organometal Halide Perovskites. *Science* **2012**, *338*, 643–647.

(17) Trots, D.; Myagkota, S. High-temperature Structural Evolution of Caesium and Rubidium Triiodoplumbates. *J. Phys. Chem. Solids* **2008**, *69*, 2520–2526.

(18) Stoumpos, C. C.; Mao, L.; Malliakas, C. D.; Kanatzidis, M. G. Structure-Band Gap Relationships in Hexagonal Polytypes and Low-Dimensional Structures of Hybrid Tin Iodide Perovskites. *Inorg. Chem.* **2017**, *56*, 56–73.

(19) Stoumpos, C. C.; Malliakas, C. D.; Kanatzidis, M. G. Semiconducting Tin and Lead Iodide Perovskites with Organic Cations: Phase Transitions, High Mobilities, and Near-Infrared Photoluminescent Properties. *Inorg. Chem.* **2013**, *52*, 9019–9038.

(20) Möller, C. K. The Structure of Caesium Plumbo Iodide CsPbI₃. *Mat. Fys. Medd. Dan. Vid. Sels.* **1959**, *32*, 1.

(21) Stoumpos, C. C.; Kanatzidis, M. G. The Renaissance of Halide Perovskites and Their Evolution as Emerging Semiconductors. *Acc. Chem. Res.* **2015**, *48*, 2791–2802.

(22) Fujii, Y.; Hoshino, S.; Yamada, Y.; Shirane, G. Neutron-scattering Study on Phase Transitions of CsPbCl₃. *Phys. Rev. B* **1974**, *9*, 4549–4559.

(23) da Silva, E. L.; Skelton, J. M.; Parker, S. C.; Walsh, A. Phase Stability and Transformations in the Halide Perovskite CsSnI₃. *Phys. Rev. B: Condens. Matter Mater. Phys.* **2015**, *91*, 144107.

(24) Patrick, C. E.; Jacobsen, K. W.; Thygesen, K. S. Anharmonic Stabilization and Band Gap Renormalization in the Perovskite CsSnI₃. *Phys. Rev. B: Condens. Matter Mater. Phys.* **2015**, *92*, 201205.

(25) Brgoch, J.; Lehner, A. J.; Chabynyc, M.; Seshadri, R. Ab Initio Calculations of Band Gaps and Absolute Band Positions of

Polymorphs of RbPbI₃ and CsPbI₃: Implications for Main-Group Halide Perovskite Photovoltaics. *J. Phys. Chem. C* **2014**, *118*, 27721–27727.

(26) Marronnier, A.; Lee, H.; Geffroy, B.; Even, J.; Bonnassieux, Y.; Roma, G. Structural Instabilities Related to Highly Anharmonic Phonons in Halide Perovskites. *J. Phys. Chem. Lett.* **2017**, *8*, 2659–2665.

(27) Whalley, L. D.; Skelton, J. M.; Frost, J. M.; Walsh, A. Phonon Anharmonicity, Lifetimes, and Thermal Transport in CH₃NH₃PbI₃ from Many-body Perturbation Theory. *Phys. Rev. B: Condens. Matter Mater. Phys.* **2016**, *94*, 220301.

(28) Beecher, A. N.; Semonin, O. E.; Skelton, J. M.; Frost, J. M.; Terban, M. W.; Zhai, H.; Alatas, A.; Owen, J. S.; Walsh, A.; Billinge, S. J. L. Direct Observation of Dynamic Symmetry Breaking above Room Temperature in Methylammonium Lead Iodide Perovskite. *ACS Energy Lett.* **2016**, *1*, 880–887.

(29) Amat, A.; Mosconi, E.; Ronca, E.; Quarti, C.; Umari, P.; Nazeeruddin, M. K.; Grätzel, M.; De Angelis, F. Cation-Induced Band-Gap Tuning in Organohalide Perovskites: Interplay of Spin-Orbit Coupling and Octahedra Tilting. *Nano Lett.* **2014**, *14*, 3608–3616.

(30) Filip, M.; Eperon, G.; Snaith, H.; Gustino, F. Steric Engineering of Metal-halide Perovskites with Tunable Optical Band Gaps. *Nat. Commun.* **2014**, *5*, 5757.

(31) Yang, J.-Y.; Hu, M. Temperature Induced Large Broadening and Blueshift in the Electronic Band Structure and Optical Absorption of Methylammonium Lead Iodide Perovskite. *J. Phys. Chem. Lett.* **2017**, *8*, 3720–3725.

(32) Saidi, W. A.; Poncé, S.; Monserrat, B. Temperature Dependence of the Energy Levels of Methylammonium Lead Iodide Perovskite from First-Principles. *J. Phys. Chem. Lett.* **2016**, *7*, 5247–5252.

(33) Boyer-Richard, S.; Katan, C.; Traoré, B.; Scholz, R.; Jancu, J.-M.; Even, J. Symmetry-Based Tight Binding Modeling of Halide Perovskite Semiconductors. *J. Phys. Chem. Lett.* **2016**, *7*, 3833–3840.

(34) Möller, C. K. The Structure of Perovskite-like Caesium Plumbo Trihalides. *Mat. Fys. Medd. Dan. Vid. Sels.* **1959**, *32*, No 2.

(35) Trots, D. M.; Myagkota, S. V.; Voloshinovskii, A. S. Crystal Structure and Thermal Expansion of CsPbBr₃ in the range of 12–300K; http://photon-science.desy.de/annual_report/files/2009/2009612.pdf, 2009.

(36) Stoumpos, C. C.; Malliakas, C. D.; Peters, J. A.; Liu, Z.; Sebastian, M.; Im, J.; Chasapis, T. C.; Wibowo, A. C.; Chung, D. Y.; Freeman, A. J.; Wessels, B. W.; Kanatzidis, M. G. Crystal Growth of the Perovskite Semiconductor CsPbBr₃: A New Material for High-energy Radiation Detection. *Cryst. Growth Des.* **2013**, *13*, 2722–2727.

(37) Mori, M.; Saito, H. An X-ray Study of Successive Phase Transitions in CsSnBr₃. *J. Phys. C: Solid State Phys.* **1986**, *19*, 2391.

(38) Fabini, D. H.; Laurita, G.; Bechtel, J. S.; Stoumpos, C. C.; Evans, H. A.; Kontos, A. G.; Raptis, Y. S.; Falaras, P.; van der Ven, A.; Kanatzidis, M. G.; Seshadri, R. Dynamic Stereochemical Activity of the Sn²⁺ Lone Pair in Perovskite CsSnBr₃. *J. Am. Chem. Soc.* **2016**, *138*, 11820–11832.

(39) Kontos, A. G.; Kaltzoglou, A.; Afranis, M.; McCall, K. M.; Stoumpos, C. C.; Kanatzidis, M. Bandgap Widening and Persistent Near-IR Photoluminescence at High Temperature in AsSnI₃ Perovskites (A = Cs⁺, CH₃NH₃⁺ and NH₂–CH=NH₂⁺). Manuscript in preparation.

(40) Božin, E. S.; Malliakas, C. D.; Souvatzis, P.; Proffen, T.; Spaldin, N. A.; Kanatzidis, M. G.; Billinge, S. J. L. Entropically Stabilized Local Dipole Formation in Lead Chalcogenides. *Science* **2010**, *330*, 1660–1663.

(41) Laurita, G.; Fabini, D. H.; Stoumpos, C. C.; Kanatzidis, M. G.; Seshadri, R. Chemical Tuning of Dynamic Cation off-centering in the Cubic Phases of Hybrid Tin and Lead Halide Perovskites. *Chem. Sci.* **2017**, *8*, 5628–5635.

(42) Pedesseau, L.; Saporì, D.; Traoré, B.; Robles, R.; Fang, H.-H.; Loi, M. A.; Tsai, H.; Nie, W.; Blancon, J.-C.; Neukirch, A.; Tretiak, S.; Mohite, A. D.; Katan, C.; Even, J.; Kepenekian, M. Advances and Promises of Layered Halide Hybrid Perovskite Semiconductors. *ACS Nano* **2016**, *10*, 9776–9786.

- (43) Even, J.; Carignano, M.; Katan, C. Molecular Disorder and Translation/Rotation Coupling in the Plastic Crystal Phase of Hybrid Perovskites. *Nanoscale* **2016**, *8*, 6222–6236.
- (44) Létoublon, A.; Paofai, S.; Rufflé, B.; Bourges, P.; Hehlen, B.; Michel, T.; Ecolivet, C.; Durand, O.; Cordier, S.; Katan, C.; Even, J. Elastic Constants, Optical Phonons, and Molecular Relaxations in the High Temperature Plastic Phase of the $\text{CH}_3\text{NH}_3\text{PbBr}_3$ Hybrid Perovskite. *J. Phys. Chem. Lett.* **2016**, *7*, 3776–3784.
- (45) Cowley, R. Structural Phase Transitions I. Landau Theory. *Adv. Phys.* **1980**, *29*, 1–110.
- (46) Rousseau, B.; Bergara, A. Giant Anharmonicity Suppresses Superconductivity in AlH_3 under Pressure. *Phys. Rev. B: Condens. Matter Mater. Phys.* **2010**, *82*, 104504.
- (47) Baroni, S.; de Gironcoli, S.; Dal Corso, A.; Giannozzi, P. Phonons and Related Crystal Properties from Density-Functional Perturbation Theory. *Rev. Mod. Phys.* **2001**, *73*, 515–562.
- (48) Burfoot, J. C. Entropy of an Order-Disorder Transition. *J. Phys., Colloq.* **1972**, *33*, C2-79–C2-81 Colloque C2.
- (49) Harrison, J. W.; Hauser, J. R. Theoretical Calculations of Electron Mobility in Ternary III-V Compounds. *J. Appl. Phys.* **1976**, *47*, 292–300.
- (50) Slater, J. C.; Koster, G. F. Simplified LCAO Method for the Periodic Potential Problem. *Phys. Rev.* **1954**, *94*, 1498–1524.
- (51) Eperon, G. E.; Stranks, S. D.; Menelaou, C.; Johnston, M. B.; Herz, L. M.; Snaith, H. J. Formamidinium Lead Trihalide: a Broadly Tunable Perovskite for Efficient Planar Heterojunction Solar Cells. *Energy Environ. Sci.* **2014**, *7*, 982.
- (52) Katan, C.; Pedesseau, L.; Kepenekian, M.; Rolland, A.; Even, J. Interplay of Spin-orbit Coupling and Lattice Distortion in Metal Substituted 3D Tri-chloride Hybrid Perovskites. *J. Mater. Chem. A* **2015**, *3*, 9232–9240.
- (53) Even, J.; Pedesseau, L.; Jancu, J.-M.; Katan, C. DFT and k-p Modelling of the Phase Transitions of Lead and Tin Halide Perovskites for Photovoltaic Cells. *Phys. Status Solidi RRL* **2014**, *8*, 31–35.
- (54) Even, J.; Pedesseau, L.; Jancu, J.-M.; Katan, C. Importance of Spin-Orbit Coupling in Hybrid Organic/Inorganic Perovskites for Photovoltaic Applications. *J. Phys. Chem. Lett.* **2013**, *4*, 2999–3005.
- (55) Marronnier, A.; Lee, H.; Lee, H.; Kim, M.; Eypert, C.; Gaston, J.-P.; Roma, G.; Tondelier, D.; Geffroy, B.; Bonnassieux, Y. Electrical and Optical Degradation Study of Methylammonium-based Perovskite Materials under Ambient Conditions. *Sol. Energy Mater. Sol. Cells* **2018**, *178*, 179–185.
- (56) Lee, P. L.; Shu, D.; Ramanathan, M.; Preissner, C.; Wang, J.; Beno, M. A.; von Dreile, R. B.; Ribaud, L.; Kurtz, C.; Antao, S. M.; Jiao, X.; Toby, B. H. A Twelve-analyzer Detector System for High-resolution Powder Diffraction. *J. Synchrotron Radiat.* **2008**, *15*, 427–432.
- (57) Dalesio, L. R.; Hill, J. O.; Kraimer, M.; Lewis, S.; Murray, D.; Hunt, S.; Watson, W.; Clausen, M.; Dalesio, J. *Nucl. Instrum. Methods Phys. Res., Sect. A* **1994**, *352*, 179.
- (58) Petříček, V.; Dušek, M.; Palatinus, L. Crystallographic Computing System JANA2006: General features. *Z. Kristallogr. - Cryst. Mater.* **2014**, *229*, 1737.
- (59) Woodward, P. M. Octahedral Tilting in Perovskites. I. Geometrical Considerations. *Acta Crystallogr., Sect. B: Struct. Sci.* **1997**, *53*, 32–43.
- (60) Hohenberg, P.; Kohn, W. Inhomogeneous Electron Gas. *Phys. Rev.* **1964**, *136*, B864–B871.
- (61) Kohn, W.; Sham, L. J. Self-Consistent Equations Including Exchange and Correlation Effects. *Phys. Rev.* **1965**, *140*, A1133–A1138.
- (62) Giannozzi, P.; Baroni, S.; Bonini, N.; Calandra, M.; Car, R.; Cavazzoni, C.; Ceresoli, D.; Chiarotti, G. L.; Cococcioni, M.; Dabo, I.; Dal Corso, A.; de Gironcoli, S.; Fabris, S.; Fratesi, G.; Gebauer, R.; Gerstmann, U.; Gougoussis, C.; Kokalj, A.; Lazzeri, M.; Martin-Samos, L.; et al. Quantum Espresso: a Modular and Open-source Software Project for Quantum Simulations of Materials. *J. Phys.: Condens. Matter* **2009**, *21*, 395502.
- (63) Monkhorst, H. J.; Pack, J. D. Special Points for Brillouin-zone Integrations. *Phys. Rev. B* **1976**, *13*, 5188–5192.
- (64) Kresse, G.; Furthmüller, J. Efficient Iterative Schemes for Ab Initio Total-energy Calculations using a Plane-wave Basis Set. *Phys. Rev. B: Condens. Matter Mater. Phys.* **1996**, *54*, 11169–11186.
- (65) Kresse, G.; Furthmüller, J. Efficiency of Ab-initio Total Energy Calculations for Metals and Semiconductors using a Plane-wave Basis set. *Comput. Mater. Sci.* **1996**, *6*, 15–50.
- (66) Shishkin, M.; Kresse, G. Implementation and Performance of the Frequency-dependent GW Method within the PAW Framework. *Phys. Rev. B: Condens. Matter Mater. Phys.* **2006**, *74*, 035101.
- (67) Perdew, J. P.; Burke, K.; Ernzerhof, M. Generalized Gradient Approximation Made Simple. *Phys. Rev. Lett.* **1996**, *77*, 3865–3868.
- (68) Perdew, J. P.; Burke, K.; Ernzerhof, M. Generalized Gradient Approximation Made Simple [Phys. Rev. Lett. 77, 3865 (1996)]. *Phys. Rev. Lett.* **1997**, *78*, 1396–1396.
- (69) Steiner, S.; Khmelevskiy, S.; Marsmann, M.; Kresse, G. Calculation of the Magnetic Anisotropy with Projected-augmented-wave Methodology and the Case Study of Disordered $\text{Fe}_{1-x}\text{Co}_x$ Alloys. *Phys. Rev. B: Condens. Matter Mater. Phys.* **2016**, *93*, 224425.
- (70) Hedin, L. New Method for Calculating the One-Particle Green's Function with Application to the Electron-Gas Problem. *Phys. Rev.* **1965**, *139*, A796–A823.
- (71) van Schilfgaarde, M.; Kotani, T.; Faleev, S. Quasiparticle Self-Consistent GW Theory. *Phys. Rev. Lett.* **2006**, *96*, 226402.
- (72) Shishkin, M.; Kresse, G. Self-consistent GW Calculations for Semiconductors and Insulators. *Phys. Rev. B: Condens. Matter Mater. Phys.* **2007**, *75*, 235102.
- (73) Fuchs, F.; Furthmüller, J.; Bechstedt, F.; Shishkin, M.; Kresse, G. Quasiparticle Band Structure Based on a Generalized Kohn-Sham Scheme. *Phys. Rev. B: Condens. Matter Mater. Phys.* **2007**, *76*, 115109.
- (74) Shishkin, M.; Marsman, M.; Kresse, G. Accurate Quasiparticle Spectra from Self-Consistent GW Calculations with Vertex Corrections. *Phys. Rev. Lett.* **2007**, *99*, 246403.
- (75) Pack, J. D.; Monkhorst, H. J. "Special Points for Brillouin-zone Integrations"-a reply. *Phys. Rev. B* **1977**, *16*, 1748–1749.

Supporting Information:

Anharmonicity and Disorder in the Black Phases of Cesium Lead Iodide used for Stable Inorganic Perovskite Solar Cells

Arthur Marronnier,^{*,†} Guido Roma,[‡] Soline Boyer-Richard,[¶] Laurent Pedesseau,[¶]
Jean-Marc Jancu,[¶] Yvan Bonnassieux,[†] Claudine Katan,[§] Constantinos C.
Stoumpos,^{*,||} Mercouri G. Kanatzidis,^{||} and Jacky Even^{*,¶}

[†]*LPICM, CNRS, Ecole Polytechnique, Université Paris-Saclay, 91128 Palaiseau, France*

[‡]*DEN - Service de Recherches de Métallurgie Physique, CEA, Université Paris-Saclay,
91191 Gif sur Yvette, France*

[¶]*Univ Rennes, INSA Rennes, CNRS, Institut FOTON — UMR 6082, F-35000 Rennes,
France*

[§]*Univ Rennes, ENSCR, INSA Rennes, CNRS, ISCR (Institut des Sciences Chimiques de
Rennes) – UMR 6226, F-35000 Rennes, France*

^{||}*Department of Chemistry and Argonne-Northwestern Solar Energy Research (ANSER)
Center, Northwestern University, Evanston, Illinois 60208, United States*

E-mail: arthur.marronnier@polytechnique.edu; konstantinos.stoumpos@northwestern.edu;
jacky.even@insa-rennes.fr

High-resolution Temperature-dependent X-ray Diffraction

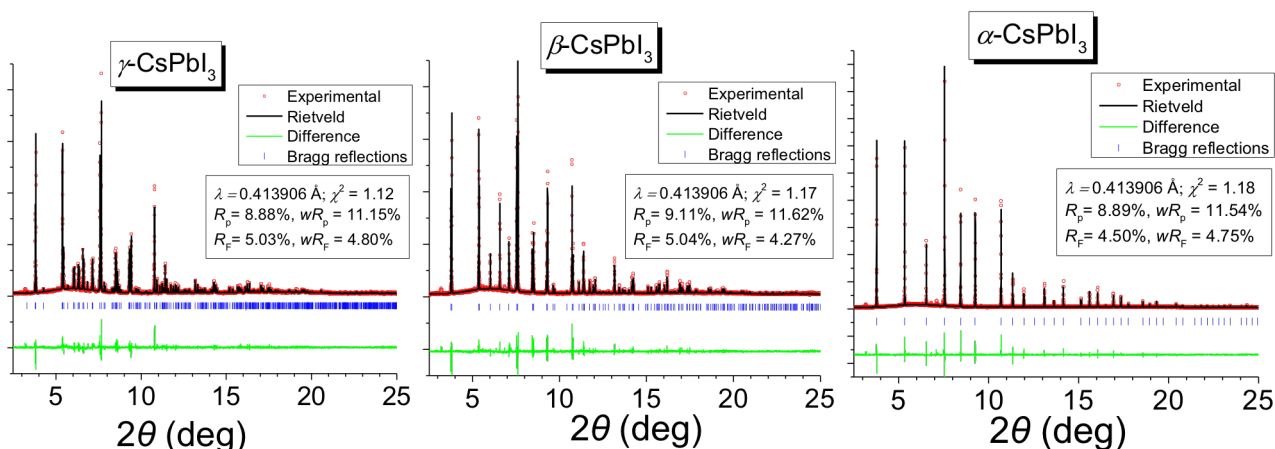


Figure S1: Refined patterns of the black phases of $CsPbI_3$.

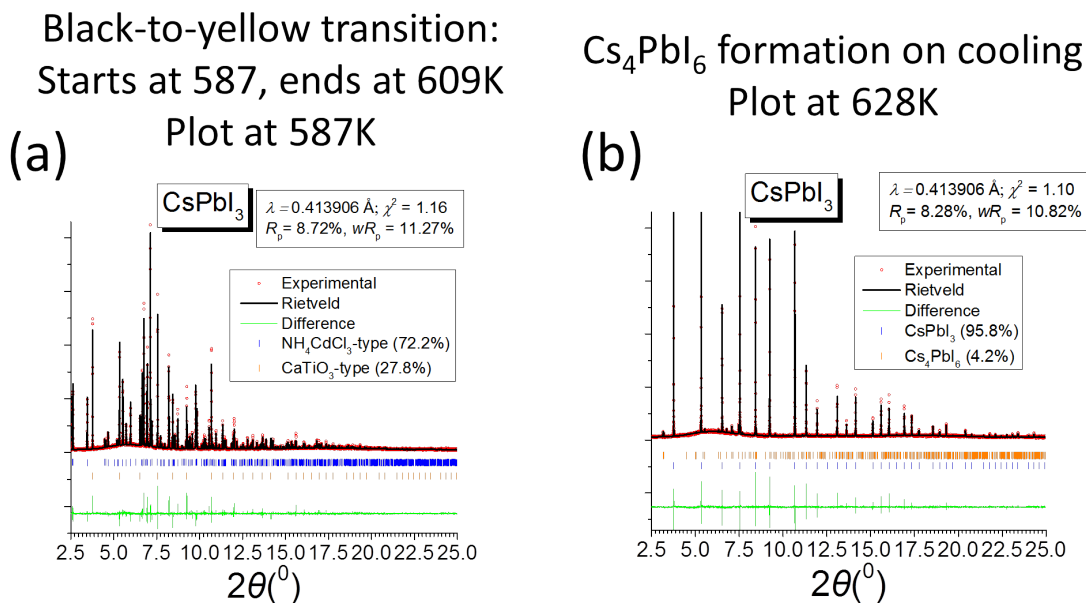


Figure S2: Refined patterns of mixed phases in the Cs-Pb-I system. (a) The diffraction pattern during the conversion of δ to α - $CsPbI_3$ spanning a 30K range where the two phases coexist. (b) Formation of an additional non-perovskitic phase upon cooling, identified as Cs_4PbI_6 using the lattice parameters of the known Cs_4PbBr_6 compound as a starting point.

The black phase can be undercooled to room temperature as reported by Møller¹ who claimed that it could be maintained for several days. The present experiment deals with

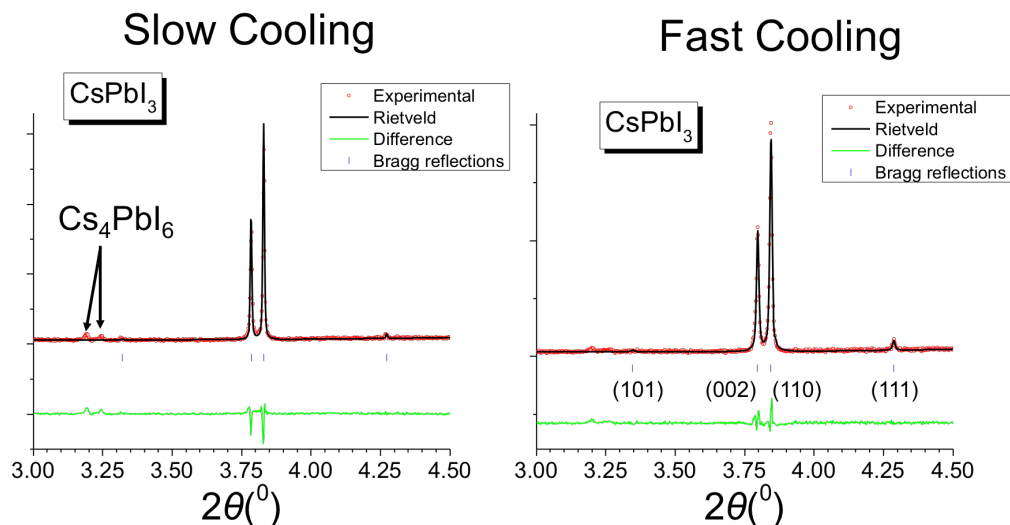


Figure S3: Influence of the cooling rate on the phase composition of the final pattern. For the slow-cooling experiment, the yellow phase was heated to 750 K and the furnace was shut down to allow natural cooling of the sample (without collecting data during cooling). The result for slow cooling is consistent with Møller’s report of a second phase¹ (left unidentified by Møller; identified here as Cs_4PbI_6). The fast cooling experiment corresponds to the main one described in the manuscript.

the correct determination of the structural parameters which were not reported confidently by Ref.¹ due to poor data quality. Therefore, the phase transition occurs irrespective of the cooling rate. In a different experiment, which was performed before the acquisition of data reported in the manuscript, the yellow phase was heated to 750 K and the furnace was shut down to allow natural cooling of the sample (without collecting data during cooling). A final pattern collected at room temperature after cooling revealed only the presence of the black γ -phase of $CsPbI_3$. The only difference between the slow cooled sample (presented in the paper) and the fast cooled one was the amount of second phase which was substantially larger for the slow cooled sample ($\approx 5\%$) vs the fast cooled one ($\approx 1\%$), see figure S3. This result is consistent with Møller’s report of a second phase (left unidentified by Møller; identified here as Cs_4PbI_6) evolution on prolonged heating.

Experimental structures

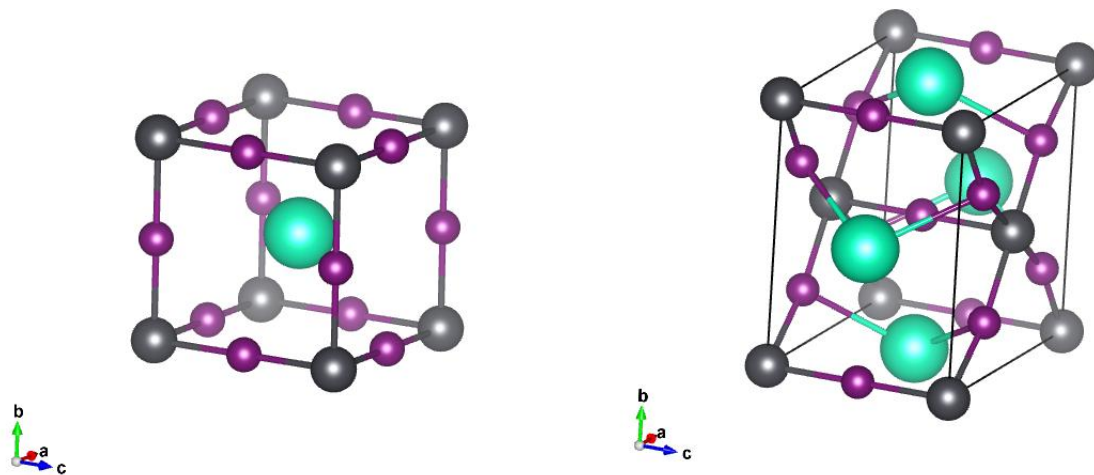
The detailed experimental crystal structures of phases α (645K), β (510K) and γ (325K), of respectively space groups $Pm\bar{3}m$, $P4/mbm$ and $Pbnm$ are shown figures S4.

Influence of spin-orbit coupling on the double well

Spin-Orbit Coupling (SOC) is known to significantly affect the electronic band structure of lead halide perovskites.^{2,3} Regarding structural parameters, it has been shown earlier that the impact of SOC is much lower.⁴ In order to verify that this also holds true for the tetragonal phase presented in this work, we have performed calculations with SOC using the PWSCF code of the QE package, using fully relativistic pseudopotentials obtained with the earlier 0.2.2 version of the pseudopotential library.⁵ The relativistic pseudopotentials used have the same number of valence electrons as the scalar relativistic ones used for calculations without SOC (i.e., 9 for Cs, 7 for I, and 14 valence electrons for Pb). Our calculations suggest that its influence on the complex energy landscape of CsPbI_3 , which is the subject of this paper, is not crucial. Figure S5 shows that the energy landscape computed for the tetragonal phase of CsPbI_3 undergoes minor changes (barrier of 2.7 meV instead of 3.1) when taking SOC into account. We further checked that the energy difference between the δ - and the γ -phases is not influenced by SOC (see next section).

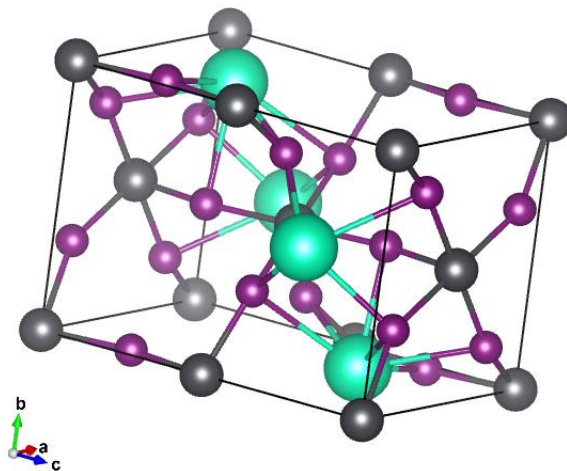
Phase competition between the δ and γ -phases

In the main manuscript, we found out that, surprisingly, the γ -phase has a lower total energy than the δ -phase. Here we give proof that this conclusion is not altered by the level of theory, considering alternative exchange-correlation functionals (PBE or HSE instead of LDA) and SOC. Computed energies are reported in table S1). PBE and HSE energies were obtained with the VASP code. HSE results were obtained with reduced k-point sampling ($4\times 4\times 4$



(a) α -phase of $CsPbI_3$.

(b) β -phase of $CsPbI_3$ with 2 perovskite structures per unit cell.



(c) γ -phase of $CsPbI_3$ with 4 perovskite structures per unit cell.

Figure S4: **Crystal structures of $CsPbI_3$ obtained from XRD.** The green, gray and purple atoms respectively denote Cs, Pb and I.

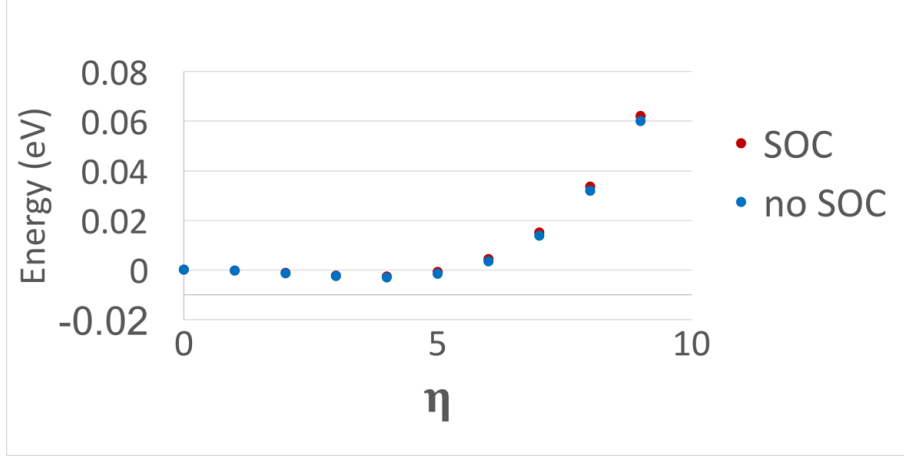


Figure S5: Energy profile for the tetragonal phase of $CsPbI_3$ along soft phonon modes computed with and without SOC.

Monkhorst-Pack mesh for the α -phase and equivalent \mathbf{k} -point density in the BZ for the other phases). We checked with PBE that this reduced sampling has negligible effects on these energy differences.

Table S1: Energies of ground state $CsPbI_3$ phases (meV per formula unit of 5 atoms), as calculated for different exchange-correlation functionals and with or without SOC. The experimental temperature at which they appear during cooling is given for comparison.

Phase	Experimental Temperature (K)	LDA	LDA+SOC	PBE	HSE
δ	325	34	44	28	56
γ	450	0	0	0	0
β	510	54	47	24	30
α	645	220	190	108	76

Vibrational Entropies

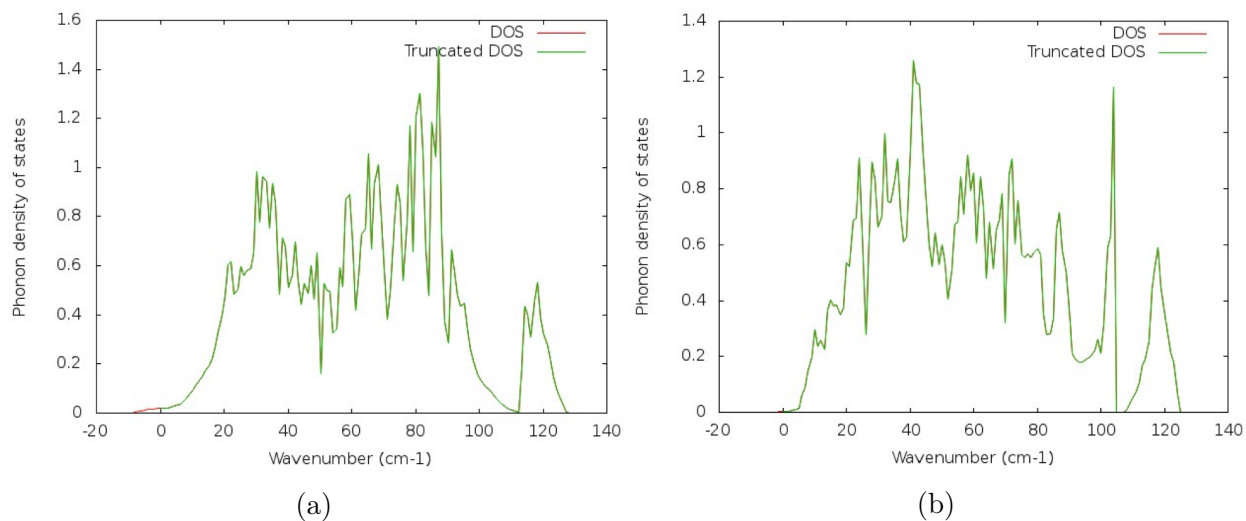


Figure S6: **Vibrational density of states for the orthorhombic δ -phase (a) and γ -phase (b) used to compute the vibrational entropies.** We have checked that removing the small remaining density at negative frequencies (truncated DOS) has negligible influence on the vibrational entropy.

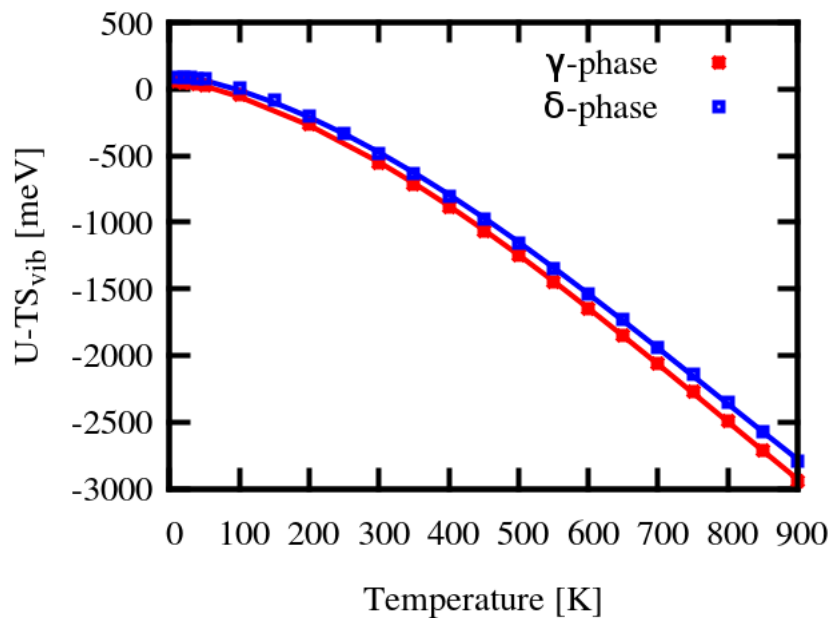


Figure S7: **Comparison of the free energies of the orthorhombic δ - and γ -phases.** The zero temperature value includes the total (LDA) energy and the vibrational zero-point energy. Lines are guides for the eye.

References

- (1) Moeller, C. K. The Structure of Caesium Plumbo Iodide CsPbI_3 . *Mat. Fys. Medd . Dan . Vid. Sels.* **1959**, *32*.
- (2) Even, J.; Pedesseau, L.; Jancu, J.-M.; Katan, C. Importance of Spin–Orbit Coupling in Hybrid Organic/Inorganic Perovskites for Photovoltaic Applications. *The Journal of Physical Chemistry Letters* **2013**, *4*, 2999–3005.
- (3) Even, J.; Pedesseau, L.; Dupertuis, M.-A.; Jancu, J.-M.; Katan, C. Electronic model for self-assembled hybrid organic/perovskite semiconductors: Reverse band edge electronic states ordering and spin-orbit coupling. *Phys. Rev. B* **2012**, *86*, 205301.
- (4) Amat, A.; Mosconi, E.; Ronca, E.; Quarti, C.; Umari, P.; Nazeeruddin, M. K.; Grätzel, M.; De Angelis, F. Cation-Induced Band-Gap Tuning in Organohalide Perovskites: Interplay of Spin–Orbit Coupling and Octahedra Tilting. *Nano Lett.* **2014**, *14*, 3608–3616.
- (5) Dal Corso, A. Pseudopotentials Periodic Table: From H to Pu. *Comput. Mater. Sci.* **2014**, *95*, 337 – 350.

4.4 RASHBA EFFECT AND MOLECULAR DYNAMICS STUDY

In this section, we aim to further analyze the Rashba effect induced by the anharmonic double well and the symmetry breaking for the cubic phase of CsPbI_3 . To summarize, in the previous two sections we have shown, using the frozen phonon method, that the highly symmetric cubic phase can be distorted to form two lower-symmetry structures with a slightly lower total energy (by a few meV). These two structures, that we will call in the following sections A and B (or "minimum" and "minimum_sym"), correspond to the two minimum structures of the double well-instability recalled on figure 4.4.1.

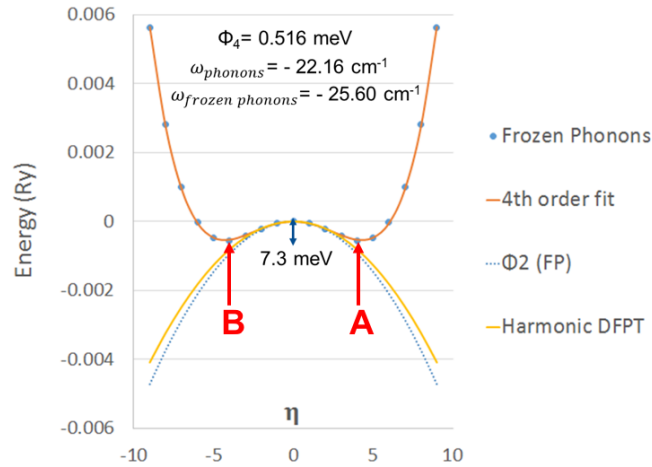


Figure 4.4.1: Potential energy surface from frozen phonon calculations of cubic CsPbI_3 along the eigenvector of the unstable optical phonon at Γ as a function of displacement parameter η . The 3N dimensional displacement needed to reach the new minimum corresponds to around 0.43\AA , including a 0.36\AA displacement for the cesium atom.

Structure A (resp. B) corresponds to the distorted structure obtained by applying a displacement positively (resp. negatively) proportional, corresponding to $\eta > 0$ on figure 4.4.1 (resp. < 0), to the eigenmode represented on figure 4.4.2. Note that with rotational symmetry similar studies could be done on the two other eigenmodes corresponding to distortions along the two remaining Cartesian axes (y and z given our labeling).

The first aim of the study here is to look at the possible formation of "A domains" and "B domains",

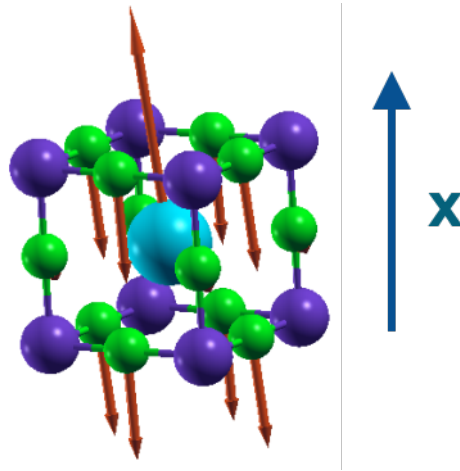


Figure 4.4.2: Displacement eigenvector corresponding to one of the 3 triply degenerated soft phonon modes found at Γ for cubic CsPbI_3 . Its irreducible representation is the infrared-active Γ_4^- representation. The blue, purple and green atoms respectively denote Cs, Pb and I. We chose to label as "x" the axis parallel to which this chosen distortion mostly occurs.

both in space (supercells, subsection 4.4.2) and in time (Car-Parinello molecular dynamics "CPMD", subsection 4.4.3).

Then, we analyze in detail in subsection 4.4.4 the dynamical Rashba effect induced by the time dynamics of the oscillations between structure A and structure B through the highly symmetric structure ($\eta = 0$). This study is done on CPMD trajectories obtained from Ref [15] in the framework of a collaboration with M. Carignano and C. Katan on the one hand, and E. Mosconi and F. De Angelis on the other hand. Here we show only preliminary results of this ongoing study.

4.4.1 METHODS

To be more precise, we will use in the following calculations for structures A and B the structures after relaxation performed with LDA (cutoff of 70 Ry) letting both the lattice parameters and the atomic positions relax (see table 4.1), keeping the cell's angles fixed. These structures are thus slightly orthorhombic (0.1 and 0.3 % distortion, see matrix 4.1). **The total energy of these relaxed structures is 11.3 meV under the maximum, high-symmetry cubic structure. (If the angles are not constrained,**

the energy difference reads 12.1 meV).

$$\begin{bmatrix} 0.9999 & 0 & 0 \\ 0 & 0.9988 & 0 \\ 0 & 0 & 0.9969 \end{bmatrix} \quad (4.1)$$

The deformation between the highly symmetric cubic structure and structure A (relaxed, non cubic, angles unchanged) is illustrated on figure 4.4.3b.

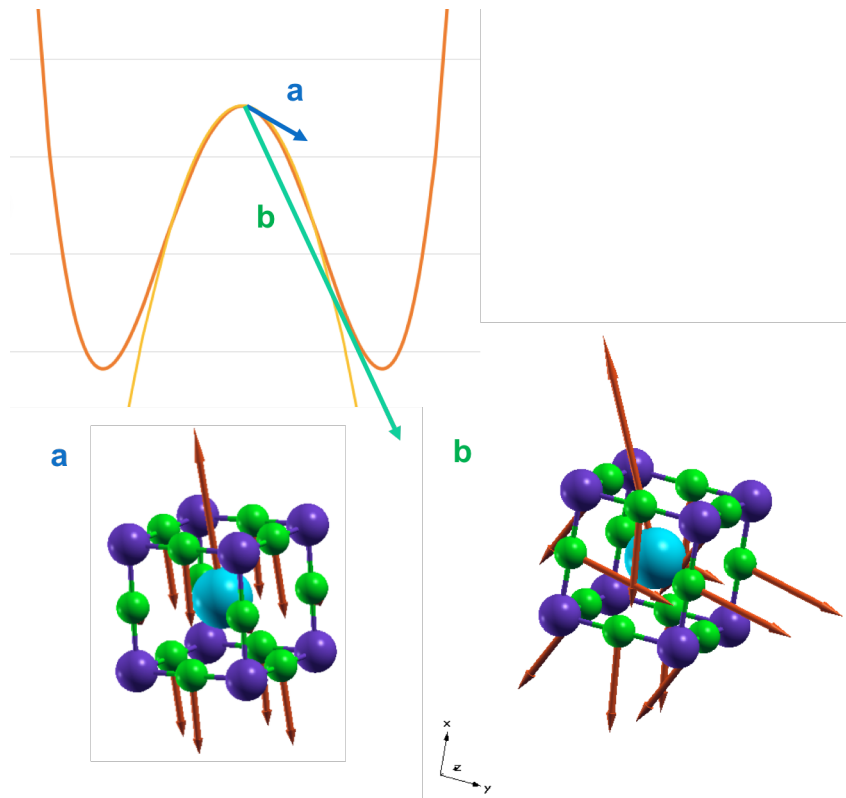


Figure 4.4.3: a. Displacement eigenvector corresponding to the soft phonon mode found at Γ for cubic $CsPbI_3$. Its irreducible representation is the infrared-active Γ_4^- representation. b. Displacement vectors to reach, from the maximum structure, the relaxed non-cubic minimum structure. The blue, purple and green atoms respectively denote Cs, Pb and I.

It is worth noticing that displacement b on figure 4.4.3 seems to correspond mainly to the vectorial sum

Mode number (i)	Frequency (cm^{-1})	a_i^2
1	-22.16	0.87
2	-22.16	0.05
3	-22..16	0.26
4	0.00	0.01
5	0.00	0.00
6	0.00	0.06
7	18.43	0.02
8	18.43	0.16
9	18.43	0.38
10	33.76	0.00
11	33.76	0.00
12	33.76	0.03
13	102.25	0.02
14	102.25	0.00
15	102.25	0.02

Table 4.4.1: Projection of the displacement vector of figure 4.4.3.b onto the basis of the phonon eigenmodes v_i at the maximum structure : $b = \sum_{i=1}^{15} a_i v_i$.

of a displacement along the soft mode (antisymmetric and optical displacement a, mostly along the x axis) and a displacement along the equivalent soft mode for the y axis. In order to further investigate this point, I computed the projection of displacement b on the basis of the 15 phonon eigenmodes at the maximum structure. The results (table 4.4.1) show that the displacement vector is composed mostly of 76% of the softmode along x (optical, $i=1$), 7% of the equivalent soft mode along y (optical, $i=3$), and 17% of two other optical modes.

As for the ab initio methods, electronic-structure calculations were performed within the Density-Functional Theory (DFT) [16, 17] framework, as implemented in the Quantum Espresso code [18].

As mentioned earlier, in a first step, geometry optimizations and force calculations were performed with the Local Density Approximation (LDA). Non-relativistic (scalar-relativistic for Pb) and norm-conserving pseudopotentials were used, with the Cs [$5s^2 5p^6 6s^1$], I [$5s^2 5p^5$] and Pb [$5d^{10} 6s^2 6p^2$] electrons treated as valence states. The choice of 14 electrons for Pb and 9 for Cs was made after testing

the influence of semi-core electrons on the potential energy surface (see an example in figure 5 of **publication 1** [8]).

In a second step:

- as for the study of the spatial domains, the band structure calculations of the constructed $2 \times 1 \times 1$ and $1 \times 1 \times 2$ supercells were performed with fully relativistic pseudopotentials (for Pb and I) with LDA.
- in order to study the time-dynamical Rashba effect from CPMD, the band structure calculations were performed with fully relativistic US pseudopotentials (for Pb, I and Cs) datasets using the PBE xc functional (with the same number of valence electrons as in the scalar or non-relativistic case). This was done in order to be coherent with the CPMD calculations taken from [15] which were done using PBE as well (with the CP2K code). We carefully checked that symmetry breaking is present even when using PBE, see **publication 2** [6].

For all the calculations of this section, the Brillouin zone was sampled with Γ -centered Monkhorst-Pack meshes [19] with subdivisions of $8 \times 8 \times 8$ k-points.

4.4.2 SPATIAL DOMAINS

Here, the aim is to investigate the influence of spatial A/B domains on the electronic band structure, in particular in terms of Rashba effect. Given that the eigenvector under study mostly corresponds to a distortion along one axis (x as labeled in figure 4.4.2), we built supercells by doubling the single cell both in the x direction, and in the z direction. These $2 \times 1 \times 1$ and $1 \times 1 \times 2$ supercells are built putting together 2 single cells: 1 single cell in configuration A (or x up), and one configuration in configuration B (or x down). These supercells are represented in a simplified way in figure 4.4.4.

The Rashba splitting obtained for a single cubic cell at the R point is recalled in figure 4.4.5. When doubling the cell along z (resp. x), the R point folds on the S point (resp. T point), using the orthorhombic convention.

The results are shown in figures 4.4.6 and 4.4.7. Whereas no Rashba effect is found in the case of an extension orthogonal to the direction of symmetry breaking, a band splitting around the valence band

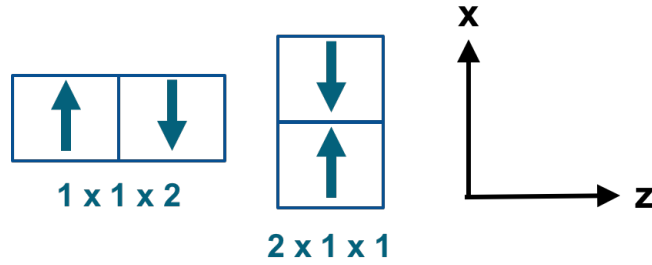


Figure 4.4.4: Simplified representations of the supercells used to study the influence of spatial domains A/B or "x up"/"x down" on the electronic band structure.

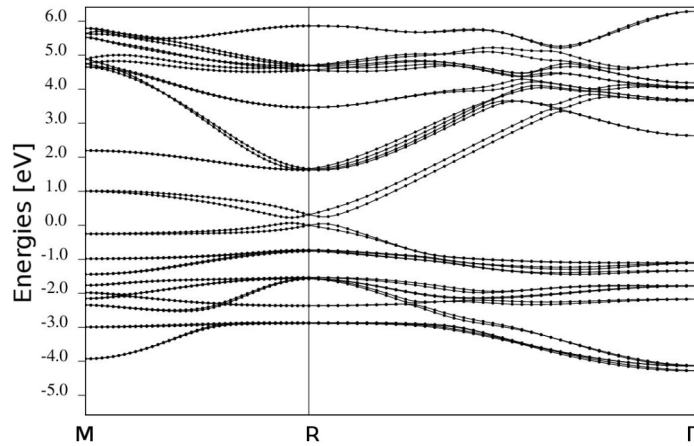


Figure 4.4.5: Electronic band structure (including SOC) of the unit cell of cubic CsPbI_3 .

maximum and the conduction band minimum is found for an extension parallel to the direction of symmetry breaking.

In general, the Rashba splitting in the band structure of a two-dimensional system results from the combined effect of atomic spin-orbit coupling and asymmetry of the potential in the direction (here x) perpendicular to the two-dimensional plane, causing a loss of inversion symmetry. In the case of an extension orthogonal to the direction of symmetry breaking ($1 \times 1 \times 2$ supercell), the symmetry along x is respected on average: the inversion symmetry is kept and the Rashba splitting is quenched.

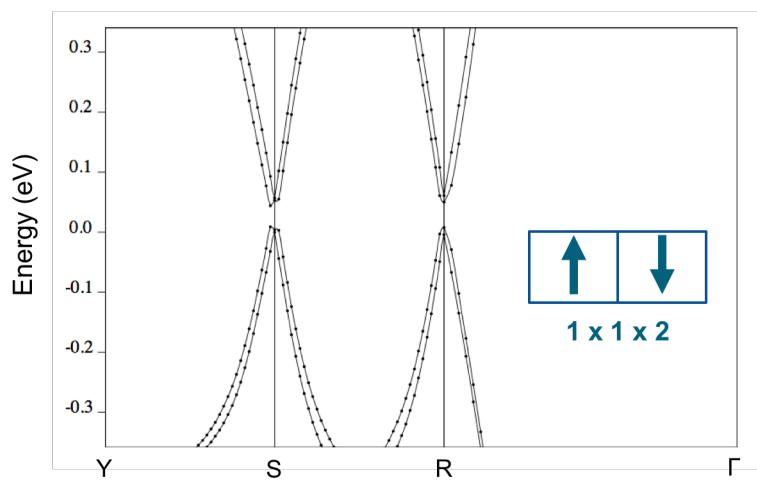


Figure 4.4.6: Electronic band structure (including SOC) of the $1 \times 1 \times 2$ supercell. As the cell is slightly orthorhombic (see the Methods subsection 4.4.1), we use here the orthorhombic q-point convention.

4.4.3 TIME DYNAMICS: CPMD

In this part, we analyze in detail CPMD trajectories of cubic CsPbI_3 in the light of our findings on the double well potential energy surface. The trajectories were computed by Carignano *et al.* in the framework of a study [15] of the anharmonic motion of the iodine atoms in CsPbI_3 and MAPbI_3 , where they showed that, at variance with FAPbI_3 , these two perovskite structures are expected to have a deviation from the perfect cubic unit cell at any time of the MD, with a probability very close to 1. This hints towards the interpretation that the $Pm\bar{3}m$ symmetry can be seen as a time average, including for CsPbI_3 . This phenomenon had already been reported for MAPbI_3 in earlier studies [20], when it was evidenced that the system strongly deviates from the perfectly cubic structure in the sub-picosecond time scale.

The molecular dynamics simulation were performed at 370 and 450 K under NPT-F conditions, which allow volume fluctuations by changing the supercell edges and angles. The temperature was controlled by a Nose-Hoover thermostat with three chains, and the pressure was controlled by the Martyna's barostat [21]. The time constant for both, the thermostat and barostat, was set at 50 fs. The system they

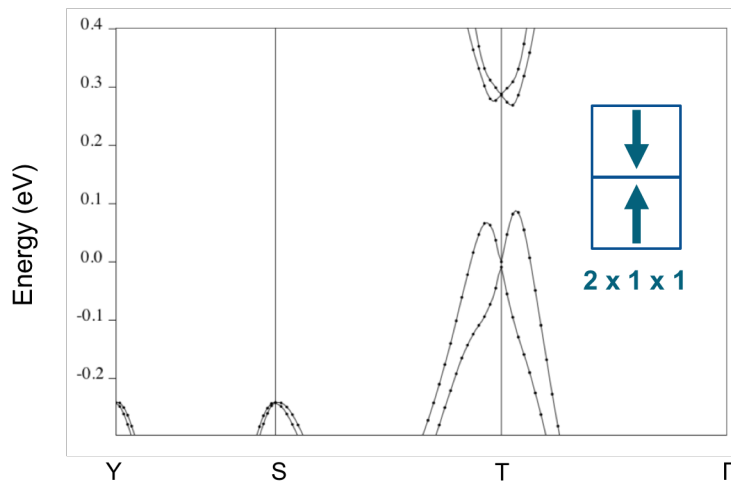


Figure 4.4.7: Electronic band structure (including SOC) of the $2 \times 1 \times 1$ supercell. As the cell is slightly orthorhombic (see the Methods subsection 4.4.1), we use here the orthorhombic q-point convention.

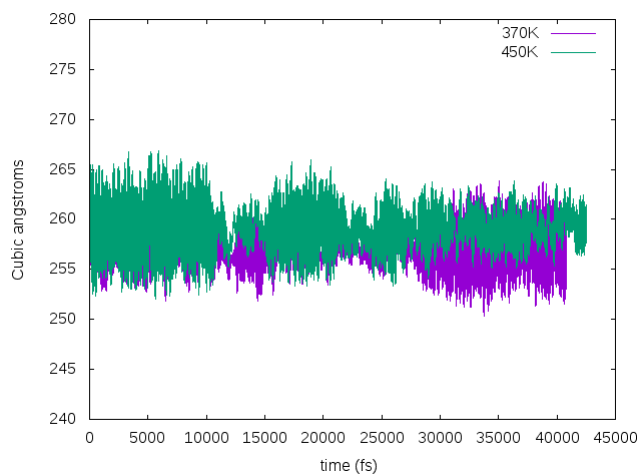


Figure 4.4.8: Volume fluctuations along the CPMD trajectories at 370 K and 450 K.

used for CsPbI_3 has 320 atoms ($4 \times 4 \times 4$ supercells). In my study I chose to focus on the 370 K trajectory.

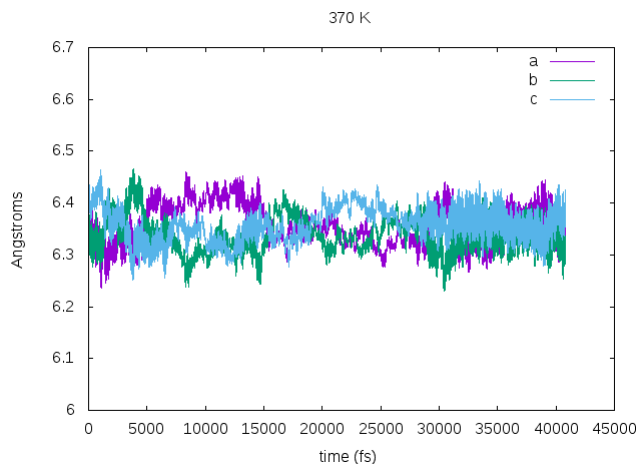


Figure 4.4.9: Lattice parameters fluctuations along the CPMD trajectory at 370 K.

In Angstroms	370 K	450 K
a	6.358	6.372
b	6.338	6.391
c	6.358	6.361

Table 4.4.2: Average lattice parameters (in Angstroms) along the CPMD trajectories at 370 K and 450 K.

In figures 4.4.8 and 4.4.9 I show the volume and lattice parameters fluctuations versus time. In particular, from this first simple analysis we can infer that the structure fluctuates a lot in a non cubic way: the difference between lattice parameters can be as high as 3%. Moreover, we do not find a cubic structure on average (see table 4.4.2). The fluctuations can be better seen in figure 4.4.10 where we plot the distance to the average pseudocubic lattice structure. This distance d is obtained as:

$$d(t) = \left(\sum_{i=1}^3 (x_i(t) - \bar{x}_i)^2 \right)^{\frac{1}{2}} \quad (4.2)$$

where x_i are the 3 lattice parameters and \bar{x}_i their time average over the whole trajectory.

On figure 4.4.11 we show how the structure explores the potential energy landscape during the 40 ps of

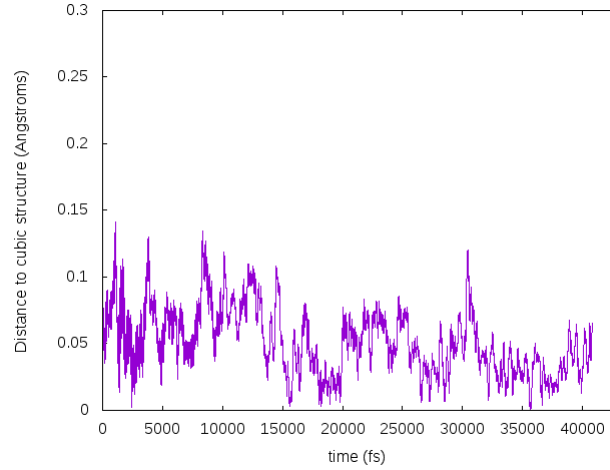


Figure 4.4.10: Fluctuations of the distance to the average pseudocubic structure, as defined in Eq. 4.2.

the simulation. This evidences one peak centered on the average and two side peaks at around $+0.15$ eV and -0.25 eV with respect to the average (approximate values given the size of the histogram boxes).

The left peak, located 0.25 eV lower than the average (thus **3.9 meV** per unit cell), could correspond to a symmetry breaking structure equivalent to the one found in our double-well potential for which we recall that the barrier was 7 to 12 meV with LDA (depending on which parameter is let free in the geometry optimization) and precisely **3.0 meV** for PBE all-relaxed structures. Even though in the MD simulation the system has a higher number of degrees of freedom (angles, axis, atomic positions) than in our frozen phonon plus relaxation DFT method, the energy barrier is found to be of the same order of magnitude.

In order to analyze the MD trajectories in the light of the double well instability we evidenced in the previous two articles, our general goal is to project these trajectories onto our two structures: the perfectly cubic symmetric structure ("maximum") and the symmetry breaking structure ("minimum"). The chosen approach is to study the radial distribution function of the cesium-lead pairs during the MD simulation and to compare it to our two reference structures ("maximum" and "minimum").

Figure 4.4.12 shows this distribution functions over the 40 ps of the 370 K trajectory, both in 3D and projected on the x or y axis. The spikes represent the Pb-Cs distance in the reference maximum structure

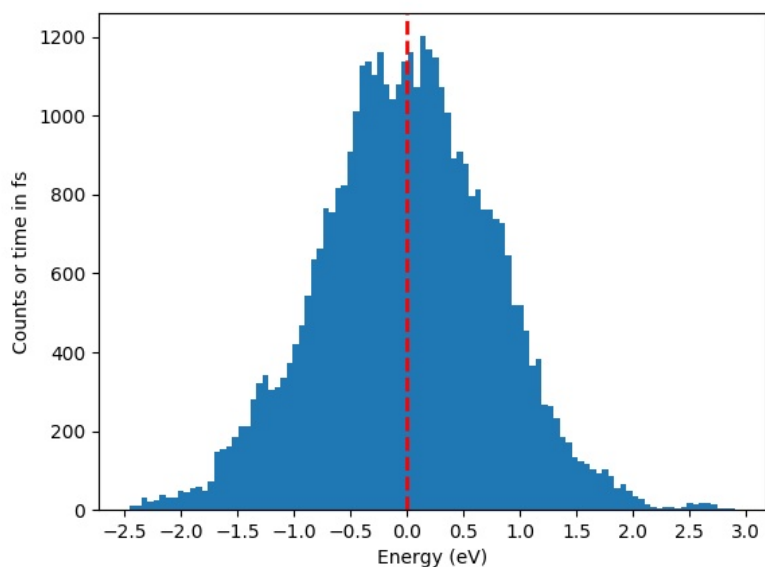


Figure 4.4.11: Energy histogram of the 40 ps trajectory at 370 K. The boxes size is 0.05 eV.

we calculated with DFT (0 Kelvin). We obtain overall a good agreement on this time average, even though for the 3D distance the peak does not correspond exactly to the maximum of the MD distribution. This can be easily understood as the average pseudocubic lattice parameters (see table 4.4.2) do not correspond to the parameters of the maximum structure (see table 4.4.3).

A better correspondence can be found for the 3D average of the Pb/Cs distance by correcting the

In Angstroms	
a	6.15
b	6.15
c	6.15

Table 4.4.3: Lattice parameters (in Angstroms) of the maximum (cubic and symmetric) structure obtained by DFT.

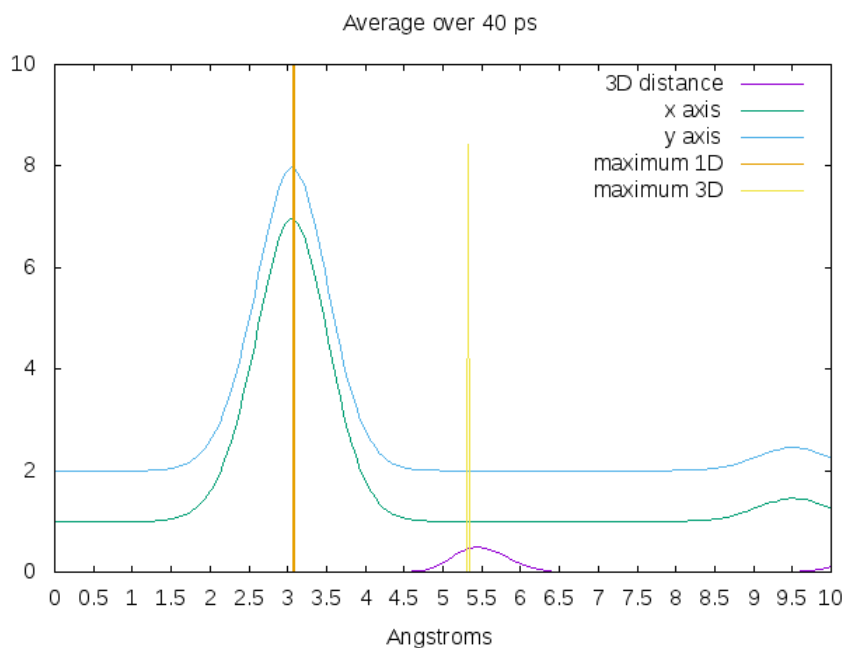


Figure 4.4.12: Distribution function of the cesium-lead pairs' distances along the MD trajectory. The narrow, Dirac-like peaks correspond to our 0 Kelvin DFT reference distances in the maximum perfectly symmetric structure. The vertical axis is arbitrary and chosen for better visibility.

”maximum” structure’s Pb/Cs reference distance proportionally to the ratio of the average MD lattice parameters to the maximum structure’s. The result can be seen in figure 4.4.13. Overall this means that for the following study we have to take great care when comparing the MD to our references and keep in mind that for any time interval of the MD the lattice parameters’ matrix can differ quite a lot from the DFT references ones.

Before focusing on specific interval’s time lengths, let us consider figure 4.4.14 where we show the Pb/Cs distance for random intervals of 1, 5, 10, and 40 ps. This gives the general picture : the oscillations between between the two minima structures seem to occur at the sub pico-second time scale. On figure 4.4.15 one can see that for most 1 ps intervals of interest the movement is averaged around the maximum.

Figure 4.4.16 focuses on averages over 0.5 ps intervals. At this time scale, our double well references seem to explain very well how the system explores the energy landscape. Whereas some intervals show a

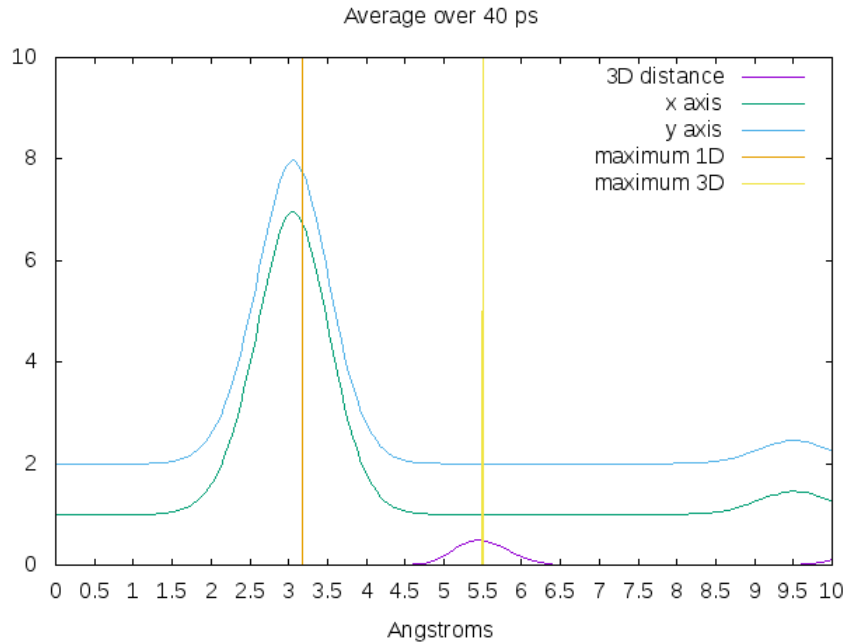


Figure 4.4.13: Distribution function of the cesium-lead pairs' distances along the MD trajectory. Here the references (narrow peaks) correspond to the distances for the maximum structure, weighted by the ratio of the average lattice parameters of the trajectory over the ones of the 0 Kelvin DFT reference.

distance peak corresponding to the distance in the average pseudocubic structure ("maximum"), for instance the [11-11.5 ps] interval show two peaks centered on both minimum structures ("minimum" and "minimum_sym"). This means that at in 0.5 ps the structure has enough time to explore the whole double well. We think that this is the most relevant time-scale to evidence the double well instabilities.

However, it is worth studying 0.1 ps intervals as well (figure 4.4.17). At this timescale, the first observation we can make is that, for most of the studied 0.1 intervals, the oscillations are too strong to draw any conclusion. The [10-10.1 ps] seems to be the exception, with two very clear peaks. Whereas with the corrected DFT references (figure 4.4.17) the right peak seems to correspond to the average pseudocubic structure and the left peak is not identified, if we analyze this interval in the light of our non-corrected DFT structures (figure 4.4.18), the structure seems to exactly oscillate between the two

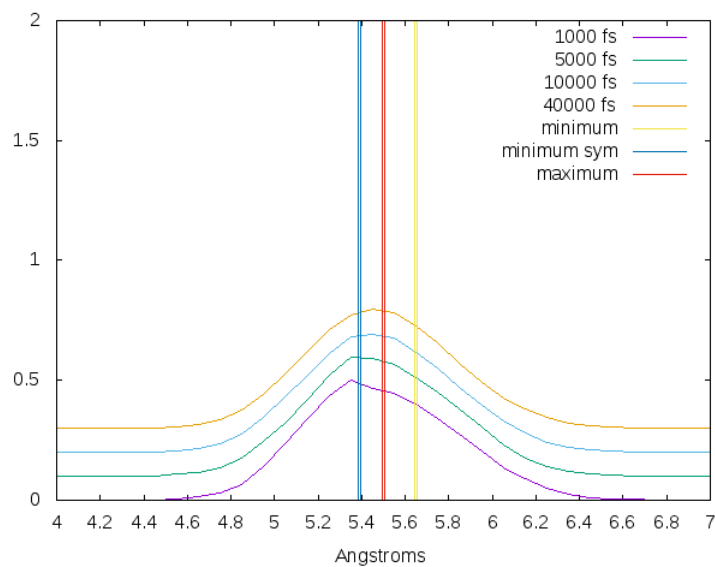


Figure 4.4.14: Distribution function of the cesium-lead pairs' distances along the MD trajectory, for intervals' lengths of 1, 5, 10 and 40 ps. Here the references (narrow peaks) correspond to the distances for the maximum structure, weighted by the ratio of the average lattice parameters of the trajectory over the ones of the DFT reference.

minima within this specific 0.1 ps interval.

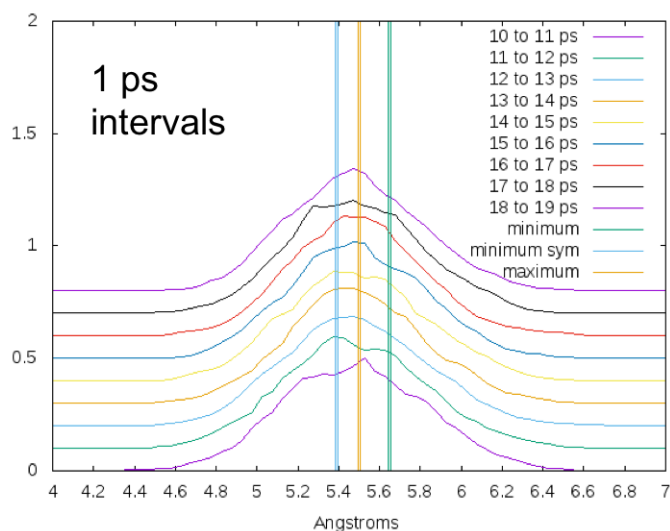


Figure 4.4.15: Distribution function of the cesium-lead pairs' distances along the MD trajectory. Here the references (narrow peaks) correspond to the distances for the maximum structure, weighted by the ratio of the average lattice parameters of the trajectory over the ones of the DFT reference.

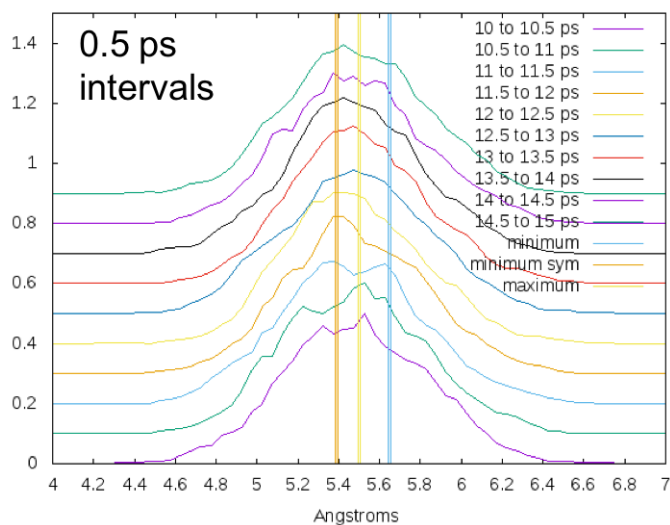


Figure 4.4.16: Distribution function of the cesium-lead pairs' distances along the MD trajectory. Here the references (narrow peaks) correspond to the distances for the maximum structure, weighted by the ratio between the lattice parameters.

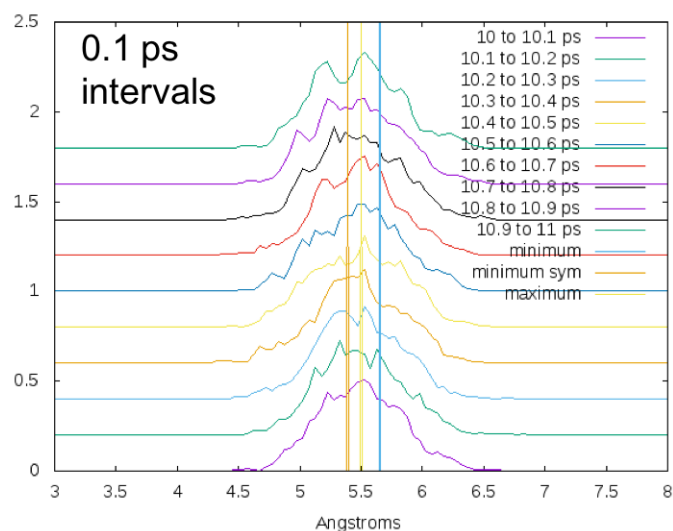


Figure 4.4.17: Distribution function of the cesium-lead pairs' distances along the MD trajectory. Here the references (narrow peaks) correspond to the distances for the maximum structure, weighted by the ratio between the lattice parameters.

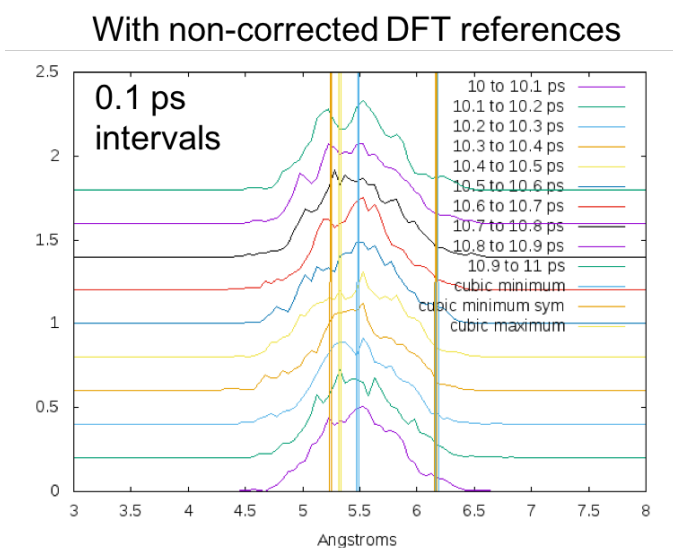


Figure 4.4.18: Distribution function of the cesium-lead pairs' distances along the MD trajectory. Here the references (narrow peaks) correspond to the distances for the maximum structure.

4.4.4 DYNAMICAL RASHBA EFFECT

Now that we have carefully analyzed the MD trajectories in terms of Pb-Cs distance and its oscillations between the symmetric structures' values and the broken symmetry ones, the idea here is to focus on the dynamical Rashba effect. We expect to find in $CsPbI_3$ an effect similar to what was evidenced for $MAPbI_3$ for which the spatially local Rashba splitting was found to fluctuate on the subpicosecond time scale typical of the methylammonium cation dynamics [22].

To investigate this effect, we calculate the electronic band structure, including spin-orbit coupling, at different snapshots along the trajectory. Given the previous results, we chose to focus these calculations on the [10-15 ps] interval in which we chose 50 regularly distributed snapshots (hence separated by 100 fs from each other) in order to better capture the sub pico-second dynamics. For each snapshot, we used the MD structure of the $4 \times 4 \times 4$ supercells (we remind the reader that the cell's atomic positions, lattice parameters and angles vary) and derived its electronic band structure (see the Methods subsection 4.4.1). These heavy calculations for $4 \times 4 \times 4$ supercells are very similar to what was previously done for $MAPbI_3$ [20]. Here, we show only preliminary results of this ongoing study.

The electronic band structure calculations are done at 7 q points of the Brillouin zone (table 4.4.4).

Point number	x	y	z
1	0.1	0	0
2	0.05	0	0
3 (Γ)	0	0	0
4	0	0.05	0
5	0	0.1	0
6	0	0	0.05
7	0	0	0.1

Table 4.4.4: q points of the Brillouin zone used in the 50 band structure calculations.

In figure 4.4.19 we plot for each snapshot i of the 50 structures chosen in the MD trajectory and for each q point the normalized energy difference :

$$\Delta E_{gap}^i(q) = [CBM^i(q) - VBT^i(q)] - [(CBM^i(\Gamma) - VBT^i(\Gamma))]$$

where CBM is the conduction band minimum and VBT the valence band top. This is necessary as the

cell is variable along the trajectory: the fluctuations on the gap value, which are large with respect to the Rashba splitting, would mask it otherwise.

This result shows that 100 fs is a good estimate of the timescale of the Rashba effect dynamics. Moreover, on average we see a band gap shift to the Y direction, the band gap being reduced of about 1.3 meV. Taking the extremum case, we can infer that the amplitude of the oscillations in the 5 ps timescale is around 10 meV.

Figures 4.4.20 and 4.4.21 show that this is mostly due to a Rashba splitting happening at the CBM rather than at the VBT. This is coherent with the fact that the most relativistic atom, Pb, is mostly contributing to the conduction band as we recalled in our introductory chapter (see section 2.3). This is also coherent with what was previously reported for MAPI [20].

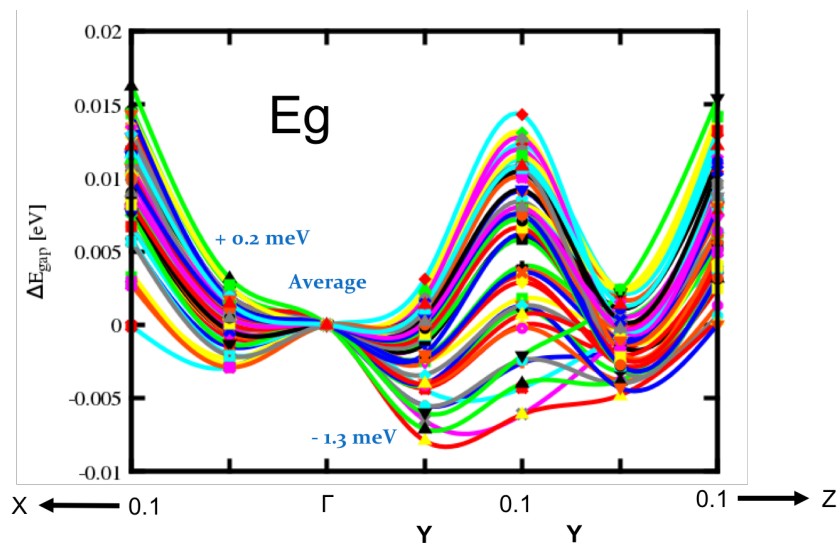


Figure 4.4.19: Energy difference between the CBM and the VBT for the 50 points chosen in the MD trajectory. For each of the 50 snapshots, this difference is set to 0 at Γ to allow better comparison. The figures in blue represent the average values over the 50 points of the trajectory.

As a conclusion, using molecular dynamics and frozen phonons, we have evidenced sub-picosecond anharmonic fluctuations in the fully inorganic CsPbI_3 perovskite. We revealed the effect of these fluctuations, combined with spin-orbit coupling, on the electronic band structure, evidencing a

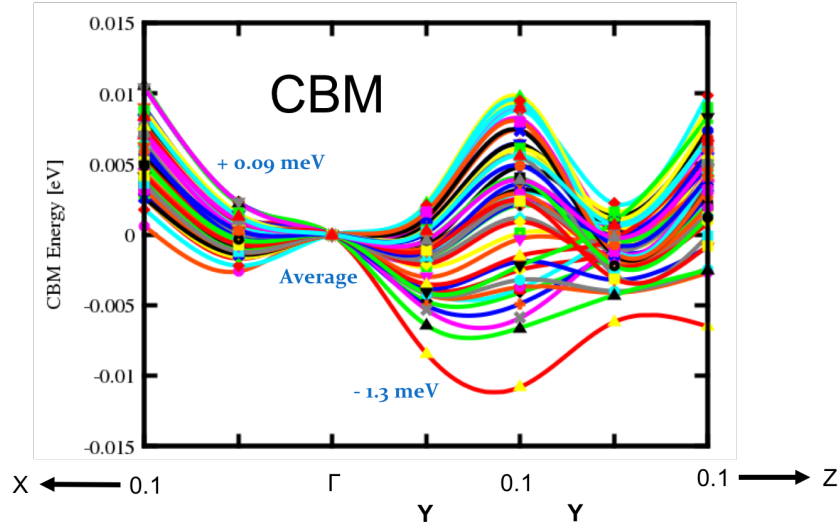


Figure 4.4.20: Conduction band minimum energy. For each of the 50 time steps, this energy is set to 0 at Γ to allow better comparison. The figures in blue represent the average values over the 50 points of the trajectory.

dynamical Rashba effect which could reduce recombination rates in these materials. Our study show that under certain conditions space disorder can quench the Rashba effect. As for time disorder, we evidence a dynamical Rashba effect which is similar to what was found for MAPbI_3 , and which is still sizable despite temperature disorder, the large investigated supercell, and the absence of the organic cations' motion. Further work is needed in this ongoing study to correlate the Rashba dynamics with the structural distortions along the molecular dynamics trajectory.

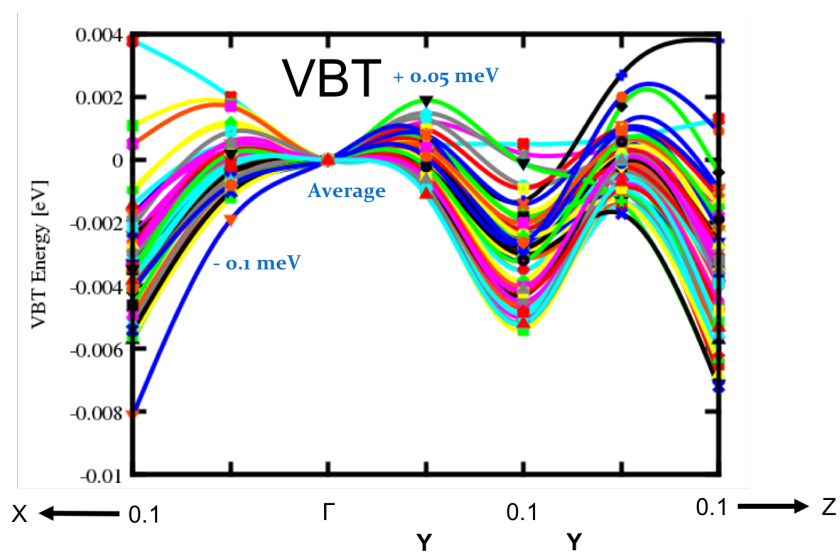


Figure 4.4.21: Valence band top energy. For each of the 50 time steps, this energy is set to 0 at Γ to allow better comparison. The figures in blue represent the average values over the 50 points of the trajectory.

REFERENCES

- [1] D.M. Trots and S.V. Myagkota. High-temperature structural evolution of caesium and rubidium triiodoplumbates. *J. Phys. Chem. Solids*, 69(10):2520 – 2526, 2008. ISSN 0022-3697. doi: <http://dx.doi.org/10.1016/j.jpcs.2008.05.007>. URL <http://www.sciencedirect.com/science/article/pii/S002236970800173X>.
- [2] In Chung, Jung-Hwan Song, Jino Im, John Androulakis, Christos D Malliakas, Hao Li, Arthur J Freeman, John T Kenney, and Mercuri G Kanatzidis. CsSnI₃: semiconductor or metal? high electrical conductivity and strong near-infrared photoluminescence from a single material. high hole mobility and phase-transitions. *Journal of the American Chemical Society*, 134(20):8579–8587, 2012.
- [3] Constantinos C. Stoumpos, Lingling Mao, Christos D. Malliakas, and Mercuri G. Kanatzidis. Structure–band gap relationships in hexagonal polytypes and low-dimensional structures of hybrid tin iodide perovskites. *Inorganic Chemistry*, 56(1):56–73, 2017. doi: 10.1021/acs.inorgchem.6b02764. URL <http://dx.doi.org/10.1021/acs.inorgchem.6b02764>. PMID: 27997156.
- [4] Constantinos C. Stoumpos, Christos D. Malliakas, and Mercuri G. Kanatzidis. Semiconducting tin and lead iodide perovskites with organic cations: Phase transitions, high mobilities, and near-infrared photoluminescent properties. *Inorg. Chem.*, 52(15):9019–9038, 2013. doi: 10.1021/ic401215x. URL <http://dx.doi.org/10.1021/ic401215x>.
- [5] Christian KN. Møller. The structure of caesium plumbo iodide CsPbI₃. *Mat. Fys. Medd. Dan. Vid. Sels.*, 32, No 1(1), 1959.
- [6] Arthur Marronnier, Guido Roma, Soline Boyer-Richard, Laurent Pedesseau, Jean-Marc Jancu, Yvan Bonnassieux, Claudine Katan, Constantinos C. Stoumpos, Mercuri G. Kanatzidis, and Jacky Even. Anharmonicity and disorder in the black phases of cesium lead iodide used for stable inorganic perovskite solar cells. *ACS Nano*, 2018. doi: 10.1021/acsnano.8b00267. URL <https://doi.org/10.1021/acsnano.8b00267>. PMID: 29565559.
- [7] Constantinos C. Stoumpos and Mercuri G. Kanatzidis. The renaissance of halide perovskites and

- their evolution as emerging semiconductors. *Acc. Chem. Res.*, 48(10):2791–2802, 2015. doi: 10.1021/acs.accounts.5b00229. URL <http://dx.doi.org/10.1021/acs.accounts.5b00229>.
- [8] Arthur Marronnier, Heejae Lee, Bernard Geffroy, Jacky Even, Yvan Bonnassieux, and Guido Roma. Structural instabilities related to highly anharmonic phonons in halide perovskites. *The Journal of Physical Chemistry Letters*, 8(12):2659–2665, 2017.
- [9] Ilka M. Hermes, Simon A. Bretschneider, Victor W. Bergmann, Dan Li, Alexander Klasen, Julian Mars, Wolfgang Tremel, Frédéric Laquai, Hans-Jürgen Butt, Markus Mezger, Rüdiger Berger, Brian J. Rodriguez, and Stefan A. L. Weber. Ferroelastic fingerprints in methylammonium lead iodide perovskite. *The Journal of Physical Chemistry C*, 120(10):5724–5731, 2016. doi: 10.1021/acs.jpcc.5b11469. URL <https://doi.org/10.1021/acs.jpcc.5b11469>.
- [10] Evgheni Strelcov, Qingfeng Dong, Tao Li, Jungseok Chae, Yuchuan Shao, Yehao Deng, Alexei Gruverman, Jinsong Huang, and Andrea Centrone. $\text{CH}_3\text{NH}_3\text{PbI}_3$ perovskites: Ferroelasticity revealed. *Science advances*, 3(4):e1602165, 2017.
- [11] Constantinos C Stoumpos, Christos D Malliakas, and Mercouri G Kanatzidis. Semiconducting tin and lead iodide perovskites with organic cations: phase transitions, high mobilities, and near-infrared photoluminescent properties. *Inorganic chemistry*, 52(15):9019–9038, 2013.
- [12] Hsin-Wei Chen, Nobuya Sakai, Masashi Ikegami, and Tsutomu Miyasaka. Emergence of hysteresis and transient ferroelectric response in organo-lead halide perovskite solar cells. *The Journal of Physical Chemistry Letters*, 6(1):164–169, 2014.
- [13] Hui-Seon Kim, Sung Kyun Kim, Byeong Jo Kim, Kyung-Sik Shin, Manoj Kumar Gupta, Hyun Suk Jung, Sang-Woo Kim, and Nam-Gyu Park. Ferroelectric polarization in $\text{CH}_3\text{NH}_3\text{PbI}_3$ perovskite. *The Journal of Physical Chemistry Letters*, 6(9):1729–1735, 2015.
- [14] Jarvist M Frost, Keith T Butler, Federico Brivio, Christopher H Hendon, Mark Van Schilfgaarde, and Aron Walsh. Atomistic origins of high-performance in hybrid halide perovskite solar cells. *Nano letters*, 14(5):2584–2590, 2014.

REFERENCES

- [15] Marcelo A Carignano, S Assa Aravindh, Iman S Roqan, Jacky Even, and Claudine Katan. Critical fluctuations and anharmonicity in lead iodide perovskites from molecular dynamics supercell simulations. *The Journal of Physical Chemistry C*, 121(38):20729–20738, 2017.
- [16] P. Hohenberg and W. Kohn. Inhomogeneous electron gas. *Phys. Rev.*, 136:B864–B871, Nov 1964. doi: 10.1103/PhysRev.136.B864. URL <http://link.aps.org/doi/10.1103/PhysRev.136.B864>.
- [17] W. Kohn and L. J. Sham. Self-consistent equations including exchange and correlation effects. *Phys. Rev.*, 140:A1133–A1138, Nov 1965. doi: 10.1103/PhysRev.140.A1133. URL <http://link.aps.org/doi/10.1103/PhysRev.140.A1133>.
- [18] Paolo Giannozzi, Stefano Baroni, Nicola Bonini, Matteo Calandra, Roberto Car, Carlo Cavazzoni, Davide Ceresoli, Guido L Chiarotti, Matteo Cococcioni, Ismaila Dabo, Andrea Dal Corso, Stefano de Gironcoli, Stefano Fabris, Guido Fratesi, Ralph Gebauer, Uwe Gerstmann, Christos Gougoussis, Anton Kokalj, Michele Lazzeri, Layla Martin-Samos, Nicola Marzari, Francesco Mauri, Riccardo Mazzarello, Stefano Paolini, Alfredo Pasquarello, Lorenzo Paulatto, Carlo Sbraccia, Sandro Scandolo, Gabriele Sclausero, Ari P Seitsonen, Alexander Smogunov, Paolo Umari, and Renata M Wentzcovitch. Quantum espresso: a modular and open-source software project for quantum simulations of materials. *J. Phys.: Condens. Matter*, 21(39):395502, 2009. URL <http://stacks.iop.org/0953-8984/21/i=39/a=395502>.
- [19] Hendrik J Monkhorst and James D Pack. Special points for brillouin-zone integrations. *Physical review B*, 13(12):5188, 1976.
- [20] Claudio Quarti, Edoardo Mosconi, James M. Ball, Valerio D’Innocenzo, Chen Tao, Sandeep Pathak, Henry J. Snaith, Annamaria Petrozza, and Filippo De Angelis. Structural and optical properties of methylammonium lead iodide across the tetragonal to cubic phase transition: implications for perovskite solar cells. *Energy Environ. Sci.*, 9:155–163, 2016.
- [21] Glenn J Martyna, Mark E Tuckerman, Douglas J Tobias, and Michael L Klein. Explicit reversible integrators for extended systems dynamics. *Molecular Physics*, 87(5):1117–1157, 1996.

- [22] Thibaud Etienne, Edoardo Mosconi, and Filippo De Angelis. Dynamical origin of the rashba effect in organohalide lead perovskites: A key to suppressed carrier recombination in perovskite solar cells? *The Journal of Physical Chemistry Letters*, 7(9):1638–1645, 2016.

La vraie valeur d'un enseignement est en raison inverse de son utilité immédiate.

Paul Valéry

5

Environmental Instabilities in Halide Perovskites

BEYOND THE ISSUE OF THE STRUCTURAL INSTABILITIES OF HALIDE PEROVSKITES, whether it be those arising from the inorganic lattice's octahedral tilting, studied in detailed in the previous chapter, or from the organic molecule's translation-rotation coupling, the issue of their thermodynamical stability in the ambient environment (temperature, oxygen, humidity, light) is probably the greatest challenge this new generation of solar cells faces. Even though this has been so far one of the major topic of study for the PSC community, along with the efficiency race, much more work is needed in order to better understand the degradation mechanisms of perovskite solar cells.

Contents

5.1	Stability issues: from ab-initio calculations to experiments	140
5.2	Ab initio perspective: stability diagrams	142
5.2.1	Methods	142
5.2.2	Results	144
5.3	[Publication 3] Light-induced degradation of perovskite thin films	146
5.4	Hybrid Perovskites: organic or inorganic semiconductors?	161
5.5	Oxygen defects in MAPI	163
5.5.1	Methods	163
5.5.2	Interstitial and substitutional oxygen defects	164
5.5.3	Formation enthalpies of neutral defects	165
5.5.4	Electronic properties and charged defects	166
5.6	[Publication 4] Hysteresis and ionic migration	173
	References	174

5.1 STABILITY ISSUES: FROM AB-INITIO CALCULATIONS TO EXPERIMENTS

This chapter encompasses both ab-initio calculations and experimental characterization. It will be structured as follows.

In **section 5.2**, we use DFT total energy calculations for the hybrid perovskite structure $MAPbI_3$ and for its constitutive elements in order to draw its stability diagram and identify the size of the stability region in terms of chemical potentials.

In **section 5.3**, corresponding to the third publication of my PhD [1], we compare the optical and the electrical light-induced degradation of $CH_3NH_3PbI_3$ ("MAPI")-based solar cells using real-time ellipsometry measurements, electrical measurements and X-Ray Diffraction (XRD) techniques. The goal is threefold. First, we aim at comparing the light-induced degradation timescale of the electrical (current-voltage studies) and optical (ellipsometry, optical indexes) properties of these materials. The

second motivation of this study is to better understand the chemical decomposition of MAPI into its two precursors: methylammonium and lead iodides. Last, we use the results of our optical constant study, completed by ab initio calculations, to answer the controversy on whether the hybrid perovskite structure $MAPbI_3$ behaves more like inorganic compounds (high dielectric constant, low exciton binding energy) or like organic materials (low dielectric constant, high exciton binding energy).

Section 5.4 is a follow-up on our study of the dielectric properties. In this part, we analyze the impact of the anharmonicity features evidenced in chapter 4, in particular for $CsPbI_3$, on the values of the dielectric tensor both in the high frequency and in the static regime.

Apart from light-induced degradation, one of the main causes of the environmental instability of halide perovskites that has been identified so far is oxygen [2]. In **Section 5.5** we use supercells DFT calculations in order to derive the formation enthalpies of various interstitial and substitutional oxygen defects in $MAPbI_3$.

Finally, in **section 5.6** we provide the reader with a brief analysis and a few comments around the fourth article [3] published during my PhD about the experimental evidence of halide ionic migration in MAPI-based solar cells. As I was not one of the primary contributors to this experimental work, my part being limited to the result analysis, I chose not to include the publication itself in this manuscript.

5.2 AB INITIO PERSPECTIVE: STABILITY DIAGRAMS

As we will see in the next section, most of the environmental stability issues (temperature, oxygen, humidity, light) of halide perovskites involve, one way or another, the issue of the chemical and thermodynamical stability of the perovskite structure itself.

Here, we would like to give the reader a first insight into the thermodynamical instability of MAPbI_3 from a first-principle perspective.

5.2.1 METHODS

The total energy of the various structures are calculated with DFT within the LDA approximation. Norm-conserving and non-relativistic pseudopotentials were used. At variance with what we found for cesium, taking into account the semi-core electrons of lead did not appear to be crucial for total energy calculations of the lead-based compounds of interest here (metallic Pb, PbI_2 and MAPbI_3).

After cautious cutoff and k-point energy convergence tests (see for instance figures 5.2.1 and 5.2.2 for PbI_2), a cutoff of 70 Ry and k-point grids of $5 \times 5 \times 4$ (PbI_2), $7 \times 7 \times 4$ (MAI), $8 \times 8 \times 8$ (MAPbI_3) and $6 \times 6 \times 6$ (CsI) were used.

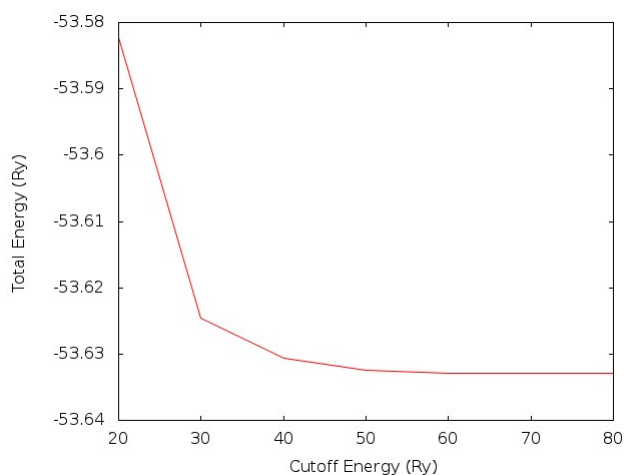


Figure 5.2.1: Convergence tests for PbI_2 on the plane waves' energy cutoff parameter.

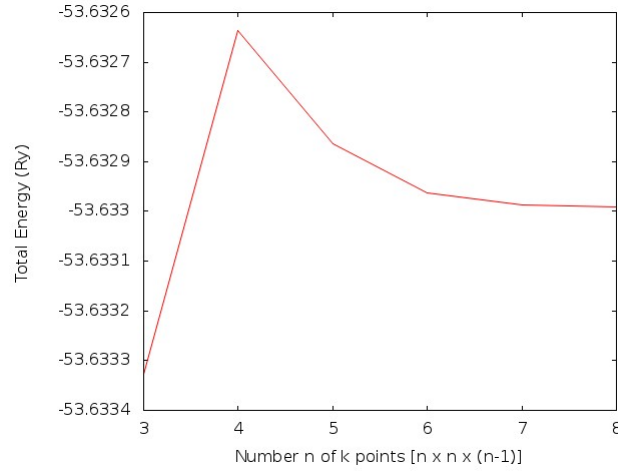


Figure 5.2.2: Convergence tests for PbI_2 on the number of k points used to sample the Brillouin zone.

The formation enthalpies of the various species were obtained directly by calculating the difference of total energy between the composed structures and its individual components.

We then draw a stability diagram using Euler identity for free enthalpy:

$$G = \sum_{i=1}^N n_i \cdot \mu_i$$

where N is the number of species, n_i the stoichiometry coefficient and μ_i the chemical potential of species i.

Thus, the stability zone of MAPI is defined by constraints 5.1a to 5.1c.

$$\mu_{CH_3NH_3} + \mu_{Pb} + 3\mu_I = \Delta H(CH_3NH_3PbI_3) \quad (5.1a)$$

$$\mu_{CH_3NH_3} + \mu_I < \Delta H(CH_3NH_3I) \quad (5.1b)$$

$$\mu_{Pb} + 2\mu_I < \Delta H(PbI_2) \quad (5.1c)$$

The quantity μ_I was calculated as $\frac{1}{2}\mu_{I_2}$.

5.2.2 RESULTS

In table 5.2.1 I report the formation enthalpies per atom for PbI_2 , MAI and cubic $MAPbI_3$ and compare of results to previous DFT calculations as well as to experimental data when available. We find a negative formation enthalpy of -14 meV/atom for MAPI, which means that it is slightly favorable at room temperature ($kT \approx 25$ meV)) and that the reverse reaction is almost thermodynamically favorable. This is a first hint towards the understanding of the chemical instability of methylammonium lead compounds. This very narrow stability window also means that MAPI will be extremely sensitive to external parameters (temperature, oxygen, humidity) and that kinetic aspects (such as the influence of light) can play a crucial role in understanding its instability.

Formation enthalpy (eV/atom)	DFT-GGA Ref [4]	Our DFT results	Experimental
$Pb + I_2 = PbI_2$	-2.09	-1.841	-1.811 (T < 200K) [5]
$MA + \frac{1}{2}I_2 = MAI$	-2.87	-3.053	-2.08 (300K) [6]
$MAI + PbI_2 = MAPbI_3$	-0.27	-0.014	

Table 5.2.1

The stability diagram of cubic $MAPbI_3$ is shown in figure 5.2.3. We find a narrower stability zone compared to what was reported earlier in the literature. This difference could be due to the usual discrepancies between LDA (used here) and GGA (used in the cited works).

Even though our aim in this chapter is to focus on hybrid perovskite $MAPbI_3$'s stability, we performed similar calculations for $CsPbI_3$ (see figure 5.2.4).

We thus find $CsPbI_3$ to be much more thermodynamically stable than its hybrid cousin.

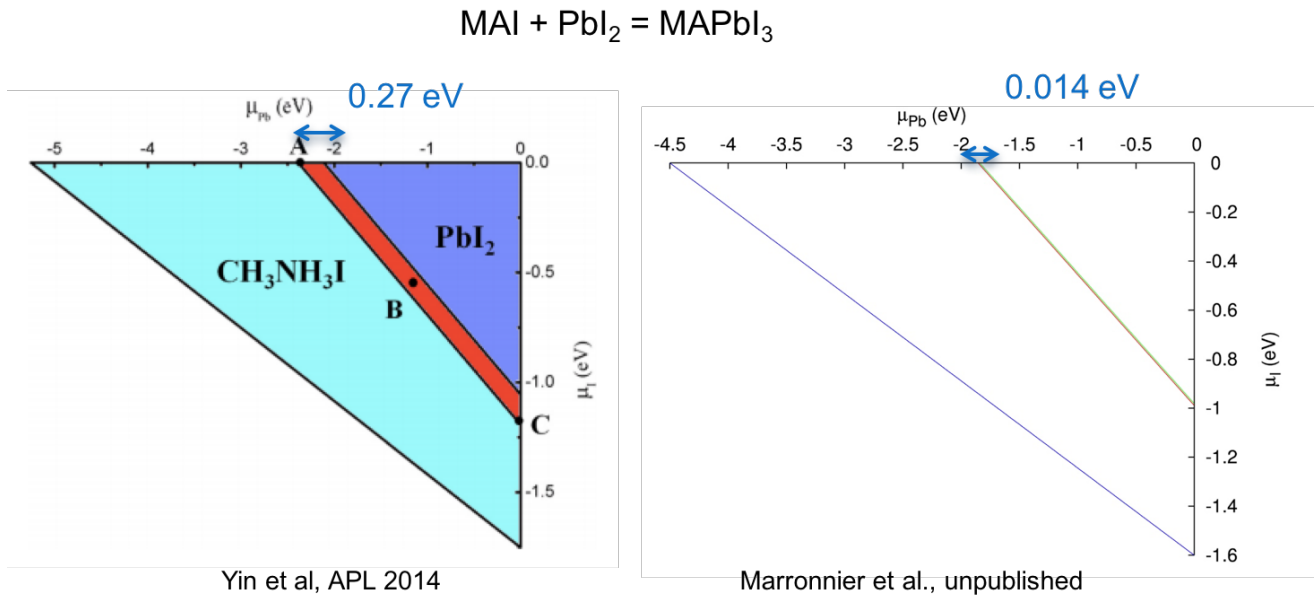


Figure 5.2.3: Stability diagrams of cubic MAPbI_3 obtained by DFT calculations. The diagram on the left is taken from Ref. [4]

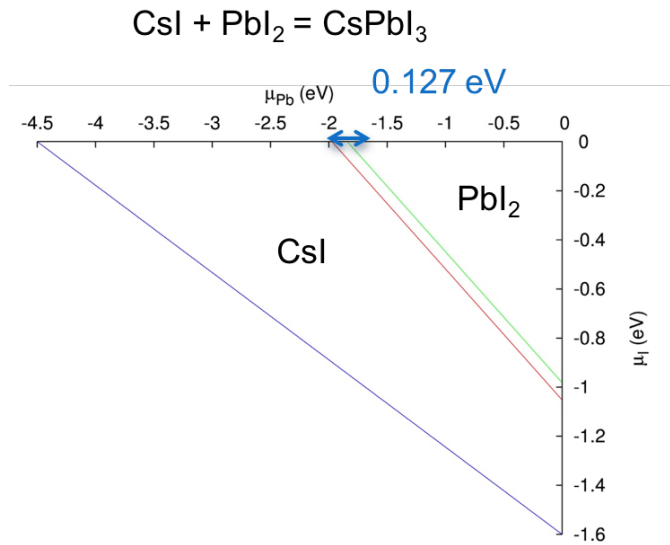


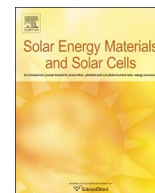
Figure 5.2.4: Stability diagram of cubic CsPbI_3 obtained by DFT calculations.

5.3 [PUBLICATION 3] LIGHT-INDUCED DEGRADATION OF PEROVSKITE THIN FILMS

After this first thermodynamical insight on the instability of *MAPI*, obtained by ab-initio calculations, in this section we study in detail, from an experimental perspective, the light-induced degradation of *MAPI* thin films.

In this work [1], we perform real-time ellipsometry measurements, in a nitrogen atmosphere, in order to study the degradation of the optical constants of perovskite thin films deposited on top of the usual Glass/ITO/PEDOT:PSS stack used to built "inverted perovskite" solar cells. We compare this change in the optical constants to the electrical degradation of complete solar cells, and use X-ray diffraction to confirm the chemical decomposition suggested by the other techniques. Last, we use the results of our optical constant study, completed by ab initio calculations, to answer the controversy on whether the hybrid perovskite structure *MAPbI₃* behaves more like inorganic compounds (high dielectric constant, low exciton binding energy) or like organic materials (low dielectric constant, high exciton binding energy).

This article is the result of a collaboration with 3 students who prepared the samples and performed XRD measurements. My personal work encompasses the ellipsometry and electrical measurements, their interpretation and exploitation, the first principles calculations of the dielectric functions, and the lead of the scientific project (scientific approach, article writing, etc).



Electrical and optical degradation study of methylammonium-based perovskite materials under ambient conditions

Arthur Marronnier^{a,*}, Heeryung Lee^a, Heejae Lee^a, Minjin Kim^a, Céline Eypert^b, Jean-Paul Gaston^b, Guido Roma^c, Denis Tondelier^a, Bernard Geffroy^{a,d}, Yvan Bonnassieux^a

^a LPICM, CNRS, Ecole Polytechnique, Université Paris-Saclay, 91128 Palaiseau, France

^b Horiba Jobin Yvon S.A.S., 91120 Palaiseau, France

^c DEN - Service de Recherches de Métallurgie Physique, CEA, Université Paris-Saclay, 91191 Gif sur Yvette, France

^d LICSEN, NIMBE, CEA, CNRS, Université Paris-Saclay, 91191 Gif sur Yvette, France

ARTICLE INFO

Keywords:

Perovskite solar cells

Degradation

Aging

Ellipsometry

Dielectric constant

DFT

ABSTRACT

Hybrid perovskites have emerged over the past five years as absorber layers for novel high-efficiency low-cost solar cells which combine the advantages of organic and inorganic semiconductors. One of the main obstacles to their commercialization is their poor stability under light, humidity, oxygen, and high temperatures. In this work, we compare the optical and the electrical light-induced degradation of $CH_3NH_3PbI_3$ (“MAPI”) based solar cells using real-time ellipsometry measurements, electrical measurements and X-Ray Diffraction (XRD) techniques. We evidence that while the electrical degradation takes place on a short time scale (2–3 days of exposure to ambient light conditions in a nitrogen atmosphere), no optical degradation is observed before 10 days when the dissociation reaction of methylammonium lead iodide starts acting. We find a very good agreement between XRD and ellipsometry measurements; both show the appearance of PbI_2 after 1 week of exposure. We also confirm that the main mechanism at play is a light-induced degradation affecting the edges of the stack and the interfaces between the perovskite and the neighbouring layers. Last, a very good match is obtained on the optical constants of MAPI between our ellipsometry measurements and density functional theory calculations we performed, and we confirm the behavior of MAPI as an inorganic semiconductor.

1. Introduction

Even though the efficiency of hybrid perovskite solar cells (PSCs) has jumped from 4% in 2009 to certified efficiencies over 20% [1] in 2015 and a record efficiency of 22.7% [2] in 2017, the mechanisms behind their fast degradation have yet to be fully understood. Long-term stability, in particular in terms of efficiency, is a crucial point for any photovoltaics technology to reach the market.

Niu et al. [3] gave a first general understanding of the possible pathways of the chemical decomposition of the perovskite layer in 2015. This fast degradation has been attributed to different factors, among them: humidity, temperature, oxygen, and light [4]. While many studies focused on the role played by H_2O molecules in air [5], the mechanism behind ambient light-induced degradation remains unclear. Ito and co-workers [6] used UV–Vis absorption and X-Ray Diffraction (XRD) to show that after 12 h of light exposure, $CH_3NH_3PbI_3$ (“MAPI” or $MAPbI_3$) transformed into PbI_2 , evidenced by the decreased UV–Vis absorption and XRD patterns. A possible mechanism to explain this

degradation process is [6]:



The evolution of the optical properties of hybrid perovskite thin films with time can be followed using real-time spectroscopic ellipsometry techniques [7]. Shirayama et al. [8] used this method, together with Density Functional Theory (DFT) calculations, to investigate the degradation of $CH_3NH_3PbI_3$ upon exposure to humid air.

In this paper, we compare the optical and the electrical light-induced degradation of $CH_3NH_3PbI_3$ -based solar cells using real-time ellipsometry measurements, electrical measurements and X-Ray Diffraction (XRD) techniques. Electrical characterization is performed on devices with a full solar cell structure using PEDOT-PSS as a hole transporting layer, and PCBM (Phenyl-C61-Butyric acid Methyl ester) as an electron transporting layer (see Section 2.1 for details). Ellipsometry

* Corresponding author.

E-mail address: arthur.marronnier@polytechnique.edu (A. Marronnier).

and XRD are performed on a stack consisting of all the layers up to the perovskite layer. We followed the degradation with ellipsometry for 17 days and 2–3 measurements per day.

In order to focus on light-induced degradation, the first measurements were made while keeping the cells in a nitrogen atmosphere, even during the ellipsometry characterization (see Section 2.1). We also performed complementary ellipsometry measurements both in the dark and in air, to check if the degradation measured here could result from other factors than ambient light. We found out that keeping the cell in a nitrogen atmosphere does not seem necessary in order to study the light-induced degradation. Unless otherwise specified, the degradation studies reported here are made on layers prepared by evaporation. Additional studies on solution-processed samples are shown for comparison.

We also perform Density Functional Theory (DFT) calculations to get ab-initio values for the optical constants of MAPI. In particular, we study in detail in Section 3.3 its dielectric properties. The dielectric constant in the high-frequency regime (taking into account only electronic contribution) is obtained as a second derivative of energy with respect to electric fields. The dielectric function in the visible range is computed in the Random Phase Approximation (RPA) from KS eigenvalues and eigenvectors and compared to ellipsometry measurements we performed under a nitrogen atmosphere (see Section 2.2 for computational details).

As for the static dielectric constant (low frequency regime), ionic contributions are taken into account through the coupling of phonons with the electric field. The phonons are obtained by using the linear response approach of DFT, as known as DFPT (Density-Functional Perturbation Theory), see Section 2.2. Given the structural instability and the anharmonicity behavior previously reported for halide perovskites [9–12], we made sure to properly relax the structure to avoid soft phonon modes.

The PSC community has for some time had trouble agreeing on MAPI's exciton binding energy, and on whether it behaves more like organic compounds (high exciton binding energy, low dielectric constant) or vice-versa like inorganic compounds. We use here the phonon spectrum obtained for the pseudocubic phase of $MAPbI_3$ to confirm that it behaves as an inorganic semiconductor.

2. Experimental and computational methods

2.1. Experimental

For solution process, the analyzed samples consist of layers of (from bottom to top) glass, ITO, PEDOT: PSS and $MAPbI_3$ (CH_{1-x}), the latter two made under a nitrogen atmosphere. The ITO coated glass is patterned using a wet etching process with zinc powder and HCl, cleaned with deionized H_2O (DI water), acetone and isopropanol. A PEDOT: PSS (40 nm thick) hole transport layer is deposited on the ITO substrate using a spin-coating process and heated at 120 °C for 20 min in N_2 conditions. A perovskite solution (in DMF) composed of PbI_2 , $PbCl_2$ and MAI with a 1:1:4 molar ratio is spun at 6000 r.p.m onto the PEDOT: PSS layer and heated at 80 °C for 2 h in N_2 conditions. The thickness of the obtained perovskite film is estimated to be 350–400 nm. We then deposited a filtered PCBM solution by spin coating (1-step process: 3000 rpm for 35 s) in the glove box (N_2 condition), and, without annealing, we deposited the Ag cathode using thermal evaporation.

For evaporation process, the analyzed samples also consist of layers of (from bottom to top) glass, ITO, PEDOT: PSS and $MAPbI_3$, the latter two made under a nitrogen atmosphere. ITO and PEDOT: PSS are prepared in the same way as for solution-processed cells. Then, the perovskite layer (around 250 nm) is deposited by thermal co-evaporation of MAI and PbI_2 with a 3:1 ratio on the PEDOT: PSS films. The evaporation rate is controlled by temperature through different parameters (current, voltage). In order to avoid a penetration of MAI inside the PEDOT: PSS layer, a thin layer (around 10–30 nm) of pure PbI_2 is

deposited prior to co-evaporation. After breaking the vacuum and cooling, we annealed the perovskite thin films at 80 °C for 1 h under a nitrogen atmosphere. PCBM and Ag were deposited the same way as in the solution process.

The samples are scanned by a UVISEL, a phase-modulated spectroscopic ellipsometer (HORIBA) with an incidence angle of 60 °C and a wavelength range of 0.6–4.6 eV (270–2100 nm). As MAPI is a direct transition semiconductor (in the first order approximation), the Tauc-Lorentz [13] formula is used to extract the optical constants of the perovskite layer, after having extracted PEDOT: PSS and ITO optical constants with Glass/ITO/PEDOT: PSS samples beforehand. The ellipsometry fitting parameter χ^2 is kept under 15, as it is usually the case in order to have a good match between our model and the actual optical parameters [13]. The study of the bottom layers allows to concentrate our efforts only on the perovskite. Thanks to a sealed box, the samples are kept in a N_2 atmosphere during the first ellipsometry measurements, but this seemed to be unnecessary as it did not influence the optical light-induced degradation.

For $t < 6$ days, the perovskite film is modeled using three layers to take into account the variation of index in the depth and a surface roughness layer (see Fig. 1). These 3 layers are described using the Bruggeman Effective Medium Approximation, which consists of a mix of $MAPbI_3$ and void, whose volume fraction varies for the bulk perovskite and the bottom layer. The surface roughness is described with 50% of $MAPbI_3$ and 50% of void as introduced by Aspnes et al. [14]. The volume fraction of $MAPbI_3$ decreases day by day for both layers and more importantly for the bottom layer.

For $t > 6$ days, the perovskite film is still modeled using 3 layers with variation of the different volume fractions for each layer from the bottom to the top. In addition, we included a fraction of PbI_2 in these layers (see Fig. 2).

The optical transitions of the perovskite thin film are reported in the Supporting Information file and are coherent with the literature [7].

The absorbance is measured using a UV-Vis spectrophotometer. Given the wavelength range where the signal is not saturated (500–800 nm), the only optical transition which can be followed day after day is the band gap one around 1.57 eV.

The XRD measurements were carried out on samples exposed to ambient light and done at regular times from right after fabrication to after 6 weeks of exposure. The incident angle was increased from 5° to 75° by steps of 0.03°.

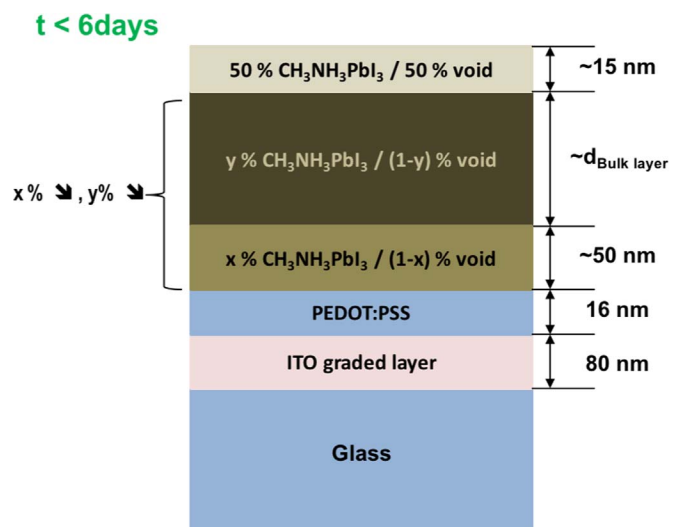


Fig. 1. Model used to fit the optical constants during the first 6 days of ageing. Layers are numbered starting from glass (L1) to the top (L6).

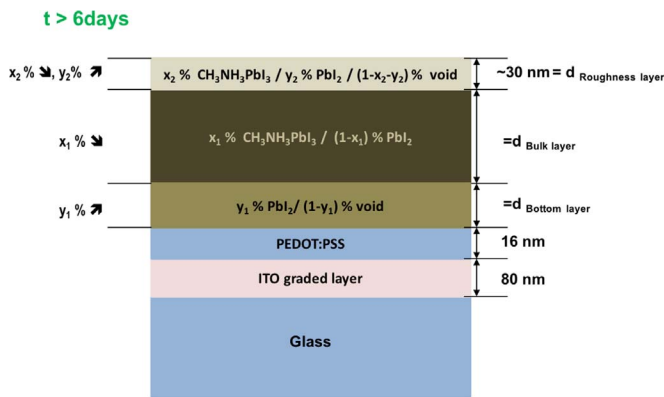


Fig. 2. Model used to fit the optical constants after the first 6 days of ageing. Layers are numbered starting from glass (L1) to the top (L6).

2.2. Computational methods

Electronic-structure calculations were performed within the Density-Functional Theory (DFT) [15,16] framework, as implemented in the Quantum Espresso (QE) code [17].

All total energy and force calculations in this work were performed with the Local Density Approximation (LDA), expanding the wave functions in a plane-wave basis set. Unless specified differently, non-relativistic (scalar-relativistic for Pb) and norm-conserving pseudopotentials were used, with the Cs [$5s^25p^6s^1$], I [$5s^25p^5$] and Pb [$5d^{10}6s^26p^2$] electrons treated as valence states.

Plane-wave cutoffs of 80 Ry were used. The Brillouin zone (BZ) was sampled with Γ -centered Monkhorst-Pack meshes [18] with a subdivision of $8 \times 8 \times 8$. Dielectric functions were calculated with the epsilon.x tool of the post-processing suite of QE, in the framework of the RPA, neglecting local field effects.

Phonon calculations were performed using the linear response approach of DFT, as known as DFPT (Density-Functional Perturbation Theory) [19], as implemented in the Quantum Espresso code [17]. High-frequency dielectric tensors and Born effective charges were calculated with linear response and used to calculate long range contributions to the dynamical matrices at Γ .

In order to eliminate some of the soft phonon modes, very tight convergence thresholds of 10^{-4} Ry/bohr for the force calculations and 10^{-14} for the phonon self-consistent algorithm were used, similar to our previous work [9].

3. Results and discussion

3.1. The first 6 days: Electrical degradation

In order to optimize the optical parameters obtained by ellipsometry during the first 6 days, we propose a model where we increase the void ratio in the MAPI layer so that the fitting parameter χ^2 is kept under 15 (see Section 2.1 for details). The results (Fig. 3) show that light-induced degradation manifests through a void ratio increasing from 0% to 30% within 3 days in the MAPI layer. The fact that such a model with only void taken into account fits the experimental optical constants means that no PbI_2 is expected to be formed during the first 6 days of exposure to light.

In parallel, we studied the electrical degradation of complete solar cells by measuring their IV characteristics over time when exposed to ambient light and nitrogen atmosphere (see Figs. 4 and 5). The electrical degradation acts very fast since the Power Conversion Efficiency (PCE) drops from 7.4% to around 4% after only 2 days for the cells made by co-evaporation. The major degradation occurs for the short circuit current (J_{SC}) and the series resistance (R_{series}). We think that the abrupt drop of series resistance (see detailed data in the Supporting

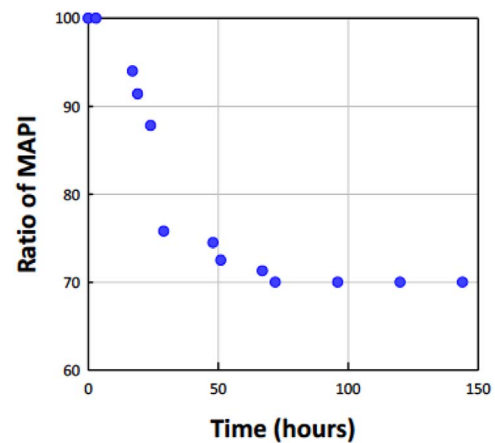


Fig. 3. Study over time of the ratio of MAPI (in %) under ambient light and nitrogen atmosphere conditions, after introducing a MAPI/void mixed layer in the ellipsometry model.

Information file) could be the sign of a degradation occurring mostly at the interfaces with other layers, as opposed to modifications in the bulk of the perovskite layer. We show in Fig. 4 (b), for comparison, the electrical degradation which occurs when the samples are exposed to both ambient light and air. The degradation in air occurs at an even higher rate than in nitrogen.

In contrast, Fig. 5 shows the electrical degradation of cells prepared using solution process instead. For such cells, the initial substantial drop in performance occurs after only 2 days, but they show better stability as J_{SC} only slightly decreases during the following 10 days.

In order to confirm the ellipsometry results showing no appearance of PbI_2 during the first 6 days of exposure, we also performed UV-Vis spectroscopy measurements. No change was observed in the optical absorption transitions. Moreover, the color of the samples did not turn to yellow, but rather remain dark brown during the first 6 days of degradation (see Fig. 6).

All these results show that whereas no optical degradation is observed for 6 days, the electrical degradation due to ambient light is very fast and the cells lose their electrical properties after only 2 days.

3.2. From day 6 to day 12: Lead iodide formation

Starting from day 6, we had to use a different ellipsometry model and include a fraction of PbI_2 in the MAPI layer in order to maintain a faithful model of the optical parameters (see Section 2.1). The results (Fig. 7 for $t > 120$ h) show that this fraction increases rapidly to more than 80% after 9–10 days. This results from the dissociation reaction of MAPI into its precursor elements lead iodide and methylammonium, as previously reported [6]. The ratio of PbI_2 reaches a limit value of approximately 88% and does not increase anymore from day 10 to day 17.

This is further confirmed by XRD measurements we performed (see Fig. 8), clearly showing the appearance of a PbI_2 peak after 1 week of exposure.

Last, the real part of the dielectric constant ϵ of the MAPI layer extracted from ellipsometry is shown in Fig. 9. Noteworthy, this data reveals that the degradation mechanism which is at play here is much faster during the day (ambient light) than during the night. This can be seen as the major changes for ϵ are observed for measurement points close to each other, which correspond to daylight conditions (see Section 2.1). This further strengthens our study and validate our approach of studying the degradation of perovskite stacks caused by ambient light. Similarly, no degradation was observed after keeping one of the samples wrapped in aluminum foil for 15 days.

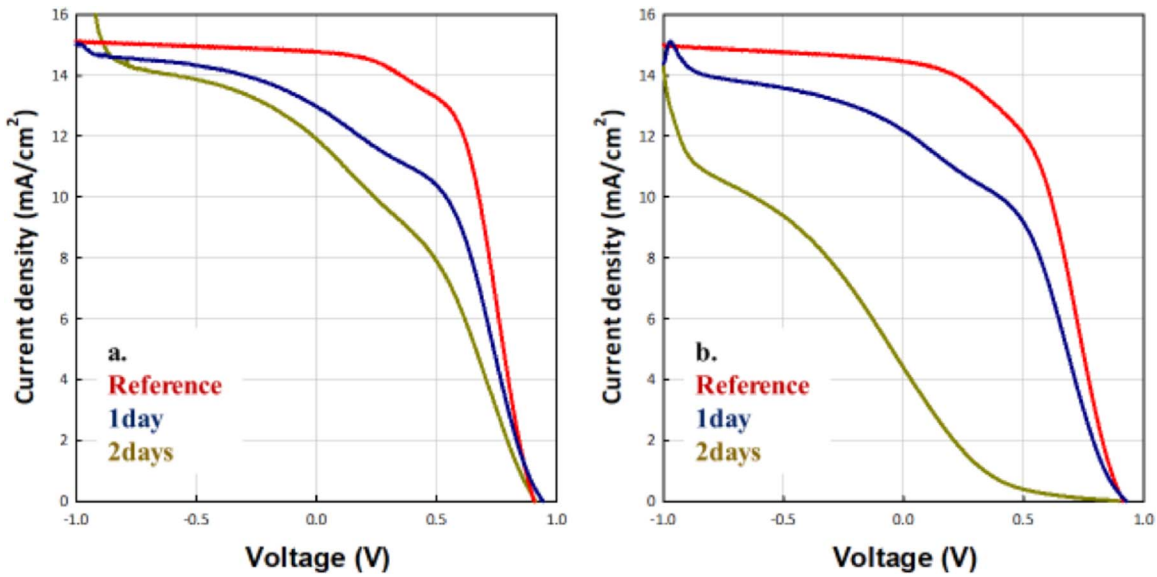


Fig. 4. Study over time of the electric properties of MAPI-based perovskite solar cells prepared by evaporation, under ambient light and nitrogen atmosphere conditions for (a) and exposed to air for (b).

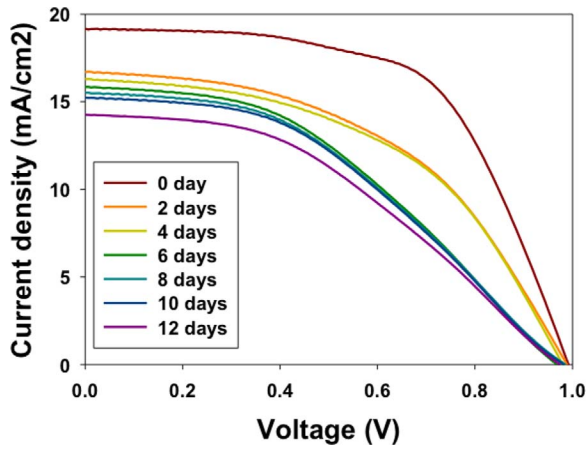


Fig. 5. Study over time of the electric properties of MAPI-based perovskite solar cells, prepared by solution process, under ambient light and nitrogen atmosphere conditions.

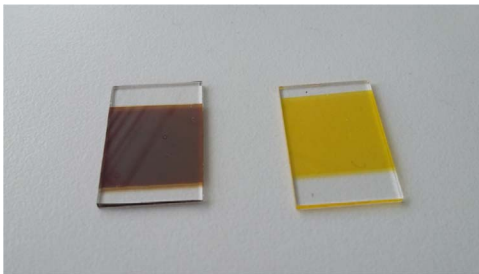


Fig. 6. MAPI-based perovskite solar cells (without the top electrodes), exposed to ambient light and kept in a nitrogen atmosphere, after 6 days (left) and 8 days (right) of degradation.

3.3. DFT analysis

The aim of our DFT analysis was to obtain the dielectric properties of $MAPbI_3$ (using its phonon spectra) and compare them to the dielectric function measured by ellipsometry.

As we previously reported [9], contrary to $CsPbI_3$, the phonon spectrum of the pseudocubic phase of the hybrid perovskite $MAPbI_3$, obtained using DFPT calculations, does not have any soft modes at the

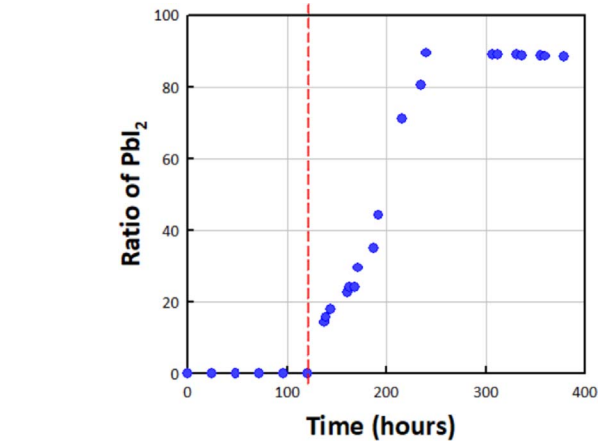


Fig. 7. Study over time of the ratio of PbI_2 (in %) in the MAPI layer under ambient light and nitrogen atmosphere conditions. The different model used for $t < 120$ hours sets $x = 0$ by definition (see Section 2.1) and is shown here for comparison.

Γ point of the Brillouin zone. This means that, provided that we use a very tight convergence threshold for the DFT relaxation, we can reach the proper equilibrium structure without the use of frozen phonon calculations.

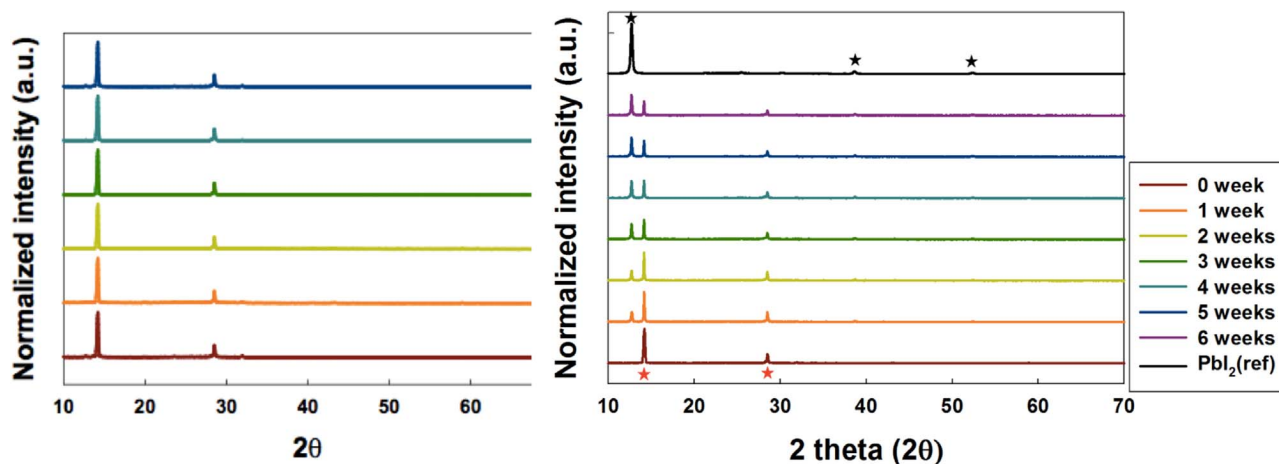
From this phonon spectrum free of soft modes, we could derive the static dielectric constant ϵ_0 . The frequency dependent dielectric function is obtained within the RPA by calculating the proper coefficients of each allowed transition between states v in the valence band and states c in the conduction band [20]:

$$\epsilon_1(\omega) = 1 + \sum_{c,v} f_{c,v} \frac{\omega_p^2}{\omega_{c,v}^2 - \omega^2} \quad (2a)$$

$$\epsilon_2(\omega) = \frac{\pi}{2} \sum_{c,v} f_{c,v} \frac{\omega_p^2}{\omega} \delta(\omega - \omega_{c,v}) \quad (2b)$$

$\omega_{c,v}$ being the transition's oscillator frequency, and ω_p the plasma frequency of the solid.

The static and high frequency dielectric constants of pseudocubic $MAPbI_3$ obtained with DFPT are:



(a) First 5 days of ageing.

(b) 6 weeks of ageing. Red and black stars represent respectively the peaks attributed to the MAPI and PbI_2 crystals.

Fig. 8. X-ray diffraction spectrum of MAPI stacks kept under a nitrogen atmosphere in ambient light.

$$\epsilon_0 = \begin{bmatrix} 14.49 & -0.06 & -0.59 \\ -0.06 & 17.64 & 0.04 \\ -0.59 & 0.04 & 18.70 \end{bmatrix} \epsilon_\infty = \begin{bmatrix} 6.19 & 0.00 & -0.22 \\ 0.00 & 6.30 & 0.00 \\ -0.22 & 0.00 & 6.44 \end{bmatrix} \quad (3)$$

The results obtained (static ϵ around 18) are coherent with low exciton binding energies, but go against the possibility of a giant dielectric constant for these hybrid perovskites, which had been reported at very low frequencies (<1 Hz) ($\epsilon \approx 1000$ in the dark [21]). They are also reasonably close to the previously reported experimental value of 30.5 [22].

The dielectric function (ϵ versus energy, Fig. 10a), calculated in the visible range, shows good concordance with the ellipsometry measurements (Fig. 10b). The real part of the dielectric function measured by ellipsometry has the same order of magnitude before the transition (5–6) as the calculated values shown in Eq. (3). The calculated imaginary part, representing the absorption of the perovskite layer, is slightly shifted to lower energies compared to ellipsometry measurements, showing an optical band gap of around 1.2 eV compared to 1.56 eV for ellipsometry. This is actually highly dependent on the smearing value chosen to calculate the different f_{cv} oscillation strength factors (see Eqs. (2a) and (2b)).

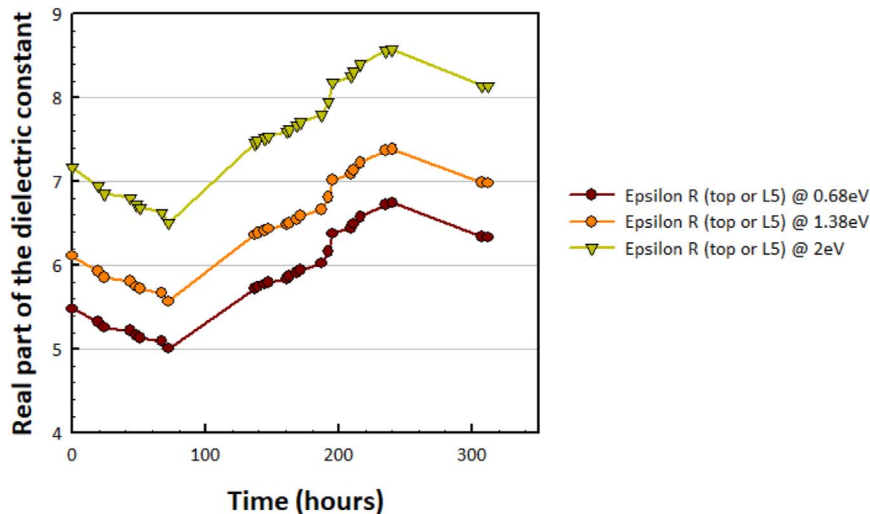
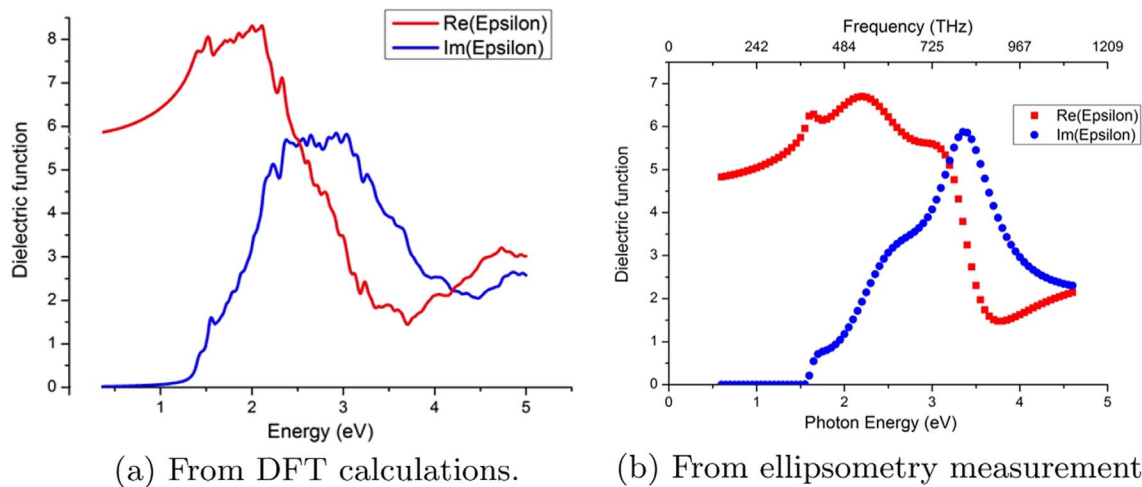


Fig. 9. Study over time of real part of the dielectric constant of the MAPI layer, as modeled from ellipsometry measurements. Close points corresponds to measures during the day, while distant points are separated by at least one night of exposure. See Section 2.1 for a detailed explanation about the layers labelling (L1 to L6).

In the Supporting Information file we show that one can play with this smearing value: the lower the smearing, the closer the band gap is to the experimental value, but also the more noise there is in the dielectric function. Check-up ab initio calculations were performed (see Supporting Information) to make sure our relaxed structure has the expected band gap, and we found a value 1.57 eV with ultrasoft pseudopotentials, this value being close to experimental values only because of a now well-known for these perovskites [23] error cancellation between the underestimation of DFT and the effect of spin orbit coupling which we do not take into account here.

In general, we think that the differences observed between Fig. 10a and 10b can be explained by several reasons. One of them is the roughness of the perovskite layer. Shirayama et al. [7] showed that ultrasmooth perovskite layers (prepared using a laser evaporation technique) can produce artifact-free measurements of $MAPbI_3$ optical constants, with an almost perfect agreement with DFT. Another reason can be the fact that our calculations are performed on the pseudocubic phase, of $MAPbI_3$ whereas the stable phase at room temperature is the tetragonal phase.

Fig. 10. Dielectric function of MAPbI_3 .

4. Concluding remarks

To summarize, we can draw two main conclusions from our degradation study under nitrogen and ambient light conditions.

First, the electrical degradation occurs on a very fast time scale: after only 2 or 3 days, the perovskite cells are almost not generating power anymore, whereas their optical absorption properties are stable at this time scale (both the optical transitions measured by UV–Vis spectroscopy and the optical constants n and ϵ obtained by ellipsometry).

Second, the dissociation reaction leading to the formation of lead iodide can be probed by fitting the optical constants obtained by ellipsometry with models including a growing ratio of PbI_2 in the MAPI layer. This model shows that the formation of lead iodide does not start before day 6, which is coherent with the stack turning yellow only after the first 6 days of exposure to light, and that the fraction of lead iodide in the MAPI layer increases until reaching a saturation value of around 90% after 9–10 days.

Using additional DFT calculations on the dielectric constants, which are in good agreement with the optical constants measured by ellipsometry, we are able to confirm the behavior of MAPI as an inorganic semiconductor with a high static dielectric constant and thus low values for the exciton binding energies.

These findings highlight the crucial importance of inhibiting the mechanisms responsible for light degradation, in addition to protecting them from oxygen, humidity and temperature, since even under a nitrogen atmosphere, the light-induced degradation is crippling for the solar cell's performance.

Further work is needed to investigate in detail the dynamics of such degradation, and especially the different mechanisms at play for the very fast electrical degradation on one hand and the slower optical degradation on the other hand.

5. Author information

5.1. Notes

The authors declare no competing financial interest.

Acknowledgements

Arthur Marronnier's PhD project is funded by the French Department of Energy (MTES) and by the Graduate School of École des Ponts ParisTech.

This work was granted access to the HPC resources of TGCC and CINES under allocation 2016090642 made by GENCI.

The authors would also like to thank A. Garcia Barker for her editing and proofreading contributions.

Appendix A. Supporting information

SI.pdf: this supporting information file is devoted to presenting some checks we made in order to show that the main differences between the DFT calculated dielectric function of MAPI and the one measured by ellipsometry measurements (see Figs. 10a and 10b) are linked to numerical artifacts and do not affect the conclusions of the paper.

We also provide detailed data about the electrical degradation and show a comparison between the dielectric properties of solution-processed and co-evaporated perovskite thin films.

Appendix B. Supplementary data

Supplementary data associated with this article can be found in the online version at <http://dx.doi.org/10.1016/j.solmat.2018.01.020>.

References

- [1] W.S. Yang, J.H. Noh, N.J. Jeon, Y.C. Kim, S. Ryu, J. Seo, S.I. Seok, High-performance photovoltaic perovskite layers fabricated through intramolecular exchange, *Science* (2015) 0036–8075.
- [2] Best Research-cell Efficiencies, 2017. (Accessed 17 October 2017) <<https://www.nrel.gov/pv/assets/images/efficiency-chart.png>>.
- [3] G. Niu, X. Guo, L. Wang, Review of recent progress in chemical stability of perovskite solar cells, *J. Mater. Chem. A* 3 (2015) 8970–8980.
- [4] D. Wang, M. Wright, N.K. Elumalai, A. Uddin, Stability of perovskite solar cells, *Sol. Energy Mater. Sol. Cells* 147 (2016) 255–275.
- [5] J.H. Noh, S.H. Im, J.H. Heo, T.N. Mandal, S.I. Seok, Chemical management for colorful, efficient, and stable inorganic-organic hybrid nanostructured solar cells, *Nano Lett.* 13 (2013) 1764–1769.
- [6] S. Ito, S. Tanaka, K. Manabe, H. Nishino, Effects of surface blocking layer of sb_2s_3 on nanocrystalline tio_2 for $\text{ch}_3\text{nh}_3\text{pb}_3$ perovskite solar cells, *J. Phys. Chem. C* 118 (2014) 16995–17000.
- [7] M. Shirayama, H. Kadowaki, T. Miyadera, T. Sugita, M. Tamakoshi, M. Kato, T. Fujiseki, D. Murata, S. Hara, T.N. Murakami, S. Fujimoto, M. Chikamatsu, H. Fujiwara, Optical transitions in hybrid perovskite solar cells: ellipsometry, density functional theory, and quantum efficiency analyses for $\text{ch}_3\text{nh}_3\text{pb}_3$, *Phys. Rev. Appl.* 5 (2016) 014012.
- [8] M. Shirayama, M. Kato, T. Miyadera, T. Sugita, T. Fujiseki, S. Hara, H. Kadowaki, D. Murata, M. Chikamatsu, H. Fujiwara, Degradation mechanism of $\text{ch}_3\text{nh}_3\text{pb}_3$ perovskite materials upon exposure to humid air, *J. Appl. Phys.* 119 (2016) 115501.
- [9] A. Marronnier, H. Lee, B. Geffroy, J. Even, Y. Bonnassieux, G. Roma, Structural instabilities related to highly anharmonic phonons in halide perovskites, *J. Phys. Chem. Lett.* 8 (2017) 2659–2665.
- [10] L.D. Whalley, J.M. Skelton, J.M. Frost, A. Walsh, Phonon anharmonicity, lifetimes, and thermal transport in $\text{ch}_3\text{nh}_3\text{pb}_3$ from many-body perturbation theory, *Phys. Rev. B* 94 (2016) 220301.
- [11] A.N. Beecher, O.E. Semonin, J.M. Skelton, J.M. Frost, M.W. Terban, H. Zhai, A. Alatas, J.S. Owen, A. Walsh, S.J.L. Billinge, Direct observation of dynamic

- symmetry breaking above room temperature in methylammonium lead iodide perovskite, *ACS Energy Lett.* 1 (2016) 880–887.
- [12] C.E. Patrick, K.W. Jacobsen, K.S. Thygesen, Anharmonic stabilization and band gap renormalization in the perovskite CsSnI_3 , *Phys. Rev. B* 92 (2015) 201205.
- [13] G.E. Jellison Jr., F.A. Modine, Parameterization of the optical functions of amorphous materials in the interband region, *Appl. Phys. Lett.* 69 (1996) 371–373.
- [14] E. Aspnes, D.J.B. Theeten, F. Hottier, Investigation of effective-medium models of microscopic surface roughness by spectroscopic ellipsometry, *Phys. Rev. B* 20 (1979).
- [15] P. Hohenberg, W. Kohn, Inhomogeneous electron gas, *Phys. Rev.* 136 (1964) B864–B871.
- [16] W. Kohn, L.J. Sham, Self-consistent equations including exchange and correlation effects, *Phys. Rev.* 140 (1965) A1133–A1138.
- [17] P. Giannozzi, S. Baroni, N. Bonini, M. Calandra, R. Car, C. Cavazzoni, D. Ceresoli, G.L. Chiarotti, M. Cococcioni, I. Dabo, A.D. Corso, S. de Gironcoli, S. Fabris, G. Fratesi, R. Gebauer, U. Gerstmann, C. Gougoussis, A. Kokalj, M. Lazzeri, L. Martin-Samos, N. Marzari, F. Mauri, R. Mazzarello, S. Paolini, A. Pasquarello, L. Paulatto, C. Sbraccia, S. Scandolo, G. Sclauzero, A.P. Seitsonen, A. Smogunov, P. Umari, R.M. Wentzcovitch, Quantum espresso: a modular and open-source software project for quantum simulations of materials, *J. Phys.: Condens. Matter* 21 (2009) 395502.
- [18] H.J. Monkhorst, J.D. Pack, Special points for brillouin-zone integrations, *Phys. Rev. B* 13 (1976) 5188–5192.
- [19] S. Baroni, S. de Gironcoli, A. Dal Corso, P. Giannozzi, Phonons and related crystal properties from density-functional perturbation theory, *Rev. Mod. Phys.* 73 (2001) 515–562.
- [20] F. Giustino, *Materials Modelling Using Density Functional Theory: Properties and Predictions*, Oxford University Press, 2014.
- [21] E.J. Juarez-Perez, R.S. Sanchez, L. Badia, G. Garcia-Belmonte, Y.S. Kang, I. Mora-Sero, J. Bisquert, Photoinduced giant dielectric constant in lead halide perovskite solar cells, *J. Phys. Chem. Lett.* 5 (2014) 2390–2394.
- [22] A. Poglitsch, D. Weber, Dynamic disorder in methylammonium-trihalogenoplumbates (ii) observed by millimeter-wave spectroscopy, *J. Chem. Phys.* 87 (1987) 6373–6378.
- [23] L. Pedesseau, J.-M. Jancu, A. Rolland, E. Deleporte, C. Katan, J. Even, Electronic properties of 2d and 3d hybrid organic/inorganic perovskites for optoelectronic and photovoltaic applications, *Opt. Quantum Electron.* 46 (2014) 1225–1232.

Supporting Information:

Electrical and Optical Degradation Study of Methylammonium-based Perovskite Materials under Ambient Conditions

Arthur Marronnier,[†] Heeryung Lee,[†] Heejae Lee,[†] Minjin Kim,[†] Céline Eypert,[‡]
Jean-Paul Gaston,[‡] Guido Roma,[¶] Denis Tondelier,[†] Bernard Geffroy,^{†,§} and Yvan
Bonnassieux*,[†]

[†]*LPICM, CNRS, Ecole Polytechnique, Université Paris-Saclay, 91128 Palaiseau, France*

[‡]*Horiba Jobin Yvon S.A.S., 91120 Palaiseau, France*

[¶]*DEN - Service de Recherches de Métallurgie Physique, CEA, Université Paris-Saclay,
91191 Gif sur Yvette, France*

[§]*LICSEN, NIMBE, CEA, CNRS, Université Paris-Saclay, 91191 Gif sur Yvette, France*

E-mail: arthur.marronnier@polytechnique.edu

This supporting information file is devoted to presenting some checks we made in order to show that the main differences between the DFT calculated dielectric function of MAPI and the one measured by ellipsometry measurements (see figure 1) are linked to numerical artifacts and do not affect the conclusions of the paper.

We also provide detailed data about the electrical degradation and show a comparison between the dielectric properties of solution-processed and co-evaporated perovskite thin films.

Influence of the smearing parameters on the absorption offset

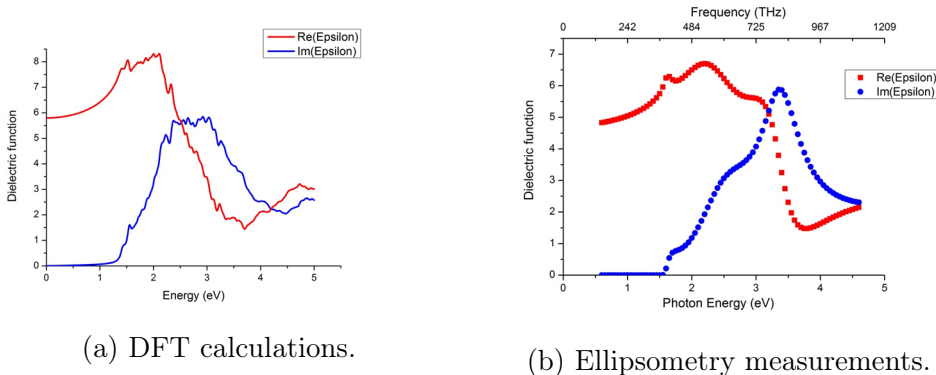


Figure 1: Dielectric function of $MAPbI_3$

The main difference is a left-shift of the calculated imaginary part of the dielectric constant (absorption) compared to the one measured by ellipsometry, which shows a good value for the band gap around 1.57 eV, whereas a band gap of around 1.2-1.3 eV can be seen on figure 1a. On figures 2 and 3 we can check that our DFT calculations give a band gap in good agreement with experiments (1.50 eV, or 1.57 if we use ultrasoft pseudopotentials). This value is very close to the experimental optical band gap only because of a (now well-known for these perovskites¹) error cancellation between the underestimation of DFT and the effect of spin orbit coupling which we do not take into account here.

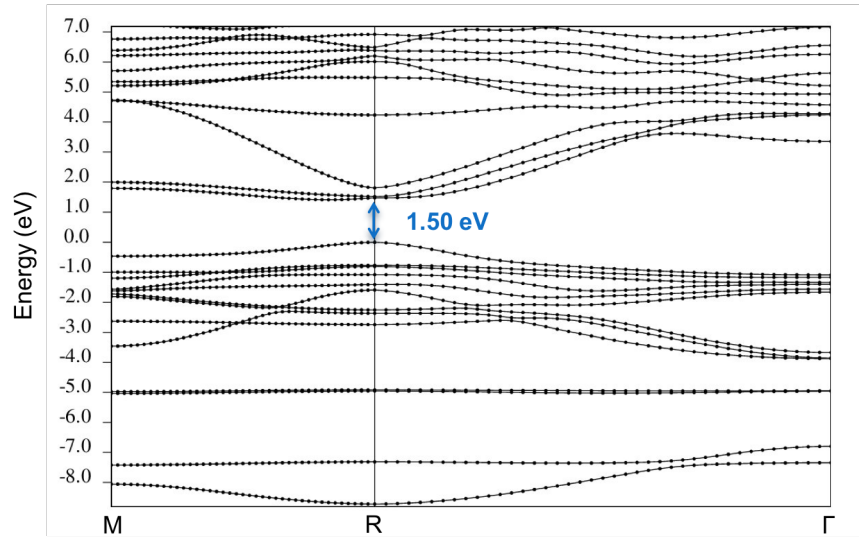


Figure 2: Energy bands of the pseudo-cubic phase of MAPI using norm-conserving pseudopotentials.

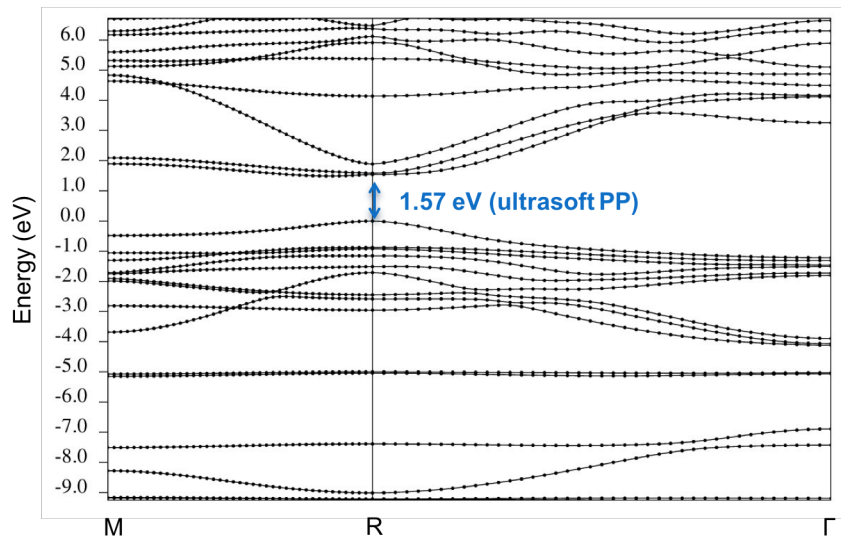


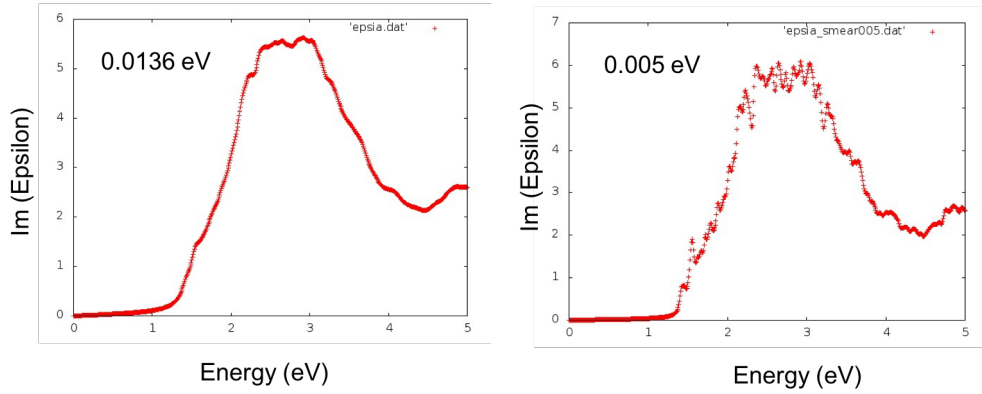
Figure 3: Energy bands of the pseudo-cubic phase of MAPI using ultra-soft pseudopotentials.

Now, in order to better understand why we have this left shift for the imaginary part of the dielectric function, we changed the smearing value chosen to calculate the oscillator strength f_{cv} for each transition (see equation 1a). The results (figure 4) show that there is

a tradeoff between the accuracy of the dielectric constant and the shift in the band gap.

$$\epsilon_1(\omega) = 1 + \sum_{c,v} f_{c,v} \frac{\omega_p^2}{\omega_{c,v}^2 - \omega^2} \quad (1a)$$

$$\epsilon_2(\omega) = \frac{\pi}{2} \sum_{c,v} f_{c,v} \frac{\omega_p^2}{\omega} \delta(\omega - \omega_{c,v}) \quad (1b)$$



(a) Smearing of 13.6 meV

(b) Smearing of 5 meV.

Figure 4: Imaginary part of the dielectric function of $MAPbI_3$ calculated by DFT for different smearing values of the f_{cv} parameter in equation 1b.

Electrical degradation

Table 5 shows detailed data about the electrical degradation of our samples prepared by evaporation.

	J_{sc} (mA/cm²)	V_{oc} (V)	FF (%)	PCE (%)	R_{shunt} (Ω)	R_{series} (Ω)
Day0 3 PM	14.9	0.9	55.8	7.41	1650	35.9
Day1 10AM	13.0	0.9	44.6	5.47	216	98.9
Day1 3PM	11.1	0.8	19.3	1.6	70.3	90.6
Day2 10AM	11.9	0.9	36.7	3.98	141	69.8

(a)

	J_{sc} (mA/cm²)	V_{oc} (V)	FF (%)	PCE (%)	R_{shunt} (Ω)	R_{series} (Ω)
Day0 3 PM	14.5	0.9	47.7	6.23	681	59.8
Day1 10AM	12.2	0.9	40.9	4.63	199	135
Day1 3PM	8.8	1.0	14.6	1.28	79.6	434
Day2 10AM	4.4	0.9	10.7	0.42	80.4	1030

(b)

Table 5: Study over time of the electric properties of MAPI-based perovskite solar cells prepared by evaporation, under ambient light and nitrogen atmosphere conditions for (a) and exposed to air for (b).

Impact of the synthesis method

Figure 6 shows a comparison between the dielectric properties of solution-processed and co-evaporated perovskite thin films.

Two observations can be made.

First of all, the optical transitions (1.55 eV, 2. eV, 3. eV) are coherent with the literature.²

Then, while the optical band gap is the same in both cases, there is a left shift on the second transition for the solution processed film: the peak is less sharp and occurs around

2.5 eV

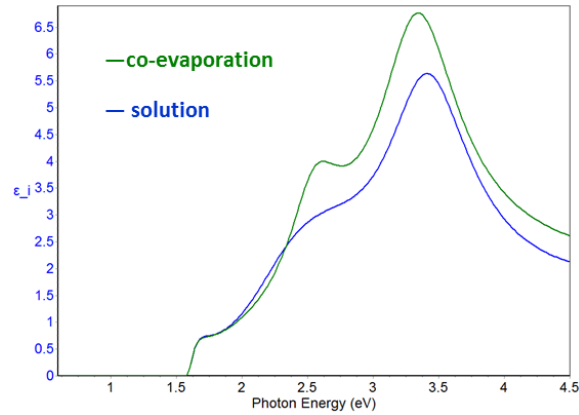


Figure 6: Imaginary part of the dielectric constant measured by ellipsometry for samples made by solution process or co-evaporation.

References

- (1) Pedesseau, L.; Jancu, J.-M.; Rolland, A.; Deleporte, E.; Katan, C.; Even, J. Electronic Properties of 2D and 3D Hybrid Organic/Inorganic Perovskites for Optoelectronic and Photovoltaic Applications. *Optical and Quantum Electronics* **2014**, *46*, 1225–1232.
- (2) Shirayama, M.; Kadowaki, H.; Miyadera, T.; Sugita, T.; Tamakoshi, M.; Kato, M.; Fujiseki, T.; Murata, D.; Hara, S.; Murakami, T. N. et al. Optical Transitions in Hybrid Perovskite Solar Cells: Ellipsometry, Density Functional Theory, and Quantum Efficiency Analyses for CH₃NH₃PbI₃. *Phys. Rev. Applied* **2016**, *5*, 014012.

5.4 HYBRID PEROVSKITES: ORGANIC OR INORGANIC SEMICONDUCTORS?

In this short section, we report additional calculations we performed to complete the results on the structural instabilities of section 4.2 and the discussion on the dielectric constant of hybrid perovskites (previous section).

The general aim here is to study how our findings on the structural instabilities in $CsPbI_3$ can impact the dielectric properties of this material.

The DFPT method used to obtain the dielectric tensor both in the high frequency and in the static regime were detailed in section 3.4.

On figures 5.4.1 and 5.4.2 we summarize all the dielectric tensors for the 4 phases of $CsPbI_3$ as well as for the pseudocubic phase of $MAPbI_3$ in both frequency regimes. The symmetric ($\eta = 0$) and broken symmetry structures ($\eta \neq 0$) correspond to relaxed structures optimized starting from respectively the maximum and the minimum of the double-well energy surface. For the cubic phase we used the volume relaxed structures (the lattice is kept perfectly cubic) and in the orthorhombic case we did a full relaxation (atomic positions and all three lattice parameters) with the lattice angles kept fixed.

In the previous section we already discussed how the results for hybrid perovskite $MAPbI_3$ allow us to confirm the behavior of MAPI as an inorganic semiconductor with a relatively high - yet not giant - static dielectric constant and thus low values for the exciton binding energies, coherently with what was experimentally evidenced with the use of high magnetic fields [7].

As for $CsPbI_3$, the dielectric matrices for the orthorhombic δ -phase show that it is only when taking into account the anharmonic potential and using the broken symmetry structure that we find a high static dielectric constant, coherent with the inorganic nature of this perovskite. The reader should recall that this increase in the static dielectric constant when breaking the symmetry is accompanied by an increase in the band gap (see Publication 2). In the cubic and tetragonal phases, the impact of the structural instabilities is reduced.

This means that our findings on the double-well energy surface are crucial to have a comprehensive understanding not only of the band structures but also in general of the dielectric and optical properties of $CsPbI_3$.

CsPbI_3	Symmetric structure $\eta = 0$		Broken symmetry $\eta \neq 0$	
	• δ -phase	$\epsilon_\infty = \begin{bmatrix} 3.83 & & \\ & 4.63 & \\ & & 4.35 \end{bmatrix}$	$\epsilon_0 = \begin{bmatrix} 5.84 & 0.00 & 0.00 \\ 0.00 & 7.90 & 0.00 \\ 0.00 & 0.00 & 7.24 \end{bmatrix}$	$\epsilon_\infty = \begin{bmatrix} 5.31 & & \\ & 5.19 & \\ & & 4.68 \end{bmatrix}$
• γ -phase	$\epsilon_\infty = \begin{bmatrix} 6.19 & & \\ & 5.71 & \\ & & 5.74 \end{bmatrix}$	$\epsilon_0 = \begin{bmatrix} 23.76 & & \\ & 17.46 & \\ & & 20.58 \end{bmatrix}$	No anharmonicity	
• β -phase	$\epsilon_\infty = \begin{bmatrix} 6.01 & & \\ & 6.01 & \\ & & 5.63 \end{bmatrix}$	$\epsilon_0 = \begin{bmatrix} 18.12 & & \\ & 18.12 & \\ & & 16.00 \end{bmatrix}$		
• α -phase	$\epsilon_\infty = \begin{bmatrix} 5.88 & & \\ & 5.88 & \\ & & 5.88 \end{bmatrix}$	$\epsilon_0 = \begin{bmatrix} 20.70 & & \\ & 20.70 & \\ & & 20.70 \end{bmatrix}$	$\epsilon_\infty = \begin{bmatrix} 6.48 & & \\ & 6.50 & \\ & & 6.45 \end{bmatrix}$	$\epsilon_0 = \begin{bmatrix} 25.67 & 2.65 & 1.08 \\ & 27.42 & -0.65 \\ & & 27.42 \end{bmatrix}$

Figure 5.4.1: Dielectric matrices of CsPbI_3 in the high-frequency (ϵ_∞) and static (ϵ_0) regimes obtained from DFPT.

MAPbI_3	Symmetric structure $\eta = 0$		Broken symmetry $\eta \neq 0$	
	Pseudocubic	$\epsilon_\infty = \begin{bmatrix} 6.19 & -0.00 & -0.22 \\ -0.00 & 6.30 & 0.00 \\ -0.22 & 0.00 & 6.44 \end{bmatrix}$	$\epsilon_0 = \begin{bmatrix} 14.49 & -0.06 & -0.59 \\ -0.06 & 17.64 & 0.04 \\ -0.59 & 0.04 & 18.70 \end{bmatrix}$	No anharmonicity

Figure 5.4.2: Dielectric matrices of MAPbI_3 in the high-frequency (ϵ_∞) and static (ϵ_0) regimes obtained from DFPT.

5.5 OXYGEN DEFECTS IN MAPI

As explained in chapter 2, Yin *et al.* published in 2014 a precious and comprehensive study of all the possible intrinsic defects in MAPI [4]. In particular, they showed that the intrinsic defects that create deep levels in the band gap and could in theory largely reduce the open circuit voltage and trigger carrier recombinations, such as I_{Pb} , I_{MA} , Pb_i and Pb_I , all have high formation energies and are thus very unlikely to be present in the material at room temperature. In 2016, Mosconi *et al.* could rationalize the annihilation of the numerous V_I^+ / I_i^- Frenkel pairs with light irradiation thanks to DFT calculations and photoluminescence measurements. They also showed that V_I^+ and I_i^- are the fastest migrating defects, consistently with previous studies [8–11].

Very recently, Meggiolaro *et al.* [12] provided a model to explain the high defect tolerance of MAPI and the deactivation of electron traps using the specificities of iodine redox chemistry in these materials. They also showed that an O_2 -rich environment can lock down the remaining hole traps. These results further understanding of the role played by oxygen in the interaction between hybrid perovskites and their environment.

In this section, we aim at obtaining, from ab-initio calculations, an insight on the thermodynamical stability of oxygen defects in the pseudocubic phase of $MAPbI_3$, as well as their consequence on the electronic band structure. We first focus on neutral oxygen defects (both interstitial and substitutional) in the perovskite lattice. Then, we study the case of charged defects for nitrogen and hydrogen substitutions.

5.5.1 METHODS

Geometry optimization, total energy calculations and electronic band structures were performed using the plane-wave projector augmented wave (PAW) implementation with the PBE method available in the VASP software [13–15], in particular with the I [$5s^2 5p^5$] and Pb [$6s^2 6p^2$] electrons treated as valence states.

We constructed $2 \times 2 \times 2$ supercells from the optimized single cells (see table 5.5.1).

A Γ -centered $6 \times 6 \times 6$ (resp. $3 \times 3 \times 3$) k points grid is used for the single (resp. super) cell.

As for the electronic band structures, we did not take into account spin-orbit coupling. The obtained band gaps are reasonably close to the experimental values due to an error cancellation between the general underestimation of the band gap in DFT ground state calculations and the giant spin-orbit coupling (SOC) that was found for the conduction band [16].

In Angstroms	Relaxed single cell	Relaxed $2 \times 2 \times 2$ supercell
a	6.364	12.717
b	6.219	12.433
c	6.285	12.546

Table 5.5.1: Lattice parameters (in Angstroms).

5.5.2 INTERSTITIAL AND SUBSTITUTIONAL OXYGEN DEFECTS

There are two possible interstitial sites in the cubic perovskite structure :

- 8 tetrahedral sites (figure 5.5.1)
- 1 octahedral sites already occupied by the organic molecule (figure 5.5.2)

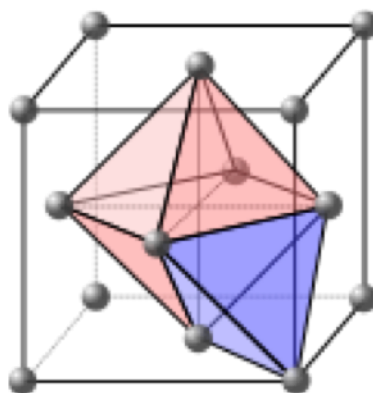


Figure 5.5.1: Tetrahedral sites (in blue) in the cubic perovskite structure.

As for substitutional oxygen defects, we explore the thermodynamics of (Kröger–Vink notation) O_I , O_N , O_H and O_{2H} .

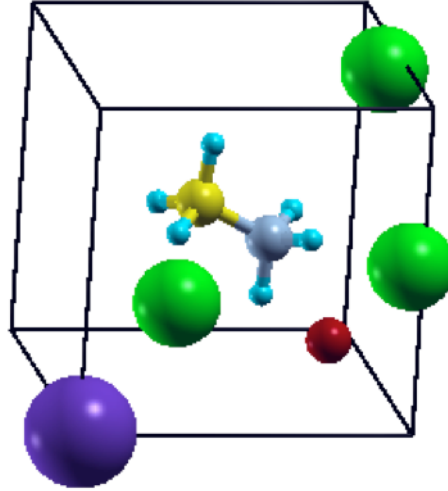


Figure 5.5.2: The octahedral site is occupied by the organic molecule. The red, purple, green, yellow, grey and blue atoms respectively denote O, Pb, I, C, N and H.

5.5.3 FORMATION ENTHALPIES OF NEUTRAL DEFECTS

In order to derive the formation enthalpies H_f^{defect} of these neutral defects, we use the following traditional approach [17]:

$$H_f^{defect}(O_X) = H(O_X) - H_{tot}^{perfect} - \mu_O + n_X \mu_X \quad (5.2)$$

for the substitution of n_X elements X by an atom of oxygen, where μ is the chemical potential of the corresponding atom. We derived μ_O as $\frac{1}{2}\mu_{O_2}$, μ_H as $\frac{1}{2}\mu_{OH}$, μ_I as $\frac{1}{2}\mu_{I_2}$ and μ_N as $\frac{1}{2}\mu_{N_2}$.

In table 5.5.2, we summarize the formation enthalpies of these various oxygen defects (constant pressure calculations). Among them, the interstitial and 2H substitutional defects appear to be the most favorable ones with a positive enthalpy close to 0.

Interstitial	O_I	O_N	O_H	O_{2H}
0.30	0.95	1.06	5.77	0.08

Table 5.5.2: Formation enthalpies (eV).

In particular this was expected for O_{2H} as this defect corresponds to the formation of a carbonyl group (see figure 5.5.3), similar to what was found in Ref [18] for polyethylene and small alkane molecules.

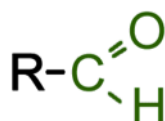


Figure 5.5.3: Carbonyl group (aldehyde).

The C=O double bond cannot be formed in the case of the O_H defects, whose formation energy is much higher: in this case the geometry optimization (figure 5.5.4) of the defective cell resulted in a migration of the inserted oxygen atom from the substitutional hydrogen site to what seems to be an interstitial site inside the inorganic octahedra PbI_6 .

The substitution of two hydrogen atoms by one oxygen leads to the formation (figure 5.5.5) of a C=O double bond, whose length, 1.19 Angstroms, is typical of double carbon-oxygen bonds (1.12 Å in CO_2) and in close agreement with the C=O double bond of a carbonyl group in polyethylene.

5.5.4 ELECTRONIC PROPERTIES AND CHARGED DEFECTS

For reference, we show on figures 5.5.6 and 5.5.7 the electronic band structures of respectively the pristine pseudocubic $MAPbI_3$ single cell and $2 \times 2 \times 2$ supercell. As expected, the band gap folds from the R point of the single cell to the Γ point of the supercell. The $2 \times 2 \times 2$ supercell has an even number of electrons: 320 electrons and thus 160 filled valence bands.

On figures 5.5.8 to 5.5.11 we report the electronic band structures of the structure with interstitial oxygen and O_I , O_N and O_H defects. Noteworthy, it is only in the nitrogen and hydrogen case that the

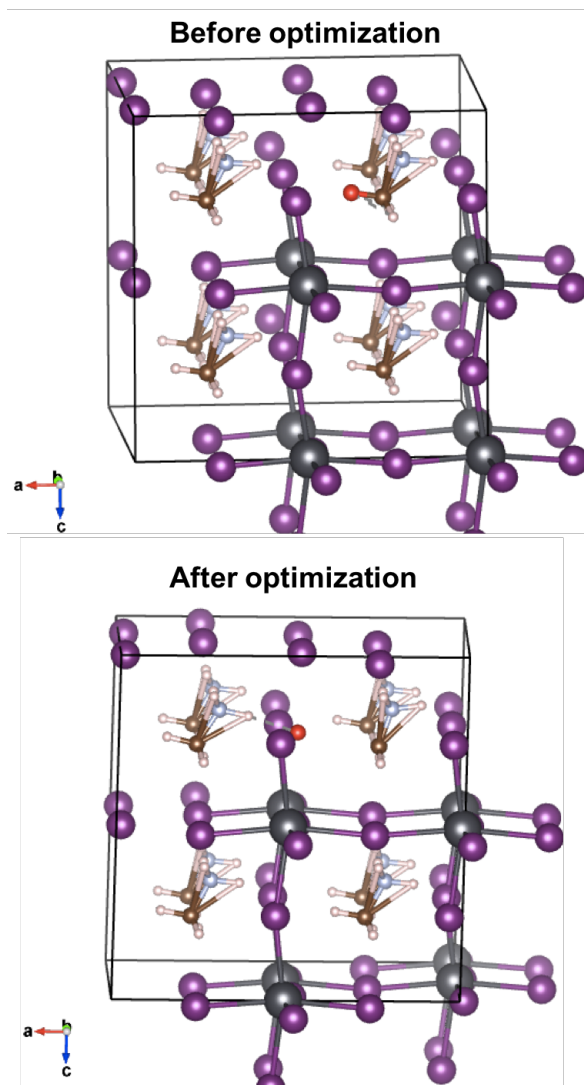


Figure 5.5.4: Migration of the inserted oxygen atom from the substitutional hydrogen site to what seems to be an interstitial site inside the inorganic octahedra PbI_6 after geometry optimization. The red, dark grey, purple, brown, light grey and white atoms respectively denote O, Pb, I, C, N and H.

oxygen defect creates a flat band, located inside the band gap, that clearly comes from the oxygen contribution as seen when projected on the oxygen states (density of states). These half-filled states (odd number of electrons in the system) constitute thus a possible trap states for electrons (O_N case) or holes (O_H case). These can act as recombination centers under the photovoltaic operation of the material. For

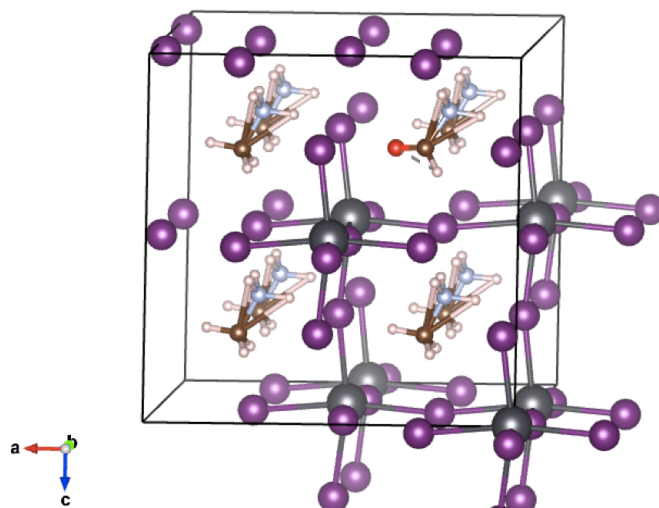


Figure 5.5.5: Substitution of 2 hydrogen atoms by 1 oxygen, structure after geometry optimization. The red, dark grey, purple, brown, light grey and white atoms respectively denote O, Pb, I, C, N and H.

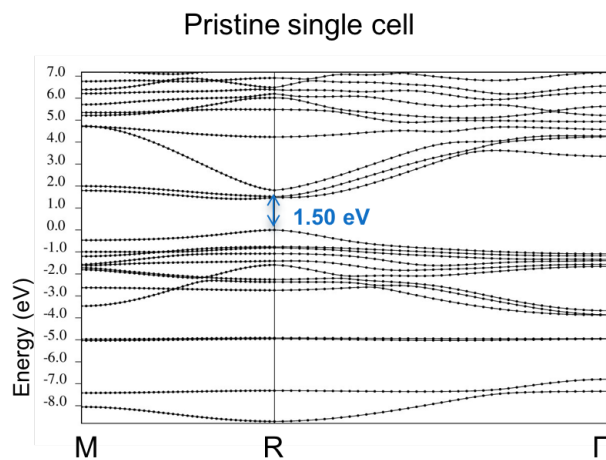


Figure 5.5.6: Electronic band structure of the pristine $MAPbI_3$ single cell.

the O_I defects, the defect creates states under the band gap that are rather deep. As for the interstitial defect, it creates rather shallow valence states.

From this electronic structure analysis, and given the presence of these trap states in the nitrogen and

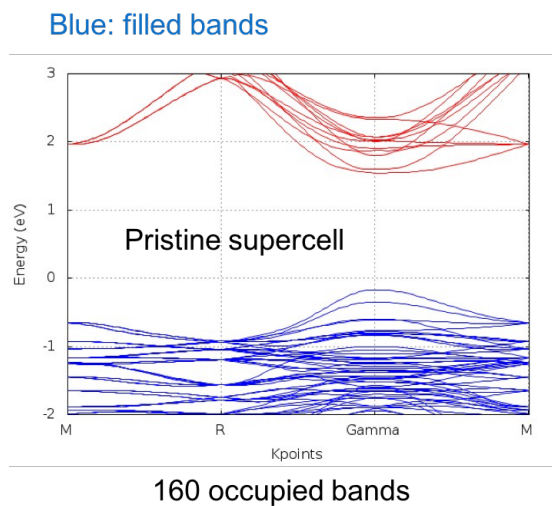


Figure 5.5.7: Electronic band structure of the pristine $MAPbI_3$ $2 \times 2 \times 2$ supercell. Fully occupied bands are shown in blue.

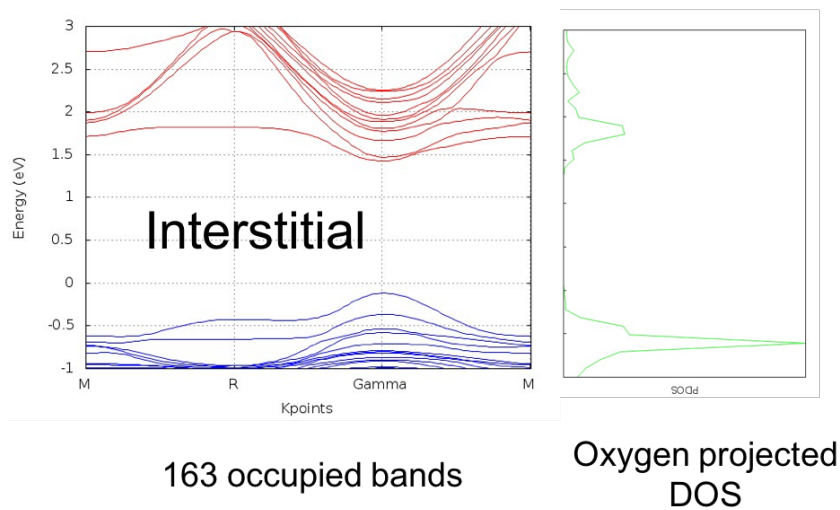


Figure 5.5.8: Electronic band structure and oxygen projected density of states (DOS) of the structure with an interstitial oxygen atom.

hydrogen substitutions, it is interesting to consider charged defects. We thus calculated the formation enthalpy (table 5.5.3) of O_H^+ , O_H^- , O_N^+ and O_N^- .

It is known that for charged defects the convergence of the long-ranged Coulomb interaction between

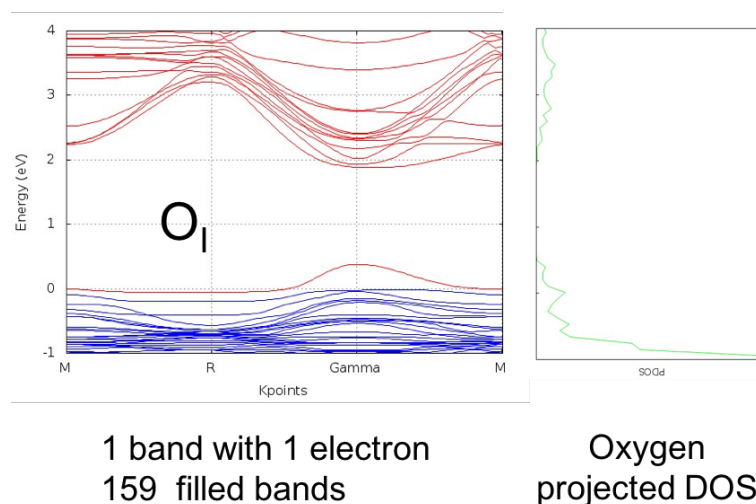


Figure 5.5.9: Electronic band structure and oxygen projected density of states (DOS) of the structure with the O_I defect.

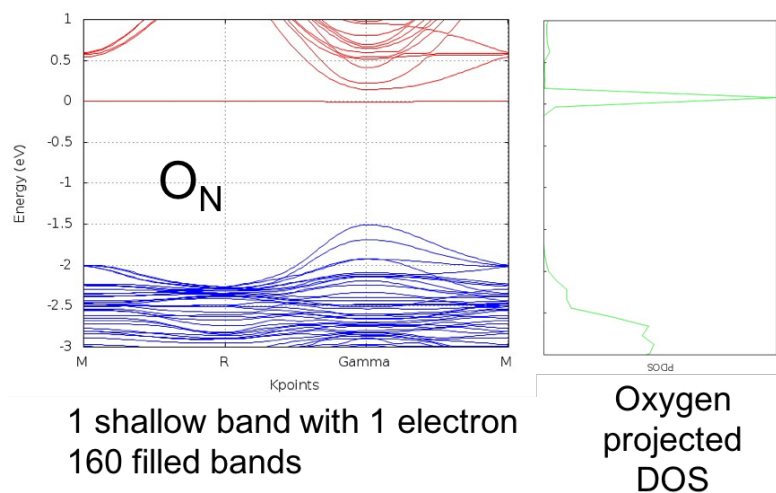


Figure 5.5.10: Electronic band structure and oxygen projected density of states (DOS) of the structure with the O_N defect.

the localized charge distributions is very slow. Instead of using very large supercells, we corrected *a posteriori* the calculated formation energies considering the model proposed by Makov and Payne [19]:

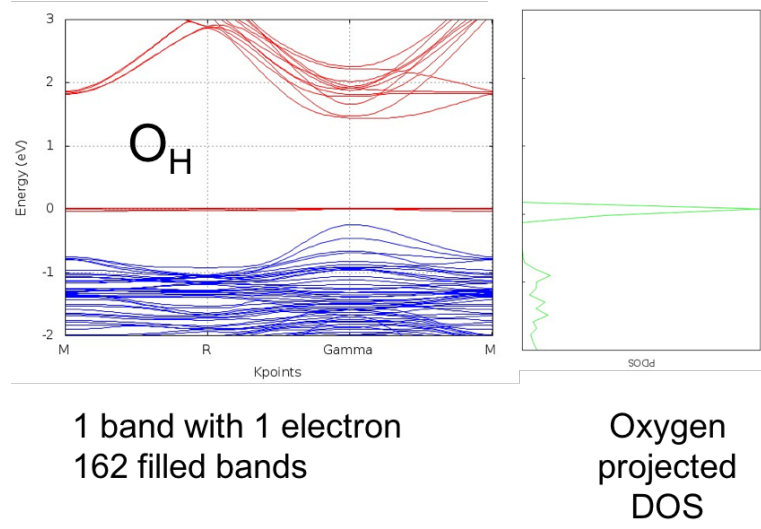


Figure 5.5.11: Electronic band structure and oxygen projected density of states (DOS) of the structure with the O_H defect.

$$E = E_o + \frac{q^2 \alpha}{2L\epsilon} + \frac{2\pi q Q}{3L^3 \epsilon} + O(L^{-5})$$

where E_o is the non-corrected ground state energy, Q the quadrupole moment, q the electrostatic charge, L the lattice parameter and α the Madelung constant.

The first term of the equation, the monopole term (also called Madelung correction) was applied in the charged defect formation enthalpy calculations.

Taking into account the electrostatic potential linked to the Fermi level, the charged defect's formation enthalpy then reads:

$$H_f^{defect}(O_X^q) = qE_{Fermi}^{abs} + H_o + \frac{q^2 \alpha}{2L\epsilon} + O(L^{-3}) \quad (5.3)$$

where the Fermi energy is defined with respect to the valence band top energy E_{VBT} as:

$$E_{Fermi}^{abs} = E_{Fermi}^{rel} + E_{VBT} \quad (5.4)$$

All the formation enthalpies of charged defects shown in table 5.5.3 are calculated for $E_{Fermi}^{abs} = E_{VBT}$. In the nitrogen substitution case, we find a negative formation enthalpy for the +1 charged defect: the

oxygen defect acts as an electron donor close to the conduction band, this corresponds to a p-like doping. On the opposite, the -1 charged defect is less favorable than its neutral equivalent. In the hydrogen substitution case, we find a lower formation enthalpy for both the +1 and -1 charged defects: the oxygen defect could act as an electron donor or acceptor but is strongly unfavorable.

O_N	O_N^+	O_N^-	O_H	O_H^+	O_H^-
1.06	-1.22	3.95	5.77	2.31	4.04

Table 5.5.3: Formation enthalpies of charged defects (in eV). The corresponding neutral defects' formation enthalpy are recalled for reference. The Fermi level is taken at the valence band top.

5.6 [PUBLICATION 4] HYSTERESIS AND IONIC MIGRATION

Apart from their environmental stability, which is the main topic of this chapter, one of the most detrimental features in perovskite solar cells is the so-called "anomalous hysteresis" phenomenon observed mostly for inverted structures. In chapter 2 we explained how the efficiency value can be overestimated if the voltage scanning rate is too high for the cell to reach its electronic steady-state equilibrium. We also detailed the several possible explanations for this phenomenon that have been reported in the literature: ferroelectric domains, giant dielectric constant, trap states and ion migration.

In this manuscript we have already encountered and studied some aspects of the first three phenomena. Indeed, in section 4.2 I showed how the structural instabilities revealed by the soft phonon polar mode can be at the origin of ferroelectricity in $CsPbI_3$. In sections 5.3 and 5.4 we investigated the dielectric properties of both *MAPI* and $CsPbI_3$, showing results that go against the possibility of a giant dielectric constant. Last, oxygen trap states were studied in detail in the previous section.

Here, we provide the reader with a brief analysis and a few comments around the forth article published during my PhD (by H. Lee *et al.* [3]) about the experimental evidence of halide ionic migration in *MAPI*-based solar cells. As I did not bring the major contribution to this experimental work, my part being limited to the result analysis, I chose not to include the publication itself in this manuscript.

In this work, we used glow discharge optical emission spectrometry (GD-OES) to evidence the ionic migration of halogen components in $CH_3NH_3PbI_{3-x}Cl_x$ thin films under an electrical bias. In particular, we show that while no migration is observed for lead and nitrogen for a polarization applied for 2 minutes, chloride and iodide ions migrate over 120 nm, which corresponds to approximately one third of the perovskite layer's thickness.

If ferroelectricity was already excluded as a possible significant factor contributing to the photocurrent hysteresis in 2014 when Xiao *et al.* [20] discovered a giant switchable photovoltaic effect and showed that ion migration could drastically impact the electric performance, much more work was needed in order to clearly and directly evidence the migrating species and the migration range. The link between ion migration and hysteresis has been formally established in a comprehensive work in 2015 [21] where it was shown that the build-up of space charge at the contact can be at the origin of the photocurrent hysteresis. This work evidenced that this phenomenon does not depend on the illumination. This is one of the reasons why we focused in our work on migration under an electrical bias.

The direct observation of ion migration within the halide perovskite layer was also evidenced by other

experimental methods, for MA^+ [22] as well as for I^- [23]. As discussed in our article [3], the activation energies for ionic migration in MAPI were derived from first principles calculations [11] which allowed to identify vacancy-assisted migration of iodide as the most likely channel of ionic conduction (activation energy of 0.6 eV). This suggests that hybrid halide perovskites behave as ionic–electronic conductors.

REFERENCES

- [1] Arthur Marronnier, Heeryung Lee, Heejae Lee, Minjin Kim, Céline Eypert, Jean-Paul Gaston, Guido Roma, Denis Tondelier, Bernard Geffroy, and Yvan Bonnassieux. Electrical and optical degradation study of methylammonium-based perovskite materials under ambient conditions. *Solar Energy Materials and Solar Cells*, 178:179–185, 2018.
- [2] Dian Wang, Matthew Wright, Naveen Kumar Elumalai, and A Uddin. Stability of perovskite solar cells. *Sol. Energy Mater. Sol. Cells*, 147:255–275, 04 2016.
- [3] Heejae Lee, Sofia Gaiaschi, Patrick Chapon, Arthur Marronnier, Heeryung Lee, Jean-Charles Vanel, Denis Tondelier, Jean-Eric Boureé, Yvan Bonnassieux, and Bernard Geffroy. Direct experimental evidence of halide ionic migration under bias in $CH_3NH_3PbI_{3-x}Cl_x$ -based perovskite solar cells using gd-oes analysis. *ACS Energy Letters*, 2(4):943–949, 2017.
- [4] Wan-Jian Yin, Tingting Shi, and Yanfa Yan. Unusual defect physics in $CH_3NH_3PbI_3$ perovskite solar cell absorber. *Applied Physics Letters*, 104(6):063903, 2014.
- [5] W. Jr. Chase. *NIST-JANAF Thermochemical Tables*. American Institute of Physics, 1998.
- [6] John W Wilson. Standard enthalpies of formation and thermodynamic cycle values of crystal lattice energies of methylammonium halides. *Journal of the Chemical Society, Dalton Transactions*, (10): 890–893, 1976.
- [7] Atsuhiko Miyata, Anatolie Mitioglu, Paulina Plochocka, Oliver Portugall, Jacob Tse-Wei Wang, Samuel D Stranks, Henry J Snaith, and Robin J Nicholas. Direct measurement of the exciton binding energy and effective masses for charge carriers in organic-inorganic tri-halide perovskites. *Nature Physics*, 11(7):582–587, 2015.
- [8] Jon M. Azpiroz, Edoardo Mosconi, Juan Bisquert, and Filippo De Angelis. Defect migration in methylammonium lead iodide and its role in perovskite solar cell operation. *Energy Environ. Sci.*, 8: 2118–2127, 2015.
- [9] Simone Meloni, Thomas Moehl, Wolfgang Tress, Marius Franckevičius, Michael Saliba, Yong Hui Lee, Peng Gao, Mohammad Khaja Nazeeruddin, Shaik Mohammed Zakeeruddin, Ursula

- Rothlisberger, et al. Ionic polarization-induced current–voltage hysteresis in $\text{CH}_3\text{NH}_3\text{PbX}_3$ perovskite solar cells. *Nature communications*, 7:10334, 2016.
- [10] Jun Haruyama, Keitaro Sodeyama, Liyuan Han, and Yoshitaka Tateyama. First-principles study of ion diffusion in perovskite solar cell sensitizers. *Journal of the American Chemical Society*, 137(32): 10048–10051, 2015.
- [11] Christopher Eames, Jarvist M Frost, Piers RF Barnes, Brian C O’regan, Aron Walsh, and M Saiful Islam. Ionic transport in hybrid lead iodide perovskite solar cells. *Nature communications*, 6:7497, 2015.
- [12] Daniele Meggiolaro, Silvia G. Motti, Edoardo Mosconi, Alex J. Barker, James Ball, Carlo Andrea Riccardo Perini, Felix Deschler, Annamaria Petrozza, and Filippo De Angelis. Iodine chemistry determines the defect tolerance of lead-halide perovskites. *Energy Environ. Sci.*, 11:702–713, 2018. doi: 10.1039/C8EE00124C. URL <http://dx.doi.org/10.1039/C8EE00124C>.
- [13] G. Kresse and J. Furthmüller. Efficient iterative schemes for ab initio total-energy calculations using a plane-wave basis set. *Phys. Rev. B*, 54:11169–11186, Oct 1996. doi: 10.1103/PhysRevB.54.11169. URL <https://link.aps.org/doi/10.1103/PhysRevB.54.11169>.
- [14] G. Kresse and J. Furthmüller. Efficiency of ab-initio total energy calculations for metals and semiconductors using a plane-wave basis set. *Comput. Mater. Sci.*, 6(1):15 – 50, 1996. ISSN 0927-0256. doi: [http://dx.doi.org/10.1016/0927-0256\(96\)00008-0](http://dx.doi.org/10.1016/0927-0256(96)00008-0). URL <http://www.sciencedirect.com/science/article/pii/0927025696000080>.
- [15] M. Shishkin and G. Kresse. Implementation and performance of the frequency-dependent *gw* method within the paw framework. *Phys. Rev. B*, 74:035101, Jul 2006. doi: 10.1103/PhysRevB.74.035101. URL <https://link.aps.org/doi/10.1103/PhysRevB.74.035101>.
- [16] Jacky Even, Laurent Pedesseau, Jean-Marc Jancu, and Claudine Katan. Importance of spin–orbit coupling in hybrid organic/inorganic perovskites for photovoltaic applications. *The Journal of Physical Chemistry Letters*, 4(17):2999–3005, 2013.

REFERENCES

- [17] Hannu-Pekka Komsa, Tapio T. Rantala, and Alfredo Pasquarello. Finite-size supercell correction schemes for charged defect calculations. *Phys. Rev. B*, 86:045112, Jul 2012. doi: 10.1103/PhysRevB.86.045112. URL <https://link.aps.org/doi/10.1103/PhysRevB.86.045112>.
- [18] Guido Roma, Fabien Bruneval, and Layla Martin-Samos. Optical properties of saturated and unsaturated carbonyl defects in polyethylene. *The Journal of Physical Chemistry B*, 122(6): 2023–2030, 2018. doi: 10.1021/acs.jpcc.7b12172. URL <https://doi.org/10.1021/acs.jpcc.7b12172>. PMID: 29360369.
- [19] G Makov and MC Payne. Periodic boundary conditions in ab initio calculations. *Physical Review B*, 51(7):4014, 1995.
- [20] Zhengguo Xiao, Yongbo Yuan, Yuchuan Shao, Qi Wang, Qingfeng Dong, Cheng Bi, Pankaj Sharma, Alexei Gruverman, and Jinsong Huang. Giant switchable photovoltaic effect in organometal trihalide perovskite devices. *Nature materials*, 14, 12 2014.
- [21] Wolfgang Tress, Nevena Marinova, Thomas Moehl, Shaik Mohammad Zakeeruddin, Mohammad Khaja Nazeeruddin, and Michael Grätzel. Understanding the rate-dependent j–v hysteresis, slow time component, and aging in $\text{CH}_3\text{NH}_3\text{PbI}_3$ perovskite solar cells: the role of a compensated electric field. *Energy & Environmental Science*, 8(3):995–1004, 2015.
- [22] Yongbo Yuan, Jungseok Chae, Yuchuan Shao, Qi Wang, Zhengguo Xiao, Andrea Centrone, and Jinsong Huang. Photovoltaic switching mechanism in lateral structure hybrid perovskite solar cells. *Advanced Energy Materials*, 5(15), 2015.
- [23] Tae-Youl Yang, Giuliano Gregori, Norman Pellet, Michael Grätzel, and Joachim Maier. The significance of ion conduction in a hybrid organic–inorganic lead-iodide-based perovskite photosensitizer. *Angewandte Chemie*, 127(27):8016–8021, 2015.

I do not know what I may appear to the world, but to myself I seem to have been only like a boy playing on the seashore, and diverting myself in now and then finding a smoother pebble or a prettier shell than ordinary, whilst the great ocean of truth lay all undiscovered before me.

Isaac Newton

6

Conclusion & Perspectives

THROUGHOUT THIS MANUSCRIPT, we have used several ab-initio and experimental methods to investigate the structural and environmental instabilities of hybrid and inorganic perovskites as well as the possible phenomena behind the hysteretic behavior of perovskite solar cells.

In regards to structural instabilities, I revealed (Publications 1 & 2) a very flat energy landscape and double well features on three of the four phases of $CsPbI_3$ (including the tetragonal phase that we evidenced for the first time in Publication 2). We have shown that taking into account the instabilities of the inorganic sublattice is crucial in order to better understand the electronic structure, the dielectric properties and the phase competition of $CsPbI_3$ in particular and halide perovskite materials in general.

Further work is needed to understand the link between these inorganic lattice fluctuations and the instability of $MAPbI_3$, in particular by taking into consideration the translation-rotation coupling of the organic molecule. The underlying ferroelectricity in these perovskites could be linked to the polar structural fluctuations we report here, also leading to a dynamical Rashba effect as previously proposed

for similar perovskite structures. Even though we gave some hints on this topic, a more detailed ferroelasticity study is needed for CsPbI_3 . The low-energy highly occupied phonon states we found will also need to be taken into account in order to give new theoretical estimates of electronic and optical properties (e.g., the band gap or the exciton binding energy). It could also help improve electron–phonon coupling calculations and help better understand the electronic properties, as it was shown that this coupling can deeply impact the charge-carrier mobilities in these perovskites. Mixing Cs with other cations, like the organic ones used in most recent versions of hybrid PSCs, affects the coupling in the double-well network, which could help explain the mechanisms through which mixed-cation PSCs have shown promising improvements in efficiency and stability with respect to MAPbI_3 -based perovskite solar cells. Further calculations are also needed in order to estimate and possibly avoid the anharmonic entropy term associated to the order–disorder or displacive transition to the non-perovskite δ -phase and be able to keep CsPbI_3 in its black phase at room temperature. This point is crucial in the quest for stable and highly efficient perovskite solar cells.

As for the sensitivity of hybrid perovskites to the environmental parameters (temperature, humidity, oxygen, light), we have evidenced (Publication 3) the light-induced degradation timescales of the electrical (current-voltage studies) and optical (ellipsometry, optical indexes) properties of these materials. Our study brings better understanding of the chemical decomposition of MAPI into its two precursors, methylammonium and lead iodides, which we predicted using DFT stability diagram calculations. Last, we used the results of our optical constant study, completed by ab initio calculations, to answer the controversy and prove that hybrid perovskite structure MAPbI_3 behaves more like inorganic compounds (high dielectric constant, low exciton binding energy) than like organic materials (low dielectric constant, high exciton binding energy).

These findings highlight the crucial importance of inhibiting the mechanisms responsible for light degradation, in addition to protecting cells from oxygen, humidity and temperature, since even under a nitrogen atmosphere, the light-induced degradation is crippling for the solar cell's performance. Further work is needed to investigate in detail the dynamics of such degradation, and especially the different mechanisms at play for the very fast electrical degradation on one hand and the slower optical degradation on the other hand.

We also analyzed the formation enthalpy and the consequences on the electronic band structures of oxygen interstitial and substitutional defects in MAPbI_3 . Throughout this study, we have shown in particular that substitutional defects O_{2H} and O_N^+ (possible p-type doping) are the most

thermodynamically favorable defects in this material. Further work is needed to investigate the thermodynamics of such oxygen defects at the surface of the material, as it was shown that interface recombination could be the limiting factor for the cells' efficiency.

The work I contributed to regarding halide migration under an electrical bias (Publication 4) must be furthered investigated in parallel with a detailed study on the I-V curves' hysteresis under dark conditions. In particular, our next goal is to study the evolution of the dark current with temperature and analyze it in terms of activation and migration energies of possible defects, which should mostly consist of iodine vacancies according to theoretical predictions.

I am confident that this thesis work will further understanding of the electronic properties and both the structural and environmental instabilities of halide perovskites, a necessary step towards the realization of fully stable and highly efficient perovskite solar cells, that can be used in various situations thanks to their flexibility and easy fabrication processes (windows, flexible surfaces, "solar paint"...) as well as to complement silicon solar cells in tandem structures.

7

Publications, Collaborations & Awards

SEVERAL PARTS OF THE WORK PRESENTED IN THIS THESIS were done in collaboration with other research groups, in particular :

- The perovskite group in Rennes, France who has a precious expertise on ab-initio studies on perovskite materials (Jacky Even, Laurent Pedesseau, Claudine Katan and Soline Boyer-Richard).
- Prof. M. Kanatzidis and Dr. C. Stoumpos from Northwestern University, USA, for their expertise in crystal synthesis and synchrotron XRD.
- Prof. P. De Angelis and Dr. E. Mosconi from Perugia University, Italy (CNR - CHLYO) for their expertise in molecular dynamics in perovskites.

Publications

- 2018 1. **Arthur Marronnier**, Guido Roma, Soline Boyer-Richard, Laurent Pedesseau, Jean-Marc Jancu, Yvan Bonnassieux, Claudine Katan, Constantinos C. Stoumpos, Mercouri G. Kanatzidis and Jacky Even.
Anharmonicity and Disorder in the Black Phases of Cesium Lead Iodide used for Stable Inorganic Perovskite Solar Cells.
ACS Nano 2018 DOI: 10.1021/acsnano.8b00267
Received January 11, 2018; Accepted March 22, 2018; Published March 22, 2018
- 2018 2. **Arthur Marronnier**, Heeryung Lee, Heejae Lee, Minjin Kim, Céline Eyfert, Jean-Paul Gaston, Guido Roma, Denis Tondelier, Bernard Geffroy and Yvan Bonnassieux.
Electrical and Optical Degradation Study of Methylammonium-based Perovskite Materials under Ambient Conditions
Solar Energy Materials and Solar Cells 2018 178:179–185.
Received November 19, 2017; Revised January 5, 2018; Published February 6, 2018
- 2017 3. **Arthur Marronnier**, Heejae Lee, Bernard Geffroy, Jacky Even, Yvan Bonnassieux, and Guido Roma. Structural Instabilities Related to Highly Anharmonic Phonons in Halide Perovskites.
The Journal of Physical Chemistry Letters 2017 8 (12), 2659-2665.
Received April 4, 2017; Accepted May 29, 2017; Published May 29, 2017
- 2017 4. Heejae Lee, Sofia Gaiaschi, Patrick Chapon, **Arthur Marronnier**, Heeryung Lee, Jean-Charles Vanel, Denis Tondelier, Jean-Eric Bourée, Yvan Bonnassieux, and Bernard Geffroy. Direct Experimental Evidence of Halide Ionic Migration under Bias in $\text{CH}_3\text{NH}_3\text{PbI}_{3-x}\text{Cl}_x$ -Based Perovskite Solar Cells Using GD-OES Analysis.
ACS Energy Letters 2017 2 (4), 943-949.
Received February 23, 2017; Accepted March 31, 2017; Published March 31, 2017

Awards

Jan. 2018 **2018 Siebel Prize in Energy Science**

Siebel Scholars form an exceptional community of leaders in business, computer science, bioengineering, and energy science. They serve as key advisors and join forces with world-renowned experts and authorities to examine today's most pressing issues and explore solutions that will have lasting impact.

Jan. 2018 **Finalist: My PhD in 180 seconds** regional competition, Paris-Saclay University, France
MT180 is a science popularization competition organized by CNRS at a national level where PhD students have to share their research work in 3 minutes¹.



May 2017 **Best Oral Presentation**, JPH Conference, Angers, France

Nov. 2016 **1st Prize: My PhD in 6 Minutes competition**, Paris-Saclay University, France
My PhD in 6 minutes is a competition organized by Paris-Saclay University where PhD students have to share their research work to the general public in a 6-minute presentation².



1. My video can be found here: <https://youtu.be/mfCA054o-g8>
2. My video can be found here: <https://youtu.be/ID117CKH4EQ>

Research Projects and Collaborations

July 2017. –
Jan. 2018

International Collaboration, Northwestern University, USA
Prof. M. Kanatzidis and Dr. C. Stoumpos
In situ synchrotron XRD analysis of the phase transitions of CsPbI₃.

Oct. – Dec. 2017

Visiting PhD Fellow at Perugia University, Italy
Advisor: Prof. F. De Angelis (CLHYO)
CPMD calculations analysis in the light of our findings on the double well instability in the cubic phase of CsPbI₃.

Jan. 2016 –
June 2017

Research Project, Horiba company, France
Advisor: J-P. Gaston
Used ellipsometry measurements, XRD and electrical characterization in order to explore the degradation mechanisms of hybrid methylammonium-based perovskites.

Jan. – Dec. 2016

Synchrotron – Perovskites Project, Synchrotron SOLEIL, France
STXM technique used for the first time on hybrid perovskites to investigate inhomogeneities and ionic migration under an external bias.

Teaching Experience

2015 –
2017

Teaching Fellow, École Polytechnique, France
Responsible for the lab class on Semiconductors and Solar Cells Physics *From Quantum Theory to Photovoltaics Applications* for senior undergraduate/first-year Master's students. In charge of the lectures, the experimental procedure and setup, and grading.

Conferences and Workshops

- June 2018 **45th IEEE PVSC Conference**, Hawaii, USA
30' *Extended* Oral Presentation
- March 2018 **Regional Final of My PhD in 180 seconds**, Paris-Saclay University, France
Oral Presentation (competition)
- Jan. 2018 **AP-HOPV 2018 Conference**, Kyushu, Japan
15' Oral Presentation
- Sept. 2017 **33rd EUPVSEC Conference**, Amsterdam, the Netherlands
15' Oral Presentation
- May 2017 **JPH Conference**, Angers, France
20' Oral Presentation
- Apr. 2017 **Webinar on Perovskite Solar Cells**, Horiba company, France
Keynote Speaker and Co-Organizer¹
- Jan. 2017 **IPEF Energy and Environmental Science Workshop**, Paris, France
20' Oral Presentation
- Dec. 2016 **JNPV Conference**, Dourdan, France
Poster Presentation
- Nov. 2016 **My PhD in 6 Minutes**, Paris-Saclay University, France
Oral Presentation (competition)
- Sept. 2016 **2nd PSCO Conference**, Genoa, Italy
15' Oral Presentation
- July 2016 **Nanotechnology Summer School**, Thessaloniki, Greece
Poster Presentation
- May 2016 **JPH Conference**, Rennes, France
20' Oral Presentation



1. My webinar video can be found here: <https://youtu.be/ZU00nfn9P84>

A

Appendix

A.1 BRILLOUIN ZONE CONVENTIONS

Figures A.1.1, A.1.2 and A.1.3 show the classic definitions of the high-symmetry points of the Brillouin zone for respectively the cubic, tetragonal and orthorhombic lattices [1]:

$\times \mathbf{b}_1$	$\times \mathbf{b}_2$	$\times \mathbf{b}_3$		$\times \mathbf{b}_1$	$\times \mathbf{b}_2$	$\times \mathbf{b}_3$	
0	0	0	Γ	$\frac{1}{2}$	$\frac{1}{2}$	$\frac{1}{2}$	R
$\frac{1}{2}$	$\frac{1}{2}$	0	M	0	$\frac{1}{2}$	0	X

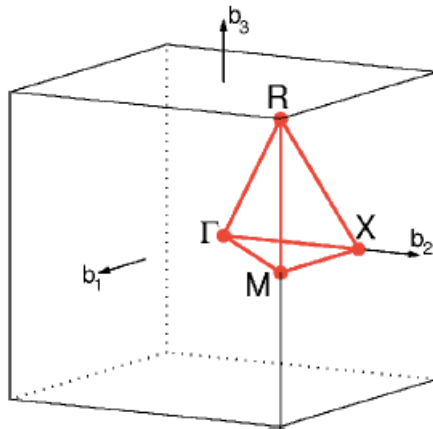


Figure A.1.1: Cubic lattice

$\times \mathbf{b}_1$	$\times \mathbf{b}_2$	$\times \mathbf{b}_3$		$\times \mathbf{b}_1$	$\times \mathbf{b}_2$	$\times \mathbf{b}_3$	
0	0	0	Γ	0	$\frac{1}{2}$	$\frac{1}{2}$	R
$\frac{1}{2}$	$\frac{1}{2}$	$\frac{1}{2}$	A	0	$\frac{1}{2}$	0	X
$\frac{1}{2}$	$\frac{1}{2}$	0	M	0	0	$\frac{1}{2}$	Z

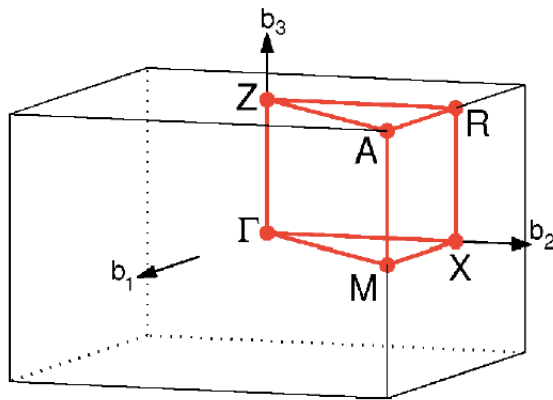


Figure A.1.2: Tetragonal lattice

$\times \mathbf{b}_1$	$\times \mathbf{b}_2$	$\times \mathbf{b}_3$		$\times \mathbf{b}_1$	$\times \mathbf{b}_2$	$\times \mathbf{b}_3$	
0	0	0	Γ	$\frac{1}{2}$	0	$\frac{1}{2}$	U
$\frac{1}{2}$	$\frac{1}{2}$	$\frac{1}{2}$	R	$\frac{1}{2}$	0	0	X
$\frac{1}{2}$	$\frac{1}{2}$	0	S	0	$\frac{1}{2}$	0	Y
0	$\frac{1}{2}$	$\frac{1}{2}$	T	0	0	$\frac{1}{2}$	Z

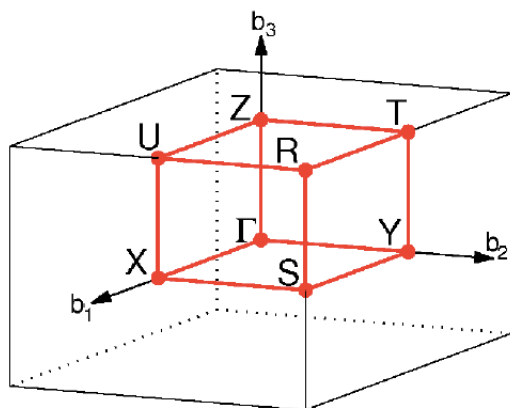


Figure A.1.3: Orthorhombic lattice

REFERENCES

- [1] Wahyu Setyawan and Stefano Curtarolo. High-throughput electronic band structure calculations: Challenges and tools. *Computational Materials Science*, 49(2):299–312, 2010.

Listing of figures

1.1.1	Evolution of the Earth’s average temperature.	3
1.1.2	Evolution of the global carbon emissions due to fossil fuels over the last century.	4
1.2.1	Comparison between the amount of solar energy absorbed by the Earth in one year and the fossil fuel recoverable reserves. Ref. [3]	5
1.2.2	Evolution of the energy cost (in dollars per watt peaks) for silicon-based solar cells since 1977. Source: Bloomberg, 2014.	6
1.2.3	Evolution and forecast of the watt cost for a PV module and possible future cost reduction triggers. To give a point of reference, a price of \$1 per Watt is the target cost to achieve to be competitive on the market. Source : SEMI PV Group, 2010.	7
1.2.4	Comparison between residential PV energy cost and the electricity cost in several countries. Source : McKinsey, 2014.	8
1.2.5	In Germany, the emergence of PV already has a noticeable impact on the overall country’s electricity production profile. Source: German Ministry of Energy, 2013.	8
1.2.6	Electricity load needed in addition to the production of variable energies (“net” load). Source: CAISO/Jordan Wirfs-Brock	9
1.2.7	Electricity production, in particular through solar PV, is only one element of the complex energy transition landscape. Ref. [7]	10
1.3.1	Shockley–Queisser limit. Ref [8]	12
1.3.2	Main generations of solar cells as defined by Martin Green in 2001 [9], much before the rise of perovskite materials as light absorbers.	13

1.3.3	General architecture of a Dye Sensitized Solar Cell (DSSC). The charges are photo-generated by the photosensitive dye and separated at the surface between the dye, the TiO_2 semiconductor and electrolyte. They are then transported through the electrolyte layer to the transparent conductive oxides (TCO). Source: wikipedia	14
2.1.1	Ideal perovskite cubic structure (ABX_3). Ref. [2]	21
2.1.2	Crystal structure of the flagship hybrid organic-inorganic material for PV $CH_3NH_3PbI_3$, also referred to as $MAPbI_3$ or "MAPI".	21
2.2.1	General architecture of a solid-state perovskite solar cell. The electron (resp. hole) interface layer is also called the electron (resp. hole) transporting layer (ETL) (resp. HTL). Ref. [10]	23
2.2.2	Evolution of perovskite solar cells structures from DSSCs to solid-state cells. Ref. [11]	24
2.2.3	Overview of the perovskite solar cells structure's evolutionary paths. Ref. [12]	24
2.2.4	Emerging thin film technologies. Ref. [13]	26
2.2.5	NREL efficiency chart. Multijunction cells, for which the Shockley–Queisser limit of 33.7% does not apply, are shown for comparison. Ref [13]	27
2.2.6	Estimation of the cost of a perovskite module depending on its power conversion efficiency. Ref. [2, 12]	28
2.3.1	Band structure (left) and density of states (right) of $MAPbI_3$ in its cubic phase calculated with density functional theory (PBE), including spin-orbit coupling. Ref. [27]	30
2.3.2	Summary of the main PV materials' band gaps and record efficiencies. Ref [30]	31
2.3.3	Comparison of the V_{OC} drop (difference between the optical band gap and the actual V_{OC} value) for different materials. Ref. [11]	32
2.4.1	Perovskite solar cells: parallel between the efficiency race and the quest for stability. Ref [49]	33
2.5.1	The hysteretic behavior strongly depends on the solar cell architecture. Ref. [60]	36
2.6.1	The band gap tunability of $FAPbI_yBr_{3-y}$ is limited for tandem applications: no structure is found in the 1.6 - 1.8 eV window. Ref [31]	38
2.6.2	Mixing FA and Cs allows the formation of solid-state alloys and prevents the formation of their δ -phases. Ref [83]	39
3.2.1	DFT self-consistency algorithm [4].	59

3.2.2	DFT geometry optimization algorithm [4]. A damping term is introduced to update the nuclear position and navigate in the potential-energy surface towards the global energy minimum.	61
3.4.1	Schematic view of the dielectric function in its different frequency regimes. Source: wikipedia.	66
3.5.1	Schematic view of a molecular dynamics algorithm. The initial temperature and the number x are inputs to the code.	69
4.1.1	Given the similarities with its tin cousin $CsSnI_3$, four phases are expected for $CsPbI_3$. The red arrow represent the phase transformation upon heating from the room temperature δ -phase while the blue ones represent the phases encountered while cooling. Figure taken from Ref [7]	75
4.2.1	Potential energy surface of the orthorhombic δ -phase of $CsPbI_3$	94
4.2.2	Zoom from figure 4.2.1.	94
4.4.1	Potential energy surface from frozen phonon calculations of cubic $CsPbI_3$ along the eigenvector of the unstable optical phonon at Γ as a function of displacement parameter η . The $3N$ dimensional displacement needed to reach the new minimum corresponds to around 0.43\AA , including a 0.36\AA displacement for the cesium atom.	115
4.4.2	Displacement eigenvector corresponding to one of the 3 triply degenerated soft phonon modes found at Γ for cubic $CsPbI_3$. Its irreducible representation is the infrared-active Γ_4^- representation. The blue, purple and green atoms respectively denote Cs, Pb and I. We chose to label as "x" the axis parallel to which this chosen distortion mostly occurs.	116
4.4.3	a. Displacement eigenvector corresponding to the soft phonon mode found at Γ for cubic $CsPbI_3$. Its irreducible representation is the infrared-active Γ_4^- representation. b. Displacement vectors to reach, from the maximum structure, the relaxed non-cubic minimum structure. The blue, purple and green atoms respectively denote Cs, Pb and I.	117
4.4.4	Simplified representations of the supercells used to study the influence of spatial domains A/B or "x up"/"x down" on the electronic band structure.	120
4.4.5	Electronic band structure (including SOC) of the unit cell of cubic $CsPbI_3$	120
4.4.6	Electronic band structure (including SOC) of the $1 \times 1 \times 2$ supercell. As the cell is slightly orthorhombic (see the Methods subsection 4.4.1), we use here the orthorhombic q-point convention.	121

4.4.7	Electronic band structure (including SOC) of the $2 \times 1 \times 1$ supercell. As the cell is slightly orthorhombic (see the Methods subsection 4.4.1), we use here the orthorhombic q-point convention.	122
4.4.8	Volume fluctuations along the CPMD trajectories at 370 K and 450 K.	122
4.4.9	Lattice parameters fluctuations along the CPMD trajectory at 370 K.	123
4.4.10	Fluctuations of the distance to the average pseudocubic structure, as defined in Eq. 4.2.	124
4.4.11	Energy histogram of the 40 ps trajectory at 370 K. The boxes size is 0.05 eV.	125
4.4.12	Distribution function of the cesium-lead pairs' distances along the MD trajectory. The narrow, Dirac-like peaks correspond to our 0 Kelvin DFT reference distances in the maximum perfectly symmetric structure. The vertical axis is arbitrary and chosen for better visibility.	126
4.4.13	Distribution function of the cesium-lead pairs' distances along the MD trajectory. Here the references (narrow peaks) correspond to the distances for the maximum structure, weighted by the ratio of the average lattice parameters of the trajectory over the ones of the 0 Kelvin DFT reference.	127
4.4.14	Distribution function of the cesium-lead pairs' distances along the MD trajectory, for intervals' lengths of 1, 5, 10 and 40 ps. Here the references (narrow peaks) correspond to the distances for the maximum structure, weighted by the ratio of the average lattice parameters of the trajectory over the ones of the DFT reference.	128
4.4.15	Distribution function of the cesium-lead pairs' distances along the MD trajectory. Here the references (narrow peaks) correspond to the distances for the maximum structure, weighted by the ratio of the average lattice parameters of the trajectory over the ones of the DFT reference.	129
4.4.16	Distribution function of the cesium-lead pairs' distances along the MD trajectory. Here the references (narrow peaks) correspond to the distances for the maximum structure, weighted by the ratio between the lattice parameters.	129
4.4.17	Distribution function of the cesium-lead pairs' distances along the MD trajectory. Here the references (narrow peaks) correspond to the distances for the maximum structure, weighted by the ratio between the lattice parameters.	130
4.4.18	Distribution function of the cesium-lead pairs' distances along the MD trajectory. Here the references (narrow peaks) correspond to the distances for the maximum structure.	130

4.4.19	Energy difference between the CBM and the VBT for the 50 points chosen in the MD trajectory. For each of the 50 snapshots, this difference is set to 0 at Γ to allow better comparison. The figures in blue represent the average values over the 50 points of the trajectory.	132
4.4.20	Conduction band minimum energy. For each of the 50 time steps, this energy is set to 0 at Γ to allow better comparison. The figures in blue represent the average values over the 50 points of the trajectory.	133
4.4.21	Valence band top energy. For each of the 50 time steps, this energy is set to 0 at Γ to allow better comparison. The figures in blue represent the average values over the 50 points of the trajectory.	134
5.2.1	Convergence tests for PbI_2 on the plane waves' energy cutoff parameter.	142
5.2.2	Convergence tests for PbI_2 on the number of k points used to sample the Brillouin zone.	143
5.2.3	Stability diagrams of cubic $MAPbI_3$ obtained by DFT calculations. The diagram on the left is taken from Ref. [4]	145
5.2.4	Stability diagram of cubic $CsPbI_3$ obtained by DFT calculations.	145
5.4.1	Dielectric matrices of $CsPbI_3$ in the high-frequency (ϵ_∞) and static (ϵ_0) regimes obtained from DFPT.	162
5.4.2	Dielectric matrices of $MAPbI_3$ in the high-frequency (ϵ_∞) and static (ϵ_0) regimes obtained from DFPT.	162
5.5.1	Tetrahedral sites (in blue) in the cubic perovskite structure.	164
5.5.2	The octahedral site is occupied by the organic molecule. The red, purple, green, yellow, grey and blue atoms respectively denote O, Pb, I, C, N and H.	165
5.5.3	Carbonyl group (aldehyde).	166
5.5.4	Migration of the inserted oxygen atom from the substitutional hydrogen site to what seems to be an interstitial site inside the inorganic octahedra PbI_6 after geometry optimization. The red, dark grey, purple, brown, light grey and white atoms respectively denote O, Pb, I, C, N and H.	167
5.5.5	Substitution of 2 hydrogen atoms by 1 oxygen, structure after geometry optimization. The red, dark grey, purple, brown, light grey and white atoms respectively denote O, Pb, I, C, N and H.	168

5.5.6	Electronic band structure of the pristine $MAPbI_3$ single cell.	168
5.5.7	Electronic band structure of the pristine $MAPbI_3$ $2 \times 2 \times 2$ supercell. Fully occupied bands are shown in blue.	169
5.5.8	Electronic band structure and oxygen projected density of states (DOS) of the structure with an interstitial oxygen atom.	169
5.5.9	Electronic band structure and oxygen projected density of states (DOS) of the structure with the O_I defect.	170
5.5.10	Electronic band structure and oxygen projected density of states (DOS) of the structure with the O_N defect.	170
5.5.11	Electronic band structure and oxygen projected density of states (DOS) of the structure with the O_H defect.	171
A.1.1	Cubic lattice	190
A.1.2	Tetragonal lattice	190
A.1.3	Orthorhombic lattice	191

LISTING OF FIGURES

Titre : Anharmonicité et instabilités dans les pérovskites halogénées pour les cellules solaires de dernière génération

Mots clés : cellules solaires pérovskites, anharmonicité, phonons, vieillissement, instabilité, DFT

Résumé : Les pérovskites hybrides halogénées (ABX_3) sont utilisées depuis cinq ans comme couches absorbantes pour de nouvelles cellules solaires à bas coût combinant les avantages des matériaux organiques (molécule A) et inorganiques (métal B et halogène X). Très récemment, des cellules solaires à boîtes quantiques à bases de pérovskites purement inorganiques ont également montré des efficacités prometteuses, ce qui en fait une alternative potentiellement stable et efficace à leurs cousins hybrides.

Le but de cette thèse de doctorat est d'étudier et de mieux comprendre les instabilités structurelles et thermodynamiques de ces pérovskites halogénées, avec un focus sur la pérovskite purement inorganique $CsPbI_3$.

Dans un premier temps les propriétés vibrationnelles et électroniques des différentes phases de $CsPbI_3$ sont étudiées grâce à différentes techniques ab-initio, dont la plupart sont basées sur la théorie de la fonctionnelle de la densité (DFT) et son approche en réponse linéaire (DFPT). Alors que la phase γ noire, cruciale pour les applications photovoltaïques, se comporte de manière harmonique autour de l'équilibre, pour les

trois autres phases nos calculs de phonons froids révèlent une instabilité de double puits au centre de la zone de Brillouin. Nos calculs montrent également que le terme d'entropie d'ordre-désordre lié à ce double puits est crucial pour empêcher la formation de la phase pérovskitoïde jaune. Nous analysons ensuite en détail les changements structurels et l'effet Rashba dynamique le long de trajectoires de dynamique moléculaire à la lumière de ces résultats.

La seconde partie de la thèse porte sur la stabilité thermodynamique de la pérovskite hybride $MAPbI_3$. Notre étude expérimentale par ellipsométrie apporte une meilleure compréhension de la décomposition chimique de $MAPbI_3$ en ses deux précurseurs, l'iodure de méthylammonium et l'iodure de plomb, que nous avons prédite grâce à des calculs de diagrammes de stabilité DFT et que nous confirmons par diffraction des rayons X. Enfin, nous démontrons que la pérovskite hybride $MAPbI_3$ se comporte davantage comme les composés inorganiques (grande constante diélectrique, faible énergie de liaison des excitons) que comme les matériaux organiques (faible constante diélectrique, forte énergie de liaison d'exciton).

Title : Anharmonicity and Instabilities in Halide Perovskites for Last Generation Solar Cells

Keywords: perovskite solar cells, anharmonicity, phonons, aging, instability, DFT

Abstract : Hybrid halide perovskites (ABX_3) have emerged over the past five years as absorber layers for novel high-efficiency low-cost solar cells combining the advantages of organic (molecule A) and inorganic (metal B, halogen X) materials. Very recently, fully inorganic perovskite quantum dots also led to promising efficiencies, making them a potentially stable and efficient alternative to their hybrid cousins.

The aim of this PhD thesis is to study and better understand both the structural and thermodynamic instabilities of these halide perovskites, with a specific focus on purely inorganic $CsPbI_3$ structures.

We first use various ab-initio techniques, the majority of which are based on Density Functional Theory (DFT) and its linear-response approach (DFPT), to investigate the vibrational and electronic properties of the different phases of $CsPbI_3$. While the black γ -phase, crucial for photovoltaic applications, is shown to behave harmonically around equilibrium, for the other three phases frozen phonon calculations reveal a Brillouin zone center

double-well instability. We also show that avoiding the order-disorder entropy term arising from these double-well instabilities is key in order to prevent the formation of the yellow perovskitoid phase, and evidence a Rashba effect when using the symmetry breaking structures obtained through frozen phonon calculations. We then analyze the structural changes and the dynamical Rashba splitting along molecular dynamics trajectories in the light of our findings.

In a second phase, we investigate the thermodynamical stability of hybrid perovskite $MAPbI_3$. Our experimental ellipsometry-based study brings better understanding of the chemical decomposition of $MAPbI_3$ into its two precursors, methylammonium and lead iodides, which we predicted using DFT stability diagram calculations and which we confirm by X-Ray diffraction. Last, we prove that hybrid perovskite structure $MAPbI_3$ behaves more like inorganic compounds (high dielectric constant, low exciton binding energy) than like organic materials (low dielectric constant, high exciton binding energy).

